Development of Metal-Free Photocatalytic Systems through Modification of Graphene Surfaces using Electron Transfer Chemistry

David Peter Martin

Submitted in accordance with the requirements for the degree of Doctor of Philosophy

The University of Leeds

School of Chemistry

March 2022

The candidate confirms that the work submitted is his own, except where work which has formed part of jointly authored publications has been included. The contribution of the candidate and the other authors to this work has been explicitly indicated below. The candidate confirms that appropriate credit has been given within the thesis where reference has been made to the work of others.

Chapter 2. The Fabrication and Characterisation of Phenazine-Graphene as a Model System uses the following publications:

1. Martin, D.P., Tariq, A., Richards, B.D.O., Jose, G., Krasnikov, S.A., Kulak, A. and Sergeeva, N.N. White light induced covalent modification of graphene using a phenazine dye. Chem Commun. 2017, 53(77), pp.10715-10718.

The work attributable to the candidate includes the synthesis, powder X-ray diffraction, FTIR, fluorescence and UV-vis data. This paper only refers to Phenazine diazonium salt and does not involve any other material mentioned in this chapter.

2. Sergeeva, N.N., Chaika, A.N., Walls, B., Murphy, B.E., Walshe, K., Martin, D.P., Richards, B.D.O., Jose, G., Fleischer, K., Aristov, V.Y., Molodtsova, O.V., Shvets, I.V. and Krasnikov, S.A. A photochemical approach for a fast and self-limited covalent modification of surface supported graphene with photoactive dyes. Nanotechnology. 2018, 29(27), p.275705.

The work attributable to the candidate includes the synthesis, powder X-ray diffraction, FTIR, fluorescence and UV-vis data of all materials, interpretation of SEM images and the collection of Raman spectra on graphene materials that were not on silicon carbide supports. Work attributable to other parties are the SEM data collection by A. Kulak, Pnz-G on silicon carbide Raman spectra, DFT and STM collected and interpreted by Krasnikov *et al.* for graphene on silicon carbide. Both papers only refer to Pnz-G and do not involve any other material mentioned in this chapter.

Acknowledgements

I would like to thank my supervisor, Natalia Sergeeva, for her support and guidance throughout this project.

I would like to thank the Clothworkers' Foundation and University of Leeds for the funding they provided to the project.

I would like to thank my group and colleagues for their support and help.

I would also like to thank all the collaborators who contributed to some of the work in this project and have been attributed with the work they have done.

Finally, I would like to thank my friends and family who have been a strong network of support along this journey.

Abstract

Herein, the fabrication of five dye-graphene hybrids is described through the formation of diazonium salts that are used to chemically modify graphene. The method involved the formation of a diazonium salt as a reactive species. The dyes attached to graphene in these hybrids were phenazine, fluorescein, chromone, purine and thionine. However, a change in methodology from a two-step to a one-pot was required for chromone and fluorescein due to the reduced stability of their diazonium salts.

The hybrids were characterised by FTIR, UV-vis, fluorescence, powder X-ray diffraction, SEM and BET, with extra analysis recorded for a model system of phenazine-graphene. The analysis showed changes to the graphene surface, including a reduction in surface area by up to 65 % according to BET data, an increase in the agglomeration in SEM, and the formation of disorder – through peak shifts (of up to $2\theta = 0.5$ °) and broadening (of up to 60 %) in the main graphitic peak of PXRD – and new diffraction patterns in PXRD. Raman spectroscopy was initially used to study phenazine-graphene system and showed an increase in the intensity of D-band corresponding to the defects brought by covalent functionalisation. However, this method later proved less useful due to fluorescence background effects from the alternative dyes used in subsequent hybrids. UV-vis absorption analysis revealed an absorbance peak shift in each of the hybrid materials containing visible light absorbing dyes. TGA analysis was also used to identify where degradations of attached dyes could be seen in those samples that had standards available from our own experiments or those in the literature. This also allowed for some approximations of surface coverage, which were found to be approximately 10 % for the phenazine-graphene and approximately 14 % for the fluorescein-graphene.

The removal of organic pollutants was chosen as a potential application of these new materials. Testing of the hybrids, using methylene blue and Rhodamine B as two common model compounds to mimic organic pollutants, was carried out under different conditions including light illumination and pH. These experiments showed that there was a process occurring to cause a permanent loss of both model compounds from solution in most cases. The most promising hybrids were phenazine-graphene, purine-graphene, and fluorescein-graphene, which could degrade methylene blue to an extent that is comparable to TiO_2. In these cases, up to 70 % of methylene blue removal was observed already after 20 minutes. Chromone-graphene showed low reactivity under light illumination but good reactivity without illumination. In contrast, thionine-graphene showed no reactivity with methylene blue except in alkaline conditions which was attributed to the alkaline medium, which is known to facilitate degradation of the dye. The results with Rhodamine B showed a slight decrease in degradation and a maximum of 50 % degradation was observed in the best case of phenazine-graphene. Another difference between these cases was the preference for alkaline conditions in the methylene blue. In the case of Rhodamine B, the conditions played no significant

role in the irreversible dye removal. This was decided to be due to methylene blue having a natural degradation in alkaline conditions.

Photocatalytic studies were carried out with several organic compounds to identify potential reaction mechanisms including redox reactions and reactive oxygen species formation. The successful hydroxylation of terephthalic acid in alkaline and neutral conditions was achieved and was an indication of the involvement of OH radical species upon excitation of the dye-graphene hybrids. The progress of the reaction was monitored by fluorescence spectroscopy to detect the conversion by the shift of emission peak at 382 nm to a peak at 430 nm. To understand the mechanism of degradation under acidic conditions, naphthyl-2-boronic acid was converted to a mixture of products, suggesting the formation of both naphthalene and naphthol. The reduction of benzyl alcohol showed low activity but was improved in oxygenated solution. Potential mechanisms and reactive oxygen species involved in the activity have been proposed as peroxide or superoxide radical formation from both characterisation and photocatalytic results.

Table of Contents

Table of Figures

Abbreviations

Abbreviation	**Meaning**
ATR	Attenuated Total Reflectance
BET	Brunauer-Emmett Teller (Theory)
br	Broad (IR)
CB	Conductance Band
Chr-G	2-methylchromone-Graphene
COSY	Correlated Spectroscopy
CT	Charge Transfer
CTE	Charge Transfer Exciton
d	d-spacing (Powder X-Ray) / Doublet (NMR)
DCM	Dichloromethane
Diazonium Salt **1** / DS1*BF_4	Neutral Red Diazonium Tetrafluoroborate Salt
DFT	Density Function Theory
DMF	Dimethylformamide
DMSO	Dimethyl Sulphoxide
DOS	Density of States
Em	Emission
E_{ox}	Oxidation Potential
ESI	Electrospray Ionisation
Ex	Excitation Wavelength
FFT	Fast Fourier Transform
Fsc-G	Fluorescein Modified Graphene
GC	Glassy Carbon
GCMS	Gas Chromatography Mass Spectroscopy
GnP	Graphene Nano-Platelet
GO	Graphene Oxide
H-MDAP	Protonated N8,N8,3-trimethyl-8-phenazineamine
HOMO	Highest Occupied Molecular Orbital
HRMS	High Resolution Mass Spectroscopy
Hz	Hertz
IFFT	Inverse Fast Fourier Transform
FTIR	Fourier Transformed Infrared
ITO	Indium Tin Oxide
J	Coupling Constant
LC-MS	Liquid Chromatography Mass Spectrometry
LED	Light Emitting Diode
LUMO	Lowest Unoccupied Molecular Orbital
m	Multiplet (NMR) / Medium (FTIR)
MB	Methylene Blue
MDAP	N8,N8,3-trimethyl-8-phenazineamine / Methyl-dimethylamino-phenazine
MS	Mass Spectroscopy
MWCNT	Multi-Walled Carbon Nanotube
m/z	Mass/Charge
NMR	Nuclear Magnetic Resonance
ORR	Oxygen Reduction Reaction
PBS	Phosphate Buffered Solution
Pnz-G	N8,N8,3-trimethyl-8-phenazineamine Modified Graphene

Pnz-G S	N8,N8,3-trimethyl-8-phenazineamine Modified 2DTech Graphene
Pnz-G.TFA	N8,N8,3-trimethyl-8-phenazineamine Modified Graphene (using trifluoroacetic acid)
Pnz-G.HCl	N8,N8,3-trimethyl-8-phenazineamine Modified Graphene (using hydrochloric acid)
ppm	Parts Per Million
Pur-G	Purine Modified Graphene
PXRD	Powder X-Ray Diffraction
q	Quartet (NMR)
rGO	Reduced Graphene Oxide
RhB	Rhodamine B
ROS	Reactive Oxygen Species
s	Singlet (NMR) / Strong (IR)
SAED	Selected Area Electron Diffraction
SCE	Standard Calomel Electrode
SEM	Scanning Electron Microscopy
SSE	Silver-Silver Chloride Electrode
STM	Scanning Tunnelling Microscopy
STS	Scanning Tunnelling Spectroscopy
t	Triplet (NMR)
TA	Terephthalic Acid
TEM	Transmission Electron Microscopy
TFA	Trifluoroacetic Acid
TGA	Thermo-Gravimetric Analysis
Thi-G	Thionine Modified Graphene
TLC	Thin Layer Chromatography
UV	Ultraviolet
VB	Valence Band
w	Weak (IR)
λ	Wavelength
λ_{max}	Maximum Intensity Wavelength
δ	Chemical Shift

Chapter 1: Research Introduction

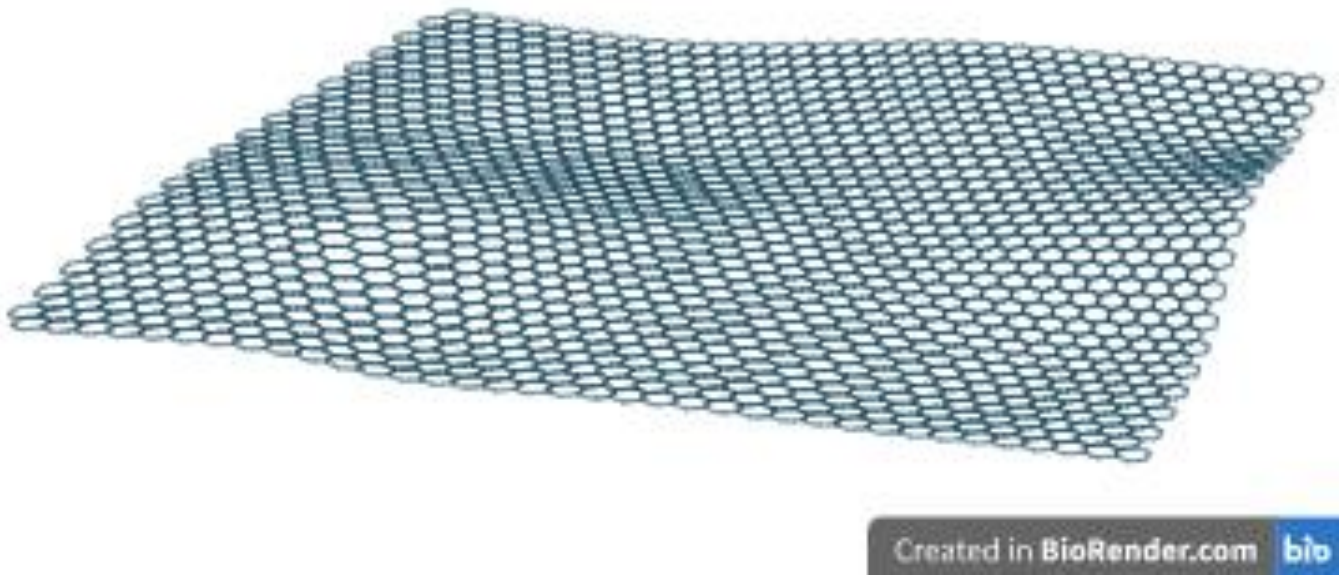

Created with BioRender.com

1.1 Graphene

The term graphene had been used to generally describe the properties of these carbon-based allotropes. However, Graphene is a single graphitic layer obtained using “sticky” or scotch tape or a mechanical exfoliation of graphite, which both entail the separation of these single layers from the bulk material. This is achieved through adhesive tape stripping these layers off or a method such as sonication or shearing which can exfoliate the layers off the bulk graphite. Its structure is a 2-dimensional, planar sheet of carbon in a honeycomb structure, consisting of single and double bonds to create a conjugated sp^2 hybridised system across the entire sheet. It is one of several allotropes of carbon, which include (but are not limited to) fullerenes, carbon nanotubes and diamond. [1-5]

Planar graphene had been presumed too unstable, in comparison to the formation of soot and other forms, to exist in a free state until 2004, where Novoselov and Geim *et al.* reported observations of the electric field effects of few-layer graphene.[1, 6] Part of this previous belief was that graphitic cone structures are driven into formation by enthalpy and their distribution of the angle of the cones driven by entropy, which could eventually form nanotubes and fullerenes, depending on the pathway.[6]

Since its discovery in 2004, research into graphene has increased dramatically, with the number of papers released on the topic over the past two decades increasing exponentially.[7] The driving force behind this ever-growing interest in graphene is the properties that are linked to it, which resulted in its nickname as a “wonder material”.[8]

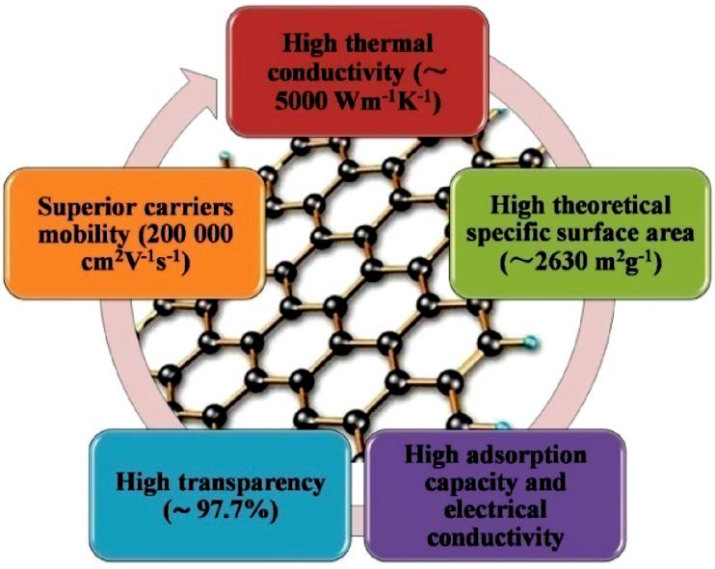

Figure 1: The properties of pristine graphene. Copied with permission from reference (7).

Graphene has many advantageous properties for catalysis and solid support usage, which are summarised in Figure 1. The first is the very high carriers mobility of up to 200,000 $cm^2V^{-1}s^{-1}$ which allows for the rapid transfer of electrons across the graphene surface from one catalytic site to

another. This means that the effect of reduction and oxidation processes in tandem can stabilise electron counts across the catalyst rapidly and also allows for the movement of holes and electrons over the catalyst to potentially avoid recombination on a site.[7, 9]

Secondly, a high theoretical surface area of approximately 2630 m^2g^{-1} allows for more reaction sites across the surface and also allows for more reactions to be possible on the catalyst.[7] Additionally, the high transparency of graphene allows the use of coloured molecules or nanoparticles as photocatalysts or photo-absorbers for catalysis as the graphene sheet should not hinder their absorption capacity.[7, 10] Graphene has also been claimed to have "excellent environmental compatibility" which means that it should be usable with lower toxicity compared to some metals.[7]

Graphene can also be modified via several other reaction types, including 1,3-dipolar cycloaddition, nitrene addition and amidation. These methods can be used to combine graphene with small photoactive molecules in order to give the surface a photo-based function.[11] It has also been noted that graphene surface can be chemically modified in a controlled manner via electron puddles, which are charge fluctuations in the graphene plane.[12] Modification through diazonium salts can be performed easily with small aromatics (Figure 2) but has been restricted to larger moieties.[11, 13] Alternatively, a small aromatic structure can be reacted onto the graphene sheet and then chemically functionalised further to form the desired structure covalently attached to the graphene surface.[11, 13]

Recently, a method has been found for the modification of surfaces using thermally unstable functional groups, where the group was able to modify a graphene oxide layer with sodium azide. This method allows controlled azide functionalisation leading towards N-doped graphene through release of N_2.[14] However, it is also possible to use well known reaction types to modify graphene, such as the click-type reaction. Also, the Diels-Alder reaction of a diene and a dienophile can be used to modify graphene, with graphene being capable of acting as both the diene and the dienophile.[15]

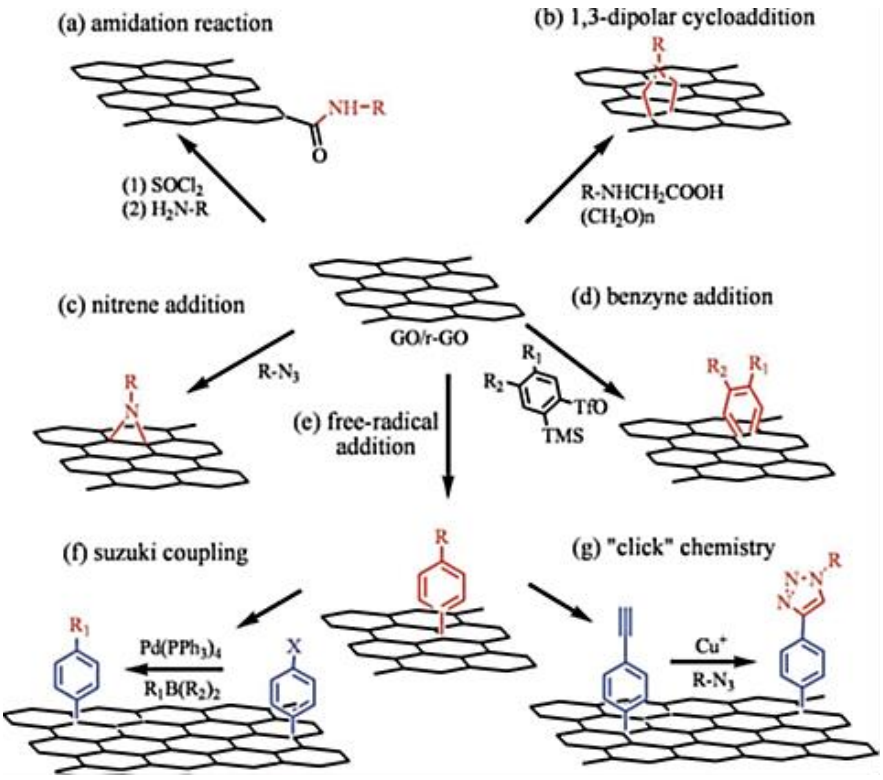

Figure 2: A collection of typical reactions for the covalent attachment of photoactive small molecules to graphene, graphene oxide and reduced-graphene oxide. Copied with permission from reference (11).

These methods can be used with small photoactive molecules in order to give the surface a photo-based function.[11] It has also been noted that graphene can be modified on its surface in a controlled manner, through the use of electron puddles.[12] The modification with organic molecules is made easier by the work function of graphene closely matching the orbital levels of such molecules, at 4.4 eV to 4.5 eV.[11]

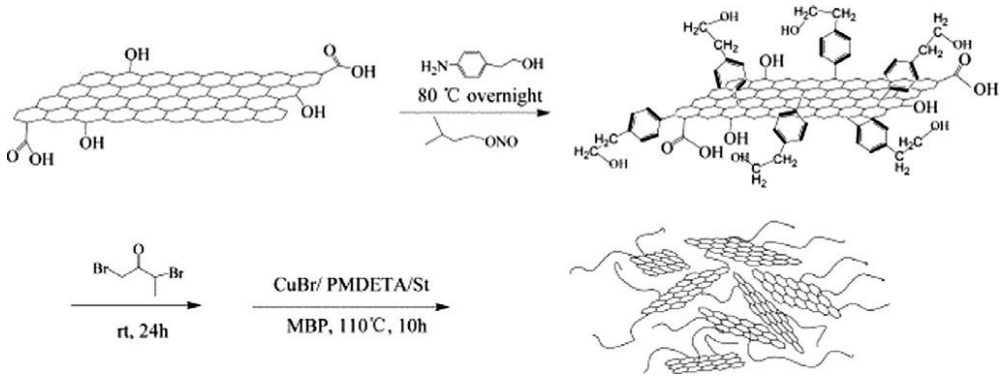

Figure 3: An example of multistep surface modification reactions to form polystyrene functionalised graphene. Copied with permission from reference (5, 11).

Additionally, it has been found that graphene oxides and reduced graphene oxides have active sites on the oxygen functional groups, such as epoxy, quinone and benzyl alcohol-type groups, alongside edges and “frustrated” Lewis pairs. The techniques and experiments that support this include density

function theory (DFT) calculations, nuclear magnetic resonance (NMR), Raman and control reactions (with CO_2 or NH_3).[10]

Other carbon materials, such as natural and synthetic graphite, fullerenes and multi-walled carbon nanotubes have shown varying catalytic performance for oxidation of acrolein. However, these reactions needed temperatures of 300 °C and led to some of the examples deactivating. This would suggest that avoiding high temperatures and extreme oxidative stress is beneficial for metal-free catalysts. [16]

1.2 Modification of Inert Surfaces

Graphene is a material of great interest in metal-free catalysis, which is driven by the excellent surface area, electron transfer to, from, and along graphene sheets, and its versatility, allowing it to be used in many applications as part of a system.[4] The covalent functionalisation of graphene surface with reactive molecules can lead to an alteration of its electronic properties, create defects in the surface or even rupture parts of the aromatic framework.[17] However, this procedure also offers the possibility to improve and to enhance physical properties, such as solubility, processability[17] or the band gap.

Such an improvement in functionality is demonstrated by the modification of glassy carbon (GC) electrode to form a p-aminophenyl terminated graphene oxide (GO). This modification gives the electrode the capability to undergo complexation with cadmium(II) and copper(II) ions in solution, to act as a unique sensor platform.[18] This study demonstrates a great potential of inert carbon-based materials, when they are modified with more reactive functional groups.

One method of graphene surface modification is doping the surface with non-metals, such as nitrogen atoms. This involves the substitution of some carbon atoms by the desired non-metallic element, which can alter the electronic structure of the graphene, potentially leading to either catalytic activity or inhibition of redox chemistry on the surface.[19] It has been shown that the use of nitrogen atoms can allow the graphene to coordinate with metal ions in solution to create a catalytic system, which is the most frequently reported catalytic system for heteroatom-doped graphene photocatalysts.[19, 20] A cobalt coordinated N-doped graphene catalyst is shown to have a highly porous structure, which aided in the enhancement of its photocatalytic oxygen reduction reaction (ORR) and the pyrrolic nitrogen atoms within the N-doped graphene are also proposed to be another reason for the enhanced catalytic activity.[20] This method has attracted attention due to its lower costs, high catalytic activity and resistance to surface poisoning by methanol and carbon dioxide.[19, 20] There are

also examples where research has been taken a step further to make a co-doped graphene using two different elements. Electrochemical data from graphene co-doped with nitrogen and sulphur show that this system could undergo the direct four electron pathway of the ORR, rather than the two-step process typical for undoped graphene. It showed improved ORR activity for the number of transferred electrons, alongside an improved current density and potential onset for a metal-free electrocatalyst.[21]

Doped graphene has been used on a silicon surface (produced either by photolithography on Si/SiO_2 or by transfer of graphene onto the silicon surface) in order to achieve a solar energy conversion of 8.6 %, compared to graphene sheets on n-type-doped Si, which gave an efficiency of 1.26 %.[19] In addition, the N-doped graphene showed greater ORR catalytic selectivity and methanol resistance compared to commercially available Pt-C catalysts.[19, 20] However, some of these N-doped graphene systems have lacked light absorption capacity and quantum efficiency therefore leading to poor photocatalysts, despite various methods being used to improve these efficiencies, such as templated methods, copolymerisation and semiconductor modification.[22]

However, not all modifications of the graphene surface need to be as intricately designed as single or multi-atom doping. In some cases, the diketone edges of the graphene sheets have been modified to create a phenazine structure capable of bidentate coordination to a ruthenium(II) metal centre as a photon absorbing group. Using this method, it has been shown that they can combine the tuning of molecular catalysts with the electronic properties of extended metallic materials through the combination of a metal centre connected directly to a conjugated aromatic system.[23] In other cases, the use of intramolecular forces has been utilised for making a composite of a polymer on graphene for transistor technologies, whilst there has also been a sandwich structure of dye-graphene or graphene-dye-graphene for photon gating.[24, 25] Similarly, it is possible to create sheets of graphene and extended metallic sheets such as MoS_2 or Fe_2O_3 in order to improve electron transfers within photodetectors and high composite supercapacitors.[26]

Fullerene, C_{60}, is an inert extended aromatic hydrocarbon that has also been modified previously, by using diazonium salts, often resulting in a 6,6-closed adduct or, in some cases, a 6,5-open adduct.[27] This method allows for the modification of fullerene at the five-membered or six-membered sites to form a cyclopropyl function, with varied yields that appear to be affected by the readiness of each regioisomer to form.[27] It has also been noted that at 300 °C fullerenes have a greater catalytic performance than natural or synthetic graphene or multi-walled carbon nanotubes for the oxidation of acrolein to acrylic acid,[16] while also being used as part of modifications into dye-sensitised solar cells.[28]

The diazonium functional group is of particular relevance for graphene surface modification and is generally highly unstable and likely to be released to leave a reactive radical species.[29] This allows for the formation of carbon-carbon covalent bond formation even between aromatic groups and retaining aromaticity. [29-33] However, this process is often catalysed by either organic or organometallic compounds.[30-32] This has led to the use of aryl-diazonium compounds for functionalising surfaces of graphene or inorganic based surfaces (e.g. indium tin oxide (ITO), gold) with an aryl layer, due to the electron-rich surface's ability to donate an electron to the diazonium and begin the reaction process in the place of a catalyst.[32-37] One application of using diazonium salts is to modify a glass surface coated with ITO and then forming a diazonium on the functionalised surface to allow the polymerisation of methacrylic acid and ethylene glycol dimethacrylate.[34] One additional benefit is that in some cases, these diazonium salts can utilise visible light to modify the inorganic surfaces and for C-H arylation reactions but can lead to polymerisation on surfaces and bifacial modification of graphitic sheets.[38, 39]

It is well-known that dyes can form diazonium salts without losing their ability to absorb visible light in the final product due to the typical use of the diazonium salt in the formation of azo dyes, a family of dyes containing a nitrogen double bond.[40] Since amino forms of many dyes exist, it is possible to match a known dye structure that is desired for use in the formation of a hybrid, with a suitable amino dye.

In materials chemistry, it is known that aryl diazonium salts can be used to modify electron rich surfaces such as gold, ITO and glassy carbon.[36] In these cases, for the surfaces to have ultrahigh sensitivity towards diazonium salt, it is key to achieve: (i) thin coatings of 20-30 nm, (ii) use of embedded nanoparticles to enhance current flow, (iii) rigidity, and (iv) polar solvents for binding.[36] Diazonium reactions can be undertaken under visible light with a suitable photocatalyst, which can then allow for modification without the need for *in situ* generation.[38, 41] It has been shown that para-substituted aryl diazonium salts can react with a gold surface in the presence of light and a photosensitiser.[38] Diazonium salts containing a para-sulfonic acid group, have been used to improve the delamination of MXenes, involving the separation of layers of molecules such as Ti_3C_2 in aqueous media.[42]

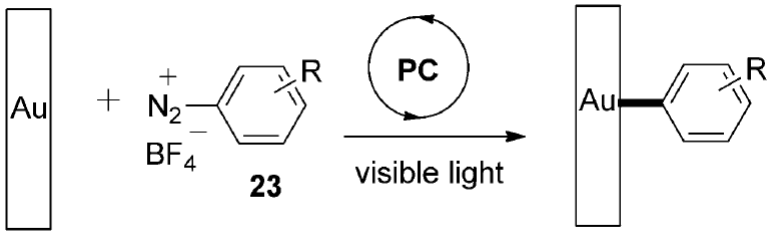

Figure 4: The photo-redox catalytic functionalisation of a gold surface using a diazonium salt. Copied with permission from reference (32).

However, it has been shown that the diazonium can be grafted to graphene through electron transfer from the graphene to release N_2 and form a radical that then reacts onto the graphene surface.[33, 43, 44] This is thanks to the overlap between the occupied graphene states and the unoccupied states of the diazonium.[33] The limiting step of these reactions is the reduction of the diazonium salt.[33]

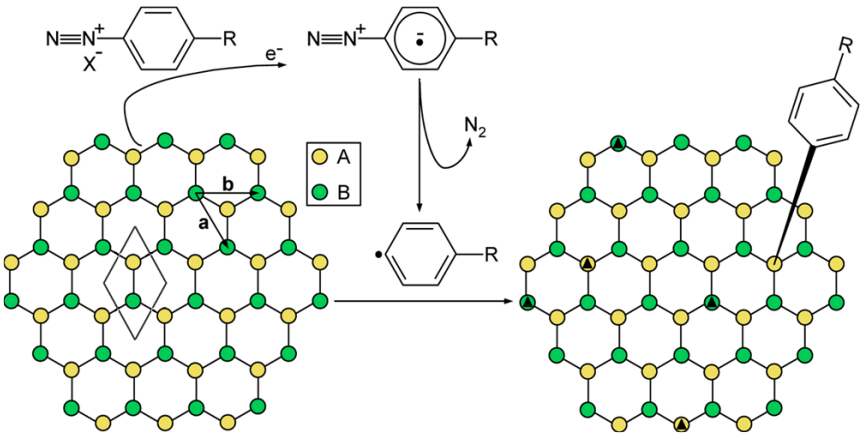

Figure 5: A scheme for the general process of covalently binding an aryl layer onto graphene via diazotisation. Reprinted with permission from reference (33).

When modifying carbon surfaces, it is often through electroreduction of the diazonium onto the carbon substrate surface, using protic ionic liquids as a solvent, where the protons have often been exchanged from the diazonium precursor in the presence of sodium nitrite. [35, 45] This electrochemical method is able to increase the rate of reaction by applying an electrical voltage through the graphene, which can draw the diazonium salts towards the surface to create a greater local concentration at the surface, or by shifting the Fermi level of graphene.[43] In these situations, the voltametric response from a modified glassy carbon electrode is the same whether the diazonium used is dissolved into the protic ionic solvent or was made *in situ*.[45] In addition, it has been shown that photoredox catalysis can also result in the modification of surfaces such as gold.[32] However, carbon surfaces have also been chemically modified using reducing agents with the diazonium salts in order to create a surface with modified properties.[46]

The electrochemical method is typically faster than passive methods, where graphene is exposed to the reagents in aqueous or organic solvent solutions. This method creates a higher density of functionalised sites, through the application of a bias that creates electron-rich areas with accelerated electron transfer step. However, the slower method of exposing the graphene to diazonium salts chemically is much simpler to implement than electrografting, whilst also providing better control over the reaction due to the slower rates.[43]

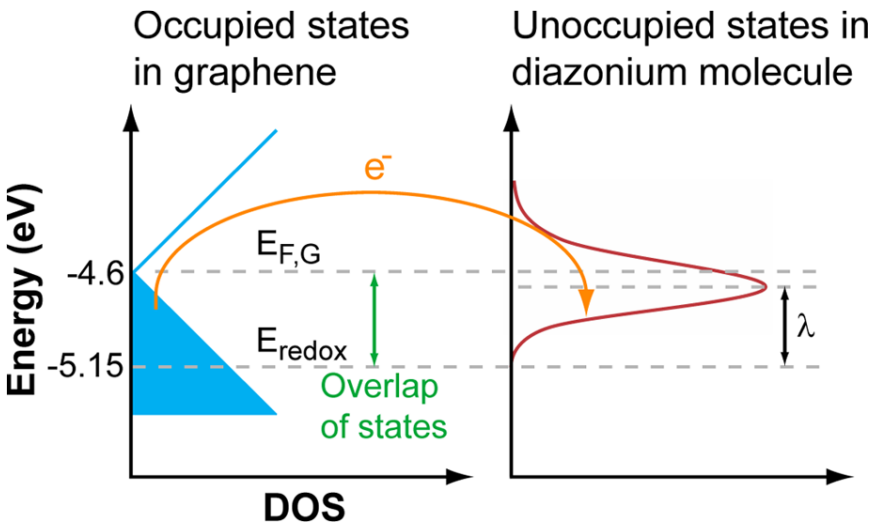

Figure 6: A representation of the density of states in graphene and the unoccupied states of a typical diazonium salt and how the electron transfer is permitted. Reprinted with permission from reference (33).

A similar radical reaction for graphene modification can occur in benzoyl peroxide, which is initiated through irradiation of the peroxide with light to form the radical. The reaction also proceeds through the donation of an electron from the graphene into the lowest unoccupied molecular orbital (LUMO) of the peroxide. [47]

An application for covalently bound diazonium compounds to electrode surfaces is in electroanalysis and many diazonium salts have formed highly sensitive and robust electroanalytical molecular grafts, particularly targeted for dopamine, quercetin, gallic acid or melamine. They have also shown to have a range of solvents that they can function within, depending upon the diazonium used for grafting to the electrode and the target for analysis. [36]

Recently, chemical companies started to sell diazonium salts of organic compounds, which can be stored and transported in the form of stable tetrafluoroborate salts. This contrasts with the less stable, but commonly used in synthetic procedures, chloride salts.[40, 48] This opportunity allows for a large scale diazonium synthesis and provides a greater range of chemical utilisation in different reactions without the need of *in situ* generation, saving on solvent, chemicals and energy usage per reaction.

In addition to these modifications, graphene in its pure form, as well as in its oxide forms, has been utilised in composites with metals and metal oxides.[5, 44, 49-56] These composites include modifications by metal atoms – silver containing composites, such as Ag-AgBr, Ag_2CO_3[49, 50] – to metal oxides, such as TiO_2, CuO_2, etc. as nanoparticles.[5] The addition of graphene is able to improve the electrochemical stability and provides a large capacity for ion intercalation, which appears to improve the energy and current densities.[5] In other cases, such as silver composites and TiO_2, it can be shown that the combination of these nanoparticles and graphene creates and increases photocatalytic activity towards organic oxidation/degradation.[49, 50, 52-54] Also, a composite of manganese and graphene oxide creates a stable free-standing peroxide sensor with improved humidity resistance.[57] These different uses and modifications show graphene to be a versatile and flexible support for many applications.

There is an example of acid black 31 being modified with graphene oxide through a five-step process to form a polyurethane-based structure attached to the dye, which was then emulsified with graphene oxide to form blended materials with reduced tensile strength but increased colour fastness. This composite also shows that as more graphene oxide was added to the emulsion, the thermal stability also improved, showing the effect of graphitic materials to improve this property for carbon-based systems.[58] However, this means an organic dye has not yet been directly attached to graphene and has only been linked to the end of an organic chain attached to graphene. This does create the challenge of potential changes to the optical properties of the attached dye, which are important to photocatalysts.[7]

1.3 The Purpose of Modification

Over recent years, research into photocatalytic systems has grown significantly, particularly for dye-sensitised solar cells and artificial photosynthetic systems.[19, 59-61] These systems often involve the modification of an electron rich surface to add functionality, which can be induced by excitation from the absorption of photons of a specific wavelength.[9, 19] A variety of molecules ranging from inorganic to organic based dyes are used to absorb photons and to enable charge transfer (CT) to and from the electron rich surface.[19] The final properties of the modified system depend on the dye, catalyst and the surface, thus any change in one of these components can result in an alteration or loss of a function or property.[19]

The purpose of modifying surfaces is to alter its electronic, optical and adsorption properties. This can be achieved by chemical functionalisation using methods such as nanoparticle deposition, radical addition, photo-polymerisation and photoinduced redox reactions.[34, 37, 62, 63] This has been successfully demonstrated using a range of materials e.g. quantum dots, organic molecules and

organometallics.[19, 64] Surfaces used for modification are usually electron rich and can be either attached to an electrode for electrochemical use or coated on a glass surface.[19, 34] A frequently used surface for an electrode is titania (TiO_2) as a thin layer, due to the innate photocatalytic properties of the TiO_2 under ultraviolet (UV) irradiation, which were first reported in 1964 and since then frequently used as a benchmark of photocatalytic activity among heterogeneous photocatalysts.[65] TiO_2 surface has a wide bandgap, reduced cost compared to similar surfaces, large available surface area in the mesoporous material for dye adsorption, and it is environmentally friendly.[63, 64] However, TiO_2 is not effective as a photocatalyst on its own due to (i) the high recombination rate of the electron-hole pair, (ii) poor phase stability and ability to tune the band gap and (iii) low solubility - all of which are issues with most semiconductors[66] - (iv) TiO_2 can also only utilise UV light.[65] However, when TiO_2 is modified with dye molecules, these systems are able to utilise visible light for catalytic functions through a process that begins with the absorption of a photon by the dye molecules.[9, 19, 67] This leads to excitation of the dye and the injection of an electron into the TiO_2 conduction band.[67] A requirement of rapid transfer of the electrons is a thermodynamic one; the transfer must either be exergonic or energy-neutral.[60]

Graphene surface activity can also be affected by the support that it has been grown on; several support systems have been tested and compared by Raman spectroscopy.[33] This variability in activity allows for graphene patterning by imprinting lines of an inert compound such as octadecyltrichlorosilane, which results in lower functionalisation of the graphene at these areas compared to SiO_2 supported sites and therefore can be used for spatially patterning proteins onto graphene without damaging the biomolecules.[33]

Similar to the system we planned to fabricate, organic solar cells always rely on a conductive polymer or small organic molecules for the absorption of light and the transport of electrons. Since the conductor involved usually needs to be transparent, graphene is a good molecule for this purpose due to both its transparency to visible light and the capability to accept electrons from low-barriered organic materials, due to a work function of 4.4 to 4.5 eV.[11] Organic solar cells face reduced efficiency when compared to more traditional inorganic semiconductors, mainly due to “energy level misalignment, insufficient light trapping and absorption, low exciton diffusion lengths, non-radiative recombination of charges or charge transfer excitons (CTEs), and low carrier mobilities”.[11]

1.4 Organic Dyes

Dyes are molecules capable of light absorption and/or emission in the visible region of the electromagnetic spectrum. They have found numerous applications in the areas of non-conventional

usage such as solar energy conservation and storage, artificial photosynthesis, biomolecular imaging, photomedicine and photocatalysis to name a few.[68]

Here, the focus is on the usage of dyes and light for photocatalysis and photochemistry.[68] Many organic dyes are efficient photocatalysts such as eosin, Rhodamines, 3-cyano-1-methylquinoline and 9-phenyl-10-methylacridinium salt, which shows their structural diversity.[69-71] These dyes have various UV-vis absorption peaks, allowing some to be solar light photocatalysts or UV-light photocatalysts with a variety of organic pollutants they are capable of photodegrading. Riboflavin and Rose Bengal being two examples of heteroatomic photocatalysts with a wide range of pollutant targets according to a literature study.[69] Meanwhile heteroatomic organic photocatalysts such as acridines are capable of oxygenating ring-substituted toluenes and other small aromatic molecules.[70, 71]

Dyes have also shown their use within graphitic systems, as Rhodamine 6G has been used in a device within a "graphene sandwich structure" to create a photogate between two gold electrodes on a silicon support. This has been possible due to matching electronic properties of Rhodamine 6G and graphene.[7, 11, 25] Electron transfer between graphene and the dye, followed by electron transfer through photoexcitation of the dye, enables this system to be used as a photodetector.[25]

In 1991 by Grätzel, *et al*. published their seminal work on photoactive system comprised of TiO_2 and a trimeric ruthenium complex as visible light photosensitiser for DSSC application. This system showed increased efficiency and long-term stability than those previously reported such as ZnO with Rose Bengal and similar dyes.[72, 73] These n-type materials function through the generation of current when a photon is absorbed and results in electron transfer from the dye to the conductance band of the semi-conductor. The Grätzel example also utilised the roughness of the TiO_2 surface to increase the dye loading onto the semi-conductor.[67] Many of these dyes are now organometallic structures and utilise metals such as ruthenium, iridium or zinc, and the dye is used for absorption of solar energy which allows for a fast transfer of electrons.[28, 40, 62, 68, 72-74]

Phenazines are naturally occurring fused aromatic heterocycles with diverse physicochemical, optical and biological properties.[75-77] They are often strongly coloured and tend to participate in photoredox processes.[76] This makes them a generally cheap dye that can be easily utilised in photoactive systems.

A phenazine dye derivative can be complexed with a metal such as aluminium and coated onto ITO anodic and Mg:Ag cathodic supports.[75] This provides one of the best yellow light emitting organic devices (OLEDs) for maximum luminous efficiency.[75]

Also, phenazines and related compounds can be considered as potential Hepatitis C viral inhibitors. Analogues were made from N8,N8,3-trimethyl-2,8-phenazineamine (MDAP), which had high activity but low selectivity. Phenazines are capable of mediating the biological transmembrane electron transport from NADH to cytochrome C.[78, 79] This was discovered through incubation of Bacillus subtilis W23 and Bacillus subtilis aroD with phenazine methosulphate and washing away excess phenazine to leave attached phenazine on the membranes.[78]

Another phenazine that shows reactivity towards NAD^+/NADH (β-nicotinamide adenine dinucleotide) is 3-amino-7-dimethylamino-2-methylphenazine (Neutral Red). This particular phenazine dye is capable of forming a diazonium salt, which can allow modification of surfaces to form modified electrodes, though it can also self-adsorb onto electrodes. As a modified electrode, it also has the highest affinity for interactions with NAD^+, while Neutral Red also has the benefit of an unexpectedly high affinity to ITO and carbon electrodes. This is similar to phenothiazine and phenoxazine, but Neutral Red shows a higher binding affinity in nN of force for each method (self-adsorption, diazotisation and electropolymerisation).[79]

Analogues of the phenazine include modification at the carbon atoms or substitution of an aromatic nitrogen for oxygen or sulphur.[77] In some of these modifications, it was necessary to generate the diazonium salt of the phenazine *in situ*, which has the potential for use in C-C coupling for surface modification.[12, 41, 77] These diazonium intermediates are highly reactive and sensitive compounds, which usually have issues for storage and as such are used *in situ*, rather than in a neat form. It has been shown that C-C bonds can be created via the reaction of aryl diazonium salts and small heterocyclic molecules, such as furans and protected pyrroles in the presence of a photocatalyst.[38, 80]

Fluorescein is a dye previously used for a photocatalytic system.[30, 81] In one example, it was used to functionalise electrospun fibres which were coated in titania and gold nanoparticles. These fibres showed a 2-3 times greater visible light induced photodegradation of methylene blue (MB) than P-25 titania.[81] Additionally, when used with a gold catalyst, it has shown activity for the formation of arylated ether from an aryl diazonium salt at 88 % yield, whilst proving cheaper than the often used organometallic $[Ru(bpy)_3](PF_6)_2]$¸as a way to merge gold catalysis with photoredox chemistry.[30] Fluorescein absorbance also occupies a similar region of the visible spectrum to phenazine, absorbing at around 500 nm but displaying a green colour rather than the red or orange of the phenazine derivatives.[82] In addition, a brominated derivative known as eosin Y is a known photocatalyst which has been used within dye-sensitised photocatalysis, and could suggest the compatibility for fluorescein in a photocatalytic system.[62]

1.5 Characterisation

Graphene-based materials also bring challenges in their characterisation techniques. They cannot be analysed through conventional NMR, due to their generally low solubility, which also affects any solution-based analysis. Therefore, solid state and surface techniques are used; of the most importance are infrared (IR) spectroscopy, Raman, transmission electron microscopy (TEM), scanning tunnelling microscopy (STM), scanning tunnelling spectroscopy (STS), scanning electron microscopy (SEM), and powder X-ray diffraction (PXRD) methods.[2, 83-86] However, solid state NMR is also possible for these kinds of materials, but can give broad signals.[14, 87]

One of the main techniques that can be useful in this work is PXRD, which is frequently used for solid state materials, especially metal-based semiconductors like TiO_2. This is because the PXRD can give several pieces of information based on shifting, broadening, asymmetry and shape of the peaks, which can be affected by internal stress, crystallite lattice and point defects.[88-90] The diffraction patterns are also determined by the crystalline lattice of a material, so a graphene material that is not destroyed should generally maintain its signals post-modification, if the 3D lattice is not reordered too significantly.[91] It is also possible to use Bragg's Law to find distances between points in the lattice and if the lattice planes are known, then it can help to elucidate the packing and structuring of the material.[92] Also, if materials are a simple mixture, it is possible to identify individual molecules from the bulk through comparisons of PXRD signals, as they should maintain their major peaks, especially as PXRD of a mixture is a sum of the scattering from each component.[89-91] However, not all planes are known and a limitation from this is that without single crystal analysis, you cannot get a definitive picture of the 3D structure, as weaker diffracting components may not remain visible.[93]

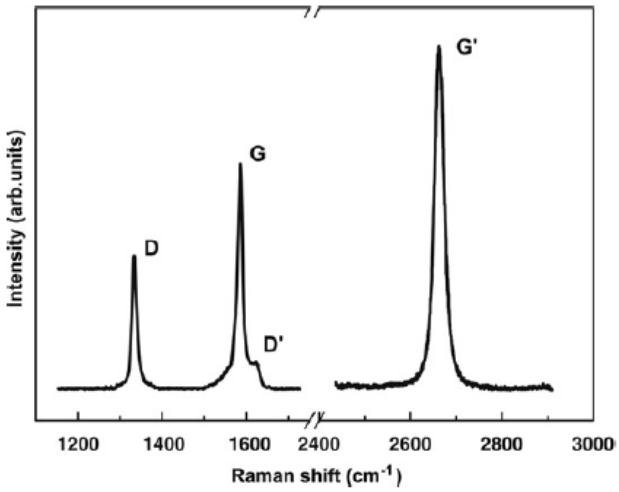

Figure 7: Raman spectra of a graphene edge. Copied with permission from reference (83).

Raman spectroscopy is a very useful technique for the analysis of graphene materials, due to the different bands present, as shown in Figure 7. These are the D, G and 2D or G' bands.[83-85] The G band that appears at approximately 1582 cm^{-1} is the most prominent feature of monolayer graphene, along with G' band at 2700 cm^{-1}, when a laser of 2.41 eV is used for excitation.[83] The D band appears at approximately half the frequency of G' at 1350 cm^{-1} using the same power laser source and is linked to the disorder or "defects" in the graphene sheet, often caused by modifications or reducing of the sheet.[83, 84] The D and G' bands also upshifts as the energy of the laser increases linearly, with the D band increasing roughly 50 cm^{-1} / eV and the G' upshifting by 100 cm^{-1} / eV.[83, 84] As the layers increase, the band most affected is the G' band, which has a slight shifting of the peak position and the shape of the curve, eventually becoming two overlaid peaks.[83] Also, the G band will sharpen and upshift if doped, meaning that Raman technique can be effective for determining layering, quality and doping of the graphene structure.[84, 93]

FTIR is another useful spectroscopic method, as it can help to identify new bond formations as well as identify changes in the functional group presence on the hybrid materials.[5, 49] This has even been shown to be useful in analysing metal-reduced graphene oxide (rGO) composites by detecting the relative decrease in certain functional groups' intensities.[49]

TEM is another technique that is often used for the analysis of solid-state materials. This is due to the ability to take images of the material at small scale and make comparisons,[24, 87, 94, 95] alongside the capability for many of the instruments to run selected area electron diffraction (SAED) experiments at the region of the image to give an electron diffraction image in reciprocal space.[24] TEM and SEM images have a contrast that can be used to help characterise surface morphologies/compositions that may have been detected or suspected from other analyses, whilst also allowing for the estimation of nanoparticle sizes, when there is sufficient clarity to define individual particles.[87, 94]

Due to the graphene layers being capable of rotating individually, they complicate the image in some microscopy techniques,[86] this is an issue to be considered when using these techniques. For example, graphene can form AA stacking, AB stacking (also known as Bernal stacking) and begin to form Moiré pattern when continued to rotate from Bernal stacking, as shown in Figure 8.[86] This can be observed by STM in loose graphene powders, which presents an issue for analysing and observing modified layers.[86] To combat this, some research teams working with graphene that has been grown as perfect monolayers on a substrate, before transferring to a substrate more suitable for STM.[2, 86]

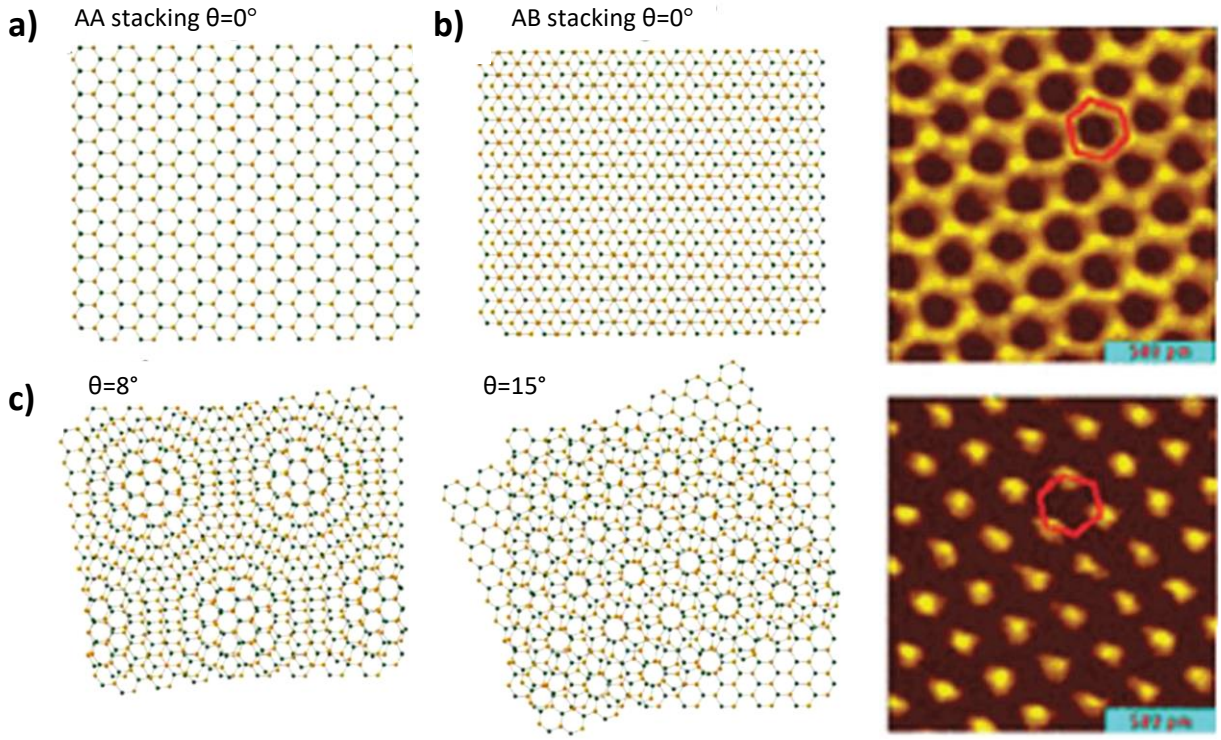

Figure 8: a) the AA stacking of graphene, b) the AB stacking of graphene and its continued rotation to c) 8° Moiré pattern and d) 15° Moiré pattern. e) The STM of AA stacking and f) AB of graphene layers. Copied and modified with permission from reference (86).

One valuable technique is Brunauer–Emmett–Teller (BET) surface area analysis, which uses nitrogen adsorption isotherms on a degassed sample to give the surface area of the material and the size of pores within the structure – providing potentially vital structural data.[53]

1.6 Photocatalysts

In photocatalysis, the catalysts can be of a heterogeneous or homogeneous nature. This project focuses on heterogeneous catalysts due to their ease in cleaning and reusing the catalyst. A heterogeneous system is often split into several components with a catalytically active site, photo-absorbers as antennae and a support to bridge the two components and hold the system together. Alternatively, some nanoparticles have the capability to act as all three, though this can be uncommon.[59, 63, 96, 97] In addition to this, it became desirable to design the catalyst to be selective in the specific reaction. This can be achieved either through a direct modification of the catalyst's structure or by variation of the external conditions.[63, 97, 98] These systems are a way to artificially mimic photosynthesis and the Z-scheme of photosynthesis in plants, which allows plants to create their "fuel" or nutrients from the photonic energy of solar radiation.[50, 59, 99]

Semiconductor photocatalysts usually function by absorbing light, which excites an electron from the valence band (VB) to conduction band (CB) and creates a hole in the VB. A newly formed hole-electron pair must be moved apart through electron transfers to avoid recombination. The use of photo-absorbers in the catalysts is to add new bands for electrons to be excited from or to.[9, 62, 97, 100, 101] Whilst this occurs, photoactive materials require the ability to negate the recombination of the excitons and holes that are formed, either electronically or through the changes in conformation of the conjugated system involved in the charge separation.[9] The efficiency of a photocatalytic system is strongly determined by the efficiency of these steps and the CB/VB with redox potentials of the reaction involved.[7]

The material, such as g-C_3N_4 and TiO_2, can act as a single photocatalytic system capable of catalysing a variety of redox reactions.[53, 65, 80, 101-105] However, TiO_2 has a limited ability to absorb solar radiation and mainly absorbs in the UV,[101] hence it is preferable to move on from a pure TiO_2 in photocatalysis.

To improve the photocatalytic activity, new developments in this area include doping strategy with metals or with single non-metal elements and growing TiO_2 on other materials such as carbon-based ones.[62, 100, 102, 106]

Mono- and bimetallic loadings such as gold-platinum, gold-palladium, and silver-platinum nanoparticles onto TiO_2 have been developed via the deposition methods. This strategy has a significant effect on the produced catalyst creating improvements comparing to unmodified TiO_2.[102, 107] To improve the visible light absorption and photoreactivity, organometallic dyes have been attached to the TiO_2 surface.[102, 106] Other examples include the modification of TiO_2 with fluorescein modified fibres and gold nanoparticles to produce a visible light responsive photocatalyst for dye photobleaching.[81]

An interesting design of tubular g-C_3N_4 which is capable of converting hydrogen peroxide into water and bubbles of oxygen has been developed. Here, the bubbling of oxygen from the reaction through the tubes allows for the tubes to be propelled under light activation.[80] Whereas, some carbon macromolecular structures have shown electrocatalytic activity, both as a catalyst and as a surface on which metal atoms can be coordinated post-modification.[23, 108]

Graphene and carbon nitride can be improved as photocatalysts by utilising metal nanoclusters on the surface and depositing them there as catalytic centres and as visible light absorbers when the nanoparticle size is adjusted correctly.[7, 22, 49, 50, 109] For example, a TiO_2-graphene nanocomposite has been previously reported to have increased catalytic activity towards the photodegradation of methyl orange and MB as a method of photocatalytic analysis.[110]

Graphene has a zero-band gap, where the Fermi level is at a Dirac point. Thus, a modification of the graphene surface can lead to a band gap forming either a n-type or a p-type composite.[51] This can be achieved in several ways, including heteroatom doping, co-modifications or composite formation.[8, 51, 52, 110] In this manner, we expected that the newly synthesised graphene-dye hybrids[85] could present some increased photocatalytic activity in the visible region.

One example of a graphene-dye complex in the literature is the use of eosin Y (EY) in EY-rGO and EY-Pt/rGO. In these systems EY is physisorbed to the graphene sheet and assembles through hydrogen bonding, according to DFT.[111] EY-rGO has been shown to have a good photocurrent response and has shown effective at H_2 generation when using triethanolamine as a sacrificial agent, though the generation of H_2 is seen to slowly decrease over time when run over several cycles. The effect on platinum for this system is a slight increase in H_2 production.[111] This system demonstrated the strength of a graphene-dye system, but in the context of non-covalent binding and provides a basis for investigating dye-graphene covalently bound systems.

1.7 Photocatalyst Testing

1.7.1 Dye Degradation Studies

Dye degradation processes by catalysts have been used to test their catalytic activity. This is in part due to the strong colouration of dyes and their ease of monitoring through spectrophotometric methods. One example is the Fenton process, whereby an iron catalyst catalyses a radical formation from hydrogen peroxide to degrade dyes.[112, 113]

MB is a dye frequently used to study the mechanism and pH effects on the reactivity of photocatalytic systems, which has absorption bands at 293 nm and 664 nm and has been well studied for both catalytic activities of literature photocatalysts[114] and the effects on aggregation of the dye molecules in aqueous solution (Figure 9).[66, 115] This is due to the requirement to move to more efficient processes than adsorbents and coagulants, which are deemed hazardous wastes, and led to the use of advanced oxidation processes with photocatalysts such as TiO_2. These new processes have involved the formation and use of very reactive species for organic pollutant oxidation.[114]

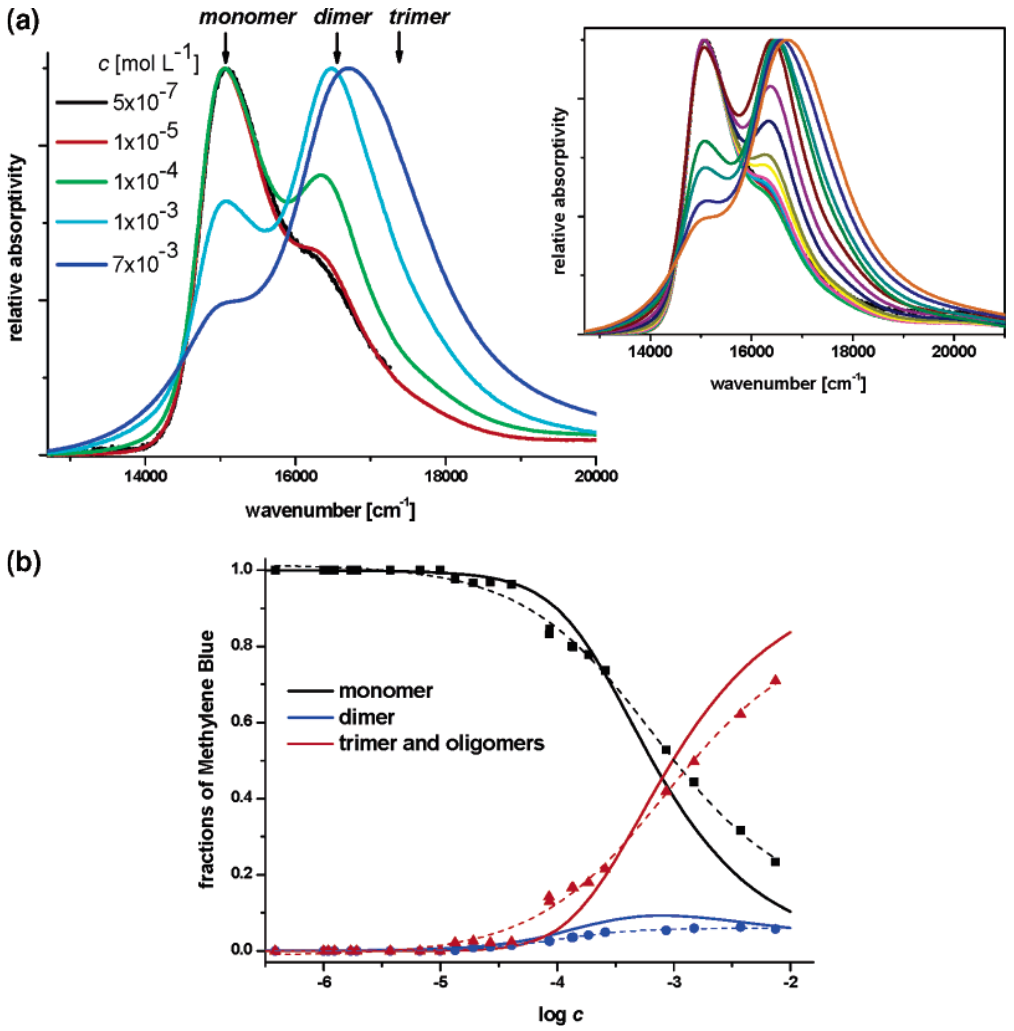

Figure 9: (a) Normalized UV-vis spectra of MB in liquid aqueous solutions. The arrows show known wavelengths, and the insert shows the change in spectra from 5 x 10^{-7} to 7.5 x 10^{-2} M. (b) The concentration-dependent abundances in MB. Dotted lines are linear regressions and solid lines are calculated profiles. Reprinted with permission from reference (115).

In the studies involving TiO_2, a rate of degradation of MB decreased slowly in acidic conditions and increased as pH also increases. The pathway appears to involve either a gradual degradation to several small aromatics or a mineralisation to nitrates, sulphates and carbon dioxide, due to hydroxyl radical attacks.[100, 114, 116-118] Similar degradation pathways utilising TiO_2 as a photocatalyst were found for Rhodamine B (RhB) and methyl orange,[117, 119] and an increase in the degradation rate was observed when TiO_2 was doped with iron and nitrogen.[65] Thus, doping TiO_2 has proven to be an effective method of increasing the photocatalytic activity.[66]

To modify the photocatalytic activity of graphene-based materials, a deposition of metal or metal oxides has been utilised. Here, the band gap is created by the dopants allowing the formation of free radicals to attack pollutants upon visible or UV light activation.[3, 54, 120-122] In the study involving TiO_2/ graphene as photocatalyst, it was noted that over sequential cycling of the reaction with MB, the catalyst has a very good recyclability and stability, with little loss in photocatalytic activity using 1-hour

cycles.[123] The rate of degradation can be increased even further by adding a porphyrin to the TiO_2/graphene oxide hybrids and increase the visible light absorption and utilisation of the material.[121]

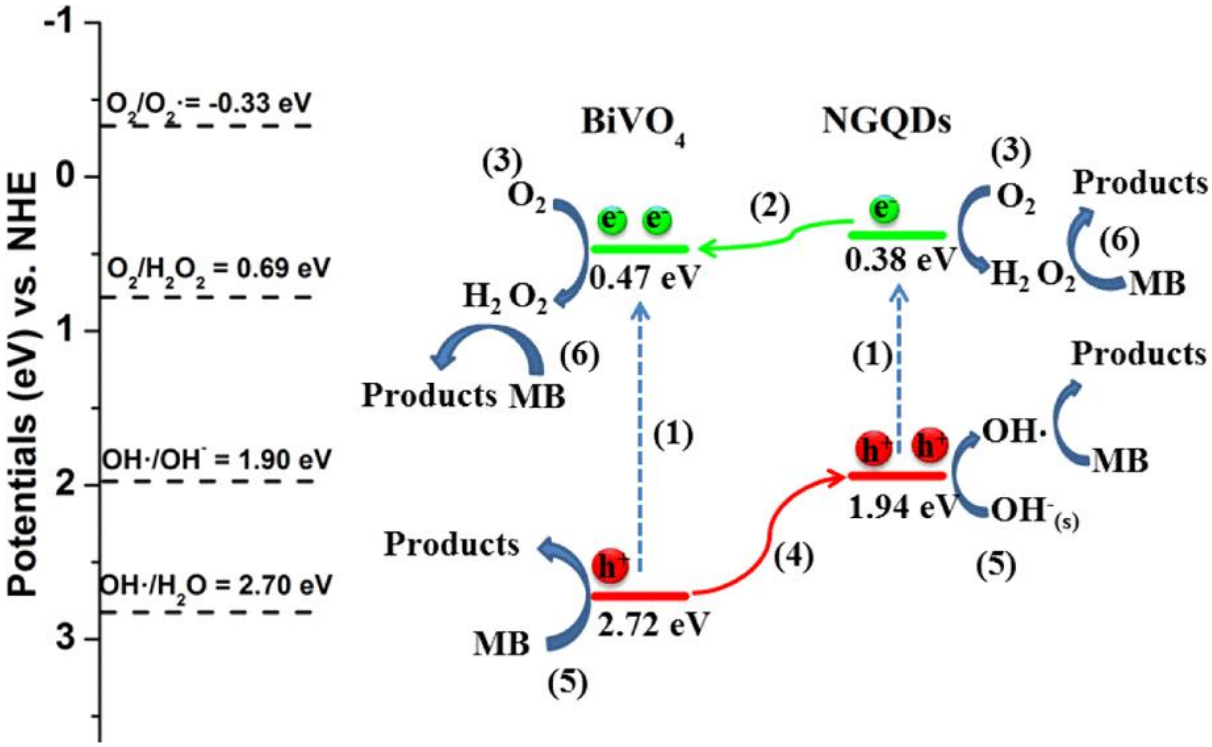

Figure 10: A scheme of the reactivity of N-doped graphene quantum dot decorated $BiVO_4$ nanojunction catalysts. Copied with permission from reference (124).

The use of quantum dots has been also reported to enhance photocatalytic activity of graphene (Figure 10).[124-126] It was found that some combinations, *e.g.* ZnS/graphene, require another bimetallic system, such as Bi_2S_3, in order to become photoactive. Without the bismuth-based bimetallic heterojunction, the composites acted only as adsorbents.[125] Meanwhile, ZnSe is capable of visible light activity, which is increased drastically with graphene present.[126] Bi_2S_3-ZnS/graphene has also been shown to be effective in the degradation of MB and RhB under light illumination, whilst also showing a BET surface area of 187 m^2g^{-1}.[125]

It has been noted that graphitic materials, including N- or P-doped graphene, graphene oxide and graphitic carbon nitrides can act as catalysts for various redox and charge transfer processes. Some of the carbon nitrides showed 52 – 90 % Friedel-Crafts acylation of benzene when formed as meso-porous materials, whereas graphitic or bulk carbon nitrides gave 0 – 1 % conversion.[127] These have been confirmed by both theoretical and experimental tests by various groups. Various techniques e.g., X-ray photoelectron spectroscopy, electron paramagnetic resonance, spin trap and DFT calculations have been employed in these experiments.[10, 127, 128]

1.7.2 Redox Chemistry

A method has been shown in the literature for a quick and simple test for the redox capabilities of catalysts, which involves the use of various benzyl alcohols, benzylamines, boronic acids and small aromatics.[129, 130] This method involves using starch indicator for oxidation reactions and pH indicator for reductions due to the by-products or intermediates that should form, such as peroxides, protons and superoxides, and it has been used for photocatalytic system tests.[113, 129] A variety of catalysts have been tested both as photocatalysts and as redox catalysts for this conversion.[130] A photocatalyst series formed from a base of TiO_2, has also been for this reaction due to its formation of hydroxyl radicals. The data showing that with these catalysts it is possible to increase the catalytic activity of TiO_2 using gold, rhodium or iridium as a bimetallic component.[131] This is a problem though, due to the high usage of expensive and rare transition metals.

A metal-free photocatalytic system was developed using 9-fluorenone, where benzylic alcohols were converted to their aldehyde derivative, using either air or oxygen atmosphere and dimethyl sulphoxide (DMSO) as solvent over 18 hours, at yields of 99 and 98 %. In the same work, they showed that fluorescein (at 3 mol%) was able to convert 22 % of the alcohol.[130, 132] Another system uses molecular oxygen and 9-phenyl-10-methylacridinium as a photocatalytic system for the conversion of benzyl alcohol to benzaldehyde, with gradual consumption of 9-phenyl-10-methylacridinium over the 15 hr reaction, though yields of benzaldehyde were not given.[71] Shorter reaction timescales were achieved with bromodimethylsulfonium bromide used with acetonitrile as a solvent. With this compound the reaction could reach up to 98 % conversion with 10 mol% of the catalysts within a 4 hr reaction.[133] Meanwhile, a plethora of organic photocatalysts have been developed to provide a way to catalyse the light-induced oxidation of pollutants, including many porphyrins, chlorins and phthalocyanines.[69]

This type of catalytic reactivity has been seen with graphitic materials previously, where N-doped multi-walled carbon nanotubes (MWCNTs) were able to convert 98-99 % of 0.1 mmol of various benzyl alcohols to their benzaldehydes with a minimum selectivity of 95 %. However these catalysts were used high loading (30 mL of benzyl alcohol in 80 mL) with run times of 3 hours using oxygen adsorption as part of the mechanism of activity.[128]

Styrene can be oxidised by some catalysts, such as dioxidomolybdenum(VI)-thiosemicarbazone complexes which showed similar reactivities across the set and better reactivity at higher temperatures with a high selectivity for styrene oxide formation.[134] Gold nanoparticles have shown activity towards styrene epoxidation when supported on cellulose aerogel, acting in a self-controlling manner to avoid acetophenone and acetaldehyde formation while using mild conditions and water as

a green solvent and hydrogen peroxide as a green oxidant, with a 1 hour reaction time, 96 % isolated yield and recyclability of the catalyst.[135]

DFT calculations of nitrogen-doped graphene of various configurations has shown the potential for them to be used in the oxygen reduction reaction (ORR), which would suggest the ability to form reactive oxygen species (ROS) such as peroxyl radicals, and hydroxyl radicals.[98]

In addition, graphene both doped and undoped, has shown catalytic activity towards the acetylene hydrogenation reaction, where conversions varied from 14.6 % to 99 %, with less doped graphene having a greater activity. This is very promising for the area of metal-free catalysts.[136] From there, graphitic materials have been further tested and shown to be carbocatalysts for the reduction of 4-nitrophenol through adsorption –> electron transfer –> desorption. This reaction was shown to work at room temperature but also required sodium borohydride to take place. However, the catalyst was stable at a 100 % conversion over 7 cycles.[137] The durability of the catalysts can be further increased to complete conversion at 60 minutes when the graphene materials are fabricated as films and the reaction is carried out in the alkaline pH; however decreasing when done so in acidic pH, which shows a form pH dependency to how these carbocatalysts function.[138]

1.7.3 Hydrogenation and Dehydration Reactions

A current frequently used catalyst for hydrogenation reactions of organic compounds is 5 % to 15 % Pd/C, as it is very effective at many hydrogenations. But, many alkaline-earth metal catalysts have also been recently found with the capability to undertake alkene transfer hydrogenations as another method of hydrogenation.[139-141] Pd/C catalysts employ hydrogen donors such as ammonium formate to hydrogenate substrates such as soybean oil to form stearic acid.[140, 141] An alternative to this is 4 % Pt/TiO_2 which can also have 4 % Re added to increase conversion and selectivity when hydrogenating bio-oil carboxylic acids.[142] Whilst many hydrogenation reactions can be performed by a range of metal catalysts for a variety of applications, such as Pd-based alloys, Lindlar catalysts and nickel catalysts. The issue with some of these catalysts is harsh reaction conditions, such as 35 bar pressure, 80 °C or 92 % acid.[143] A multitude of varied palladium catalysts with varied metal ratios and supports have been developed for a variety of applications from formic acid dehydrogenation to fuel cell usage, with turn over factors reaching as high as 8414 h^{-1}.[144] Some have also been used in small alkene hydrogenations, such as hexene.[145]

A Pd/PCN-KCl catalyst shows good reactivity, with additives, allows for blue light induced catalysis of styrene hydrogenation to ethylbenzene. The catalyst works at room temperature achieving 40 % conversion during 1-hour reaction.[146]

Ruthenium and iridium complexes show activity towards the hydrogenation of aryl ketone to alcohols through the dehydrogenation of isopropanol to acetone, with yields of 97-99 % on a timescale ranging from 10 mins to 14 hrs, depending on the catalyst and aryl ketone used.[147, 148] In a similar fashion, a ZnO_2 catalyst can be used to convert ethanol and methyl levulinate to methyl 4-hydroxypentoate and finally γ-valerolactone with high temperatures and 2-hour reaction times.[149, 150]

An interesting direction towards framework heterocatalysts is a recyclable triazine framework with ruthenium catalysts anchored by bidentate ligands for carbonyl hydrogenation, requiring 4 hrs at 80 °C and shown to undergo a minimum of 5 cycles.[151] Similar reactivity has been shown with a Mo and Pd or Au nanoparticles MOF for a tandem reaction of H_2O_2 formation and alkene oxidation, rather than hydrogenation.[152]

Nickel has been used within lignin as a means of hydrodepolymerisation in liquid phase by mixing different lignin percentages in and then keeping within a reactor with 95-100 atm of hydrogen at 400 °C, showing extreme conditions to get this reaction to proceed. However, the process of using a colloidal solution creates ferromagnetic particles, which further enhance the reactivity.[153] As a composite, metal oxides such as zinc and aluminium oxide have been mixed and used as a support for nickel and niobium oxides as a catalyst for lignin hydrogenolysis, where the niobium oxide activates C-O bond and nickel acts as the hydrogenolysis site, resulting in the formation of mainly bio-oils and some monomers of lignin.[154]

With these developments in hydrogenation catalysts, a way to improve them was to anchor metal alloys and nanoparticles on supports like graphitic materials, likely driven by the successes of palladium on carbon.[144, 155-159] One catalyst formed for the opposing dehydrogenation reaction was a NiPd on NH_2-N-rGO catalyst as well as Au/rGO composites, which was designed for lower cost and high efficiency at room temperature and successfully manages to rapidly produce gas from the decomposition depending on the metal ratios.[155, 156]

Platinum has been supported on reduced graphene oxide in order to act as a hydrogenation catalyst for soybean oil, through well dispersion of platinum over the graphene surface in an electrocatalyst, improving on previous catalysts by moving to “moderate temperature and normal pressure”.[158] Furthering this is the use of palladium nanoparticles on a reduced graphene support for activity towards the hydrogenation of *o*-chloronitrobenzene at a higher selectivity than commercial catalysts.[159] Similar catalysts of palladium/g-C_3N_4 can be used as a microreactor to store hydrogen for use in alkene hydrogenations with ammonia borane.[160]

Copper on TiO_2 support has been used for photocatalytic hydrogenation of alkenes using visible light. Here, protons have been generated as the active hydrogen species for alkyne hydrogenation.[161] Copper when paired with alumina has shown high reactivity with nitrobenzenes at 140 °C during a 2-day reaction in the presence of 2.5 mol % of copper and 50 bar of hydrogen pressure.[162] Nitrobenzene can also be catalytically hydrogenated by fullerene C_{60} and C_{70} under 1 bar of hydrogen pressure using UV light to achieve 82-100 % conversion with 78.9 % to 92.4 % selectivity of aniline formation. The work even showed that C_{60} was also effective to 39.1 % conversion and 74.8 % selectivity in visible light, showing the photocatalytic potential for large carbon allotropes.[163]

1.7.4 Radical Presence Testing

Hydroxyl radicals have been known for some time and have shown that they have an important role in the formation of ozone in the environment. In the 1930's they were produced through the Fenton reaction and used to monitor the degradation of some materials.[56, 112, 113, 164] This includes the conversion of benzyl alcohol to benzaldehyde by N-hydroxyphthalimide with an iron Fenton catalyst.[113]

Due to the capability of some graphene-based materials to form radicals, according to theoretical studies, it may become important to test for these oxygen-based radicals.[98] For the testing of the presence of these radicals, it will be necessary to employ a radical specific scavenging molecules. For example, peroxyl radicals could be detected using simple coumarins or coumarin−chalcone systems, according to DFT analysis.[165, 166] Meanwhile terephthalic acid and phospholipid-linked coumarins can also be used to detect hydroxyl radicals.[167, 168]

For oxygen radical anions, peroxyl radicals and proton-based radicals, aryl boronic acids can be utilised to detect the formation of the phenolates or a proton substituted product.[129, 169] Protodeboronation has been shown in copper-catalysed reactions through a multi-process catalytic cycle.[169]

In the case of ZrO_2/g-C_3N_4 photocatalyst and the degradation of Rhodamine B dye, an oxygen radical anion is formed under light excitation, which then attacks and mineralises the dye.[170]

Some organic dyes are capable of forming hydrogen peroxide from oxygen during their catalytic cycles, which could be another source of radicals in solution,[70] especially in graphene-dye systems. These processes employing organic dye photocatalysts with HBr or oxygen can lead to photobromination or oxygenation of aromatic molecules, respectively.[70]

For the detection of hydroxyl radicals, terephthalic acid is often used; here the presence of newly formed hydroxyteraphthalic acid can be detected by a change in the fluorescence intensity and the

shift. This is due to its selectivity towards these radicals, which is not hampered by the presence of other ROS species such as peroxides often formed in such processes.[168] This method has proved to be helpful with TiO_2 and bismuth molybdate systems used to degrade organic pollutants, where the fluorescent signal for terephthalic acid falls and hydroxyterephthalic acid increases suggesting the photo-induced reactivity of the catalysts to be due hydroxyl radicals.[168, 171] Similarly, this can be achieved with naphthalene 2-boronic acid to detect peroxides in solution, but at a much slower rate if the boronic acid was not immobilised prior to reaction with the peroxide.[172] Interestingly, if there is the presence of a compound that could alter the OH group to OMe in naphthol, the emission should still be almost the same according to the literature when in acetonitrile, making reaction solvent important.[173]

1.8 Aims

The aims of the project are as follows:

1. To fabricate different metal-free modified graphene-based materials with visible light absorption properties for the use in photocatalysis, starting with the degradation of hazardous wastewater dyes (MB and RhB).

2. To characterise intrinsic properties of these materials, through a variety of spectroscopic and microscopic methods including PXRD, IR, Raman, UV-vis, and fluorescence spectroscopy, SEM and TEM.

3. To understand and assess the materials' photochemical behaviour and the potential mechanism of activity through study of the removal of organic dyes in aqueous media.

1.9 Objectives

The objectives of the project are to first develop a method to easily modify graphene surface with dyes via a radical addition. To achieve this, the development of the method to convert dye into the corresponding diazonium salt is developed. These graphene materials are then to be analysed through a range of techniques, such as UV-vis, TEM, BET, FTIR and PXRD. This is done to understand whether the dye forms a covalent bond with graphene and how this affects the light absorption of the hybrid system.

Once the graphene materials' fabrication has been confirmed, their (photo)activity and adsorption ability are to be tested through removal of two known hazardous dyes (MB and RhB) using UV-vis spectrophotometry under white light illumination and under dark conditions. Desorption experiments to separate degradation from physisorption processes during the dye removal are also to be studied.

Materials that show successful degradation of the dye have to be tested further with a collection of redox substrates, to create an understanding of whether the materials are reductive or oxidative in nature. Experiments to detect a type of reactive oxygen species and radicals are also to be conducted.

Chapter 2. The Fabrication and Characterisation of Phenazine-Graphene as a Model System

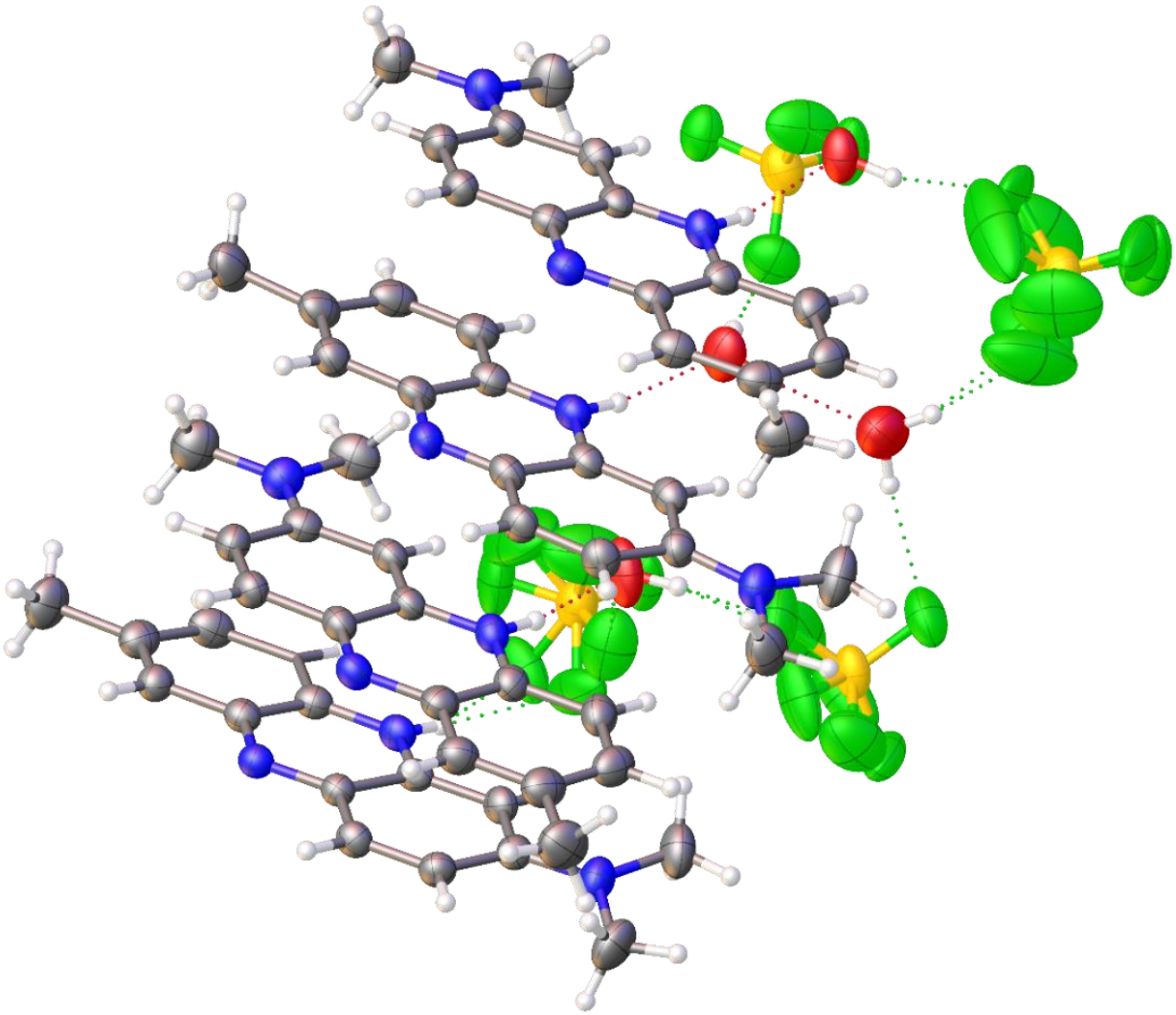

2.1 Abstract

Herein, the phenazine dye "neutral red" is transformed into its related diazonium salt and tested in photoinduced carbon-carbon coupling reactions with a small range of hydrocarbon materials including larger structures such as graphene, pyrene, and fullerene C_{60}. It was found that the photoinduced C-C coupling reaction involving diazonium salt is unique to graphene reactivity, and it can be used to modify graphene surface under mild reaction conditions using white light.

Solubility of the phenazine-graphene hybrid has been greatly improved in the solvents such as DMF and DMSO. An orange colour of suspension in DMF suggests the C-C bond has formed; further UV-vis spectroscopic analysis of the hybrid shows a new band in the visible region of the absorption spectrum, which has hypsochromically shifted by 15 nm. The effects of covalent modification on the alteration of the optical and electronic band gap in the new material have been studied with DFT calculations from STM methods. It was found that every eighth carbon atom of the graphene basal plane had been modified by the dye molecules. The use of graphene nanoplatelets and graphene on silicon carbide has allowed for a multitude of analysis to be carried out including STM, SEM, TEM, and Raman spectroscopic techniques to understand the effects of modification in the hybrid systems.

2.2 Aims

The aims of this chapter were:

1) to alter optical and catalytic properties of graphene through modification of its surface by photoactive molecules;

2) to develop an efficient and mild chemical method for the covalent modification of the graphene surface with large organic molecules using visible light activation;

3) to study the mechanism of the surface modification using a model compound – phenazine dye (Neutral Red);

4) to determine analytical techniques to characterise novel phenazine-graphene system.

2.3 Results and Discussion

2.3.1 Synthesis of Neutral Red Diazonium Tetrafluoroborate Salt and 3-Methyl-8-dimethylaminophenazine

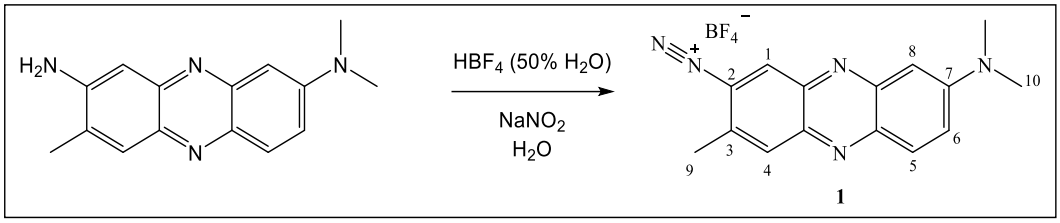

*Scheme 1: The reaction of Neutral Red with sodium nitrite in the presence of tetrafluoroboric acid to form the tetrafluoroborate diazonium salt **1**.*

This reaction involved the diazotisation of Neutral Red in the presence of tetrafluoroboric acid to form the respective diazonium salt with a tetrafluoroboric acid counter ion. The counter ion was chosen for the purpose of increasing the stability of the salt, because diazonium compounds are generally unstable.

Due to the high solubility of the salt, isolation is not a simple matter, so minimal water and acid must be used in the reaction and some diethyl ether appears to aid isolation, though tests have shown some solubility in ether.

^{1}H NMR in $CDCl_3$ confirms the formation of Neutral Red diazonium tetrafluoroborate salt (diazonium **1**) showing the aromatic peaks at 8.06 (d, J = 10.2 Hz), 8.02, 7.81 and 7.67 (d, J = 10.3 Hz) (shown in Figure 120 and Table 25, appendix). Mass spectrometry (MS) analysis also confirms the formation of the diazonium and gives the peak at 341.17 which corresponds to $[M\text{-}N_2+H]^+$. Though there is a loss of N_2 in the mass spectrum, this may be expected from an unstable functional group, which is also known to destabilise and react when a single electron is donated.[33]

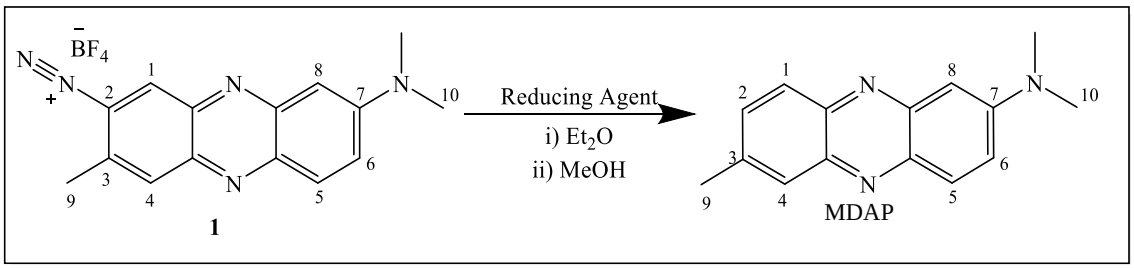

Scheme 2: The general reaction scheme of Neutral Red diazonium with reducing agents.

Care was required in the amount of time the diazonium salt was left in water or ether, as a conversion to a sole product had occurred under these conditions. To identify a product of the spontaneous

reaction of the diazonium salt 1, further study has been undertaken. NMR, MS, and X-ray single crystal analysis were used to confirm the structure. The product was identified as 3-methyl-8-dimethylaminophenazine (MDAP) suggesting a chemical reduction. To prove this suggestion, the synthesis of MDAP from diazonium salt 1 was attempted using several reducing agents such as $NaNO_2$, H_2O_2 and CuI under illumination with white light. The reaction with $NaNO_2$ was the most rapid, however the yield of MDAP was low due to the difficulty in isolating the product and the use of aprotic solvent such as ether. Nevertheless, it was found that the diazonium salt can be instantly reduced into MDAP when stirred in a methanol and $NaNO_2$ solution, however the solubility of MDAP resulted in some salt impurities, which were deemed to likely have insignificant effect on the planned use of MDAP. This could be due to the ease with which a proton can be abstracted from methanol.

2.3.2 Physical Properties of Diazonium Salt **1** and 3-methyl-8-dimethylaminophenazine

To efficiently analyse the organic moieties in the graphene-dye materials, it is important to establish routine analytical methods suitable for the materials of low solubility. Thus, a further analysis of the diazonium salt 1 and MDAP has been carried out. The FTIR spectrum (Figure 11) confirms the formation of the nitrogen-nitrogen triple bond of the diazonium functional group at 2300 cm^{-1} and the presence of the B-F stretches at 549 cm^{-1} (w), 518 cm^{-1} (m), 474 cm^{-1} (m) also indicate that tetrafluoroborate is present as a counterion.

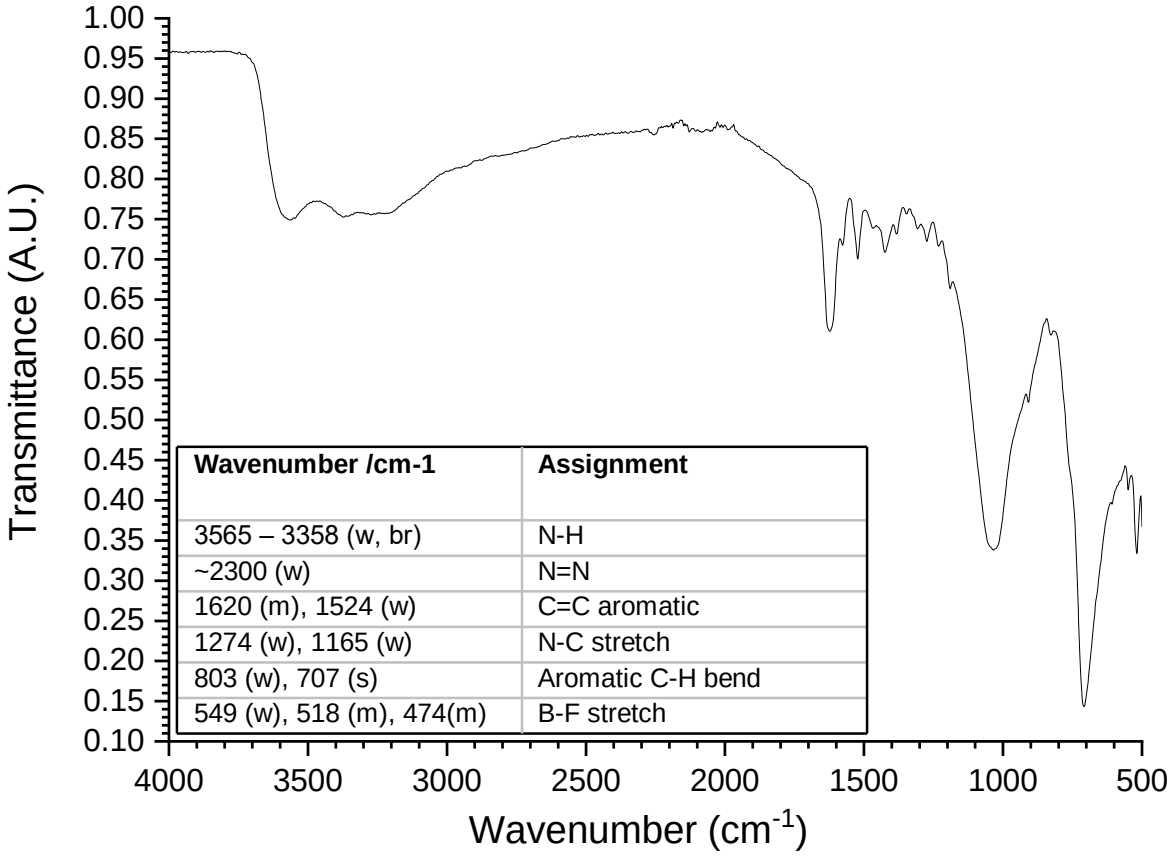

Wavenumber /cm-1	Assignment
3565 – 3358 (w, br)	N-H
~2300 (w)	N=N
1620 (m), 1524 (w)	C=C aromatic
1274 (w), 1165 (w)	N-C stretch
803 (w), 707 (s)	Aromatic C-H bend
549 (w), 518 (m), 474(m)	B-F stretch

*Figure 11: The FTIR spectrum of solid Diazonium **1** with inlaid table of peaks. S = strong, m= medium, w = weak, br = broad.*

For the FTIR spectrum of MDAP (Figure 12) we can see that the spectrum is much the same, except for the peaks in the lower wavelengths around 700 cm^{-1}, which have weakened and there is no longer a clear sign of the nitrogen-nitrogen triple bond seen in the diazonium. The change in the lower frequencies could be attributed to the change in the aromatic substitution from $-N_2^+$ to -H, which would affect the C-H bending in this region.

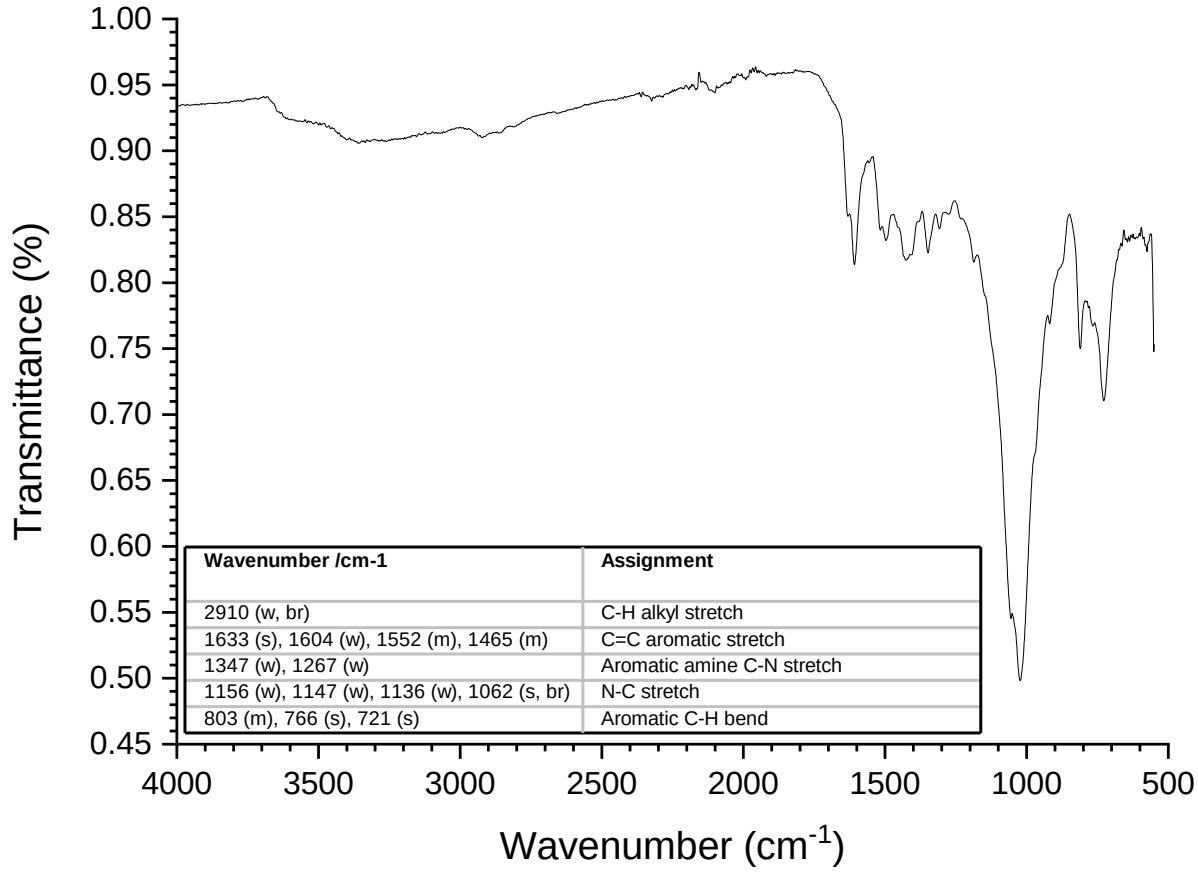

Wavenumber /cm-1	Assignment
2910 (w, br)	C-H alkyl stretch
1633 (s), 1604 (w), 1552 (m), 1465 (m)	C=C aromatic stretch
1347 (w), 1267 (w)	Aromatic amine C-N stretch
1156 (w), 1147 (w), 1136 (w), 1062 (s, br)	N-C stretch
803 (m), 766 (s), 721 (s)	Aromatic C-H bend

Figure 12: The FTIR spectrum for MDPA with inlaid data table. s = strong, m= medium, w = weak, br = broad.

The UV-vis spectrum of the diazonium salt (Figure 13) was recorded in methanol and gave a maximum intensity peak at 534 nm in the visible region and 375 nm in the UV at a concentration of 5×10^{-4} M. It has a molar extinction coefficient, ε, of 17433 $M^{-1}cm^{-1}$. In addition, the fluorescence spectrum (Figure *14*) was also collected in methanol, using a reduced concentration of 5.125×10^{-5} M, giving a maximum emission at 619 nm.

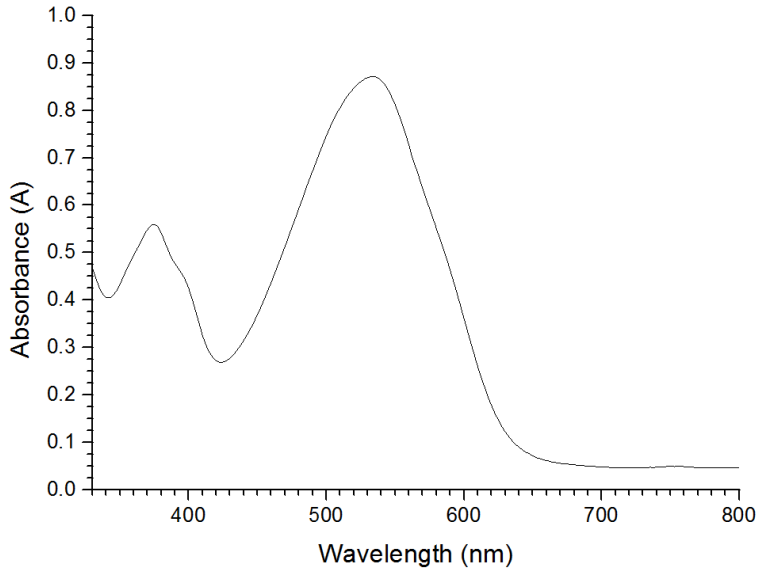

*Figure 13: The UV-vis spectrum for diazonium **1** in methanol, showing a visible region peak at 534 nm.*

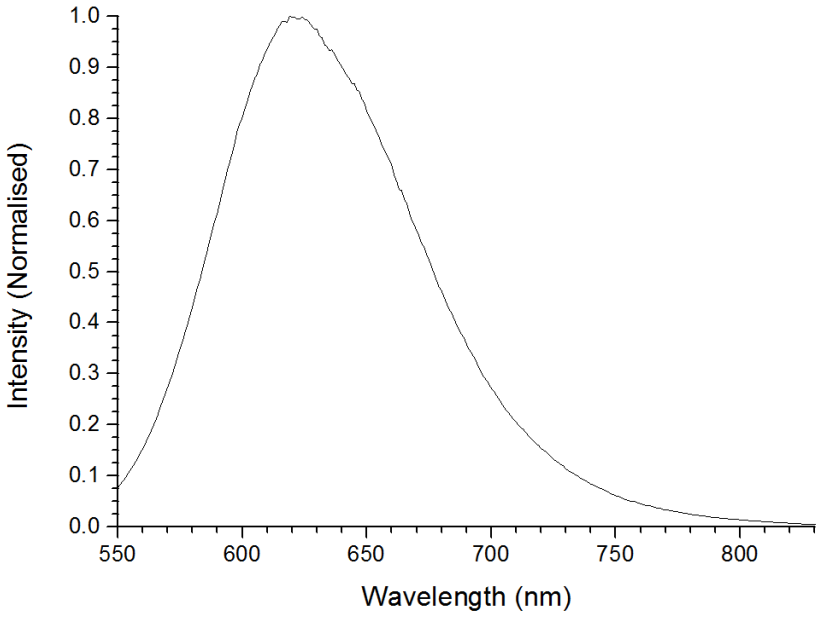

*Figure 14: The fluorescence spectrum of diazonium **1** with excitation wavelength of 534 nm and emission at 619 nm using 3 nm slit widths.*

The UV-vis spectrum (Figure 15) for MDAP was also collected in methanol and gave a maximum intensity peak at 479 nm at a concentration of 8.4×10^{-4} M. This can be attributed to a n-π* excitation, as this is the most likely transition at this wavelength in an organic dye.[174] In addition, the fluorescence spectrum (Figure 16) was also recorded in methanol, using a reduced concentration of 5.25×10^{-5} M to give a maximum emission at 611 nm. This shows a significant shift from the UV-vis and fluorescence spectra of the diazonium salt in the same solvent and indicates a change in the aromatic system that forms the chromophore of the molecule, which could be explained by the loss of the cationic $-N_2^+$ functional group for -H substituent, which would be less electron withdrawing.

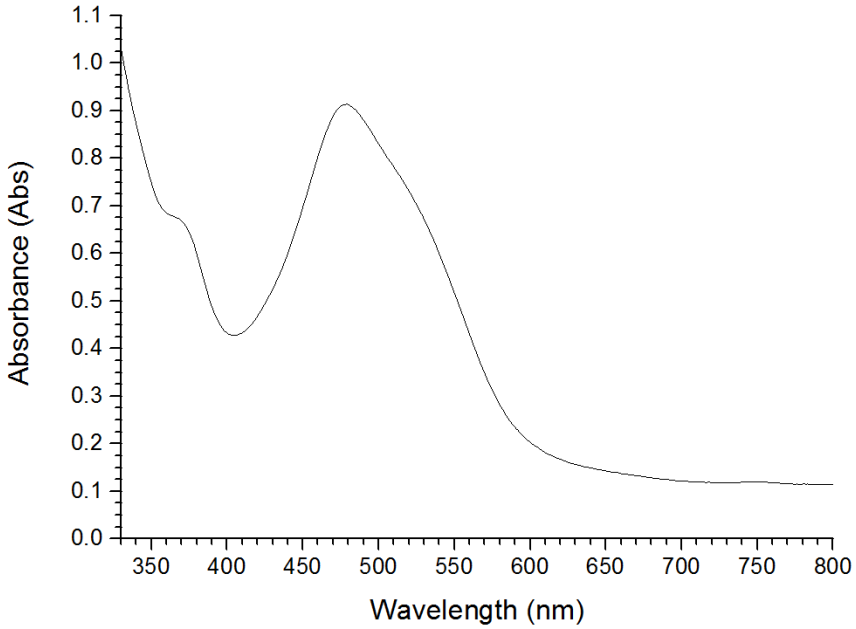

Figure 15: The UV-vis spectrum of MDAP showing a visible region peak at 479 nm.

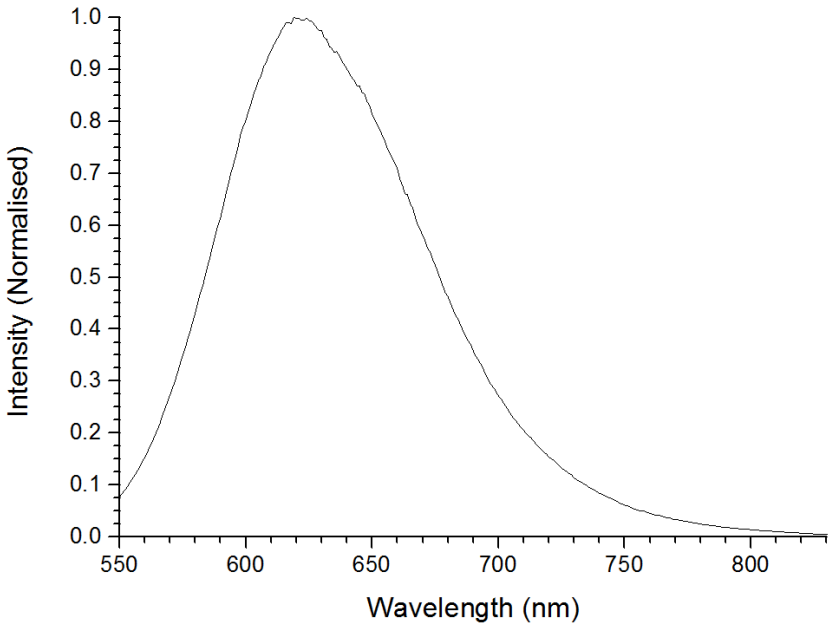

Figure 16: The fluorescence spectrum of MDAP emission at 611 nm when excited at 479 nm using 3 nm slit widths.

Single Crystal X-Ray Analysis of 3-methyl-8-dimethylaminophenazine

A set of MDAP crystals were grown from water after being left for several weeks. The crystals were a very dark orange colour, making them seem black until viewed through a polariser. A single molecule of the Protonated N8,N8,3-trimethyl-8-phenazineamine (H-MDAP), with labels, is shown in Figure 17. The crystal structure was obtained showing a packing of two columns of the phenazine molecules with

a layer of a solvent and BF_4 counter-ions before the next pair of columns. In addition, the column pairs appeared to rotate 90 ^{o} each time (Figure 18).

The BF_4^- counter-ions in Figure 19 appear to have more fluorine atoms than they should, but this is due to disorder in the crystal lattice, which results in partial occupancy in several positions. As you look at each phenazine up the column, it is also apparent that they are inverted with respect to one another.

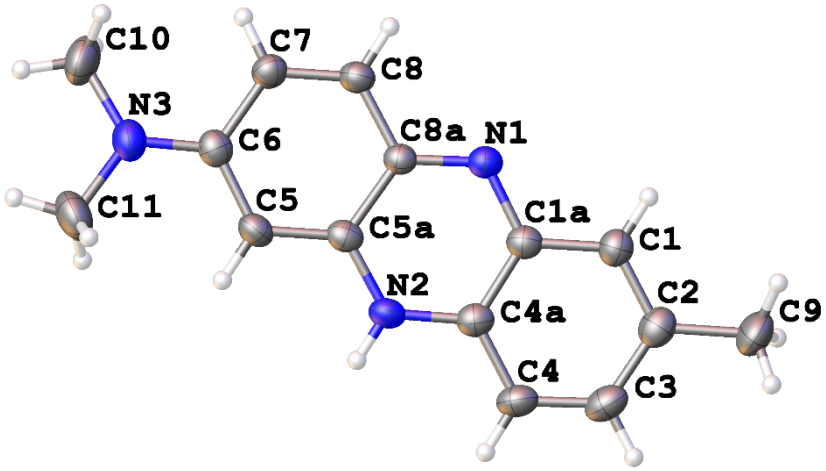

Figure 17: A single molecule of [H-MDAP]$^+$ with labels.

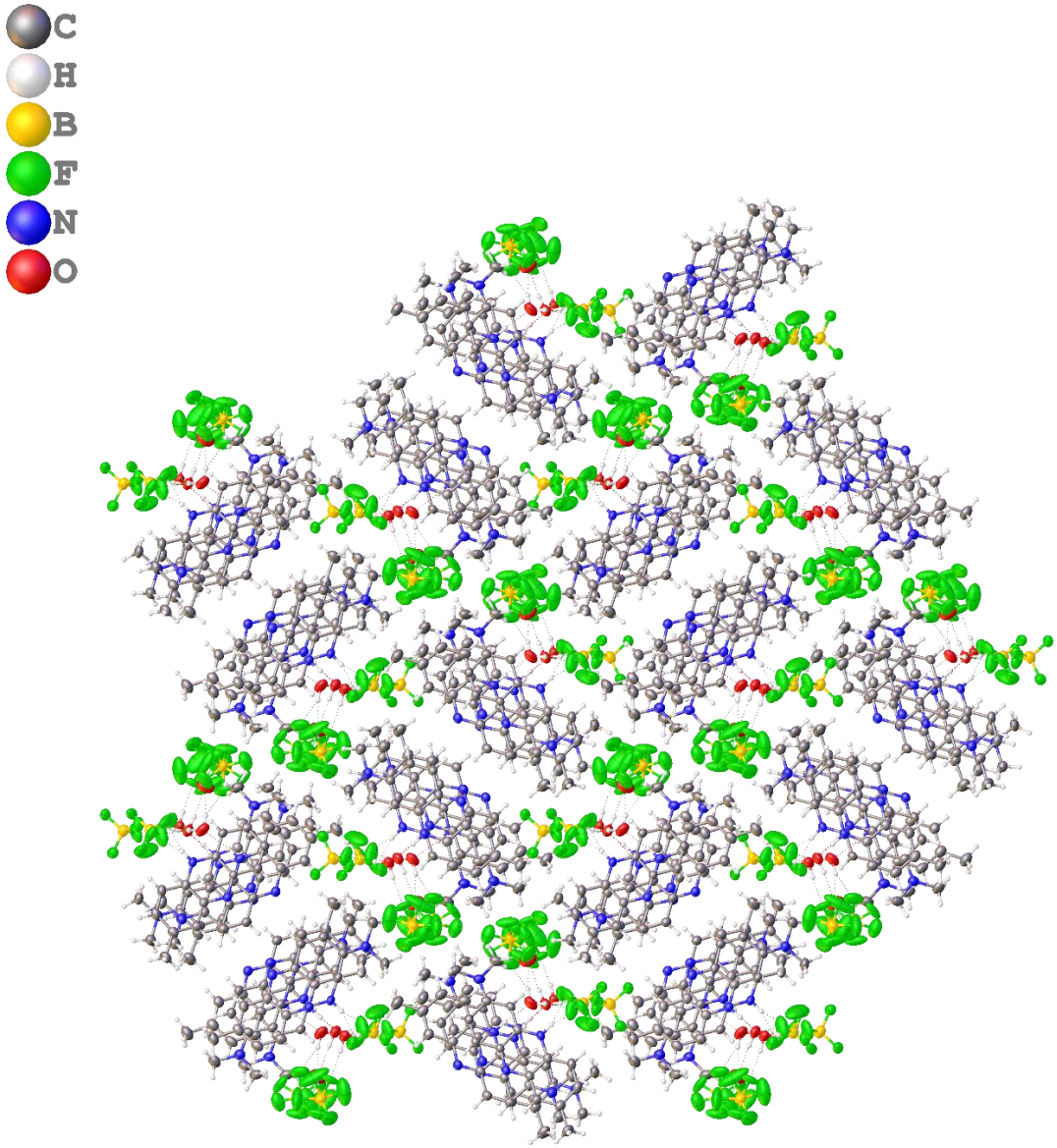

Figure 18: The crystal lattice of [H-MDAP]$^{+}BF_4^{-}.H_2O$ showing the positioning of the counter-ion and water solvent in the lattice

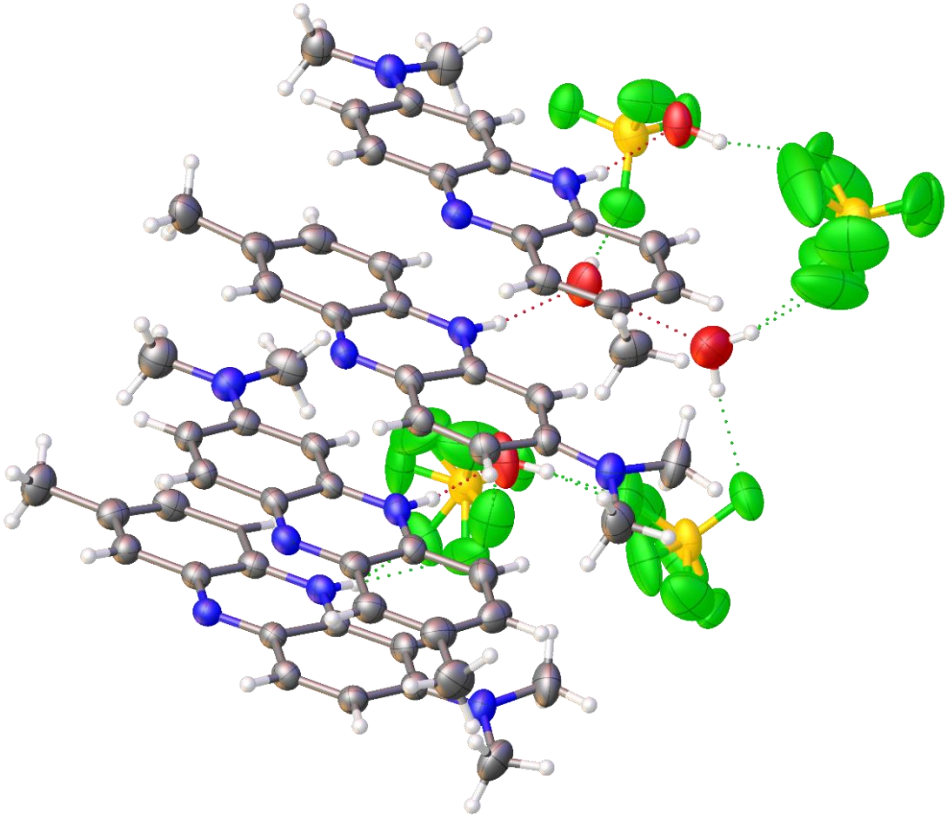

Figure 19: The asymmetric unit of the [H-MDAP]$^{+}BF_4^{-}.H_2O$ crystal.

Crystallographic data was acquired using a Cu-X-ray source, at a temperature of 119.97 K. It has a primitive monoclinic unit cell ($P2_1/n$), described by Z = 16, Z' = 4, a = 13.7966(5) Å, b = 23.5549(8) Å, c = 19.4763(5) Å, α = 90.00 °, β = 91.636(3) °, γ = 90.00 °, V = 6326.8(4), with a crystal density diffraction of 1.441 g cm^{-3}. The R factor = 7.32 %, which shows that the experimental data fits well with the model created. It seems the dye is flipped over each molecule down in the stack, likely to avoid steric clashes between the -N(CH_3)$_2$ groups. This stacking nature could also take place on the graphene surface either before a successful reaction with graphene or after a side reaction that forms MDAP. It would also relate to the diffraction peak closest to the main graphene peak in the PXRD of MDAP, as this d-spacing shows the closest distance to a π–π stacking distance.

Selected Bond Lengths (Å)		Selected Bond Angles (°)	
NH···F (H-bonded)	2.054	C-N-C (amine)	114.9(3)
OH···F (H-bonded)	1.982	C-N-C (pyridyl)	122.4(3)
B-F	1.364(6)	C-C-N(CH_3)$_2$	121.2(3)
N-C (amine)	1.472(5)		
N-C (pyridyl)	1.356(4)		
C-C (aromatic)	1.375(5) and 1.417(5)		
C-CH_3	1.503(5)		
C-N(CH_3)$_2$	1.341(4)		
N···H-C	2.795 - 2.916		

Table 1: A selection of the bond lengths and angles within the structure.

2.3.3 Synthesis of Phenazine-Graphene with Graphene Nano-platelets

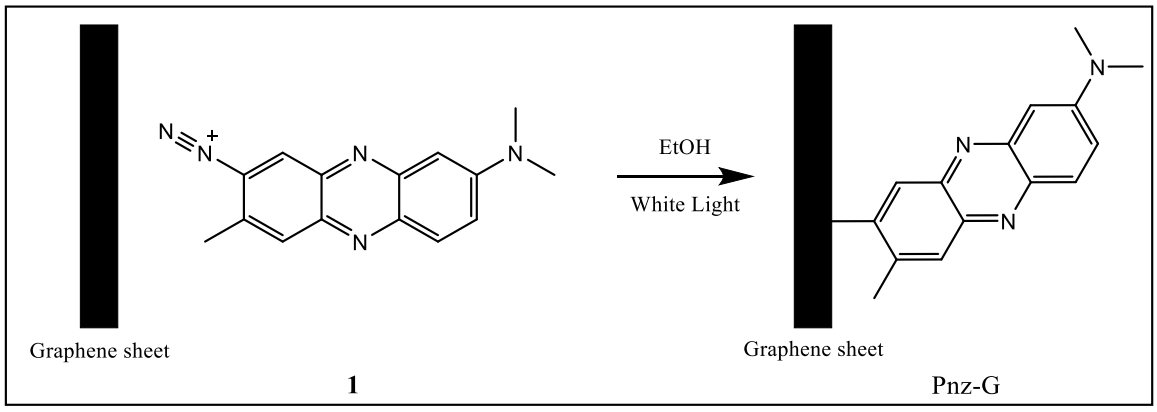

*Scheme 3: The modification of a graphene sheet using diazonium **1**.*

Since the diazonium salt dissolves easily in ethanol, which enables greater loading onto the graphene nanoplatelets, the synthesis of Pnz-G with nanoplatelets was carried out in ethanol.[85]

The mechanism, described in Scheme 3, is believed to be the radical addition process which is postulated in the literature.[33] We propose that the mechanism takes place through a radical addition, due to the transfer of an electron to the diazonium salt.[46] This results in the cleavage of N_2 and the formation of a radical dye, which attacks the C-sp^2 system of the graphene to form C-sp^3 hybridised defects in the 2D graphene lattice, leaving a radical within the carbon structure on the graphene surface. The radical can then be moved around the sheet to allow a further reaction with a second dye molecule creating an organised structure of covalently bound dyes on graphene.

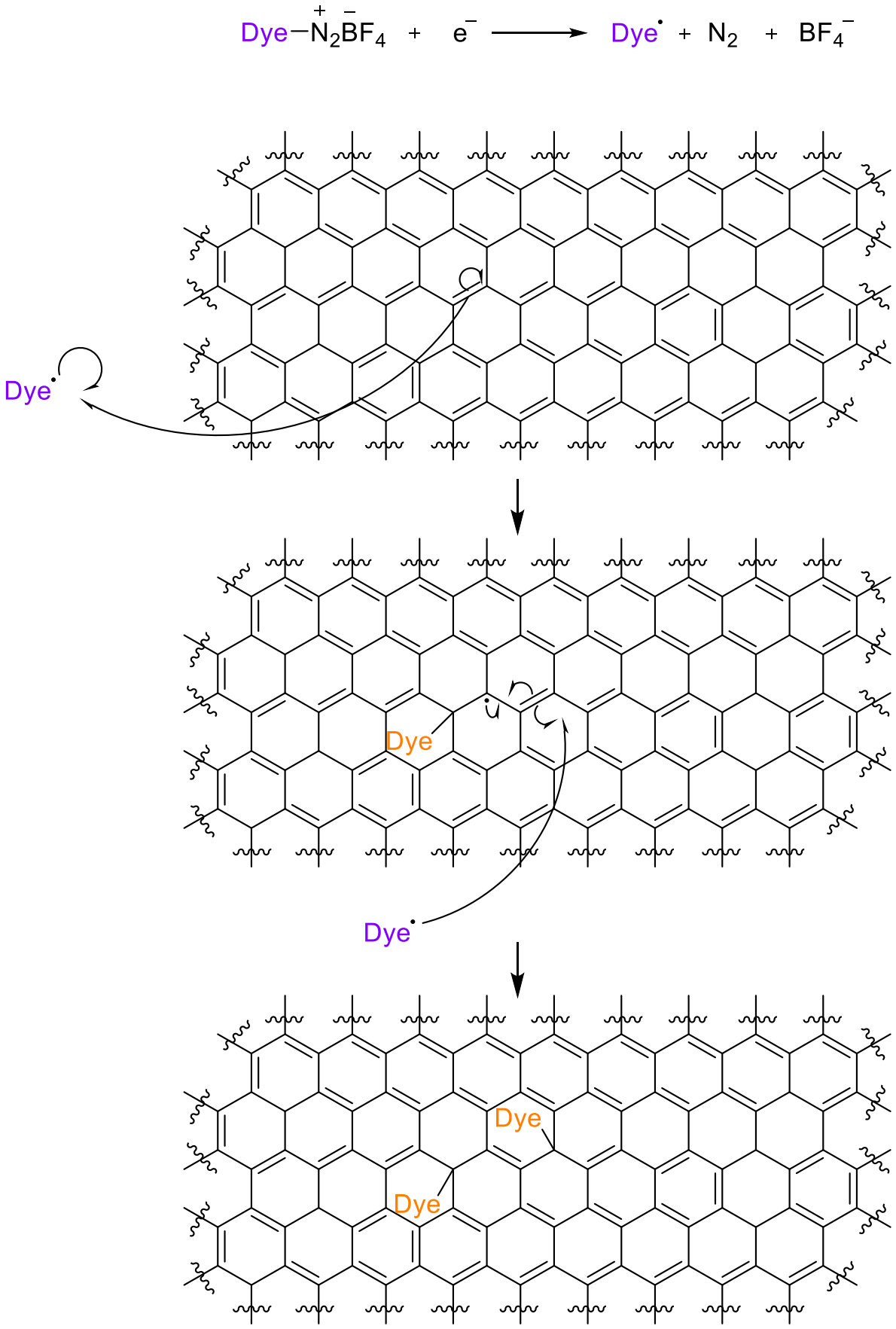

Scheme 4: The postulated mechanism for the attachment of dyes one and two in an area of the graphene sheet.

To understand the effect of light, the reaction was followed under light and dark conditions (Figure *20*). The diazonium salt showed reasonable stability in absence of electron donors, within a suitable concentration range for Beer-Lambert law to be applicable. The change in concentration of diazonium salt was recorded at 537 nm for both conditions. The photochemical reaction progresses rapidly and shows no change in diazonium salt concentration beyond 20 minutes and left only 46 % of free diazonium salt in solution. The initial drop in concentration for both conditions can be explained by physisorption of the diazonium to the graphene platelets through π-π stacking and Van der Waals interactions, which are reversible and shown by the stabilization of free diazonium salt after 10 minutes to 91 % (dark) and 44 % (light).

The comparison of dark and light reaction suggests that the illumination with white light aids the reaction of the diazonium salt and graphene, either through excitation of the diazonium or the formation of hot electrons from graphene. This is shown through the rapid fall of diazonium salt concentration in both conditions, where within 5 minutes the concentrations fell to roughly 65 % and 30 % for dark and light conditions, respectively. Within the next 20 minutes, this stabilised to a physisorption process of 80-100 % variable concentration for dark conditions and roughly 45-50 % variable concentration for illuminated conditions.

Initial decrease was caused by physisorption processes onto the graphitic surface, followed by desorption of unreacted diazonium. In the case of the dark reaction, much more diazonium desorbs from the surface, whilst the white light illuminated sample has much less desorption, due to the consumption of the diazonium.

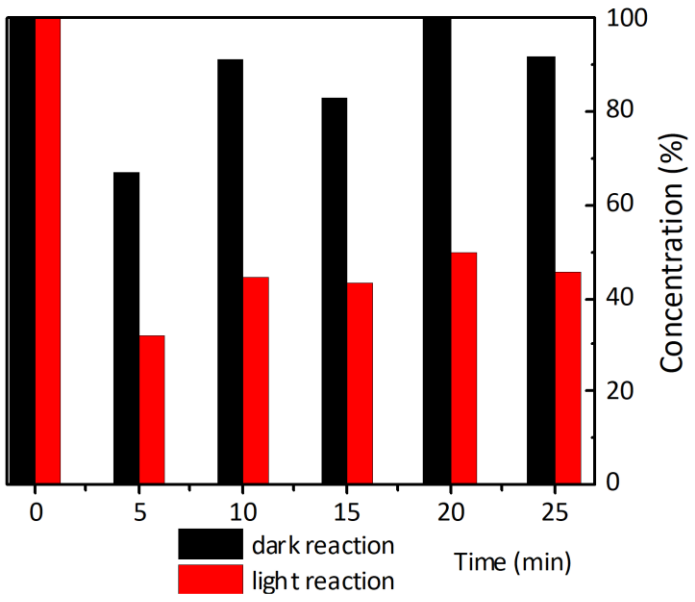

Figure 20: The UV-vis monitoring of diazonium salt concentration in solution over the time of reaction. Copied with permission from author's publication.

Following this, the powders of graphene, the diazonium salt, MDAP and both the light-induced and dark reactions were analysed by powder X-ray diffraction. This gave the diffraction patterns shown in Figure 21. They show that MDAP has many lattice lines and is a complicated array, while all three graphitic materials show the characteristic peak at 2θ = 26 °, confirming that graphene is present in all. The reaction under white light illumination shows new diffraction peaks at approximately 2θ = 20, 21.5, 30, and 40 °, alongside some broad amorphousness at 2θ = 31 °. The dark reaction shows no defined peaks in these areas, but a slight broad peak at 2θ = 21 °. What can also be noted is that the width of the graphitic peak is increased slightly (2θ = 0.5 °) and is less sharp, which suggests the formation of disorder within the material when compared to pristine graphene.

The new diffraction peaks in the light-induced sample do not closely match those of MDAP or the diazonium salt, despite the diazonium salt having a set of peaks very close to that of the graphitic peak. This would suggest that the diffraction pattern of the light induced reaction is not due to a mixing of the graphene with MDAP or diazonium salt crystals.

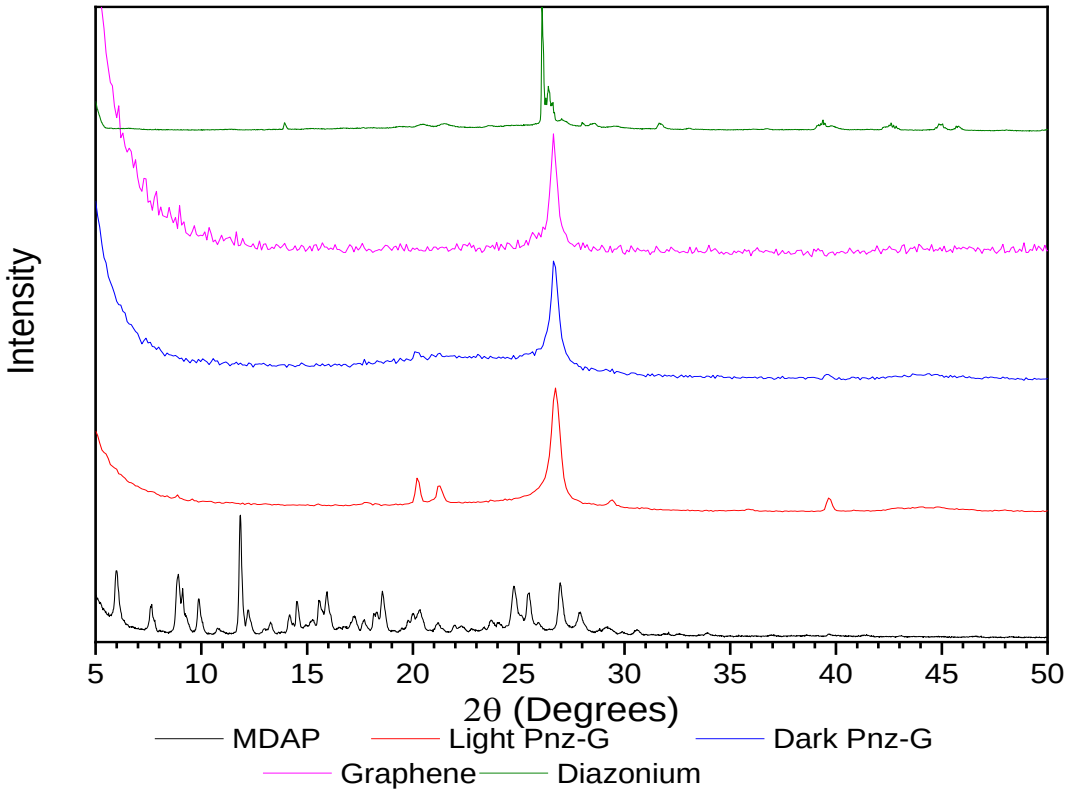

Figure 21: The normalised PXRD pattern for MDAP, Light Pnz-G formation product, dark Pnz-G formation product and graphene. Copper X-ray radiation source used (λ = 1.541 Å).

This PXRD data can then be used to find the d-spacings through rearranging Bragg's Law from

$$\lambda = 2d\sin(\theta) \quad (1)$$

to

$$d = \frac{\lambda}{2\sin(\theta)} \quad (2)$$

From there we can use the diffraction pattern to find the d-spacing in angstroms of each diffraction peak.

Sample	2θ	θ	2sin(θ)	d / Å
Graphene	26.43	13.22	0.46	3.37
Light Pnz-G	26.74	13.37	0.46	3.33
Dark Pnz-G	26.64	13.32	0.46	3.34

Table 2: The tabulated data gathered from the PXRD of Light Pnz-G, Dark Pnz-G and graphene and the d-spacings calculated.

Table 2 shows that the dark reaction not only has weaker patterns around the graphitic peak, but also has fewer and less definition of the features that the light induced reaction has, with the greater mix of broad peaks potentially suggesting more contamination than modification.

Compared with the diffraction pattern data of the dye and phenazine, we can see that the 2θ = 20 and 21 ° peaks are present in the diazonium salt, but with very weak intensity. The other Pnz-G peaks are not clearly present within the free dye or the diazonium, with the dye having a much more complex diffraction pattern and the diazonium having a simple and weak pattern (excluding the 2θ = 26 ° peak). This suggests it is not the growth of the dye or diazonium crystals upon the graphene surface, however the mixture of broad and sharp peaks suggests that there could be contamination. Also, the main peak at 2θ = 26.7 ° has shifted slightly from graphene's 2θ = 26.4 °, showing a decrease in the d-spacing but remaining within the distance expected for π-stacking that would be observed between graphene sheets.

Further comparative analysis of the graphene-based powders was performed by Raman spectroscopy. It showed a change in the D:G ratios of the graphitic peaks in the Raman spectrum. The G band (~1570 cm^{-1}) corresponds to the sp^2 system and the D band (~1350 cm^{-1}) corresponds to the vibrations of the sp^3 defects[86], so a modified surface should show an increase in the D:G intensity ratio. Indeed, an increase in this ratio has been observed, from 0.24 in pristine graphene to 0.33 in the light and finally 0.38 in the dark. This suggests that the dark reaction creates more defects on the surface and is not showing the same trend as other analyses. However, it was noticed that the bands of the dye also lie in this region, potentially influencing the D:G ratio in a way that makes this data less reliable. Although it does help to show that there has been some effect by the dye, since the bands do not align perfectly to cause an exact shift of the D:G band ratio.[83, 84]

The 2D band (~2700 cm^{-1}) provides an insight into the number of layers stacked to create the graphitic sample. The alteration of this band in Figure 22 could mean there is a change in the number and type of layering within these samples as the shape and position of the 2D band of the light and graphene is similar to that of 2-layered graphene. The shape of the dark conditions suggests a four-layered graphene though without the according to the literature.[83, 84, 86] Meanwhile a highly oriented pyrolytic graphite sample would be observed with two peaks around 1675 and 1725 cm^{-1}, suggesting this is not the stacking of these flakes.[83]

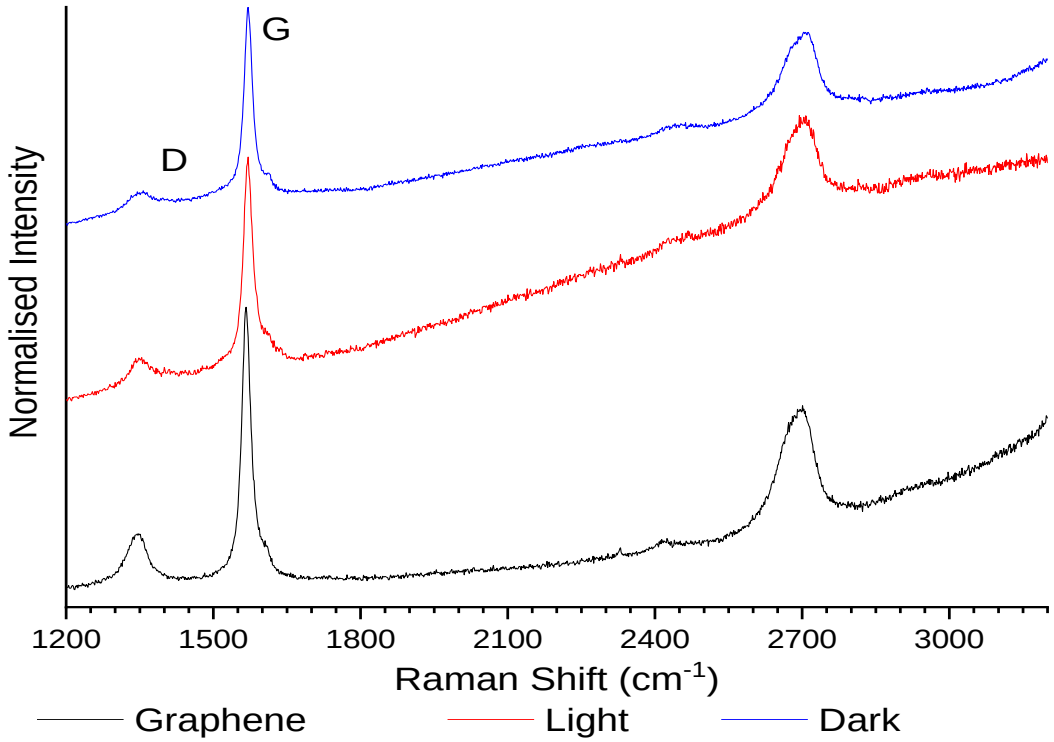

Figure 22: Raman spectrum of the graphene nanoplatelets, light illuminated modification and dark modification.

The Raman spectrum of the diazonium was collected using a 514 nm laser source with 10 % laser power to protect diazonium salt 1 from degradation. Broad peaks were observed between 1383 cm^{-1} and 1627 cm^{-1} (Figure 23). This is one reason for the uncertainty in the Raman of Pnz-G, as they overlap one of the key peaks and could interfere with the second.

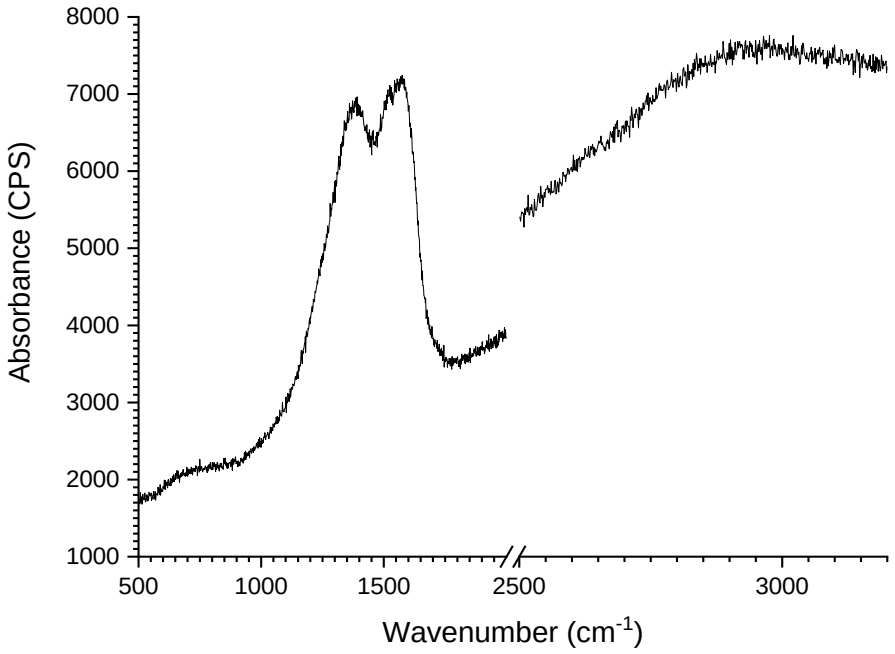

Figure 23: The Raman spectrum of diazonium one using a 514 nm laser source. Break inserted between 2000 cm^{-1} and 2500 cm^{-1}.

The Raman spectra of the MDAP was recorded using a 514 nm laser source (Figure 24 and Figure 25) at 5 % power output. The spectrum appears similar to that of the diazonium salt but with a much higher number of counts. Peaks were found at 1557 cm^{-1}, 1526 cm^{-1} and 1407 cm^{-1}. However, the bands are of much lower intensity and less defined from the background. This would be due to the low laser power and the tendency of MDAP to "melt" and degrade under the higher power beam.

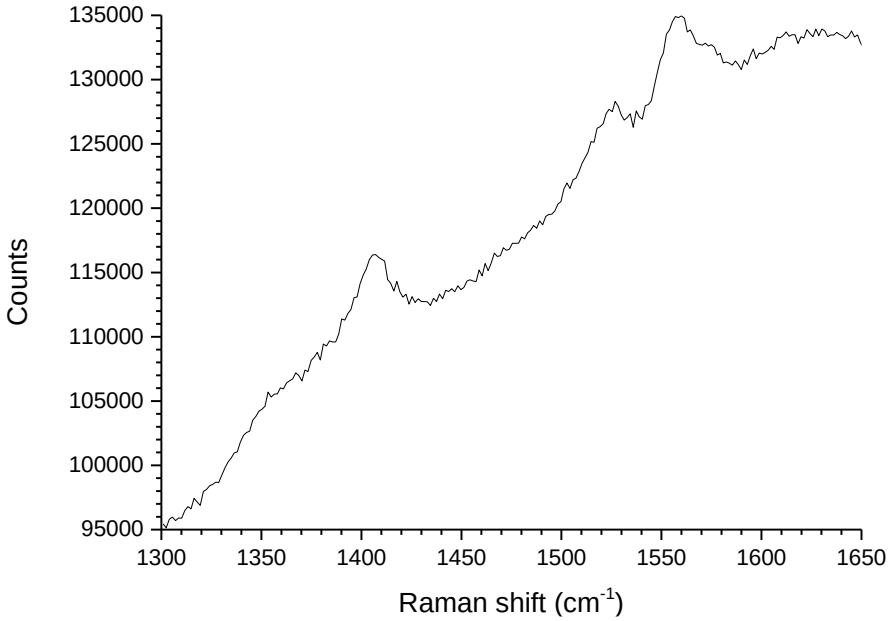

Figure 24: Raman spectrum (between 1300 and 1650 cm^{-1}), of MDAP obtained using 514 nm laser source.

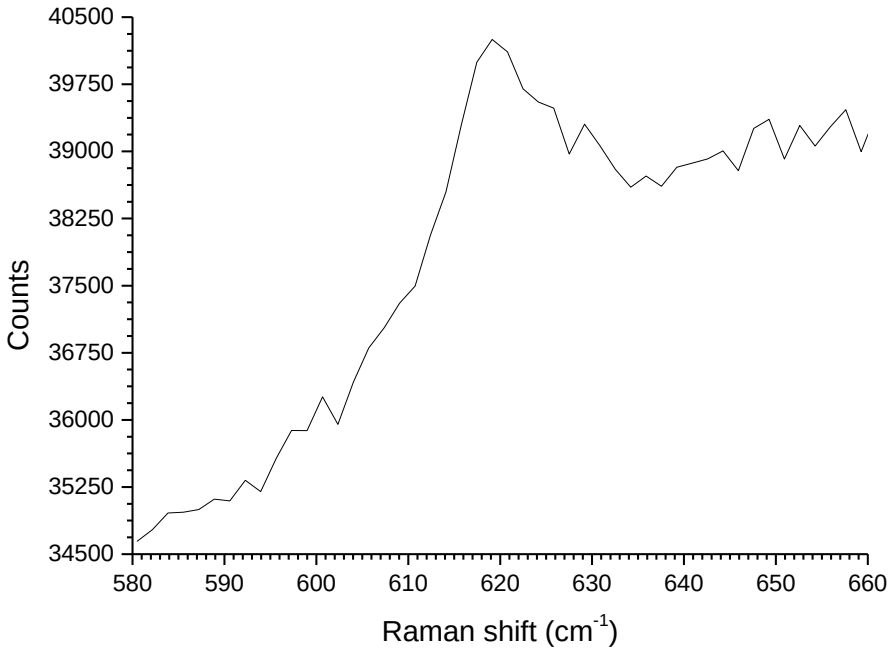

Figure 25: Raman spectrum of MDAP between 580 and 660 cm^{-1}.

Thermo-gravimetric analysis (TGA) was run from 25-515 °C (Figure 26). The maximum temperature of 515 °C was chosen due to limitations of equipment and it is assumed that the majority of the dye's specific degradation should be observed by this point. This is also the closest temperature the instrument could achieve to the onset of graphene degradation.[175] The data for the samples has been plotted from 100 °C due to initial losses associated with residual solvents (e.g. ethanol, water or HBF_4), including those left from the manufacture of the graphene nanoplatelets, which were used without prior purification/ drying. The first derivative is of greater interest than the mass loss plot, due to the inflection points (the negative peaks) showing the point of greatest mass loss and these can be compared between the samples.

TGA data of graphene nano platelets show two distinct regions of mass loss: the first region around 350 °C corresponds to onset of the decomposition of graphene,[175] and the second region is above 500 °C of bulk degradation. [175]

TGA results of the light and dark modified Pnz-G samples show a greater percentage of mass loss compared to graphene nanoplatelets within this temperature range (Figure 26a). The first derivative of TGA for Pnz-G samples (Figure 26b) reveals three distinct regions of mass loss for light Pnz-G and only two regions for dark Pnz-G. For light Pnz-G sample, the first region is between 190-280 °C. The second inflection point observed for the light Pnz-G lies between 300-340 °C and is also present for dark Pnz-G sample. The thermal decomposition is more rapid for the Pnz-G dark sample at this inflection point as its value is more negative.[176] The final region is 400-500 °C, with clear inflection

point at *ca*. 480 °C for the Pnz-G light sample; although, no clear inflection point for dark Pnz-G is recorded, onset of a rapid decomposition for the sample is observed.

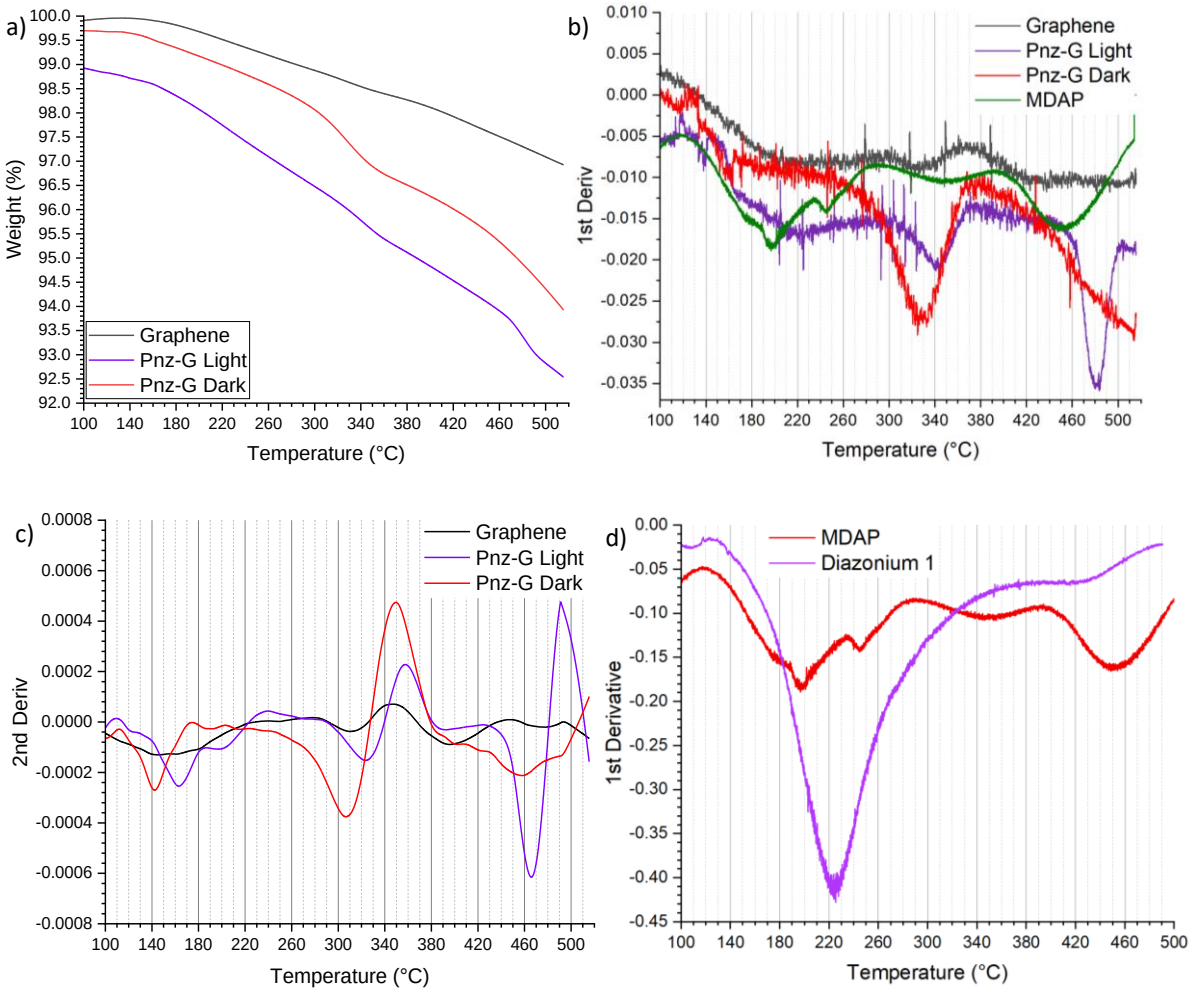

*Figure 26: a) TGA curves, b) first derivatives and c) second derivatives for pristine graphene and Pnz-G fabricated under dark and light-induced conditions, d) first derivatives for diazonium **1** and MDAP.*

Further analysis of the TGA results for Pnz-G was done as a comparison to TGA data for MDAP and diazonium **1** samples.

TGA first derivatives for diazonium **1** and MDAP (Figure 26d) show that the fragmentation pattern is quite different for these two molecules. Diazonium **1** is not a suitable standard for comparison as it has a very different fragmentation pattern, when compared to TGAs of Pnz-G. In contrast, the general shape of the first and second derivatives of MDAP is similar to ones observed for Pnz-G but with a significant shift in the decomposition temperatures. This can provide a suitable pathway of the mass loss in the hybrid structures and how it is related to the attached phenazine moiety.

TGA first derivative of MDAP is shown in Figure 26d, first region with two inflection points of 197 °C and 245 °C. The first inflection in this region at 197 °C connects to the mass loss of 10 %, which can be

attributed to [MDAP-2Me]. The second inflection in this region results in a total loss of 25 % which can correspond to [MDAP-N(Me)$_2$-Me] degradation pattern. For the Pnz-G light sample, this region has a broad inflection of *ca*. 220 °C and the mass loss covers the region. This can be explained by the total mass loss being very low, making any detailed understanding very difficult as smaller peaks may be hidden by low dye population of the total sample.

At 451 °C the mass loss of 51 % in the MDAP sample indicates the fragmentation of the phenazine ring system. A similar temperature range is observed in both Pnz-G, indicating a similar degradation. Given that there is a bond formed which is connected to the graphene sheet, if modification has occurred, it is suggested higher inflection at 480 °C is due to the stabilisation of the phenazine by the chemisorption to graphene.

The second derivative of the TGA for both hybrids shows that the two materials have a similar trend of onset temperatures, however the light sample shows higher onsets at each degradation stage. This suggests a greater stabilisation of the moiety being degraded, which would be an expected trend for a chemisorption compared to a physisorption of the dye.[177]

When assuming that the degradation is the same for the bound molecule and for MDAP, it could be estimated that 7.5 % modification of the surface has occurred, given that there is 4.5 % increase in Pnz-G mass loss (compared to graphene) and MDAP loses 60 % of its mass over this temperature range.

IR was employed to examine the functional groups present on the surface of the plates. As expected, the FTIR spectrum of the hybrid is similar to unmodified graphene, due to a large percentage of unmodified graphitic sheets in the sample, and the coverage of modified surface is a maximum of 20 %. There is also the presence of new, weak bands at 1055 cm^{-1} and 730 cm^{-1}, which are within the boundaries for C-N stretches, =C-H bending out-of-plane and the ring torsion within the materials.[85] This indicates the presence of the phenazine structure, whose only difference in bonding to pristine graphene is the presence of nitrogen atoms bonded to carbon. One problem here is the high base absorbance of the sample, which creates uncertainty in the spectrum.

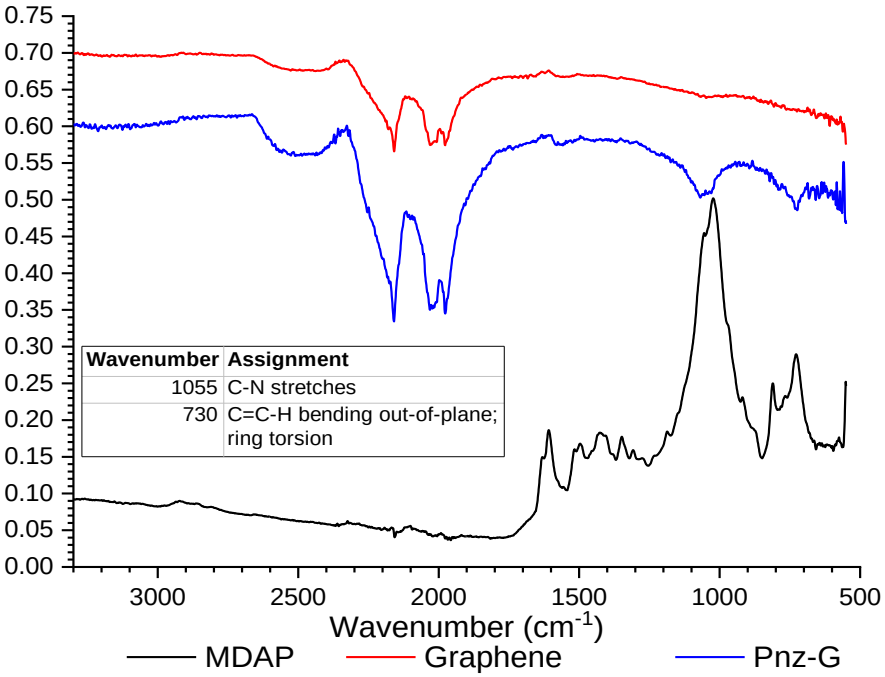

Figure 27: FTIR spectra of MDAP, Graphene and Pnz-G to show the new bands formed in Pnz-G and their similarity to MDAP.

Using dimethylformamide (DMF) as a solvent, it was possible to sonicate the modified graphene material and allow the excess powder to slowly precipitate. As it did, the solution gradually became a transparent, orange colour. This colour is likely due to the formation of colloids as the DMF is capable of interacting with the graphitic surfaces like rGO and GO[178] and should be able to do so with the hybrid. The absorption of the orange solution was measured by UV-vis spectroscopy, alongside the free dye (MDAP) and unmodified graphene (Figure 28a). The unmodified graphene that we used shows no distinct absorbance peaks and simply absorbs across the spectrum, while MDAP shows absorbance at 362 nm and 480 nm. The modified graphene has a hypsochromic shift to 465 nm in the visible region, compared to MDAP, and a stronger UV absorption going beyond 320 nm, which cannot be observed due to the cut-off from DMF.[85] What this suggests is that there is now a chromophore present that can absorb at 465 nm, close to the absorption of the dye whilst still being significantly shifted to be more than just adsorption.

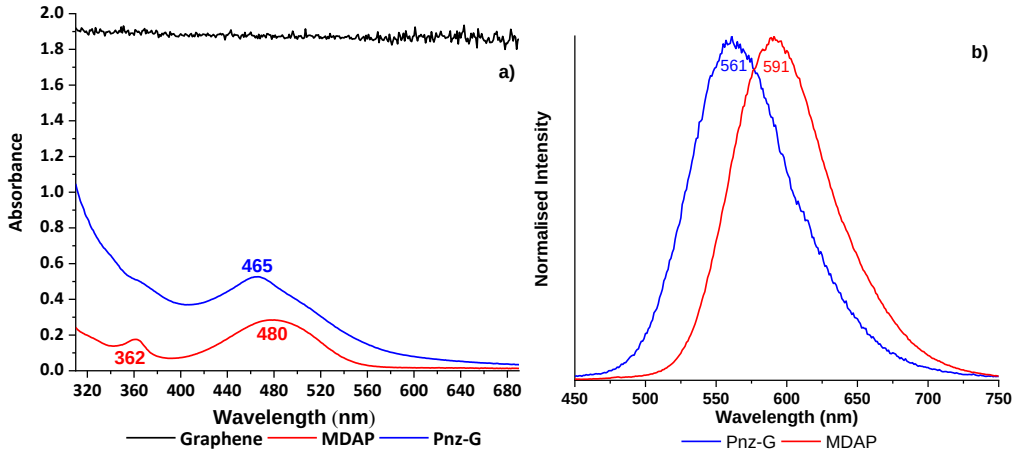

Figure 28: a) UV-vis absorption of MDAP, Pnz-G and Graphene in DMF and b) The normalised emission spectra of Pnz-G and MDAP with excitation at 440 nm in DMF. Copied with permission from author's publication.

Fluorescence spectrum of the modified graphene (Figure 28b), gives a peak of emission at 561 nm, compared to the 591 nm of MDAP. These changes in optical and fluorescence properties of the modified graphene samples also confirm successful modification of graphene surface, as an adsorption would not be expected to change the emission of the dye under these conditions, as Mou *et al*. show that eosin Y does not change in UV-vis wavelength or intensity with additions of GO sheets.[85, 111]

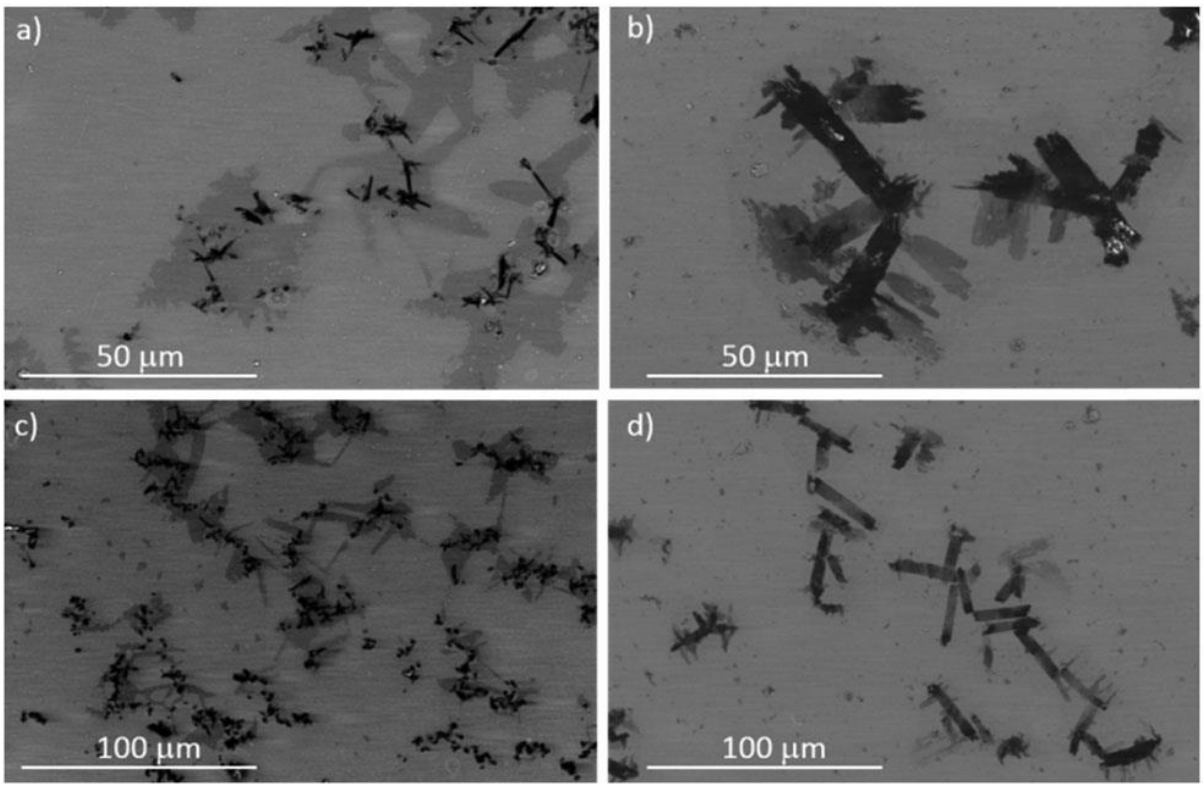

Figure 29: 3 kV SEM images recorded with a CBS detector of (a and c) pristine graphene nanoplatelets and (b and d) Pnz-G. Copied with permission from author's publication. All images taken operating 3 kV using the deceleration mode and a CBS detector by Alexander Kulak.

Using SEM analysis (Figure 29) of the starting graphene nanoplatelets (29a and 29c) and the modified platelets (29b and 29d), it is possible to see that the macrostructure of the plates has changed, causing the thin, widespread layering of the graphene to start aggregating and forming much thicker, darker layers of material. This would suggest that the intermolecular or interlayer forces, which cause the stacking and attraction of the layers, have been altered and have become stronger in the modified material. This is unlikely to occur through just sonication and aggregation of a dye on the surface, as the dye should be washed away by sonication and both materials have been sonicated for equivalent times. Additionally, the structure of the dye, if stacked unbound as flat layers on the graphene, would have similar π-stacking intermolecular forces with weaker Van der Waals forces present compared to that of the graphene sheets, giving no clear reasoning for increased aggregation and reduced film formation. However, if the dye is covalently bound and has stacks between modified planes, the dyes could create new π-π interactions if they slot between one another on separate sheets, allowing thick stacks to form as seen. This could also be related to the reduced d-spacings seen in PXRD data, where closer stacking of the sheets has resulted in thicker stacks of graphene sheets.

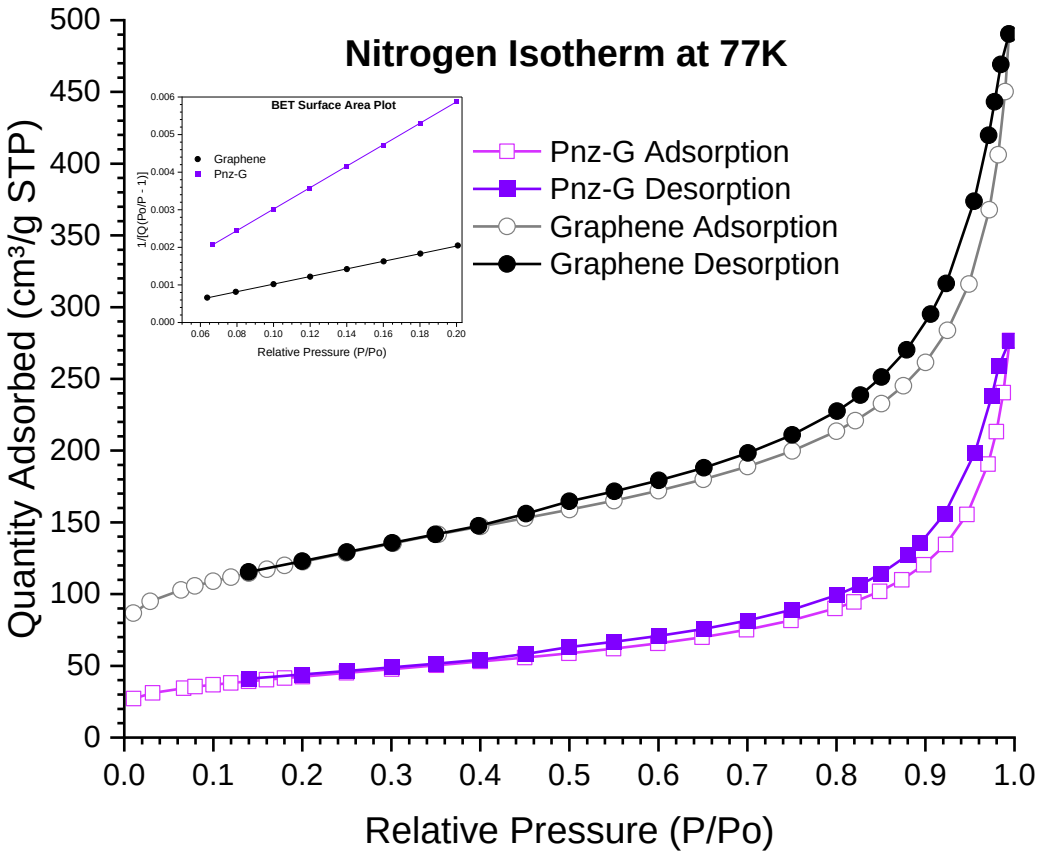

Figure 30: Nitrogen isotherm plot for Pnz-G and graphene nanoplatelets at 77K with inlaid BET surface area plot.

Sample	Single Point Surface Area (m^2/g)	BET Surface Area (m^2/g)	BET constant (C) value	Langmuir Surface Area (m^2/g)	t-Plot Micropore Area (m^2/g)	Average Pore Size (Å)
Graphene	426	430	888	586	126	53
Pnz-G	148	152	175	209	25	78

Table 3: Tabulated surface area data for Pnz-G and graphene nanoplatelets.

BET analysis was used to gain an insight into the changes on the hybrid's surface through the adsorption of nitrogen gas onto the surface (Figure 30, and tabulated in Table 3). The results showed that the pristine material, sold as 500 m^2/g, had a BET surface area of 430.16 m^2/g and Langmuir surface area of 585.64 m^2/g. The modified material showed a BET surface area of 151.64 m^2/g and a Langmuir surface area of 209.12 m^2/g. This shows a 64-65 % decrease in both surface area plot types and suggests that the surface has changed in a way that severely hinders its ability to adsorb nitrogen gas, which could also be explained by the formation of larger aggregates, as seen in SEM images (Figure 29). The difference in these two surface area measurements is that BET takes multilayers of adsorbent (nitrogen gas) into account. A similar surface area decrease has been shown by an active Bi_2S_3-ZnS/graphene composite, where BET showed a surface area of 187 m^2g^{-1} while still having strong photocatalytic activity, suggesting the loss of surface area is not unexpected and should not hinder photocatalytic functions.[125]

To find further proof of covalent modification rather than physisorption, it was necessary to investigate the effect of adsorbing MDAP onto the surface of graphene by recording the PXRD spectra of the produced powder (Figure 31). The physisorption samples were prepared by using an equal amount of free dye as diazonium salt and graphene, which were mixed vigorously together in EtOH. PXRD analysis showed no change in the diffraction pattern compared to the graphene sample, leaving just the graphitic peak at $2\theta = 26$ °, with a similar width seen for pristine graphene samples.

When the concentration is increased further to double that used of the diazonium salt, the diffraction remains similar to that of graphene, though with the addition of two more diffractions at $2\theta = 36.5$ ° and $2\theta = 56$ °. This could indicate that these diffractions are related to a dye crystal structure forming on the graphene as an agglomerate, or a rearranging of the layering on the graphene. What can be taken from this is the lack of any disorder being added to the system.

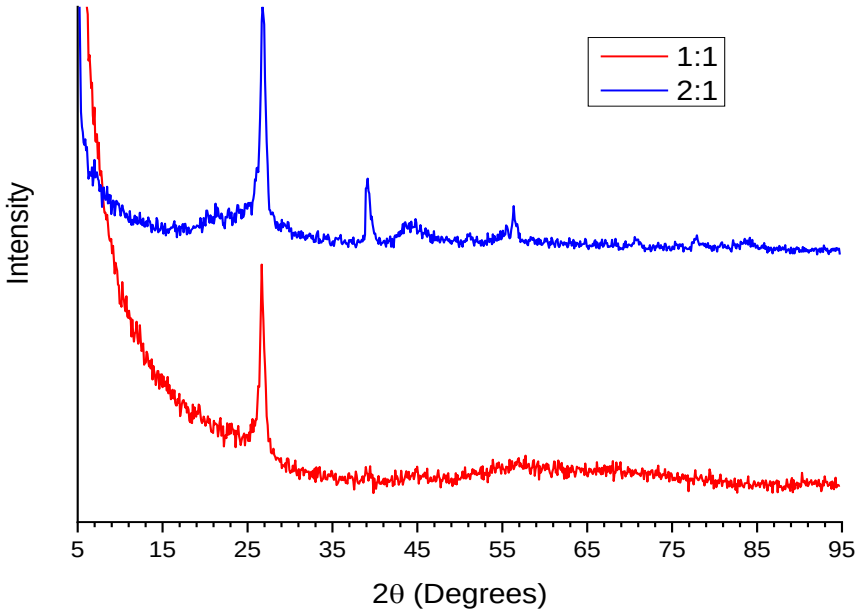

Figure 31: PXRD pattern for adsorption experiments between graphene and phenazine free dye, using varying dye concentrations. The ratios describe the amount of free dye added compared to the amount of diazonium added to solution as separate reactions.

One-Pot Synthesis of Phenazine-Graphene using Trifluoroacetic Acid and Hydrochloric Acid

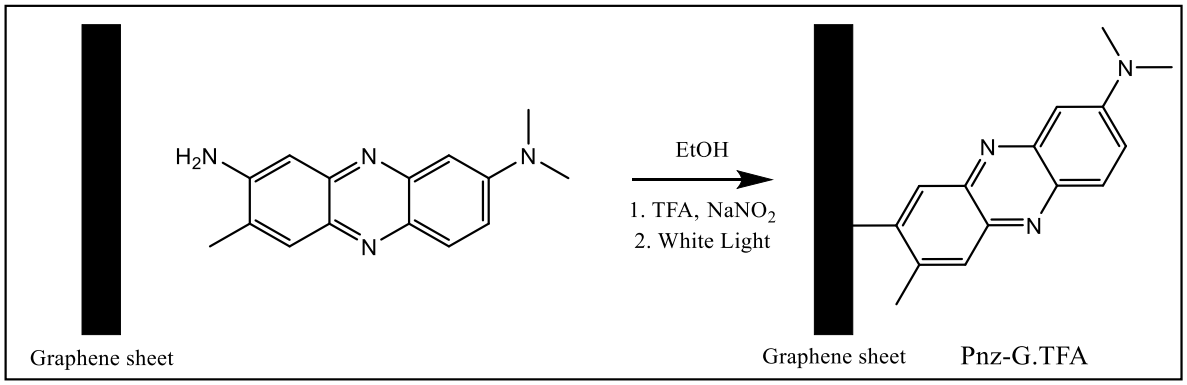

Scheme 5: The reaction scheme of graphene and neutral red as a one-pot synthesis with TFA as the acid.

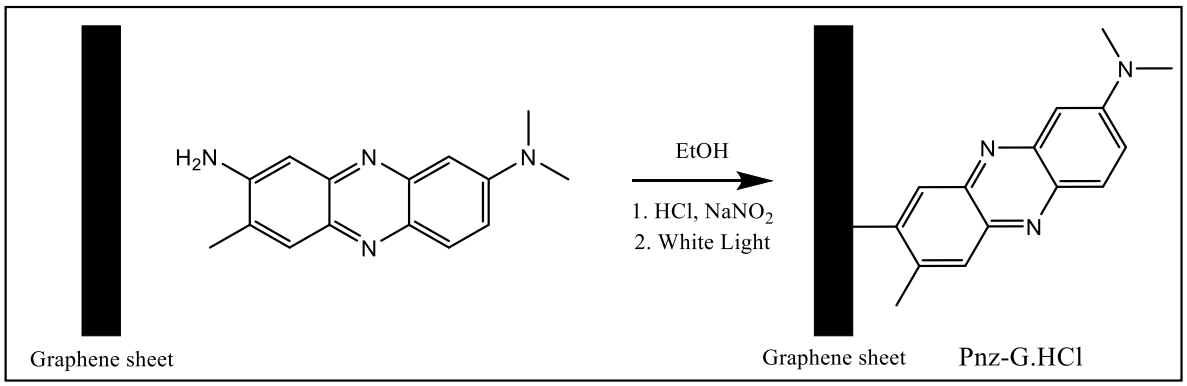

Scheme 6: The reaction scheme of graphene and neutral red as a one-pot synthesis in the presence of HCl.

Hydrochloric acid and trifluoroacetic acid (TFA) were chosen as alternative acids for the formation of the diazonium salt of Neutral Red. The method used was changed to an *in-situ* method, due to the literature showing this method for changing small substituents on the phenazine structure when using hydrochloric acid.[77] These reactions (shown in Schemes 5 and 6) were allowed 10 minutes for diazonium formation prior to graphene addition and white light irradiation. This was done to minimise any degradation of these alternative phenazine diazonium salts. The samples were then washed with ethanol, centrifuged, and the washing repeated several times before drying.

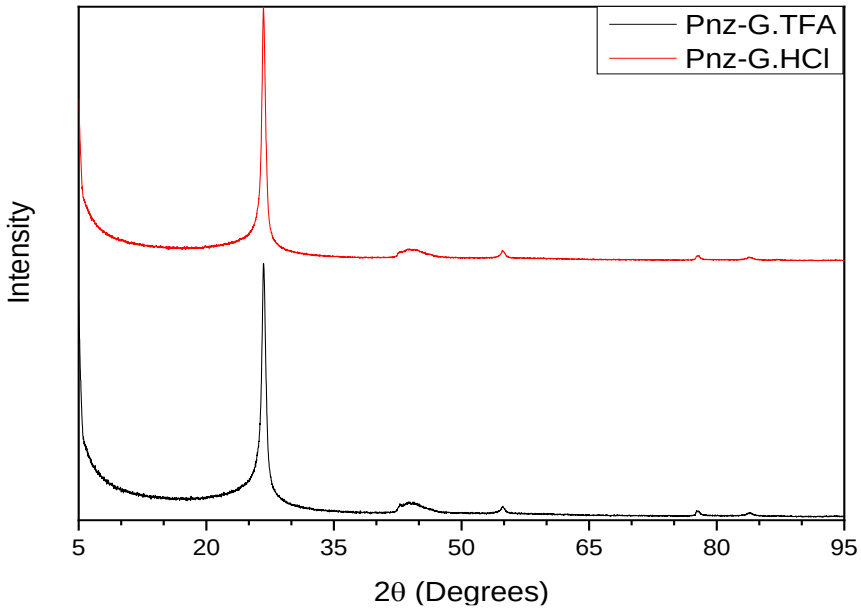

Figure 32: PXRD pattern for the two one-pot syntheses of Pnz-G using TFA and HCl as the acid in solution.

In the PXRD of the two variants of Pnz-G (Figure 32) show very little change compared to pristine graphene. However, what can be seen is a widening of the graphitic peak in the case of Pnz-G.TFA by 60 % and 45 % increase for Pnz-G.HCl obtained by using Voigtian type fitting of the graphitic peak and comparing the calculated FWMH with that of the calculated FWMH of graphene.[179] There was also a shift in the peak of both hybrids to 26.74 ° – the same change seen with the original Pnz-G. These two data show an addition of disorder to graphene which suggests modification of the surface and shows that an alternative acid and method can be used in the modification of graphene.[90]

<u>Preparation of Pnz-Graphene samples for TEM and STM studies</u>

To prepare Pnz-Graphene samples for TEM analysis, graphene flakes of high quality from 2DTech as a suspension in iPrOH were used under the same reaction conditions as in the original reaction with graphene under light-induced conditions. The samples were analysed by PXRD and in this case a stronger graphitic diffraction angle of 2θ = 26 ° has been recorded while the additional pattern peaks

were weaker than previously seen, when compared as a ratio to this stronger graphitic peak. This could be due to the suspension graphene being better at forming a larger number of layers, with or without modification, and not necessarily suggestive of poor modification since this peak is related to the π-π stacking of the sample.

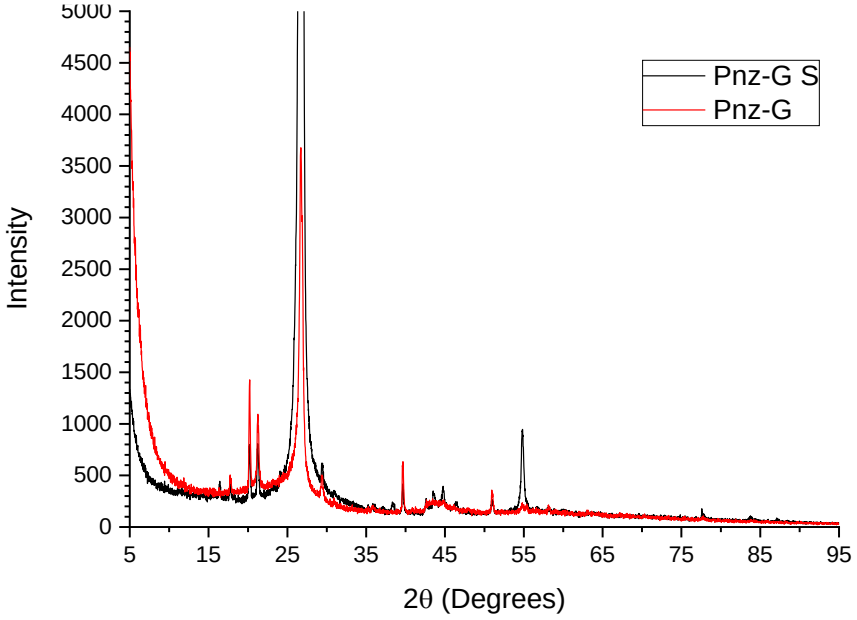

Figure 33: The PXRD pattern of the standard hybrid (Pnz-G) and the hybrid formed from 2DTech graphene (Pnz-G S), showing the much larger diffraction angle intensity for the graphitic peak to suggest a greater graphitic nature.

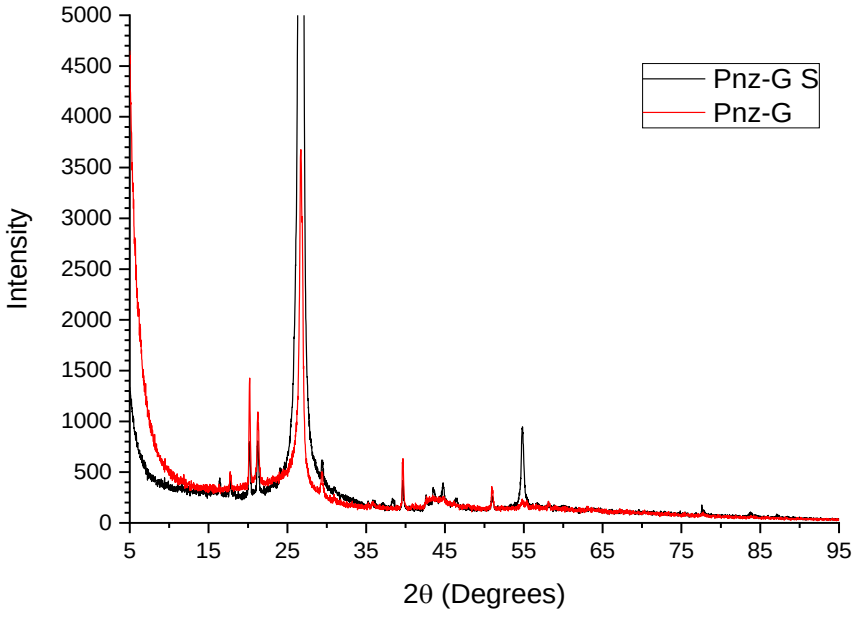

Figure 34: The PXRD pattern of the standard hybrid (PNZ-G) and the hybrid formed from 2DTech graphene (Pnz-G S), showing the diffraction pattern that is from the dye is still present within the higher quality graphene sample.

This sample was additionally analysed by TEM (Figure 35), by Li-Shang Lin in the Faculty of Engineering at the University of Leeds. The TEM results showed an area with a new lattice pattern; the image analysis was used to determine the coverage of the surface with dye molecules (Figure 36).

Within the fast Fourier transformation (FFT) electron diffraction pattern, the graphene diffraction pattern is hexagonal (red dashed lines, Figure 36) and appear far out from the centre point. This is because the FFT represents an inverse space, and larger distances in real space (TEM images) correspond to smaller distances from the centre point in reciprocal space (FFT images). The FFT taken from the modified graphene sample showed two hexagonal diffraction patterns with a ~0.21 nm lattice parameter, as well as new lattice structures with ~0.42 nm and ~0.5 nm lattice parameters. The hexagonal lattices correspond to graphene, as expected, with several overlapping sheets that are rotated off one another to create multiple patterns of the same nature. Furthermore, inversed fast Fourier transform (IFFT) images from unmodified graphene samples clearly show the honeycomb pattern of graphene surface (Figure 34A, right). What can be taken from the change in the IFFT is that there has been the addition of disorder to the sample as well as the new diffraction.

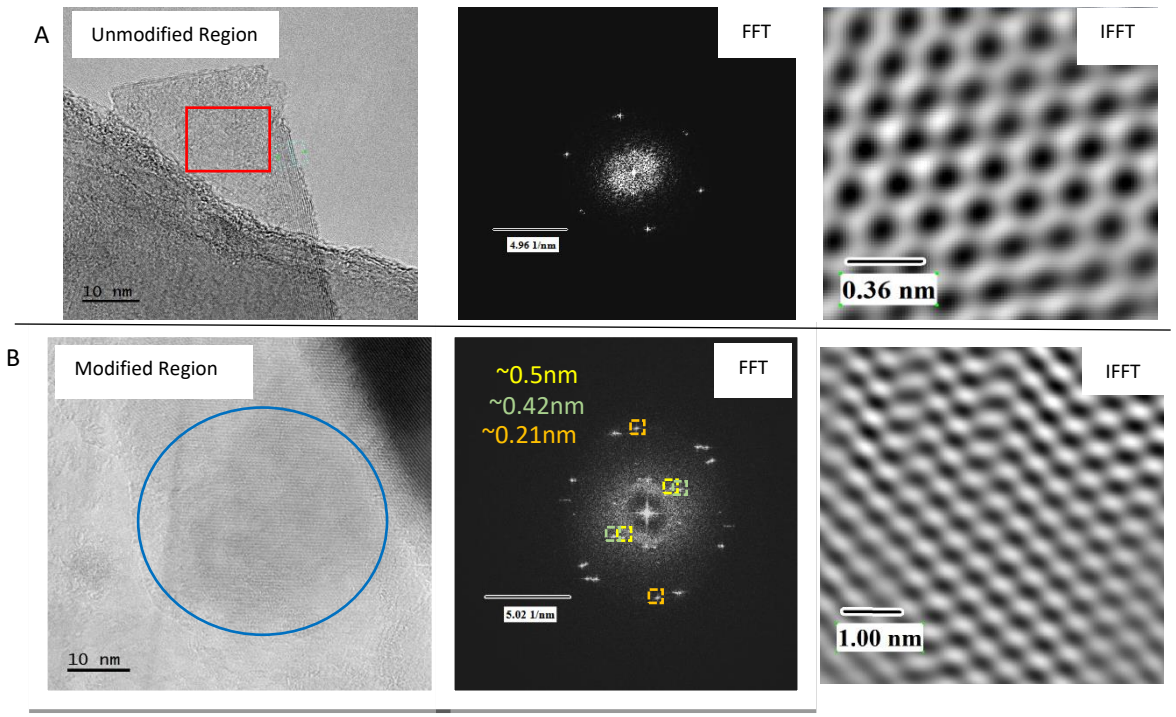

Figure 35: (A) TEM image, FFT and IFFT of the unmodified graphene in the region of the red box; (B) TEM, FFT and IFFT of the region of altered lattice region.

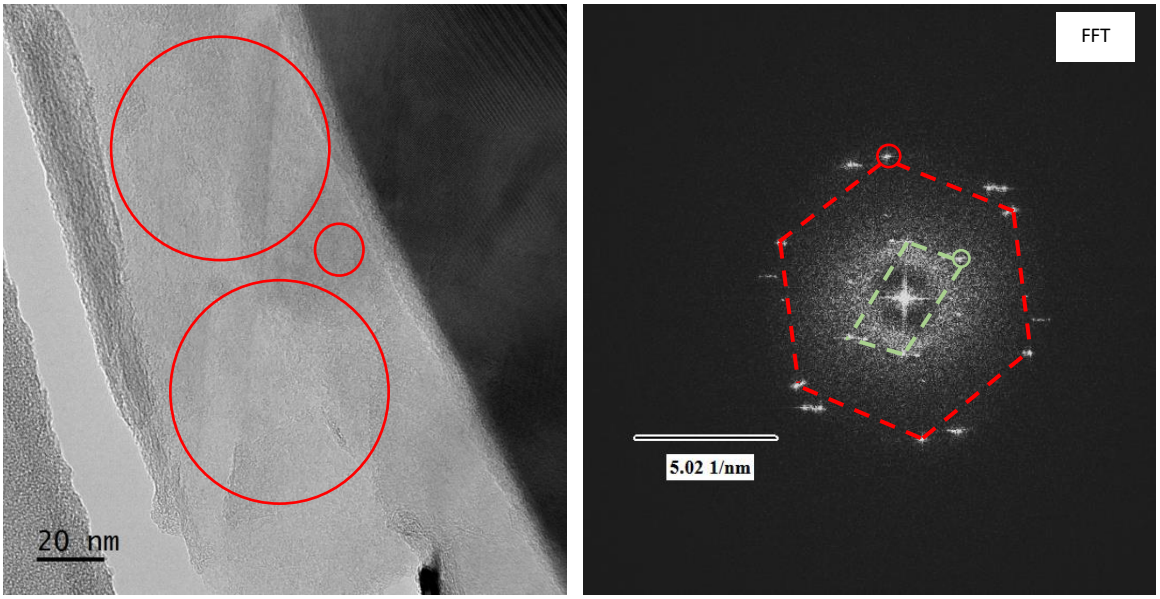

Figure 36: The TEM (left) and FFT from the sites highlighted by circles (right) of Pnz-G on 2DTech graphene nanoplatelets.

Preparation of Phenazine-Graphene on SiC for STM and STS analysis

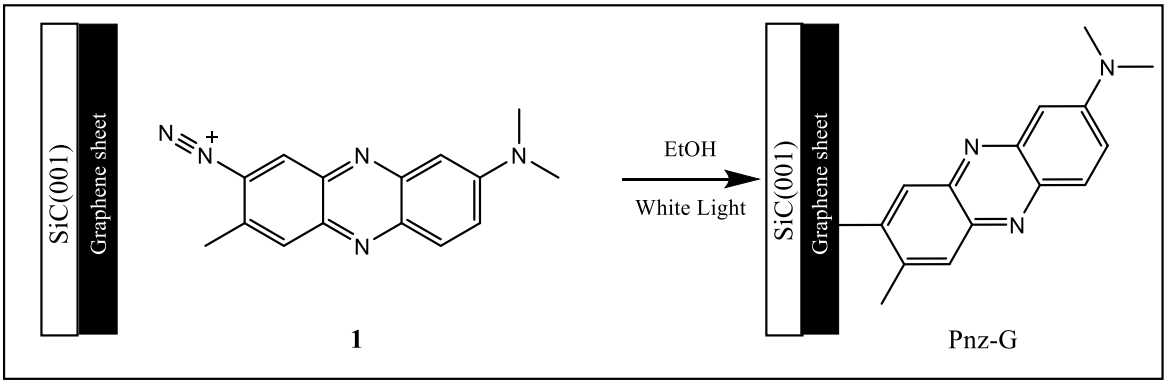

*Scheme 7: The modification of graphene/SiC(001) using diazonium **1**.*

The Si-C supported graphene (graphene/SiC(001)) was analysed by Raman spectroscopy: 1) before the reaction with diazonium salt 1, 2) after 20 minutes in the diazonium solution in the dark, 3) after 20 minutes with light exposure in diazonium solution and 4) after 40 minutes with light exposure in diazonium solution. This allows the identification of the changes in the G and D peaks in the Raman spectra of the graphene as the reaction occurred. Typical Raman spectrum of graphene consists of several bands, namely D, G and 2D, where D peak represents the number of defects within graphene layer and G peak reflects the quality of graphene surface.[83, 84] An interesting observation was an increase in the G peak intensity, with respect to the D peak, after the graphene surface was exposed to light whilst in the diazonium solution (Figure 37). This is interesting because the D peak should increase as the reaction goes on, due to the increasing number of defects caused by functionalisation

of the graphene surface. However, this change can be attributed to the Raman spectrum displayed by the diazonium backbone.[2, 83-85]

Also, there is a decrease in the D peak intensity, which may be due to the different defects at different points on the graphene. Over the course of 40 minutes, the 2D peak increases despite the decrease in the D peak and is unusual due to their relation to one another. An explanation for this could be due to the structural framework of the diazonium salt and its close resemblance to an N-doped graphene fragment.[2, 85]

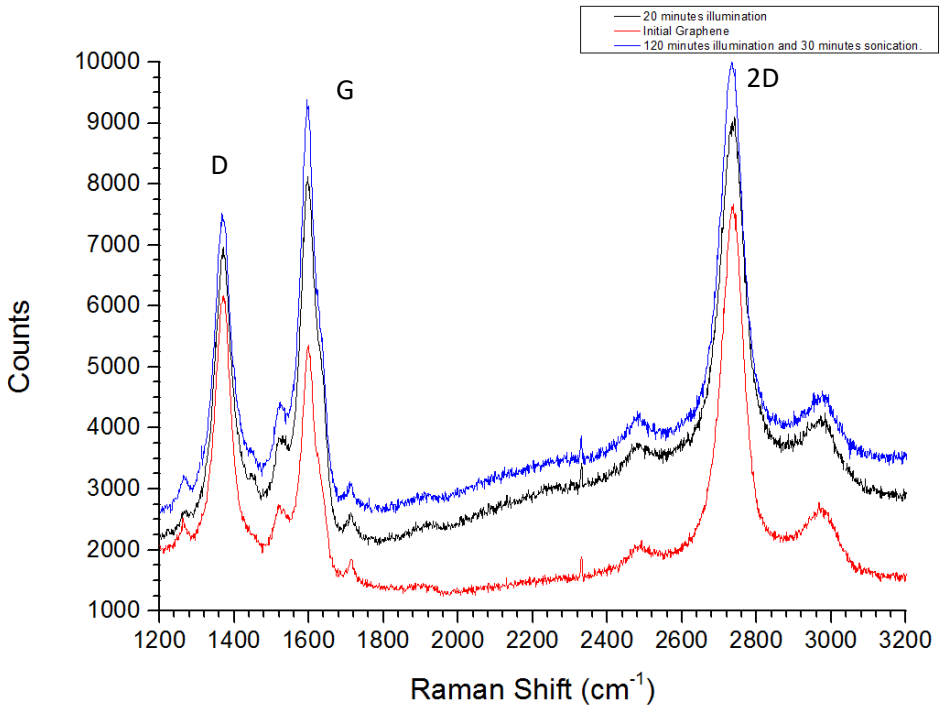

Figure 37: The overlaid Raman spectrum for the graphene modification after different times in solution and different conditions, showing changes in the D, G and 2D bands.

The Raman spectrum (Figure 37) shows that the I_D/I_G ratio, the ratio between the D band and G band, is 0.85 after 20 minutes of irradiation in the presence of the diazonium salt. This ratio then reduces to 0.8 after 120 minutes of irradiation, showing a gradual decrease in the population density of defects. This can occur when the interdefect distance falls below 3 nm, even when the number of defects is increasing because the contributions will no longer sum up independently below this distance.[2, 85]

The second sample on SiC was synthesised by our collaborators at Trinity College Dublin (Krasnikov, *et al*.) using the same methodology described above for the first sample. They have carried out STM measurements on the SiC supported graphene and the modified sample 2. The STM (Figure 38) showed that the side-on surface changed to a “cloudy” morphology. Meanwhile, the upper surface

changed from the very regular and recognised honeycomb structure of graphene to large, elongated spots across the surface. This suggested that the dye molecule had sat upon the surface vertically and had most likely bound covalently. [2, 85]

They use the STM data to perform a DFT simulation of the hybrid's surface structure, shown in Figure *39*. This shows that the molecular overlayer was a portion of the phenazine dye and that the unit cell showed that the dye was modifying graphene on every eighth carbon position and was in an ordered structure upon the surface. [2, 85] This overlayer's unit cell (outlined in Figure 38f and Figure 39) is similar in shape to the new electron diffraction pattern seen in the FFT analysis (Figure 365B) and could also be related to new patterns seen in the PXRD of the powder samples, if the pattern is as regular in the powder reactions.

Where IFFT images from phenazine modified samples (Figure 35B, right) reconstruct molecular overlayer on the surface with a structure similar to the one observed by STM. Put together, this confirms that the reactions we see within STM on Pnz-G/SiC(001) can be replicated on the powdered bulk samples of graphene, rather than only on trilayered graphene.

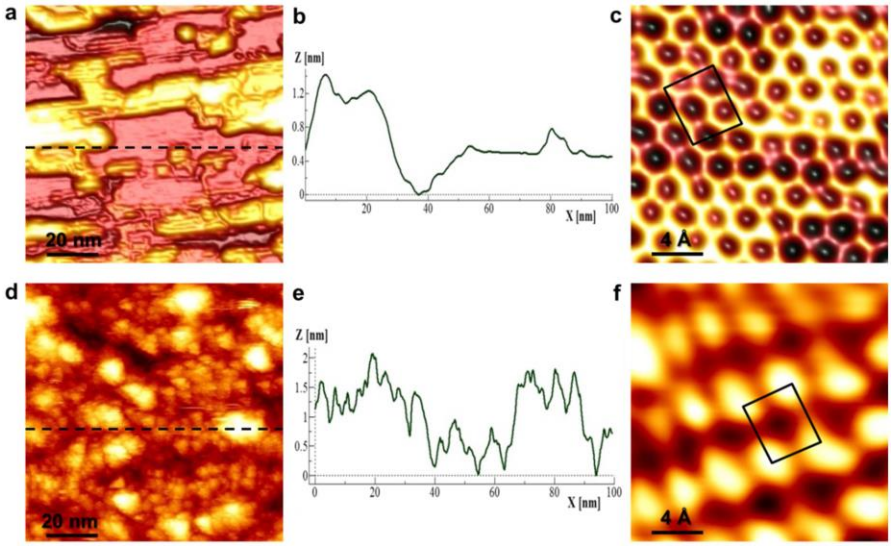

Figure 38: STM images of pristine graphene/SiC(001) V_{sample} = −0.8 V, I = 60 pA, 100 nm × 100 nm (a) and V_{sample} = 10 mV, I = 150 pA, 2 nm × 2 nm (c), Pnz-G/SiC(001) V_{sample} = −2.5 V, I = 60 pA, 100 nm × 100 nm (d) and V_{sample} = −2.5 V, I = 50 pA, 2 nm × 2 nm (f). The line profiles measured along the dashed lines of a and d are provided (b and c). The unit cell of the molecular overlayer is described by the solid line in (c) and (f). Copied with permission from author's publication.

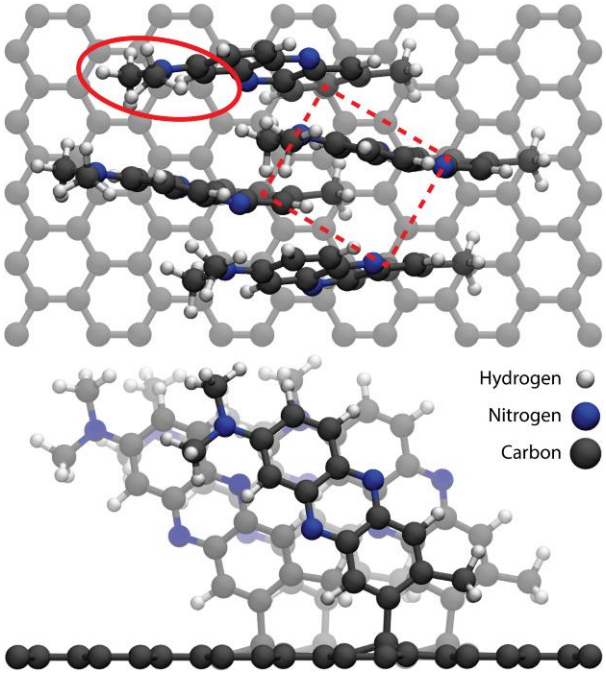

Figure 39: Top and side views of Pnz-G in a relaxed model. The unit cell of the molecular overlayer is outlined by the dashed line, while the oval is used to highlight the top part of the molecule, suggested as the visible part of the STM (Figure 38). Copied with permission from author's publication.

Krasnikov, *et al.* then proceeded to run STS experiments on both the pristine graphene/SiC(001) and Pnz-G/ SiC(001) (Figure 40). The data showed the expected zero band gap of the graphene/SiC(001), which is well documented, and that the Pnz-G/SiC(001) has a band gap of around 0.8 eV, which is outlined by the prominent features at -0.4 and 0.65 eV. Density of states calculations show that the occupied states around the Fermi Level of the hybrid consists mainly of contributions from the graphene sheet, whilst the unoccupied states in Fermi level vicinity consist of contributions from both the phenazine dye and the graphene – directly confirming that the dye is covalently attached and creating a hybrid surface with a sizeable band gap.[(2)]

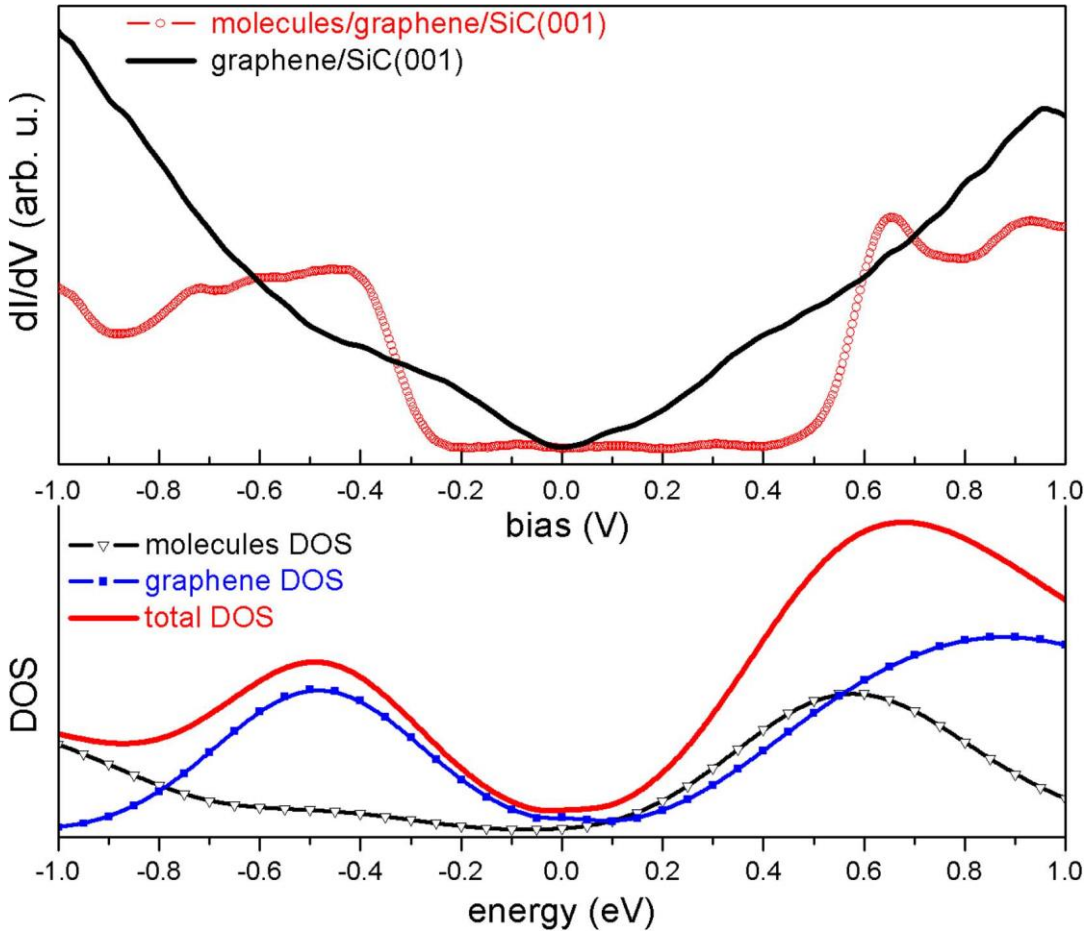

Figure 40: STS measured from graphene/SiC(001) and molecules/graphene/SiC(001) (top) and the density of states (DOS) for total the total system alongside the partials for the attached molecules and graphene (bottom). Copied with permission from author's publication.

The STS dI/dV curves show that the pristine graphene/SiC(001) has no band gap, a typical behaviour for a gapless material. Pnz-G/SiC(001) exhibits two features in the vicinity of the Fermi level at -0.45 and 0.65 eV, which allows an approximation of a 0.8 eV band gap when extrapolated to zero intensity. This also has good agreement with the calculated density of states (DOS) for a four-molecule model of Pnz-G, meaning both the theoretical and experimental result agree. Further to this, the DOS show that the occupied states near the fermi level are mainly a graphene contribution, and the unoccupied states consist of both graphene and the phenazine molecules, according to the partial DOS calculated separately for the molecules and the graphene. This is a confirmation of covalent modification of the graphene by phenazine molecules leads to a hybrid with a sizeable band gap.

2.3.4 Chemistry and reactivity of Neutral Red Diazonium Tetrafluoroborate Salt

These reactions were undertaken to provide insight into the reactivity of diazonium salt 1 and how specific the reactions previously discussed are to graphene or graphitic materials.

Reactions of Diazonium **1** with 2-methyl-3-butyn-2-ol

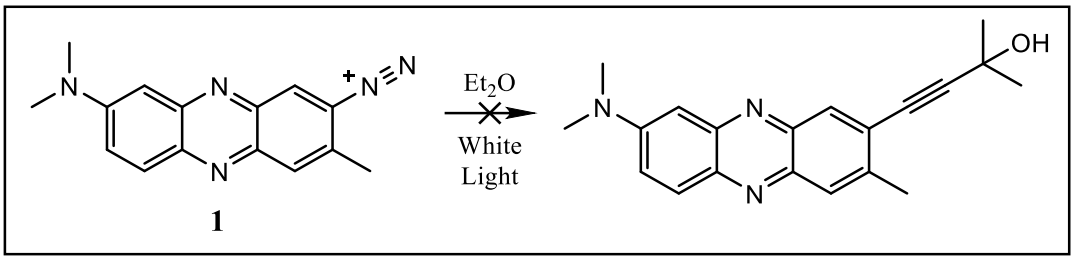

*Scheme 8: Expected reaction for modification of diazonium **1** with 2-methyl-3-butyn-2-ol.*

The modification of diazonium salt 1 with 2-methyl-3-butyn-2-ol was undertaken in order to explore the reactivity of the diazonium salt with small molecules (Scheme 8). The reaction was run under illumination with intense white light, in order to excite the dye and initiate a photochemical reaction. However, after the reaction had been running for a suitable period of time and the solution had been analysed by mass spectroscopy, there were no peaks to indicate the product had been formed from the reaction. With graphene the photochemical reaction of the compound had only taken 40 minutes to occur in our heterogeneous process, but the reaction had been given longer than this to match literature reaction times of 2 hours,[31] leading to the decision that it had failed. It is suspected that the reaction did not take place due to a lack of an electron donating species, which would be needed to provide the electron to destabilise the $-N_2^+$ functional group, as seen with the use of graphene and the hot electron donation.

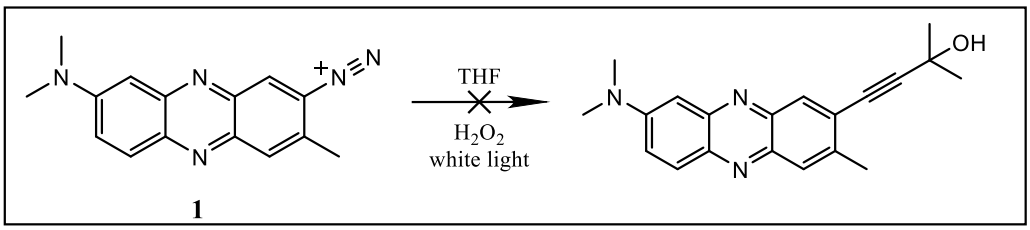

*Scheme 9: Expected reaction for modification of diazonium **1** with 2-methyl-3-butyn-2-ol using methanol solvent and peroxide as a provider of electrons.*

The presence of an electron donating species was thought to facilitate the reaction, therefore an oxidising agent was introduced into the mixture (Scheme 9). However, this resulted in the immediate reduction of the diazonium to MDAP, when carried out in methanol. Alternative solvents for the reaction were not compatible with oxidising agents such as $NaNO_2$ and hydrogen peroxide.

The conversion of diazonium to MDAP was caused by the hydrogen abstraction from methanol, as this is an easily accomplished process. The destabilisation of the diazonium group would usually result in an aryl radical being formed in solution, which will react rapidly with the closest possible molecule, which would be the methanol solvent. The destabilisation by hydrogen peroxide is a homogeneous

process, so the usual effects of adsorption, seen with graphene to maximise the reaction of the destabilised salt, is not observed with 2-methyl-3-butyn-2-ol.

These two reactions suggest that the alkyne bond is not reactive with the phenazine diazonium salt, which we propose is due to the lack of an electron of sufficient energy to transfer into the diazonium bond and destabilize it.

Reactions of Diazonium **1** with 4-Nitrobenzaldehyde, Imidazole, 4-Bromobenzoic Acid and Trimethylsilylacetylene

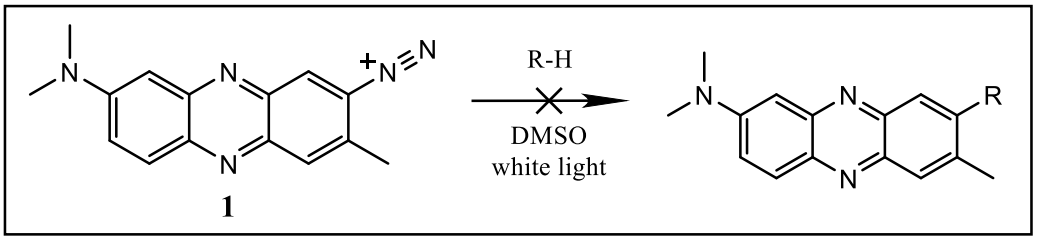

Scheme 10: The general scheme for the modification of the diazonium with small molecules.

As a continuation of the reactivity testing of the diazonium, four more small molecules (4-nitrobenzaldehyde, imidazole, 4-bromobenzoic acid and trimethylsilylacetylene) were each dissolved and illuminated with the diazonium salt (Scheme 10). The reaction was an attempt to create a covalent bond between the molecules. After illumination in solution for several hours, there appeared to be no colour change or product peaks from the mass spectrum that was collected. Thin layer chromatography (TLC) showed no new spots, suggesting there were no new compounds formed and that the reaction was not proceeding in the intended direction. Once again, this could be due to a lack of electron donating species available and known reagents to induce reaction would not be suitable for the solvent. Additionally, it is also probable that the highest occupied molecular orbital (HOMO) and LUMO energies of the molecules do not match, even with excitation of the dye with white light.

The only exception was imidazole, which had an instant change from white to a bright orange and then red upon contact with the dark purple solution of diazonium salt. However, this was likely due to a rapid conversion of the diazonium to MDAP because mass spectroscopy showed no signals that matched the expected product, whilst it did contain a peak corresponding to either MDAP or the diazonium salt.

Much like the reaction with 2-methyl-3-butyn-2-ol, it is possible that there may not have been sufficiently high energy HOMO electrons to transfer to the diazonium LUMO to initiate a reaction between the molecules, resulting in a lack of reaction.

Reaction of Diazonium **1** with Fullerene

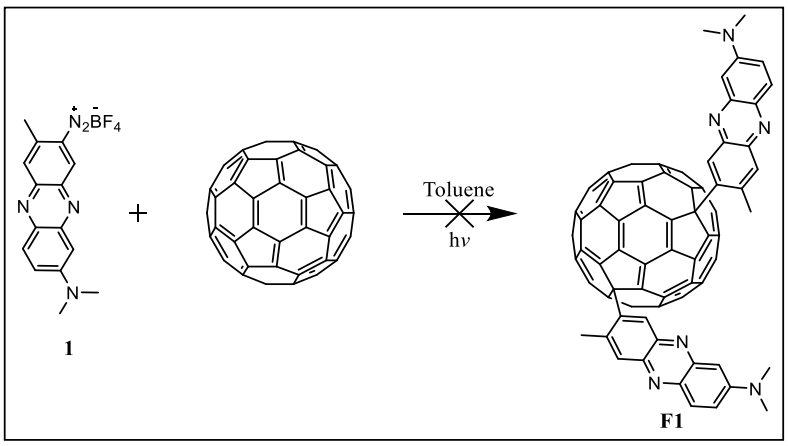

*Scheme 11: Fullerene Modification using diazonium **1**.*

The next substrate chosen was fullerene, shown in Scheme 11. This reaction was carried out in toluene to solubilise fullerene C_{60}. The reaction was allowed a longer period of time than the graphene due to reactions in the literature requiring several hours at high temperatures.[27] However, this still did not facilitate the modification of the fullerene, as TLC monitoring showed no changes in the monitored spot. The reaction was also analysed by ^{1}H NMR and showed no distinct peaks that could correspond to fullerene. Although there were several new peaks in the lower shift region (2-3 ppm) and a change in the integrations of the known peaks of both MDAP and the diazonium salt. This made it difficult to determine what had occurred during the reaction and whether the diazonium had reduced or was still active within the solution.

Due to the thermal decomposition of diazonium salts, it was necessary to remain at ambient temperatures. This meant that the higher temperatures seen in the literature were not feasible.[27] This provides more proof that graphene is the most suitable carbon material for the synthesis of the photocatalytic system, as it has shown to be more effective in milder and greener conditions.

Reactions of Diazonium **1** with pyrene

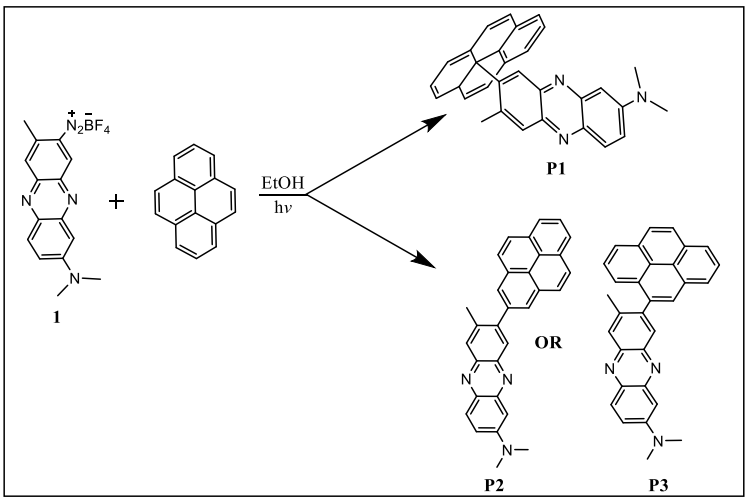

Scheme 12: Modification of pyrene with diazonium salt 1.

Another compound that had been identified as a modification target was pyrene, which is a fusion of four aromatic rings in the same way as graphene, and therefore expected to react successfully with the diazonium (Scheme 9). The mass spectrum did show potential reactions between the two molecules, but there were also unusual radical species peaks of both the pyrene and the diazonium. The isolation of the molecule was attempted by addition of water, which appeared to form a thin precipitate from a small portion of the whole solution but isolating the precipitate through filtration proved difficult as it passed through filter paper. An improvement on this could be to centrifuge the products to isolate them, rather than filtration, as this method was not possible at the time of the reaction.

When the reaction was repeated at an increased scale and the product appeared to be formed (TLC monitoring), water was added to form two different precipitates which behaved differently in the solution. A black solid formed at the bottom of the flask and a grey/purple film/suspension formed on the upper surface of the solution. These were each isolated, dried, and analysed by ^{1}H NMR ($CDCl_3$), where the solutions formed were two shades of orange. The grey sample appeared to be largely pyrene by NMR analysis, with a small number of phenazine peaks present, and the black solid showed signals only corresponding to the pyrene, but at a lower intensity signal.

These data sets would suggest the pyrene had limited solubility in the ethanol but was still able to undergo some reactions due to the different materials that had been formed and detected. This was the first sign of ambient reactivity from the diazonium salt and suggests that materials chemically similar to graphene could be used to complete the goal of ambient or photochemical modification.

2.4 Conclusions

In this study the method used for the diazonium salt synthesis was complex because the solubility, stability and depth of colour made many isolation methods difficult to achieve. Using known methods, we have successfully shown a simple way to synthesise and isolate a dye-based diazonium salt with improved stability.

We have shown, for the first time, that it is possible to attain direct covalent attachment of organic dyes to graphene *via* a powerful, but simple and mild photochemically induced radical addition reaction using a diazonium functional group. It has also been shown that optical properties of the dye have been maintained after attachment. Photochemical modification of the graphene was confirmed by UV-vis monitoring, PXRD, TGA, Raman and IR, whilst also confirming the preservation of the crystallinity on the GnP basal plane, which minimises the sacrifice of graphene's natural properties. Both the size of the molecule and speed at which the surface can be modified is an improvement to what has been found in the literature, where a monolayer of aryl required 25 hrs and 500 °C annealing.

Through analysis by Raman, TEM, STS and STM, we have confirmed the attachment to graphene is similar for both a supported thin layer of graphene and bulk batches of graphene powder. We can also confirm that this method is applicable for band gap modification of graphene surfaces, as Pnz-G has been shown to have an electronic band gap of 0.8 eV through STS and DOS.

A surprising effect of the modification was the increased solubility of the dye-graphene system in DMF, which allowed for the recording of the system's UV-vis spectrum and the emission spectrum. This meant that it was made easier to confirm the presence of the dye on the surface and estimate a visible optical band gap of 1.95 eV.

BET data shows a decrease in the surface area of Pnz-G of 64.75 %, which helps to suggest that some of the layers of the system have been modified to reduce the surface area. The reduction of the surface area is also supported by SEM images, which show agglomeration of the Pnz-G sheets compared to pristine graphene.

From the study into the phenazine-based diazonium salt's reactivity, only pyrene showed reactivity which may suggest that graphene is participating in the mechanism of modification directly, likely through electron donation. This would explain why other materials were unsuccessful due to poor electron donation capabilities compared to graphene.

Future work from here would be to broaden the range of dyes used to form these isolated diazonium salts and to find a way to make use of the less stable salts, potentially through diazonium formation *in situ* of other reactions.

2.5 Experimental

2.5.1 General Methods and Materials

Graphene layers were fabricated on cubic-SiC(001) films grown on on-axis Si(001) wafers using Si-atom sublimation followed by surface layer graphitisation at high temperatures prior to our use. Graphene used for TEM experiments was obtained from 2DTech and used without further purification. All other reagents were obtained from Sigma Aldrich, Alfa Aesar, VWR and Acros and used without further purification. All ^{1}H and ^{13}C NMR were recorded on a Bruker AV3-400 or a Bruker Avance 500 spectrometer. Chemical shifts (δ) were reported in part per million (ppm) relative to the residual solvent peak, and peaks are described as singlet (s), doublet (d), triplet (t), quartet (q), multiplet (m), broad singlet (br), and coupling constants (J) are quoted in Hertz (Hz). Spectra were measured at room temperature unless otherwise stated. High resolution mass spectrometry was performed on Bruker Maxis Impact (EI+) by positive and negative electrospray ionisation (ESI). The accepted error is <4 ppm. Infrared spectra (IR) were recorded in solid phase on a Bruker Alpha Platinum attenuated total reflectance (ATR) FTIR spectrometer with vibrational frequencies given in cm^{-1}. Peaks described as weak (w) medium (m), strong (s) or broad (br). The electronic absorption spectra were recorded on a Cary 100 UV-vis scanning spectrophotometer. The fluorescence spectra were recorded on a FluoroMax-3 or a Fluoromax Plus C spectrofluorimeter, with excitation wavelengths (Ex) used stated in parenthesis. Powder X-ray diffraction analysis was performed using a Bruker D2Phaser diffractometer. The light source for photochemical reactions was a nightsearcher workstar SMT light emitting diode (LED) Portable Rechargeable Floodlight (2200 Lumens station, 10 LEDs in station) positioned 12 cm from the sample. Dry “composite crystals” were dispersed in ethanol and one drop of suspension was put on silicon wafers, which was mounted on a SEM stub using adhesive copper film, and samples were viewed, without coating, with a FEI Nova FEG-SEM operating at 3kV using deceleration mode and CBS detector.[85] TEM images were recorded using FEI Titan3 Themis 300 and images were processed using Gatan Microscopy Suite 3.

The STM experiments (Krasnikov *et al.*) were “performed at 78 K in UHV conditions. Electrochemically etched [111] and [100]-oriented single crystalline W tips, sharpened in UHV by electron beam heating and ion sputtering, were used to record STM images in constant-current mode and STM topographic images were processed using WSxM software. DFT calculations were performed using the plane-wave self-consistent field package from the Quantum ESPRESSO software distribution and electron exchange and correlation were treated within the local density approximation with the Perdew–Zunger parametrisation”.[2]

2.5.2 Synthesis of Neutral Red Diazonium Tetrafluoroborate Salt

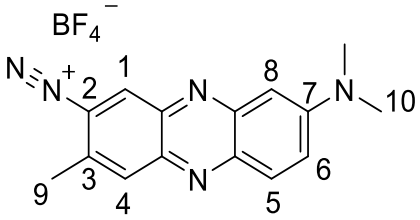

Scheme 13: The product of the diazotisation reaction of neutral red with sodium nitrite in the presence of tetrafluoroboric acid.

Neutral Red (1.47 g; 5.04 mmol) was dissolved in tetrafluoroboric acid (7 mL; 50 % w/w H_2O) and stirred. A saturated solution of sodium nitrite (1.35 g in 2 mL H_2O; 5.04 mmol) was added dropwise and the solution was left stirring for 2 hours. A small volume of diethyl ether (5 mL) was added and the diazonium salt was filtered as a purple powder by vacuum filtration. Yield 1.2 g, 68 %. ^{1}H NMR (500 MHz, $CDCl_3$) δ_H: 2.64 (3H, s, H^9), 3.49 (6H, s, H^{10}), 6.70 (1H, s, H^8), 7.67 (1H, d, *J* = 10.3, H^6), 7.81 (1H, s, H^4), 8.02 (1H, s, H^1), 8.06 (1H, d, *J* = 10.2, H^5) [(180)]; ^{13}C NMR (101 MHz, CD_3CN) δ_C: 157.1 (C-4a), 145.1 (C-7), 139.9 (C-3), 139.4 (C-5a), 138.6 (C-1), 135.8 (C-2), 133.7 (C-8a), 129.7 (C-5), 12`6.3 (C-4), 118.07 (C-6), 91.5 (C-8), 41.8 (C-10), 21.4 (C-9)[(180)]; HRMS *m/z* (ESI^+) 341.1759 (Found 341.1759 for M+2MeCN+Na^+-N_2, expected 341.1609); IR: 3564.90 (wet or N-H), 3357.50 (wet or N-H), 1619.98 (C=C aromatic), 1523.69 (C=C aromatic), 1274.46 (N-C stretch), 1210.74 (N-C stretch), 1165.43 (N-C stretch), 802.91 (aromatic C-H bend), 706.62 (aromatic C-H bend), 549.44 (B-F stretch), 518.28 (B-F stretch), 474.38 (B-F stretch), 472.97 (B-F stretch); UV-vis maximum wavelength (λ_{max}) = 534 nm, wavelength (λ) of absorption peak = 375 nm; fluorescence (Ex = 534) 619 nm (attributed to degradation of the material). It was found that isolating a by-product salt from the diazonium was not possible with our setup and solubility, but was an impurity allowed forward for easy removal from graphene in later stages and was believed to be unlikely to affect the reaction adversely.

2.5.3 Synthesis of 7-dimethylamino-3-methylphenazine

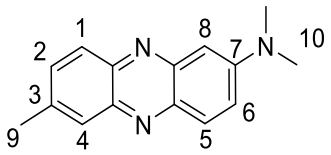

Scheme 14: The product of neutral red diazonium with reducing agents.

Method A. Diazonium **1** (1.4 g; 4 mmol) was dissolved partially into stirred diethyl ether (20 mL) and CuI (1.53 g; 8 mmol) dissolved in minimal water was added to the solution. This purple mixture was stirred for 24 hours. Crude solid product was collected by vacuum filtration. Then the solid was dissolved in brine and extracted with dichloromethane (DCM; 5 × 100 mL) to give a dark red/purple solution and was dried over Na_2SO_4 and the solvents were removed *in vacuo* to leave a thin solid purple film on the flask. Sonication in diethyl ether produced a yellow/brown solution, which became a red/black solid upon rotary evaporation. Yield 0.05 g, 5 %; ^{1}H NMR (500 MHz, $CDCl_3$) δ_H 8.01(1H, d, *J* = 9.6, H^1), 7.96 (1H, d, *J* = 8.8, H^3), 7.88 (1H, s, H^4), 7.57 (1H, dd, *J* = 9.5 and 2.3, H^6), 7.57 (1H, dd, *J* = 9.3 and 2.3, H^5), 7.06 (1H, d, *J* = 2.6, H^8), 3.19 (6H, s, H^{10}), 2.59 (3H, s, H^9)[(180)]; ^{13}C NMR (126 MHz, $CDCl_3$) δ_C 150.8 (C-7), 145.1 (C-3), 139.4 (C-4a), 137.9 (C-1a), 137.4 (C-5a), 133.0 (C-5), 130.0 (C-2), 128.0 (C-1), 127.8 (C-4), 122.6 (C-6), 103.0 (C-8), 40.5 (C-10), 21.9 (C-9)[(180)]; HRMS *m/z* (ESI^+) 341.18 (100%, M+2MeCN+Na^+-H·); (Found M+2MeCN+Na^+-H·, 341.1759. $C_{15}H_{14}N_3$ requires M+2MeCN+Na^+-H·, 341.1611); FTIR (cm^{-1}): 2910.02 (C-H alkyl), 1632.73 (C=C aromatic), 1604.41 (C=C aromatic), 1552.01 (C=C aromatic), 1346.68 (aromatic amine C-N stretch), 1267.38 (aromatic amine C-N stretch), 1155.51 (N-C stretch), 1147.07 (N-C stretch), 1135.69 (N-C stretch), 1062.05 (N-C stretch), 802.91 (aromatic C-H bend), 766.09 (aromatic C-H bend), 720.78 (aromatic C-H bend); UV-vis 479 nm (Lit. = 475 nm) [(75)]; fluorescence 607 nm (479 nm excitation) [(75)]; Raman peaks found at 1627 cm^{-1}, 1575 cm^{-1}, 1527 cm^{-1}, 1416 cm^{-1}, 1348 cm^{-1}, 607 cm^{-1}. CV (cyclic voltammetry) shows oxidation potentials at 0.51, 0.69 and -1.79 V and reduction potentials at -1.92 and -0.712 V (vs Fc/Fc^+ reference standard in DCM).

Method B. Diazonium **1** (64 mg; 0.18 mmol) and sodium nitrite (25 mg; 0.36 mmol) were dissolved into stirred diethyl ether (3 mL). This purple mixture was sealed with parafilm and stirred for 24 hours with TLC monitoring and then the yellow solution was left to evaporate. Following this the solid was dissolved in brine and extracted with DCM (5 × 100 mL) to give a dark red/purple solution and was

dried (Na_2SO_4) and the solvent was removed *in vacuo* to leave a thin solid red film on the flask. Yield 4 mg, 9 %; HRMS *m/z* (ESI^+) found 238.13 for [$M+H^+$] and 341.18 for [$M+2MeCN+Na^+-H$].

Method C. To a stirring suspension of diazonium **1** (0.5 g; 1.4 mmol) in water (5 mL), hydrogen peroxide (30 % in water, 0.05 mL; 2.1 mmol) was added. This purple mixture was stirred for 68 hours (TLC control). Following this the solid was dissolved in brine (20 mL) and DCM (30 mL) to give a dark red/purple solution and was dried (Na_2SO_4) and the solvent was removed *in vacuo* to leave a thin solid red film on the flask. Yield 43.1 mg, 13 %; HRMS (ESI^+) 238.13 ($M+H^+$); (Found $M+H^+$; 238.14. $C_{15}H_{15}N_3$ requires $M+H^+$, 238.1339).

Method D. Diazonium **1** (70 mg; 0.23 mmol) was dissolved in methanol (5 mL) and sodium nitrite (25 mg; 0.46 mmol) was added. Rapid colour change from purple to red was observed upon stirring. The compound was isolated by evaporation of the solvent. Yield 40.5 mg, 256 %. Excess mass due to salt impurities. LCMS *m/z* (ESI^+) 238.14 ($M+H^+$); (Found 238.14 for $M+H^+$; $C_{15}H_{15}N_3$ requires $M+H^+$, 238.1339).

X-Ray Structure

In a reaction flask, black needles of the compound had grown from the aqueous reaction solution for forming diazonium **1**, containing any residual HBF_4, $NaNO_2$ and water from the reaction. Under a microscope these showed to be single dark orange needles with some being both orange and purple. One of these orange crystals was used to collect crystallographic data using a copper X-ray radiation source. Crystal size was reported as min 0.04 mm, mid 0.05 mm, max 0.25 mm.

	$[H\text{-}MDAP]^{+}BF_4^{-}.H_2O$
Formula	$C_{15}H_{18}N_3OBF_4$
Molecular Weight	341.94
Temperature, K	119.97(15)
Crystal System	Primitive monoclinic
Space Group	$P2_1/n$
a (Å)	13.7966(5)
b (Å)	23.5549(8)
c (Å)	19.4763(5)
α^o	90
β^o	91.636(3)
γ^o	90
$V\ Å^3$	6326.8(4)
Z	16
Z'	4
F(000)	2848
$D_{calc}\ (g\ cm^{-3})$	1.441
R_1	0.0732
R_{int}	0.1183

Table 4: The full crystallographic data for $[H\text{-}MDAP]^{+}BF_4^{-}.H_2O$

2.5.4 Synthesis of Phenazine-Graphene

Synthesis of Phenazine-Graphene with Graphene Nano-platelets

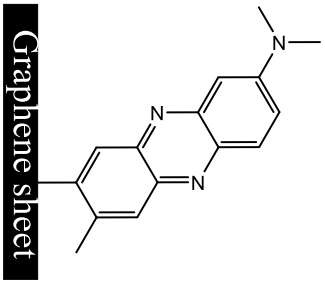

Scheme 15: Proposed structure of Pnz-G as synthesised.

With Light:

Neutral Red diazonium salt (92 mg; 0.26 mmol) was dissolved fully into ethanol (100 mL) before graphene (100 mg) was dispersed into the solution and stirred vigorously for 2 hrs with white light illumination. After 2 hrs, the solution was filtered *in vacuo* and washed on the filter with ethanol (15 mL) until the solution ran colourless from the filter. Later modified to replace the use of a filter with a centrifuge (approx. 4500 RPM for 20 minutes) and water washing after clear solution to remove any salt impurities.

UV-vis λ_{max} = 465 nm; emission = 561 nm, excitation = 440 nm; BET = 151.64 m^2/g.

Without Light:

Neutral Red diazonium salt (18 mg; 0.05 mmol) was dissolved fully into ethanol (20 mL) before graphene (20 mg) was dispersed into the solution and stirred vigorously for 2 hrs with white light illumination. After 2 hrs, the solution was filtered *in vacuo* and washed on the filter with ethanol (15 mL) until the solution ran colourless from the filter.

MDAP Adsorption test:

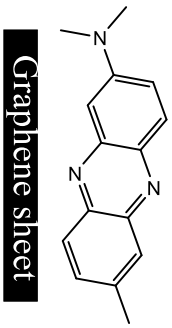

Scheme 16: Proposed structure of adsorbed MDAP on graphene.

MDAP (10 mg, 12.5 mg, 20 mg) were individually dissolved fully into ethanol (20 mL) before graphene (20 mg) was dispersed into the solution and stirred vigorously for 2 hrs with white light illumination.

After 2 hrs, the solution was filtered *in vacuo* and washed on the filter with ethanol (15 mL) until the solution ran colourless from the filter.

Synthesis of Phenazine-Graphene with Graphene Nano-platelets as one-pot Phenazine-Graphene.TFA:

Neutral Red (92 mg) was dissolved fully into ethanol (100 mL) with TFA (4.2 mL) and stirred whilst adding $NaNO_2$ (40 mg) and covering in foil for 10 minutes. After 10 minutes of stirring, graphene (100 mg) was dispersed into the solution and stirred vigorously for 2 hrs with white light illumination. After 2 hrs, the solution centrifuged in 2 tubes at 4500 rpm and each tube was washed on the centrifuge with 15 mL portions of ethanol until solution contains no purple/pink trace and then washed with 15 mL H_2O.

Phenazine-Graphene.HCl:

As described with Pnz-G.TFA but exchanging TFA for HCl (4.5 mL).

Synthesis of Phenazine-Graphene with Higher Quality Graphene Powder

Neutral Red diazonium salt (18 mg) was dissolved fully into ethanol (20 mL) before graphene (20 mg) was dispersed into the solution and stirred vigorously for 2 hrs with white light illumination. After 2 hrs, the solution was transferred to a centrifuge tube and centrifuged at 4000 rpm for 20 minutes. The supernatant was removed carefully, and fresh ethanol (15 mL) was added, sonicated, and centrifuged again. This washing process was repeated until the solution no longer exhibited the purple/red colour of the diazonium or free dye.

Synthesis of Phenazine-Graphene with SiC Supported Graphene

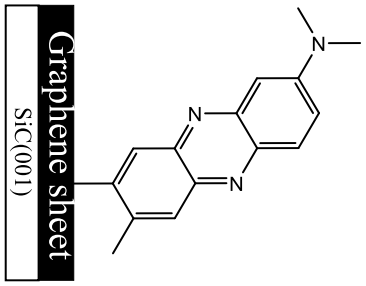

Scheme 17: Proposed structure of Pnz-G/SiC(001) as synthesised.

Prior to the reaction, the graphene on silicon support (graphene/SiC(001)) was analysed by Raman in order to allow the reaction to be followed by Raman spectroscopy. Diazonium **1** (25 mg; 0.07 mmol) was dissolved in ethanol (25 mL) and a small volume (coverage of graphene) was added to a small petri dish containing the graphene on silicon carbide support. The mixture was left in the dark for

20 minutes. After this the solution was removed via pipette and then the sample of graphene was washed with ethanol twice and was then analysed by Raman. The sample was then replaced into the dish and allowed to cool before a fresh solution of diazonium was added from the stock was added. The sample was then illuminated under white light for 20 minutes and then the sample was removed from the solution and cleaned in ethanol before Raman analysis. Following this, it was illuminated under white light for a further 20 minutes in an ethanolic solution of the diazonium. The sample was once again removed and cleaned thoroughly with ethanol before a final Raman analysis and the reaction was seen to be successful. Next the sample was illuminated whilst submerged in diazonium solution (1 mg/mL, ethanol) and illuminated for 90 minutes and then cleaned with ethanol before further Raman analysis in order to observe the change in the G peak. Raman (513 nm): 1347.92, 1571.17 and 2707.26 cm^{-1}.

This was repeated with a second wafer of graphene/SiC(001) but with the vessel covered with foil and no white light excitation. Raman: 1347.92, 1571.17 and 2712.44 cm^{-1}.

2.5.5 Modification of Diazonium **1** with 2-Methyl-3-butyn-2-ol

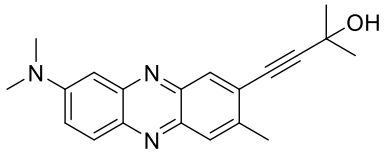

*Scheme 18: Expected product for modification of Diazonium **1** with 2-methyl-3-butyn-2-ol.*

Diazonium **1** (70 mg; 0.23 mmol) was dissolved into diethyl ether (1 mL) and stirred. 2-methyl-3-butyn-2-ol (0.1 mL; 0.46 mmol) was added and the sample was irradiated under intense white light. After 2 hrs, the reaction showed completion by TLC. When LCMS was run, only peaks for MDAP were present. Due to this the reaction was not worked up.

Diazonium **1** (70 mg; 0.23 mmol) was dissolved into THF (10 mL) and stirred. 2-methyl-3-butyn-2-ol (0.1 mL; 0.46 mmol) followed by hydrogen peroxide (5-6 drops; 30 % w/w water) was added. The sample was then irradiated under intense white light. After 20 hrs with some TLC monitoring, a liquid chromatography mass spectrometry (LC-MS) analysis was run for the solution, however there was very little evidence of the expected compound and clear evidence of MDAP.

2.5.6 Covalently Binding Diazonium **1** to Fullerene

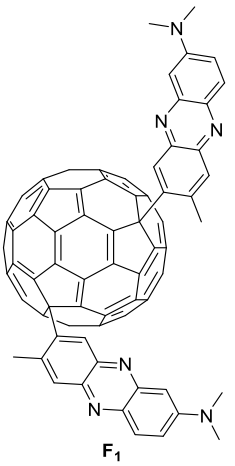

Scheme 19: Expected fullerene modification product using diazonium 1.

Diazonium **1** (20 mg, 0.057 mmol, 3 eq.) was dissolved in toluene (5 mL) and was then added this solution to fullerene powder (19 mg, 0.016 mmol) and then allowed the solution to stir under white light irradiation and monitored by TLC. Spot for potential product does not move in attempted eluents, but also forms black precipitate in solution. ^{1}H NMR analysis was used to determine completion and the reaction was found to be unsuccessful.

2.5.7 Modifying Pyrene with Diazonium **1**

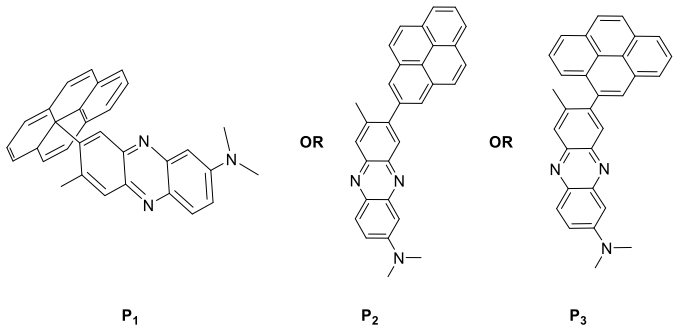

Scheme 20: Products expected from the modification of pyrene with diazonium salt 1.

Diazonium **1** (50 mg, 0.14 mmol) was dissolved in EtOH (4 mL) and added to pyrene (7.2 mg, 0.036 mmol) and left to stir under white light for 4 hours with hourly LC-MS analyses. The LC-MS showed that there were at least two regioisomers (P1 and P2 or P3) that could be identified from each other. P1 has a mass peak at 476.54 ($M+2H_2O+H^+$, expected 476.23) and P2/3 has a mass peak at 459.81 ($M+Na^+$, expected 460.18). Due to the frequent reduction of diazonium and cleavage of material in LC-MS, this method was no longer deemed feasible for monitoring and TLC monitoring was attempted. A spot was seen to appear that did not move and corresponded to no other spot on the plate.

The reaction was redone using Diazonium **1** (250 mg, 0.71 mmol) was dissolved in ethanol (25 mL) and added to pyrene (72 mg, 0.36 mmol) and left to stir under white light for 4 hours with TLC monitoring. Once it was noticed that there was a spot of a different colour, but same position as the diazonium, after drying that did not move in the eluent it was decided that the reaction was finished. When water was added, a black precipitate and a thin grey/purple suspension are formed and can each be isolated by filtration and left to dry on their respective filters. Each has low solubility in $CDCl_3$ and form orange solutions, which were analysed by ^1H NMR. The ^1H NMR showed the reaction was unsuccessful.

2.5.8 Screening Reactions for Dye Modification

Reagent	**Solvent**	**Success**
4-Nitrobenzaldehyde	DMSO	**N**
Imidazole	DMSO	**N**
4-Bromobenzoic acid	DMSO	**N**
Trimethylsilylacetylene	DMSO	**N**

Table 5: Screening reactions for Diazonium 1.

Diazonium **1** (0.04 mmol) and the given reagent (0.08 mmol) were dissolved in DMSO (1 mL). They were then irradiated in white light and monitored by LCMS and TLC. Imidazole had an immediate colour change from purple to orange and then red, whilst all other reactions showed no change and LCMS suggested reduction to MDAP.

Chapter 3. Expanding Upon the Graphene Modification Method and Library

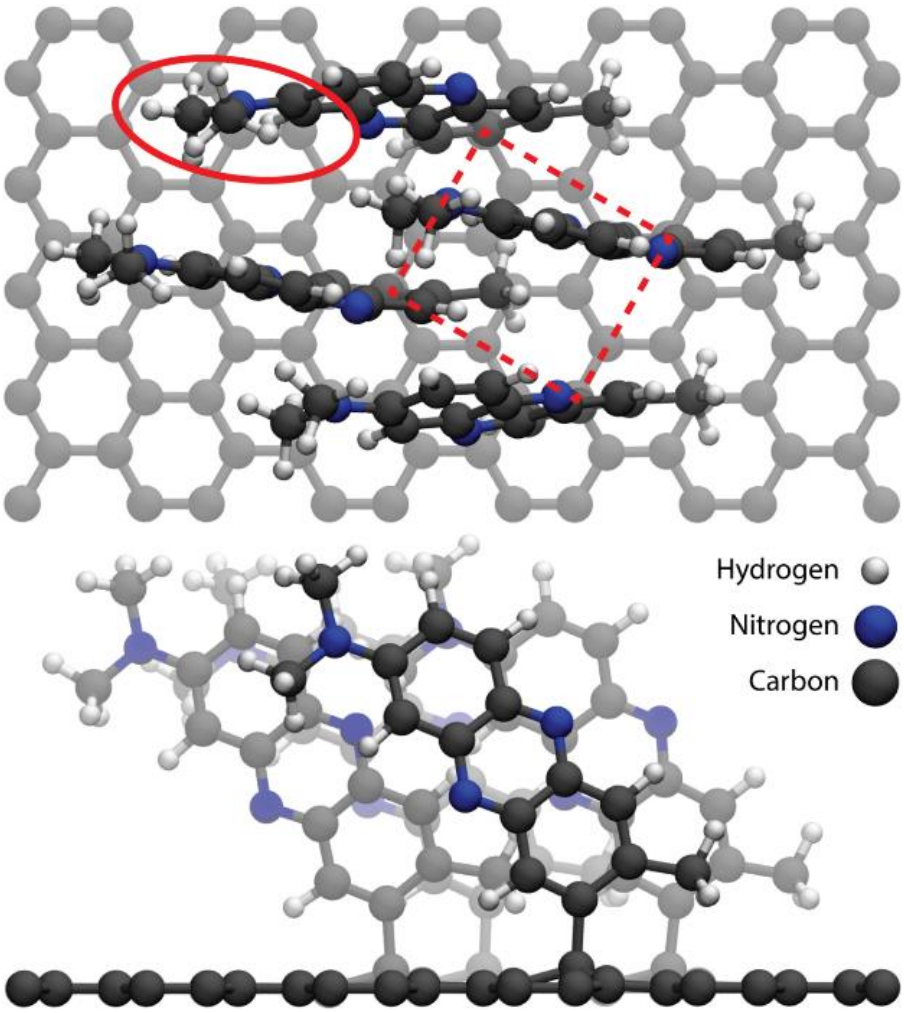

Reproduced with permission from reference (2)

3.1 Abstract

In this chapter, the method of graphene modification is expanded to a range of dyes such as fluorescein, purine, chromone and thionine. It was found that the preparation method for Phenazine-Graphene utilising stable diazonium salt 1 can be translated to purine and thionine. However, chromone and fluorescein diazonium salts were too unstable to be isolated and used to modify the graphene surface. This led to the development of a one-pot method utilising *in situ* generation of a diazonium salt, which has proved to be a more efficient method for graphene modification.

The modified graphene materials have been characterised by multiple solid state analysis techniques (SEM, IR, UV-vis, and fluorescence), showing changes in the solid surface of the graphene sheets including the presence of some new elemental composition compared to graphene. It was found that the modified samples have an increased solubility in acidified acetonitrile which allows the formation of an optical band gap to be measured through UV-vis spectroscopy.

3.2 Aims

The aims of this chapter were:

1) to expand upon the graphene modification in chapter 2 through the fabrication of a range of dye-graphene hybrids using the same methods used therein;

2) the novel hybrids were to be analysed fully by techniques used for Pnz-G;

3) alterations to the method would be investigated as and when problems with the procedure arose.

3.3 Results and Discussion

3.3.1 Synthesis of 7H-purine-6-diazonium Tetrafluoroborate

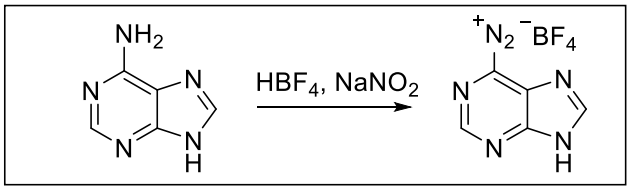

Scheme 21: The formation of 7H-purine-6-diazonium Tetrafluoroborate from adenine under acidic conditions.

Following the success in fabricating the initial covalently bound graphene-dye hybrid, Pnz-G, the next step was the synthesis of another diazonium salt derived from an organic dye. Using the concept of graphene nitride's nitrogen content increasing catalytic activity,[3, 19] we chose to increase the nitrogen

content of the system. Therefore, we opted to use the UV dye adenine to form a second diazonium salt (Scheme 21). The reaction conditions used for the phenazine diazonium salt were replicated here and the initially colourless solution changed to a pale yellow as sodium nitrate was added to the mixture. This colour changed to a pale green upon drying the final solid.

For the analysis of the diazonium salt, NMR, IR, UV-vis, and high-resolution mass spectrometry (HRMS) were employed. However, it was anticipated that the diazonium salt would be likely to degrade as it passes along the mass spectroscopy column, due to the data observed from the phenazine.

The ^{1}H NMR for 7H-purine-6-diazonium tetrafluoroborate (Figure 41, Table 6) shows very little information, except the presence of the two aromatic protons being present and the potentially pyridinic proton from the acidic conditions of synthesis. One peak that is not present is the NH_2 of the adenine starting material, though this would not always be visible.[180]

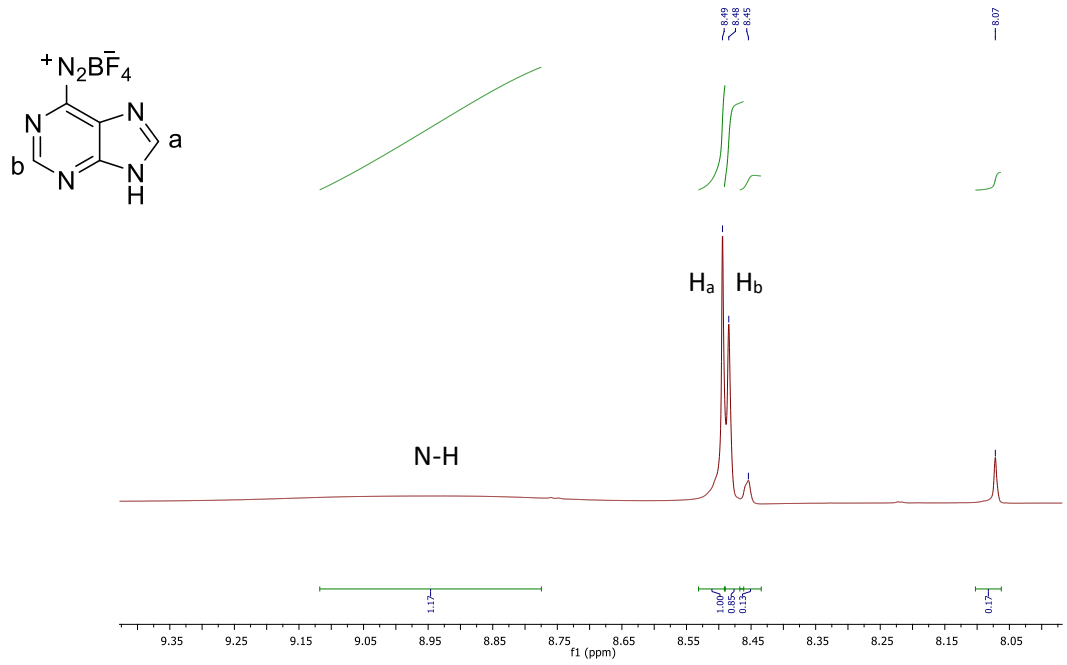

Figure 41: ^{1}H NMR of purine diazonium salt in d_6-DMSO.

Chemical Shift δ	Number of Hydrogens	Multiplicity	Assignment
8.49	1	s	Hb
8.48	1	s	Ha
8.95	1	S, broad	H pyridinic

Table 6: The tabulated NMR data for Purine diazonium in d_6-DMSO

The FTIR spectrum of 7H-purine-6-diazonium tetrafluoroborate (Figure 42) shows a very weak absorption around 2193 cm^{-1}, which is close to the normal band for diazonium salt functional groups. In addition, the N-H bands appear to still be intact from the purine's own structure and some potential protonation on pyridine-like nitrogen atoms.

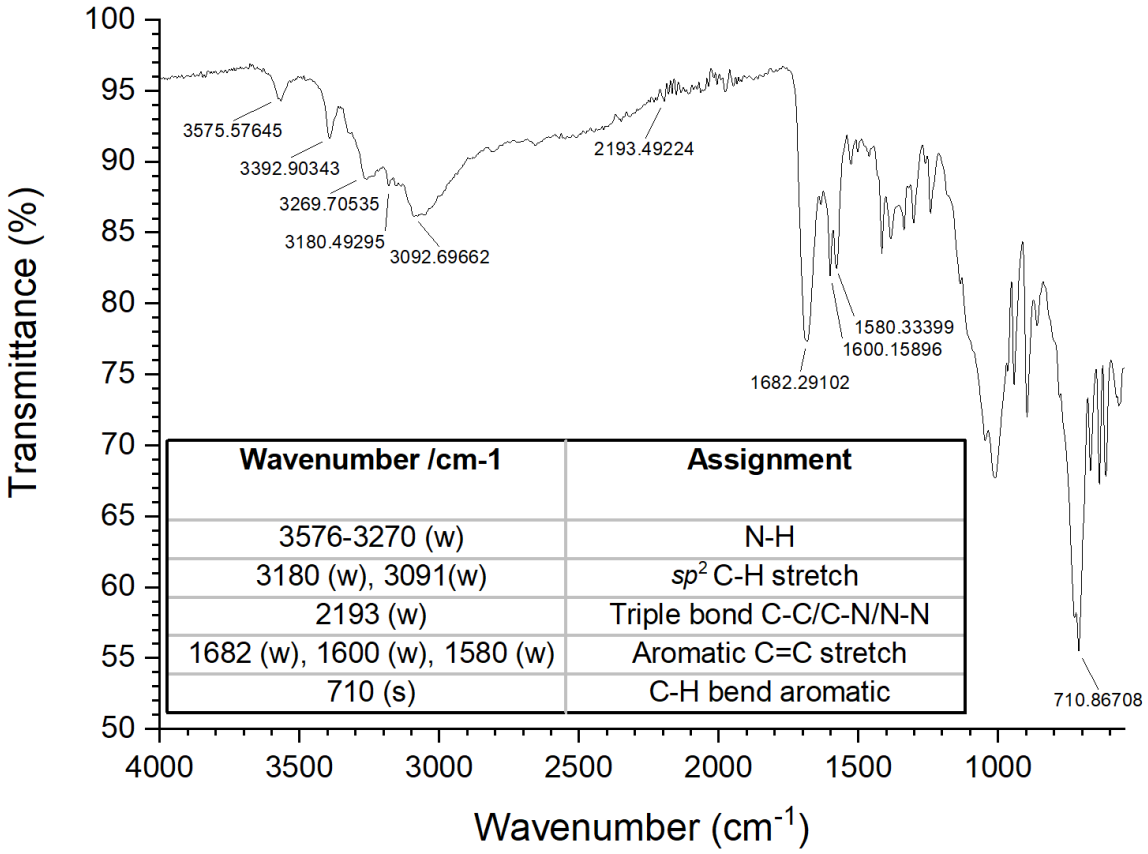

Figure 42: The FTIR spectrum of 7H-purine-6-diazonium tetrafluoroborate.

UV-vis spectroscopic analysis (Figure 43) of this diazonium salt sample revealed that despite the green colour of the powder, in solution the UV signature still dominated its spectrum with a peak at 310 nm. However, there is faint absorbance at 437 nm and 588 nm, which may be why there is a faint green colouration to the powder. This also meant that the dye would not absorb visible light as strongly or efficiently as the phenazine dye. Though this could be a detriment to the photocatalytic system, it could still prove of interest as a carbocatalyst and may provide an insight to the effects of increased nitrogen content on the system.

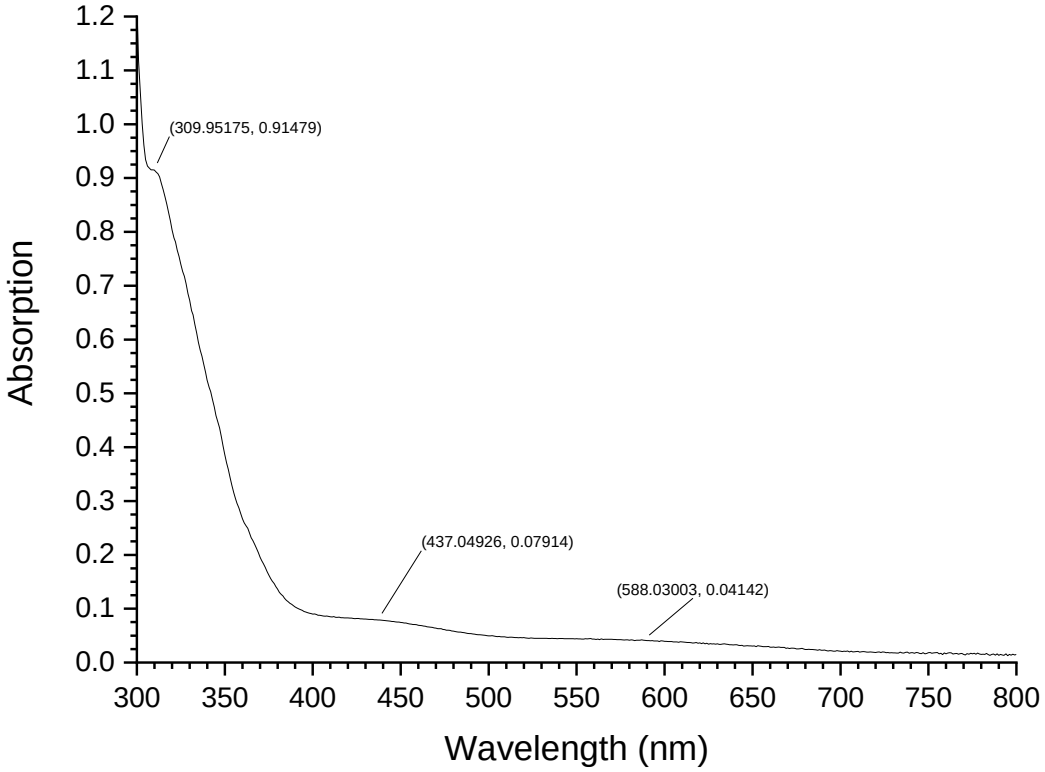

Figure 43: UV-vis spectrum of Adenine diazonium salt in DMF.

3.3.2 Synthesis of Fluorescein-4-diazonium Tetrafluoroborate and 2-Methylchromone Diazonium Tetrafluoroborate

Following the success of forming a hybrid using nitrogen containing a heterocycle, it was decided that two examples of oxygen containing heterocycles would make for an interesting comparison when testing the photocatalytic activity of the graphitic materials.

Therefore, to match the nitrogen heterocycles used for successful diazonium formations, a visible dye and a UV dye were chosen – fluorescein and 2-methylchromone. Fluorescein was chosen due to its green colour, allowing for the utilisation of another section of the visible spectrum, while 2-methylchromone was chosen for its similar blue fluorescence to purine. The amine containing derivatives were chosen for the purpose of diazonification and to utilise the methods that had been used in our previous examples of graphene modification.

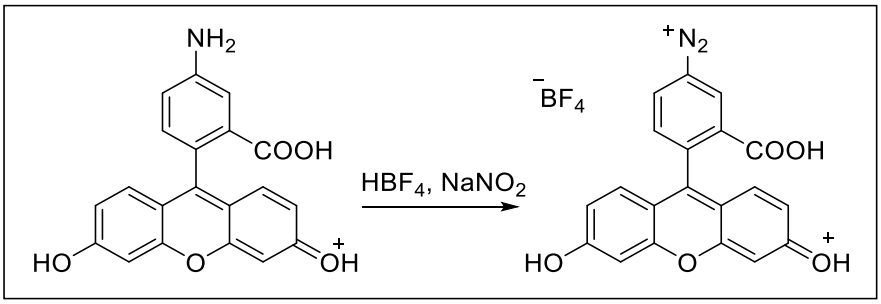

Scheme 22: The failed attempt at the diazonification of fluorescein amine isomer 1.

Starting with 5-aminofluorescein* (Scheme 22), the reaction and the work up were performed as stated in Chapter 2. However, the ^{1}H NMR spectrum of the product was not as expected (Figure 44). Rather than a spectrum that showed a clear formation of the diazonium salt or no reaction, the spectrum showed signals that are similar to that of fluorescein seen in the literature.[181] In addition to this, when the reaction was reattempted several times, the proton integration in this region frequently changed and did not match the expected number of protons. This suggests that the reaction is neither reliable nor consistent and cannot produce a clean product and likely leads to a rapid degradation of the formed diazonium salt.

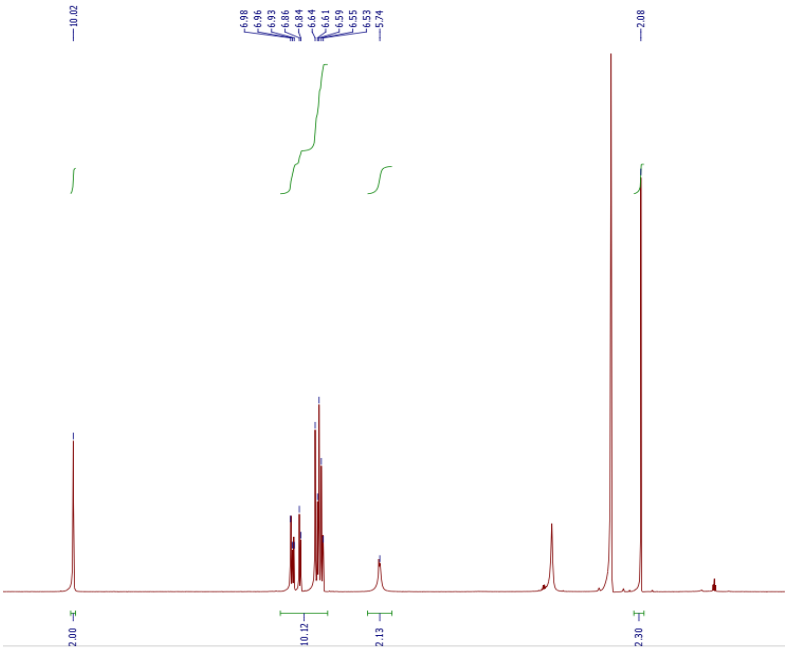

Figure 44: The ^{1}H NMR spectrum of the attempted synthesis of fluorescein-4-diazonium tetrafluoroborate in d_6-DMSO.

IR spectroscopy was used as a fast test for a diazonium functional group and was found to be present at 2349 cm^{-1}, however there is the addition of peaks at 3362, 3091 and 3065 cm^{-1}. These additional peaks can be assigned to the OH groups present and N-H signatures of the starting material, the broad

*Reaction performed by Connor Sherwin under guidance of the author.

nature suggesting a higher likelihood of them representing O-H (alcohol and acid). This does suggest that a diazonium can be formed, but NMR analysis does not agree well with this and could suggest a limited stability of the diazonium salt.

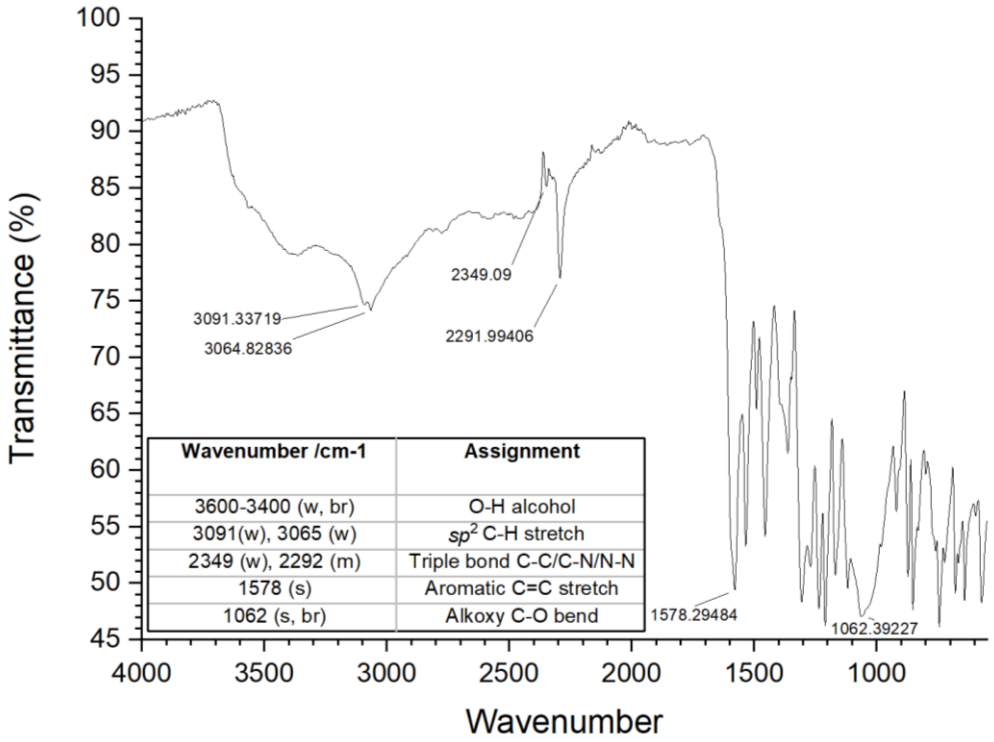

Figure 45: The FTIR spectrum for the attempted synthesis of fluorescein diazonium salt from 5-aminofluorescein.

Mass spectrometry was also utilised to identify if the reaction had succeeded or failed. However, this also provided data showing no mass peak for the diazonium and a peak close to that of the starting material (351 and 348 m/z respectively) which suggested either only partial or no reaction had occurred.

Put together, these data sets tell us that the reaction is not reliable for forming the diazonium salt and a new method for such unstable species would be required. It was also decided that another dye could be tried, to see whether it was fluorescein or the method that was the problem for this attempted synthesis.

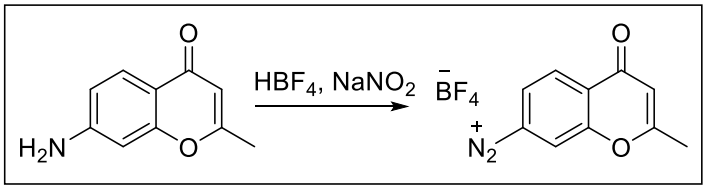

Scheme 23: The failed attempt at the diazonification of 2-methyl-7-aminochromone.

The next dye used for the formation of a storable, reactive diazonium salt was 4-amino-2-methylchromone (Scheme 23), which is a UV absorbing organic molecule with the required amine group for diazonification reactions.*

The reaction was run in the same way as with the previous three dyes and after completion the NMR and FTIR spectra were taken. Once again, NMR showed a complex picture than expected, meanwhile the FTIR spectrum (Figure 46) showed no clear sign of the diazonium functional group, despite a potential, but weak peak at 2349 cm^{-1}. The issue with this peak being that it is not far from the baseline and only forms due to a sudden spike in transmittance.

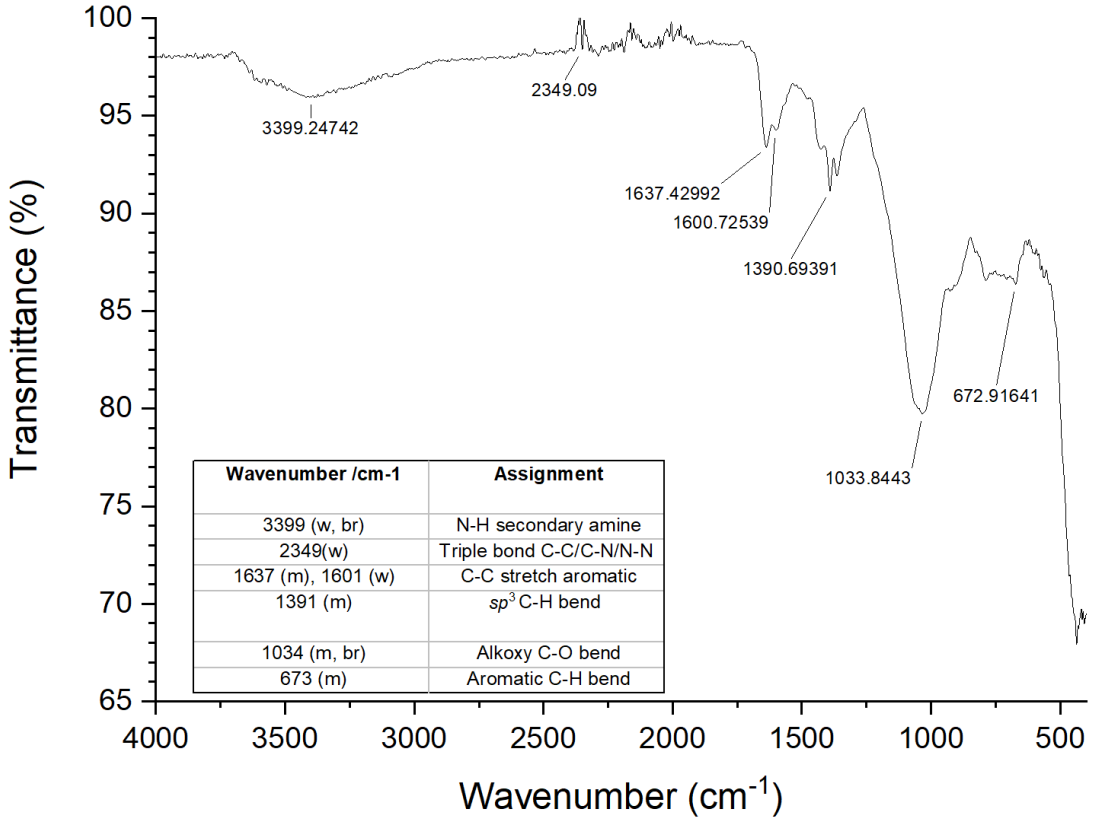

Figure 46: FTIR of 2-methyl chromone diazonium tetrafluoroborate reaction product.

It is postulated that the diazonium salt formed by the chromone is unstable and begins to breakdown in an uncertain manner in solution. This means that alternate methods would need to be used which do not isolate the diazonium when using these dyes in any modification studies.

*Reaction performed by Connor Sherwin under guidance and direction of the author.

3.3.3 Synthesis of Thionine Diazonium Salt

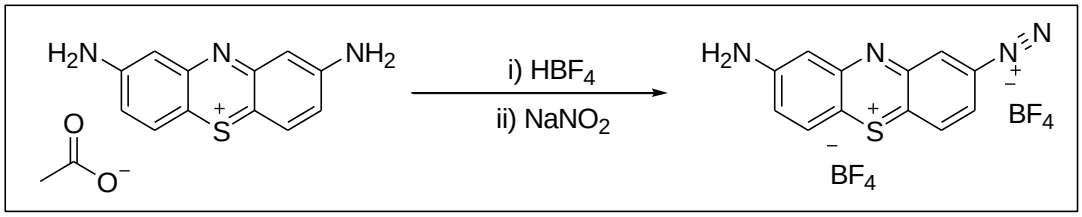

Scheme 24: A scheme for the reaction of thionine acetate into its corresponding diazonium salt.

In order to complete the use of the visible spectrum, thionine acetate salt was used for the formation of a fifth diazonium salt. This blue dye has two amine groups as part of its chemical structure, meaning that it was important to moderate the quantity of sodium nitrite used, otherwise both amine groups would be converted into a diazonium functional group. Therefore, a much lower ratio of sodium nitrite was used for this reaction.

The HRMS shown in Figure 47 gave a surprising result. Unlike previous diazonium salts, this product gave a m/z of 259.9, which matches closely with the molecular mass of thionine diazonium salt. This is unusual because previous examples have degraded before fully passing through the mass column and could be a sign to greater stability of this product.

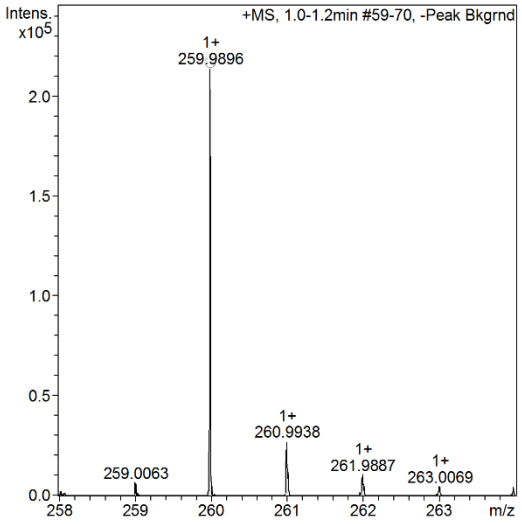

Figure 47: The HRMS results showing the peak of interest.

However, NMR spectroscopy showed that if the diazonium salt is subjected to the presence of DMSO there is a chemical change that causes the spectrum to be very different and far more complicated than when the NMR was later retaken in D_2O, suggesting that the product degrades in such conditions. In addition, the colour of the solution was brown, rather than the purple colour seen in water and DMF.

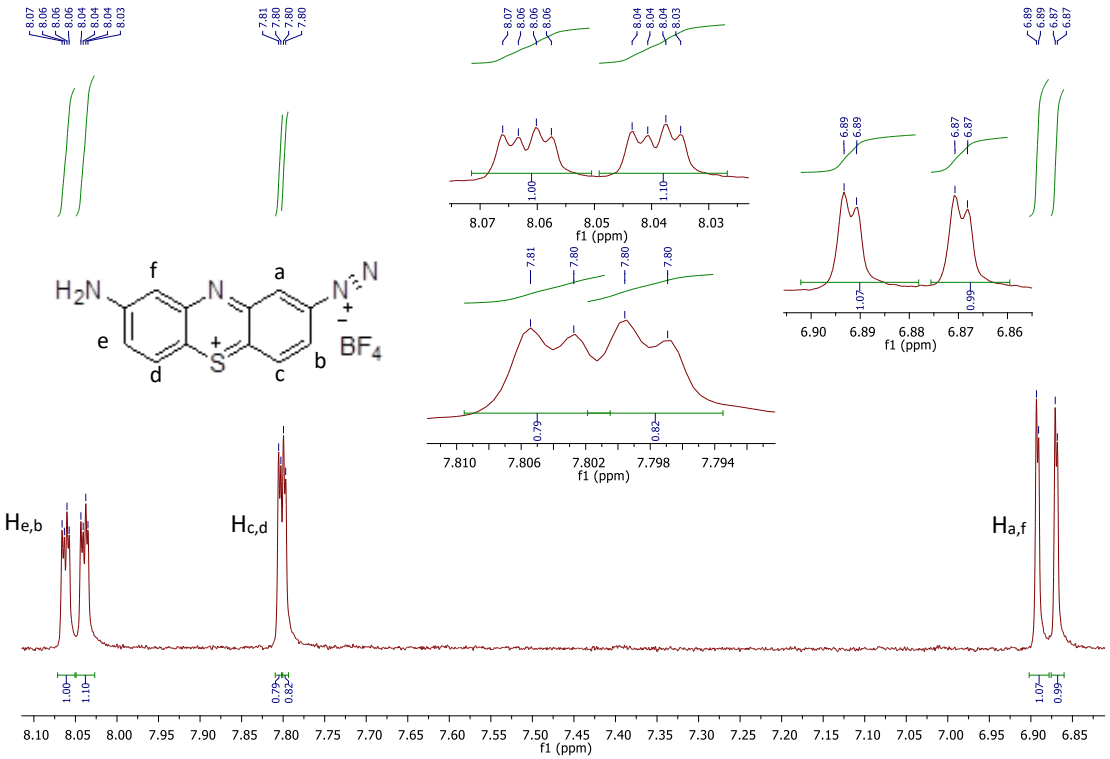

Figure 48: ^{1}H NMR spectrum of thionine diazonium salt. Taken in D_2O.

One possibility of this is a degradation in DMSO and in CD_3OD, since both show a complex spectrum with many additional peaks, whilst D_2O gives a strong and clean spectrum (Figure 48). One thing to note is that all three solvents show a change in the peak shift that is similar to one another but different to the thionine starting material, which would suggest that the reaction is making the product, all three methods are detecting the same product and that later exposure to certain solvents results in a second reaction.

Chemical Shift δ	No. of Hydrogens	Multiplicity	J/ Hz	Assignment
6.87	1	d	1.0	Ha
6.89	1	d	1.0	Hf
7.80	1	d	2.3	Hc
7.80	1	d	2.3	Hd
8.06	1	dd	2.3, 1.1	Hb
8.06	1	dd	2.3, 1.1	He

Table 7: The NMR data for thionine diazonium salt in tabulated form. D_2O solvent.

The FTIR spectrum of thionine's diazonium salt (Figure 49) shows a change in the C-H bending bands as well as the N-H bands for the amines. The latter of these would be expected due to the conversion of at least one of the two amine functional groups into a diazonium salt. In addition, a band at 2124 cm^{-1} is lost and the formation of a very strong band at 2245 cm^{-1} and a weak band at 2324 cm^{-1},

both of which are in a region of diazonium functional group stretches but 2245 cm^{-1} is the more likely diazonium band as it is normally a weak peak in the FTIR spectrum.

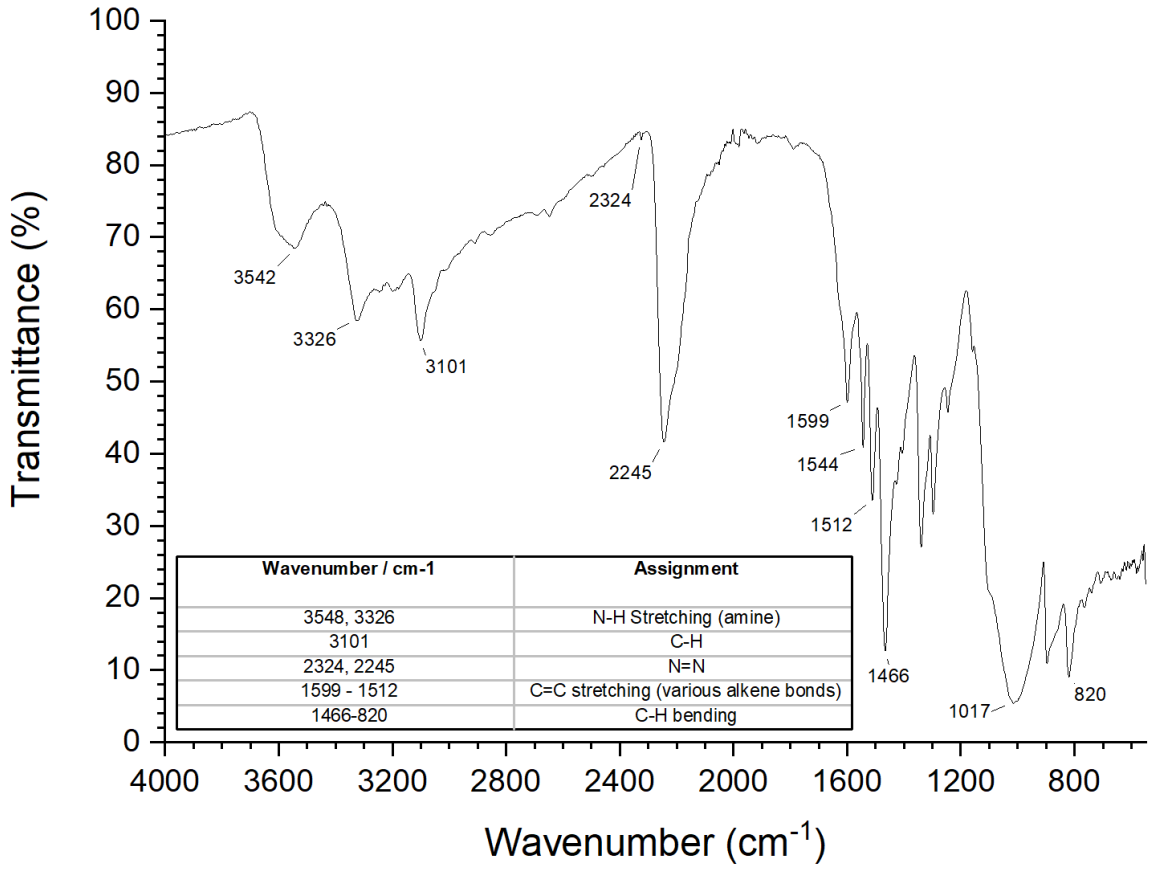

Figure 49: FTIR spectrum of thionine diazonium salt on a diamond ATR probe.

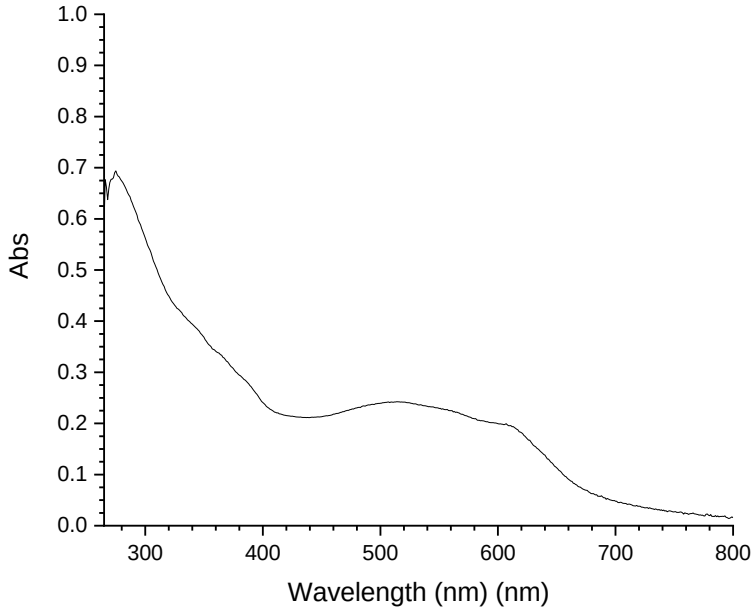

Figure 50: UV-vis spectrum of thionine diazonium salt in MeCN with H_2SO_4.

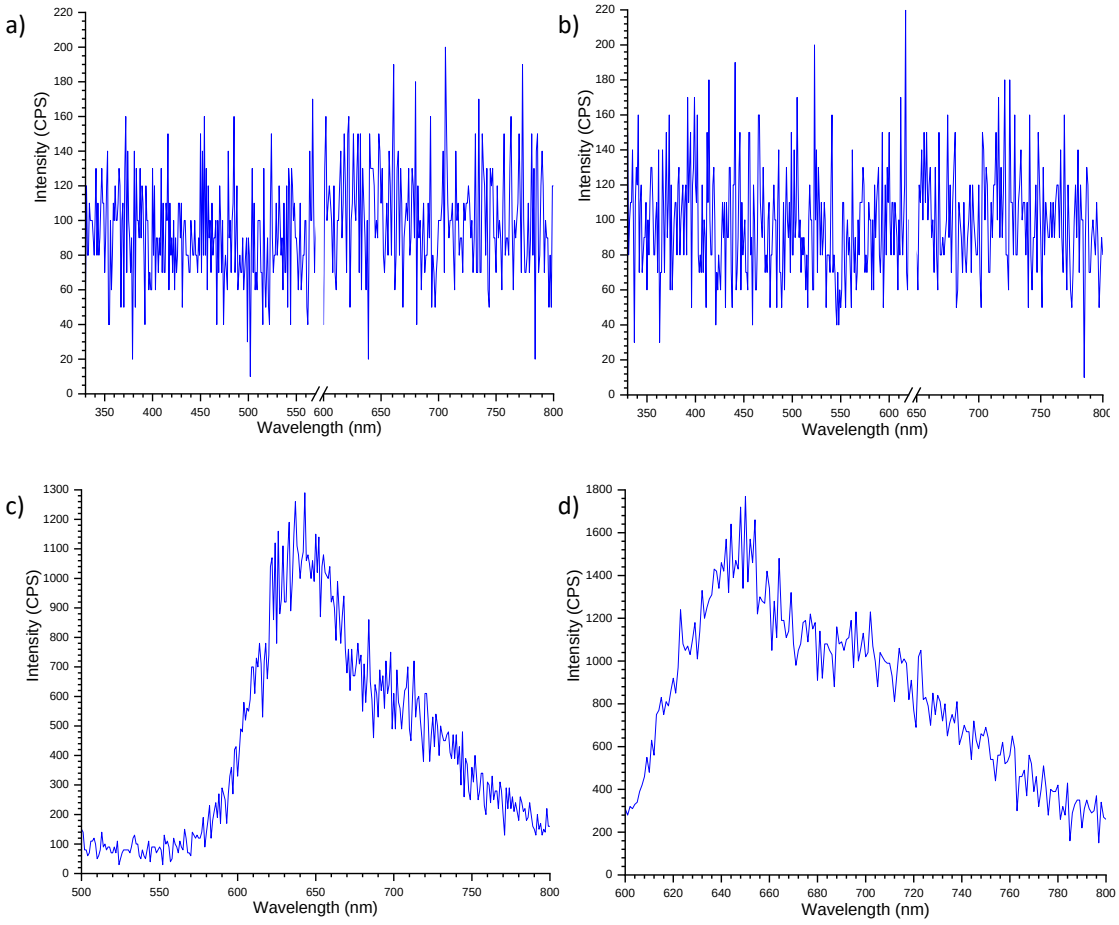

Figure 51: Fluorescence spectra for thionine based diazonium salt excited at a) 290 nm, b) 315 nm, c) 491 nm, d) 583 nm. Solvent is MeCN with H_2SO_4. Emission 643 nm, slit widths 3 nm.

The UV-vis spectrum for thionine diazonium salt (Figure 49) shows a drastic decrease in the peak at 606 nm, alongside a broadening in the UV region. A small shoulder on the UV peak has lost definition

in the diazonium compared to thionine. These suggest a change in the chromic system, which would not be caused by protonation, since the UV-vis spectra were taken in acidic media. The visible colour in solution had also changed from blue to purple which the UV-vis spectrum shows with a decreased absorbance in the red region. The fluorescence emission (Figure 51) for these peaks shows little emission from the UV and blue regions, but broad and weak emission from the red region, which may suggest an activity using red spectrum of light, as electronic transitions are occurring here. However, for testing purposes, white light would be more practical and preferred.

3.3.4 Synthesis of Purine-Graphene with Graphene Nano-Platelets

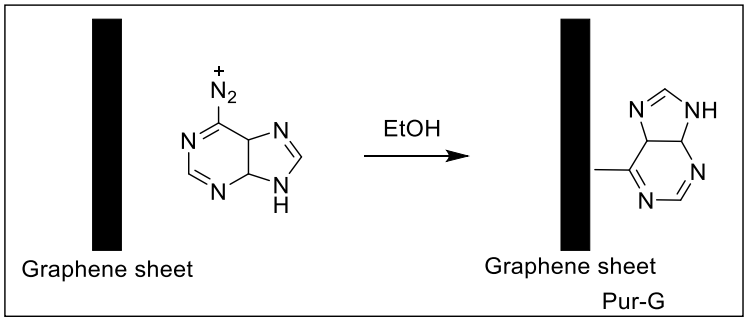

Scheme 25: The reaction between 7H-purine-6-diazonium tetrafluoroborate and graphene to form Pur-G.

Using previous methods detailed for Pnz-G, Purine-Graphene (Pur-G) was synthesised using 7H-purine-6-diazonium tetrafluoroborate in ethanol, only this time without light due to the lack of strong visible light absorption in the UV-vis spectrum of 7H-purine-6-diazonium tetrafluoroborate. This material was synthesised under white light illumination and in the dark, with the same spectra being obtained from each, and showing a change in spectra from unmodified graphene plates.

The Raman analysis was attempted for both purine diazonium and the hybrid species, however the background fluorescence was too strong to give any useful or useable data from the spectrometer due to the saturation of the detector and was therefore abandoned as an analysis technique from here on. This added a new consideration when developing the characterisation methods for these solid-state materials.

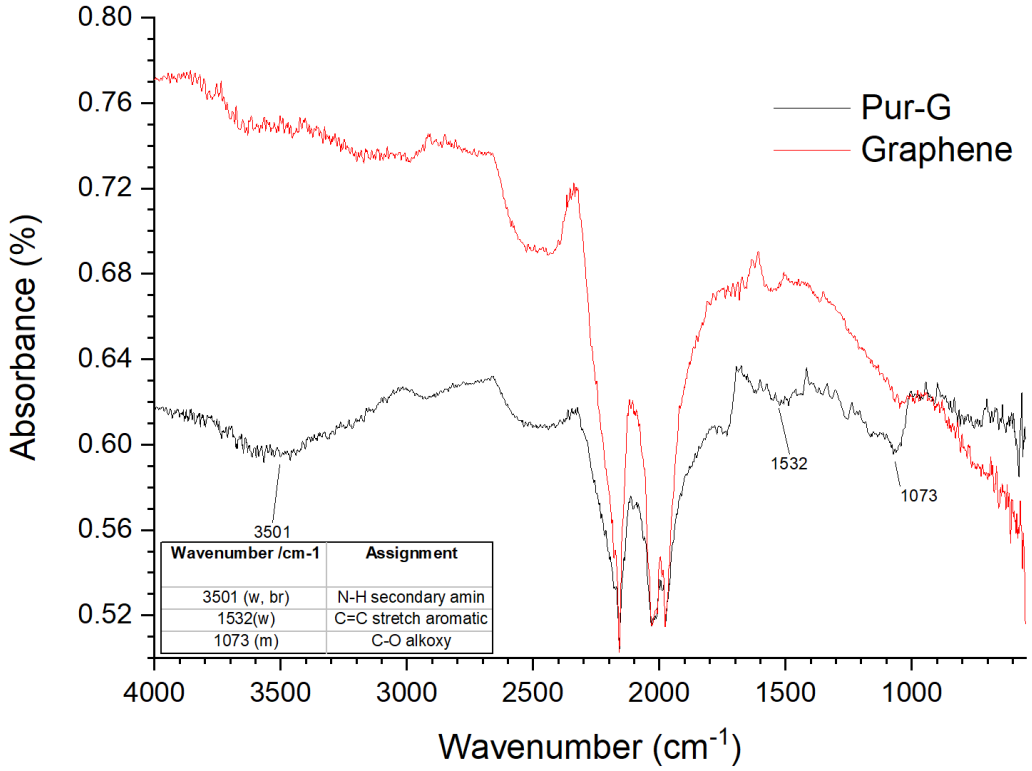

Figure 52: The FTIR spectrum of Pur-G and Graphene overlaid to show the changes in the spectrum. Absorbance scale displays amount of light transmitted.

IR spectroscopy (Figure 52) shows that the material has changed in comparison to the as-purchased graphene. In particular, the 3500 cm^{-1} region and 1500-1600 cm^{-1} regions have changes in their bands, relating to N-H vibrations and aromatic vibrations, respectively. Given the structure of purine, this would be expected as additional structures added to graphene by the reaction.

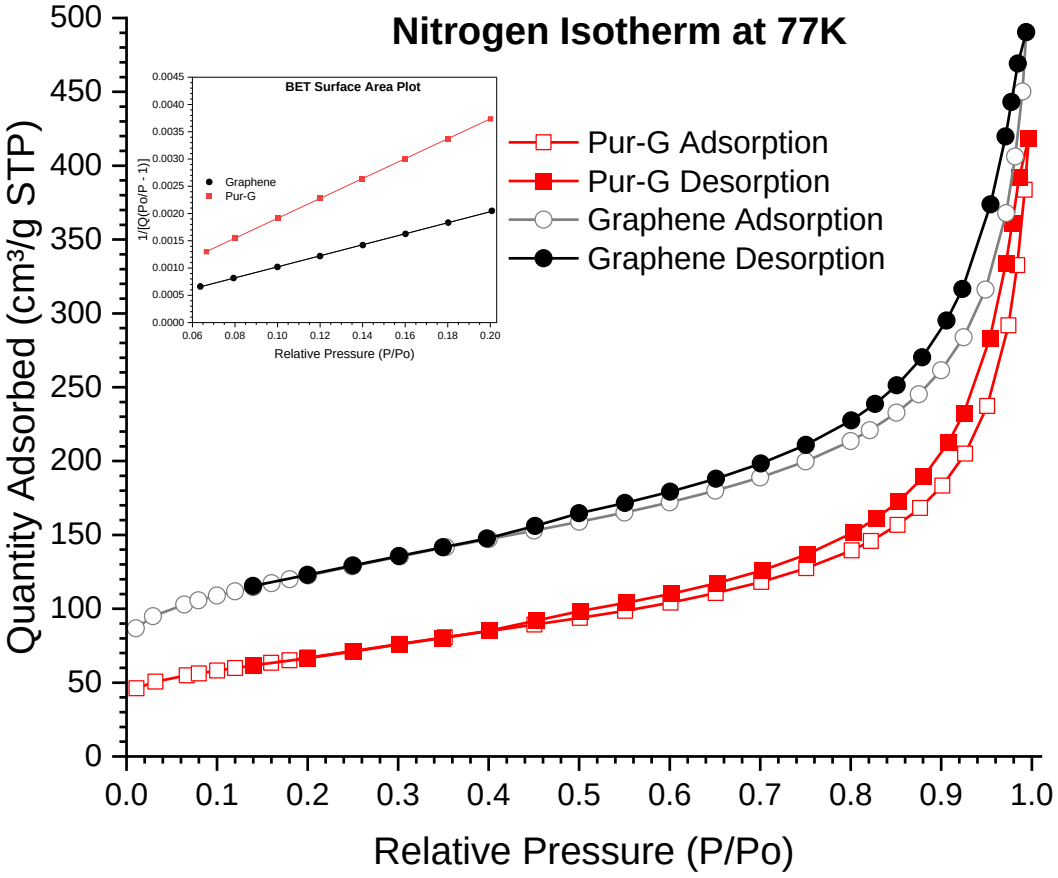

Figure 53: Nitrogen isotherm plot at 77 K for graphene nanoplatelets and Pur-G with inlaid BET surface area plot.

Sample	Single Point Surface Area (m^2/g)	BET Surface Area (m^2/g)	BET constant (C) value	Langmuir Surface Area (m^2/g)	t-Plot Micropore Area (m^2/g)	Average Pore Size (Å)
Graphene	426	430	888	586	126	53
Pur-G	233	237	208	327	37	76

Table 8: Tabulated surface area data for graphene nanoplatelets and Pur-G.

BET analysis (Figure 53, and tabulated in Table 8) also gave an insight into the changes in the available surface of these hybrid materials, giving us a surface area of 237.5 m^2/g, which is 55.21 % of the area the pristine graphene provides. The Langmuir area was 326.7 m^2/g, a fall to 55.79 % compared to pristine graphene. This suggests alterations to the graphene sheets' surfaces and possibly to the agglomeration seen in Pnz-G samples to significantly reduce the available surface for nitrogen adsorption. The pore size was also found to be 77.8 Å, an increase from 52.9 Å in graphene. These pores could act as the sites of catalytic activity if the material proves to be active.

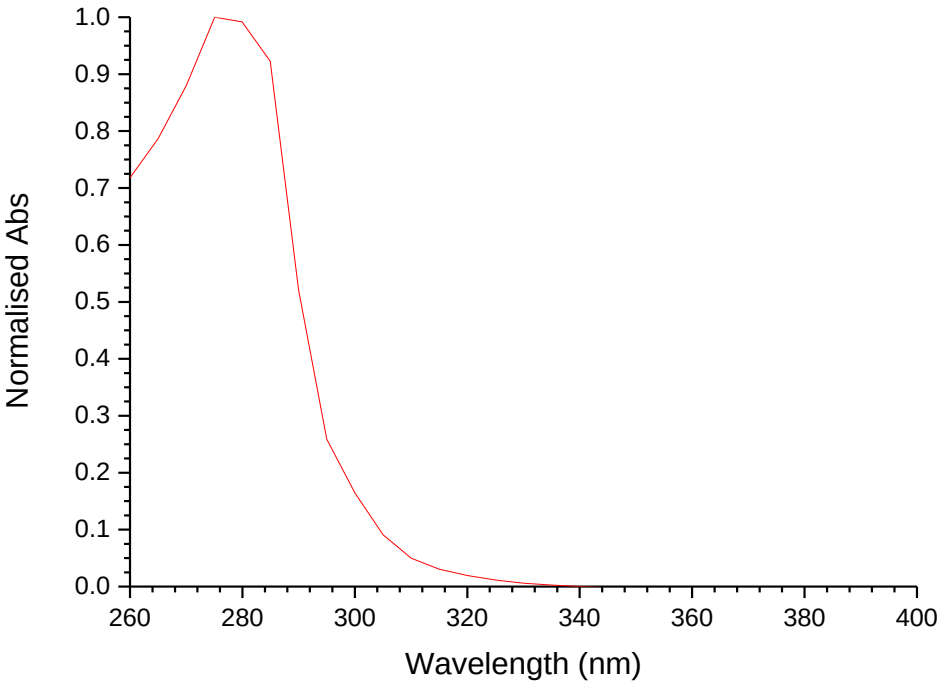

Figure 54: UV-vis of Pur-G in acetonitrile and few drops sulphuric acid.

The UV-vis spectrum of Pur-G (Figure 54) shows a maximum absorbance at 275 nm, which is a bathochromic shift of 15 nm, when compared to unattached purine in acetonitrile which is seen within the literature (approx. 260 nm).[182] This suggests that the attachment to graphene has happened, if we assume the effect would be similar to that seen in Pnz-G. The downside of this absorbance spectrum is that the visible light activity of the species is likely to be low but did not dissuade us from its use in this work.

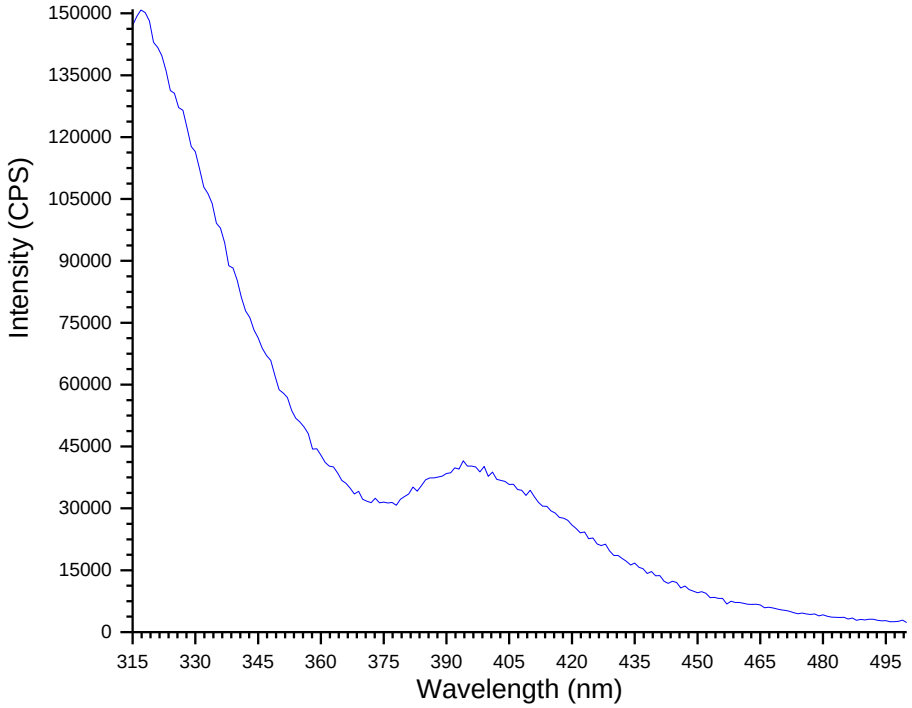

Figure 55: Fluorescence of Pur-G in acetonitrile and few drops sulphuric acid. Excitation at 290 nm, slit width 3 nm.

It is similar for the fluorescence (Figure 55). The fluorescence maximum is approx. 400 nm when excited at 290 nm with a slit width of 3 nm.[182] When compared to free purine excited at 267 nm (maximum emission 375 nm), there is an increase in the fluorescence wavelength of Pur-G of 25 nm, which suggests attachment has occurred.

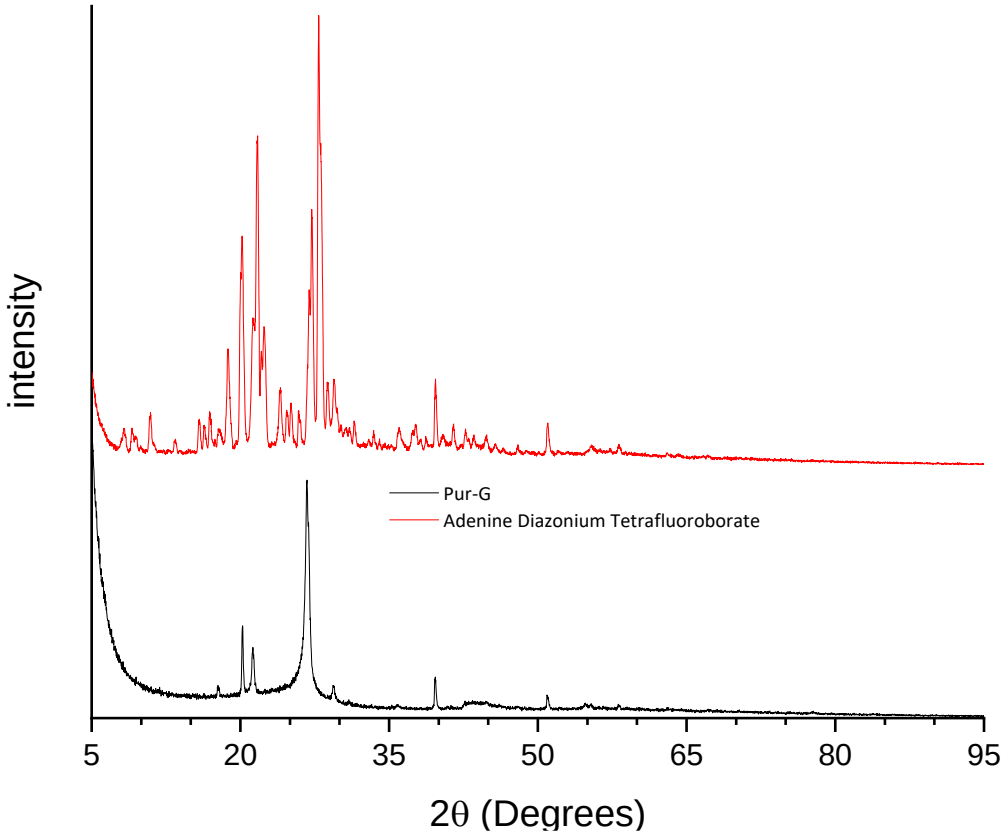

Figure 56: PXRD pattern for Pur-G and 7H-purine-6-diazonium tetrafluoroborate.

Sample	2-theta	theta	2sin(theta)	d / Å
Pur-G	26.70	13.35	0.46	3.34
Graphene	26.43	13.22	0.46	3.37

Table 9: Tabulated PXRD main peak for Pur-G and graphene.

Powder X-ray analysis (Figure 56, Table 9) of Pur-G shows that the graphitic nature has been maintained as the peak at 26 ° has been retained, along with the same peaks observed in Pnz-G. This is a positive sign that similar lattice planes are being formed, which would suggest similar structuring along the graphitic sheets when modified. The width of the main peak, at 2θ = 26.68 °, has doubled in width from that of pristine graphene, showing a decrease in the crystallinity and order of the graphene sheets,[90] which would be expected when modifying the surface. In addition, the peak has shifted to within 2θ = 0.06 ° of the peak position seen in Pnz-G, suggesting a similar change in the spacing. Like with Pnz-G, the additional peaks and broad peaks mixed with sharp peaks could suggest a contamination, though later study of this was prevented by the covid pandemic, though a change to the work-up had been made.

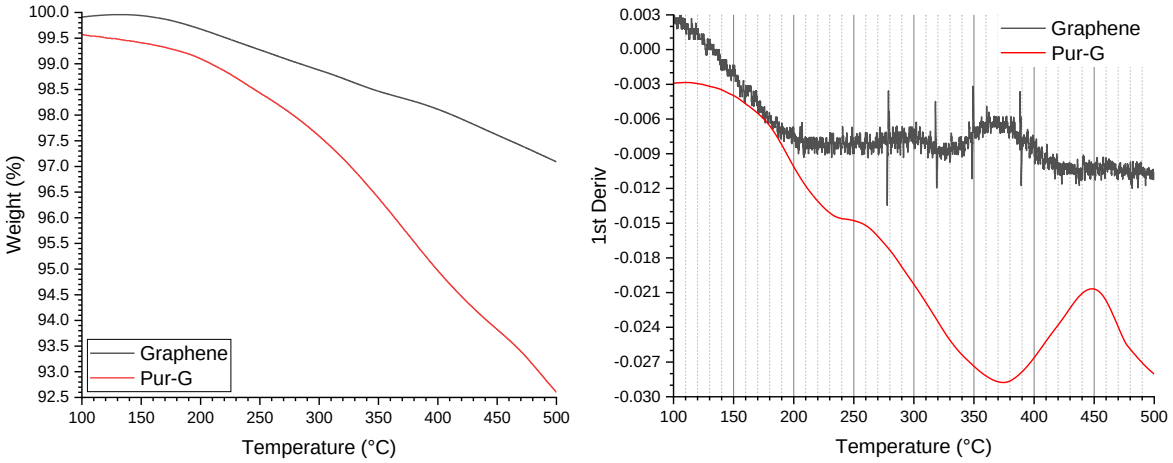

Figure 57: TGA for Pur-G and graphene, and the first derivative of both with lowess smoothing for Pur-G (left and right respectively).

TGA analysis of Pur-G is presented in Figure 57, alongside the pristine graphene. Mass losses prior to 100 °C are assigned to the loss of volatile solvents from fabrication. Lowes's smoothing was used in this analysis to improve the clarity of the first derivative of Pur-G, as the low mass loss creates increased noise in the data, which required remediation through this mathematical method and was used for all smoothing unless otherwise stated.

The total mass loss in Pur-G is 7 % between 100-500 °C, a further mass loss of approximately 4.5 % from the graphene standard and can be attributed to the degradation of the hybrid material. In contrast to graphene, the first derivative shows one defined inflection point at 375 °C and a second point above 500 °C, which is beyond the limit of the equipment used.

The first inflection point at 235 °C could be assigned to physiosorbed purine residue, due to a small shoulder of matching temperature seen in the TGA thermogram of the diazonium salt of purine (appendix, Figure 138). The second inflection point is at 375 °C and can be associated with the attached moiety of purine with an approximate 50 °C increase from the greatest loss rate (and 30 % mass loss) of the moiety. The 50 °C shift seen in Pnz-G is similar here. The final broader area going beyond 500 °C can be assigned to the residual decomposition of purine and the graphene backbone with greater defects present.[175, 183]

3.3.5 Synthesis of Thionine-Graphene with Graphene Nano-Platelets

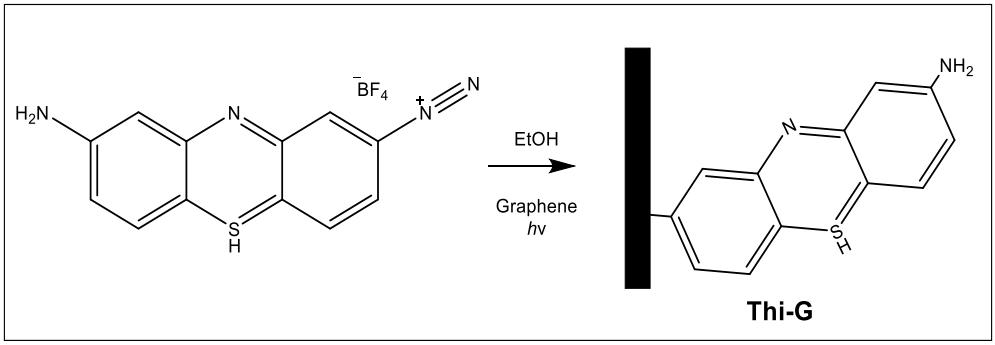

Scheme 26: Scheme for the modification of graphene using thionine diazonium tetrafluoroborate.

Using previous methods detailed for Pnz-G, Thionine-Graphene (Thi-G) was synthesised using thionine diazonium tetrafluoroborate in ethanol using light induced conditions, as shown in Scheme 26. Some analyses were unable to be completed due to time constraints and the occurrence of a global pandemic.

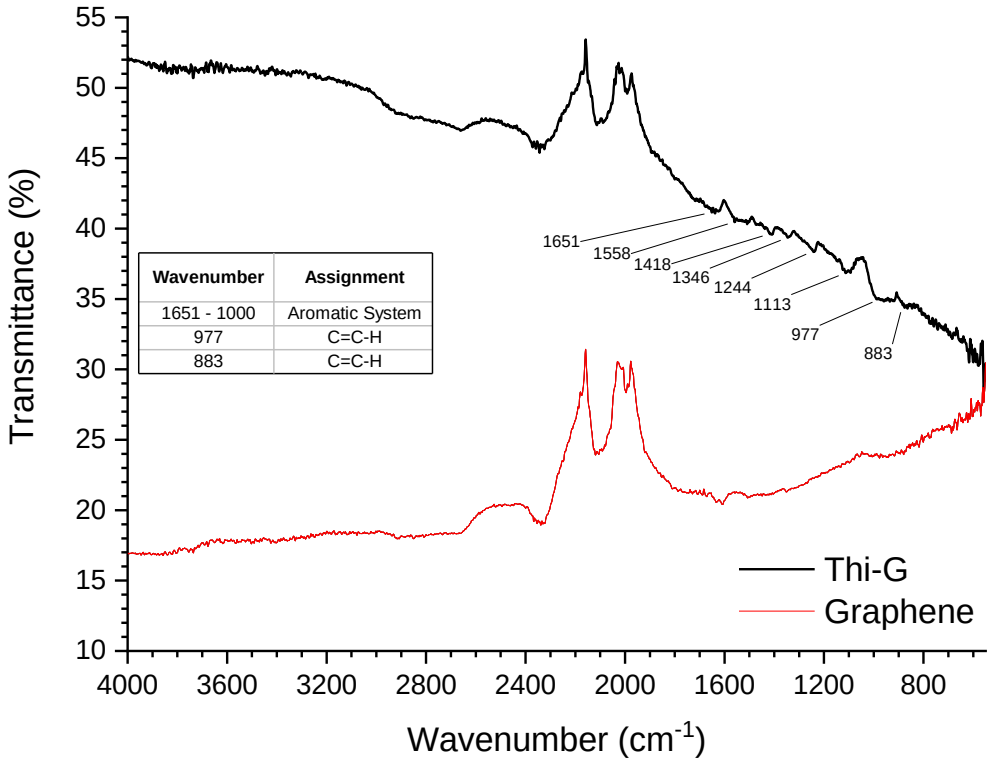

Figure 58: FTIR spectrum of Thi-G.

The FTIR spectrum of Thi-G (Figure 58) shows little resolution of bands as seen in other hybrids. However, this hybrid shows a collection of weak bands from 1600 to 1200 cm^{-1} that means that the FTIR spectrum is more easily interpreted. This set of bands shows a similar pattern and position to those in thionine and thionine diazonium and means that on this occasion we can see that they are present on the surface and likely as a covalently bound molecule.

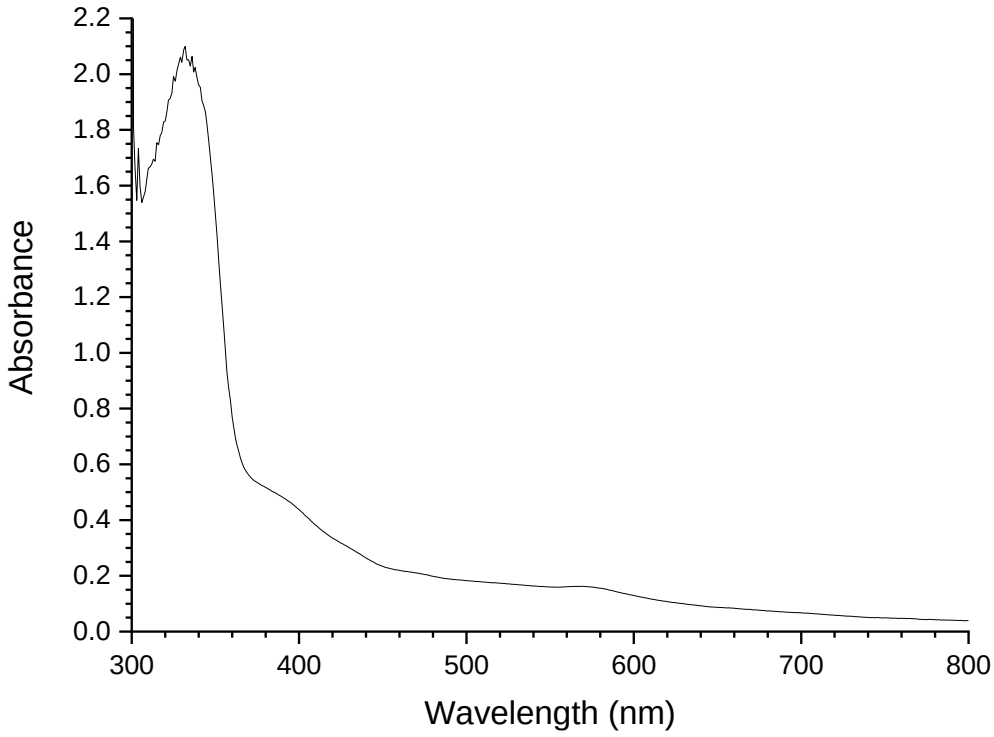

Figure 59: UV-vis spectrum of Thi-G in acidified MeCN.

The UV-vis spectrum of Thi-G, shown in Figure 59, was once again recorded in acidified acetonitrile, as DMF created a suspension that did not precipitate and did not filter to a non-black solution. The spectrum that was obtained showed a very strong UV absorption at 331 nm, a saturation of the detector at 300 nm and a shoulder at 391 nm. These features are shifted from the diazonium as the UV peak is only at 274 nm, though the 300 nm is an expected peak for the graphene system. The only visible region peak appears to be at 560 nm, which is a bathochromic shift from one diazonium peak, but a hypsochromic from its second visible peak. The visible peak has lower absorbance, but the absorption band is broad and covers the region of 400 nm to 620 nm, which may allow more utilisation of white light. This spectrum shows a shifted visible peak and new UV peaks, suggesting a new material has been formed where the chromophore has been modified along with the conjugated system.

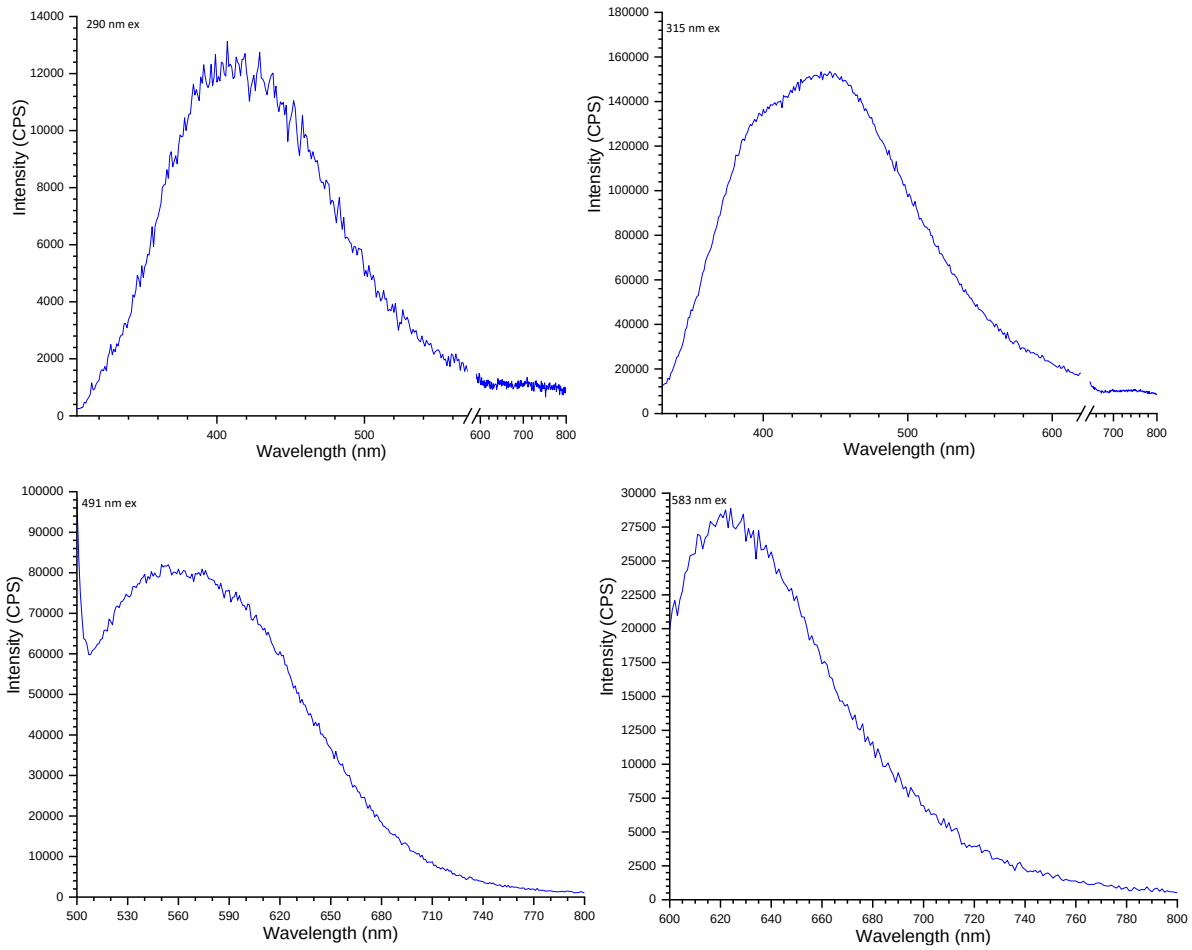

Figure 60: The fluorescence spectra of Thi-G measured in acidified MeCN, with excitations at 290 nm, 315 nm, 491 nm, and 583 nm. Slit widths 3 nm.

Following this, the fluorescence spectrum of Thi-G was recorded and compared to the diazonium salt starting material (Figure 60). Thi-G shows a fluorescent signature when excited in the UV region, giving a peak of 413 nm with a 290 nm excitation and 440 nm with a 315 nm excitation. This shows an equal shift between the excitation and emission wavelength as seen previously in the graphitic hybrids. The visible excitation of 491 nm gives an emission of 560 nm, which is a hypsochromic shift from the emission spectrum of the diazonium salt starting material. When excited at 583 nm the emission was 623 nm.

Unlike in PXRD of previous hybrids, there are no peaks to show lattice planes below the graphene sheet diffraction angle and few or no changes to the peaks at higher diffraction angles for Thi-G (Figure *61*). This suggests that no new lattice planes are forming, and that the main composition of this material is in the graphitic planes as the main peak is at 2θ = 26.7 °. In addition, the lack of a large shift at 2θ = 26.7 ° suggests that the second amine group was not converted to a diazonium salt as the interplane distance has not formed a lower 2θ angle.[184] However, this may not be due to a lack of

modification, since there is the introduction of disorder to the crystallinity shown by an increased peak width in comparison to pristine graphene.[90] Additionally, the peak has once again shifted to 2θ = 26.73 °, which is almost identical to Pnz-G and a deviation from pristine graphene, suggesting a slight decrease in the spacing between layers and an alteration to the stacking. The addition of broader peaks here could also suggest the addition of contaminants, as seen previously, though some potential contaminant peaks are missing in this sample compared to others.

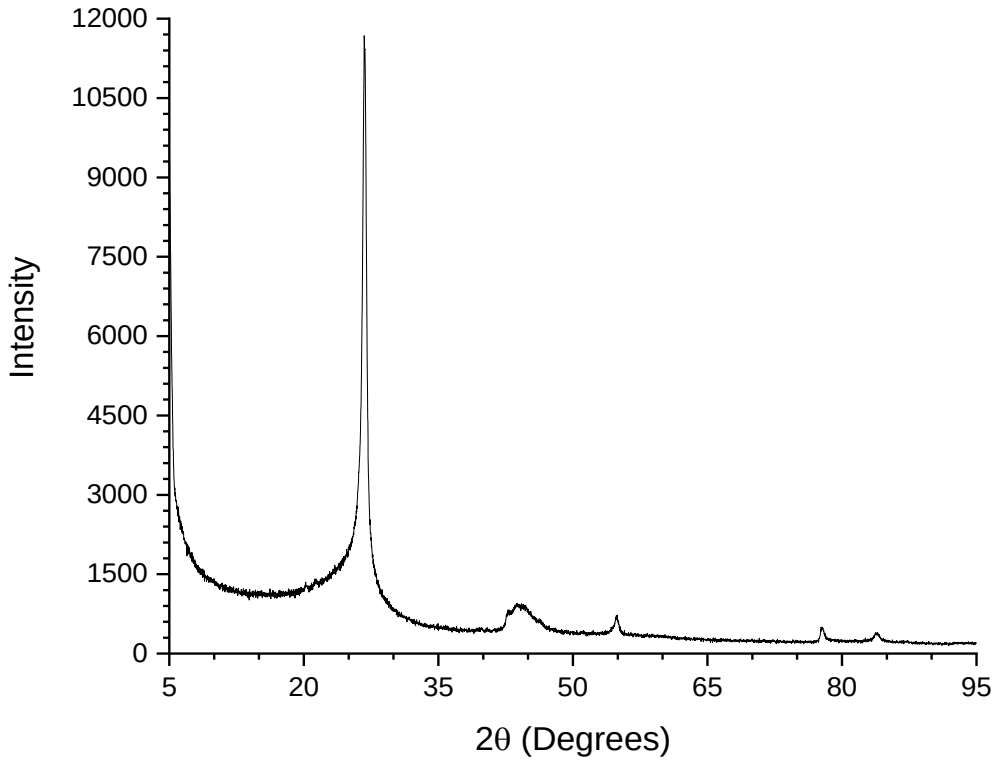

Figure 61: The PXRD pattern for Thi-G.

Sample	2-theta	theta	2sin(theta)	d / Å
Thi-G	26.73	13.36	0.46	3.33
Graphene	26.43	13.22	0.46	3.37

Table 10: Tabulated PXRD main peak for Thi-G and graphene.

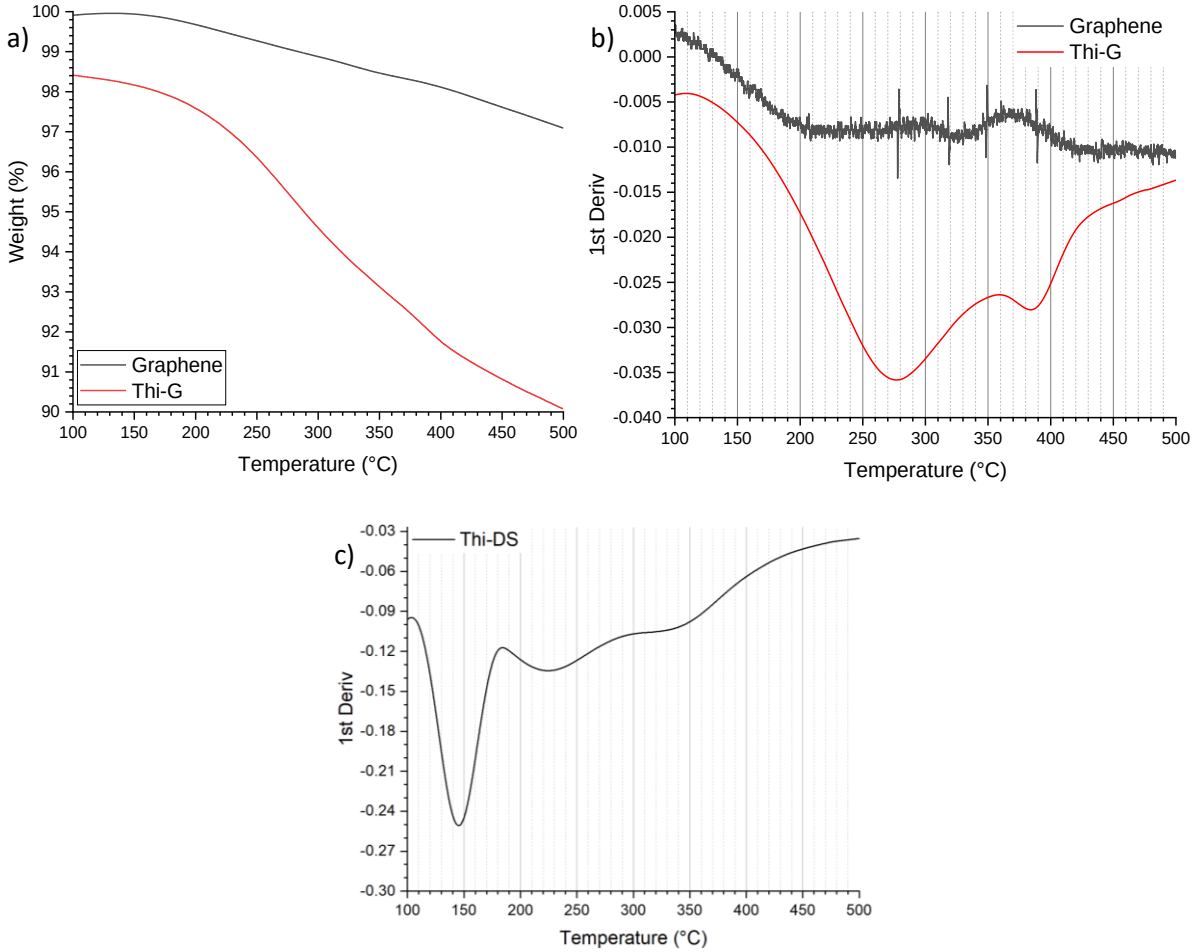

Figure 62: TGA (a) and first derivatives (b) of graphene and Thi-G, with the TGA first derivative of thionine diazonium salt (c).

TGA in Figure 62 shows the mass losses for Thi-G, alongside graphene as a comparison. As previously, mass losses were seen prior to 100 °C and were assigned to residual solvents from fabrication. The TGA shows two defined inflection points at 275 °C and 385 °C.

The general pattern of the first derivative is comparable to that of thionine diazonium salt, but with a 50 °C shift and a lack of a 145 °C inflection, which is assigned to the loss of the diazonium functional group. It can therefore be proposed that the inflections at 275 °C and 385 °C belong to the structure of the dye. The shift in both inflection point temperatures also suggest a chemisorption to the surface due to the thermal stabilisation of the dye. This follows the decomposition trend seen in Pnz-G and Pur-G samples.

The surface modification percentage is also difficult to calculate, as too many assumptions are required in order to use the diazonium salt as a standard for the calculation, due to the presence of the diazonium functional group and any BF_4 counterion, whose degradation would be uncertain in this scenario.

3.3.6 Synthesis of Fluorescein-Graphene and 2-methylchromone-Graphene with Graphene Nano-Platelets

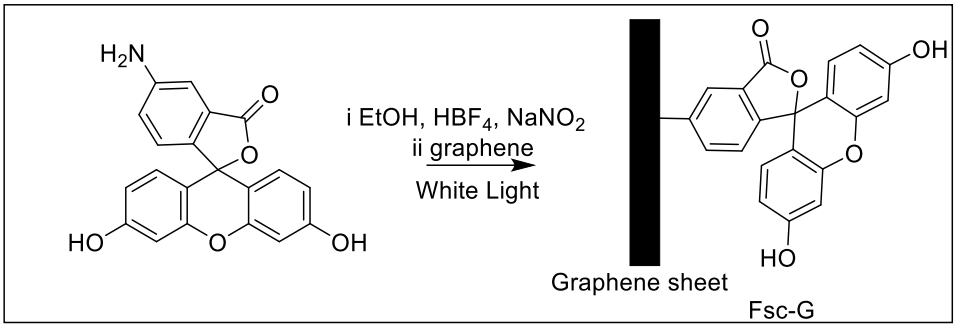

Scheme 27: The one pot synthesis of Fsc-G through white light illumination.

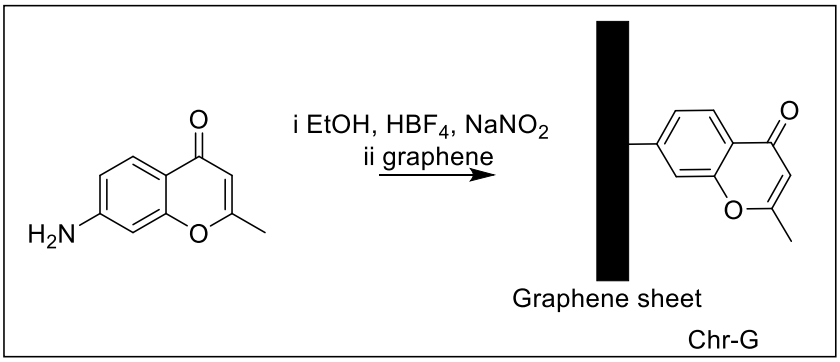

Scheme 28: The one pot synthesis of Chr-G.

Unlike with the graphitic materials up to this point, both fluorescein and chromone required a new methodology, due to the lack of stable diazonium formation, as described previously. Considering this, the method was altered to undergo the diazonium formation with sodium nitrite in ethanol for 10 minutes with vigorous stirring in the absence of light. After the 10 minutes, graphene was added to the reaction mixture and the reaction could then be illuminated with white light. This method was used due to literature methods seen with the phenazine diazonium, as a less stable salt, to form phenazine derivatives using single atom (iodine) or R group substituents.[77] The reaction created a black powder that was washed and isolated as previously stated. For fluorescein, white light was required but this was not the case with chromone (Scheme 27 and Scheme 28).

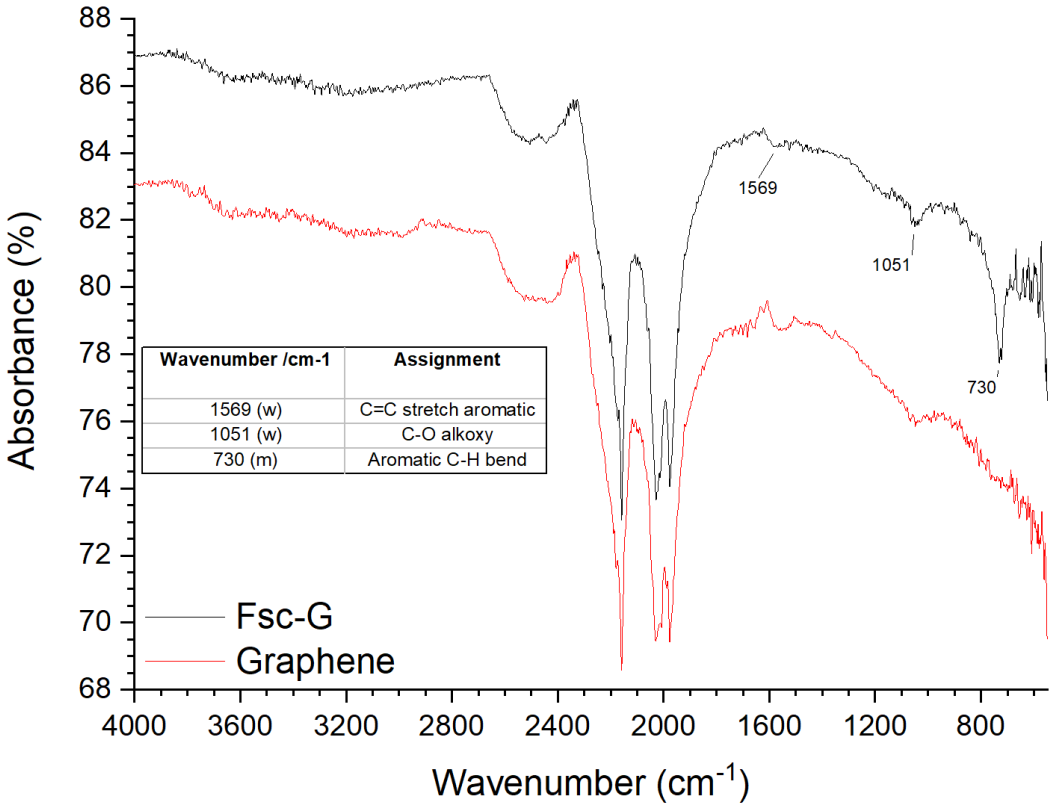

Figure 63: FTIR spectrum of Fsc-G. Absorbance scale displays amount of light transmitted.

IR spectra of Fluorescein-Graphene (Fsc-G) was recorded and displayed in absorbance for easier viewing of the spectrum, as these spectra are often unusual in shape (as seen in Figure 63). Much like in Pnz-G, the FTIR spectrum comprises mainly graphene bands with some changes in the fingerprint regions. In particular, an increased absorbance at 730 cm^{-1}, which would be characteristic of the C-H bending in aromatic systems.

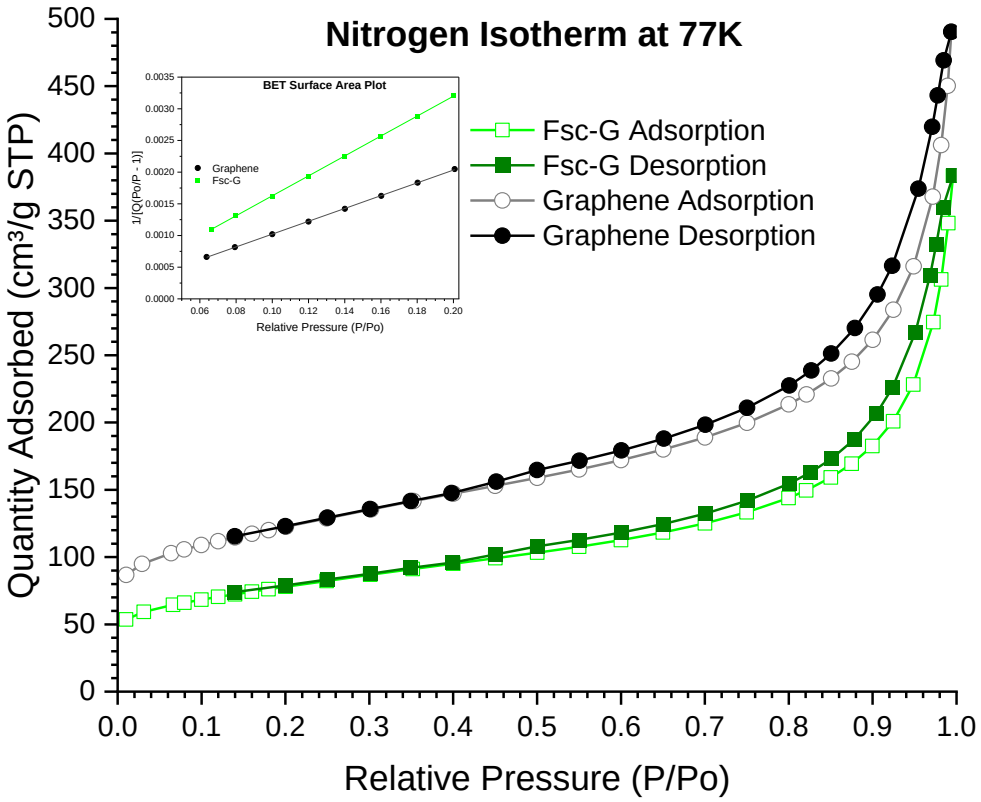

Figure 64: Nitrogen isotherm plot for graphene nanoplatelets and Fsc-G at 77 K with inlaid BET surface area plot.

Sample	Single Point Surface Area (m^2/g)	BET Surface Area (m^2/g)	BET constant (C) value	Langmuir Surface Area (m^2/g)	t-Plot Micropore Area (m^2/g)	Average Pore Size (Å)
Graphene	426	430	888	586	126	53
Fsc-G	271	276	208	378	62	62

Table 11: Tabulated surface area data for graphene nanoplatelets and Fsc-G.

BET analysis (Figure 64, tabulated in Table 11) also gave an insight into the changes in the available surface of these hybrid materials, giving a surface area of 271.36 m^2/g, which is 63.08 % of the area the pristine graphene provides. The Langmuir area was 378.09 m^2/g, a fall to 64.56 % compared to pristine graphene. This is proposed to be due to the dye modifying the surface of the outer platelets in the stacks and reproducing the agglomeration seen with phenazine, as well as the dye blocking surface adsorption. The pore size was also found to be 61.6 Å, an increase from 52.9 Å in graphene, but is also a decrease compared to other hybrids. If these pores are the active sites for the hybrid materials, this smaller size may limit Fsc-G's catalytic capabilities unless the larger accessible surface area can compensate.

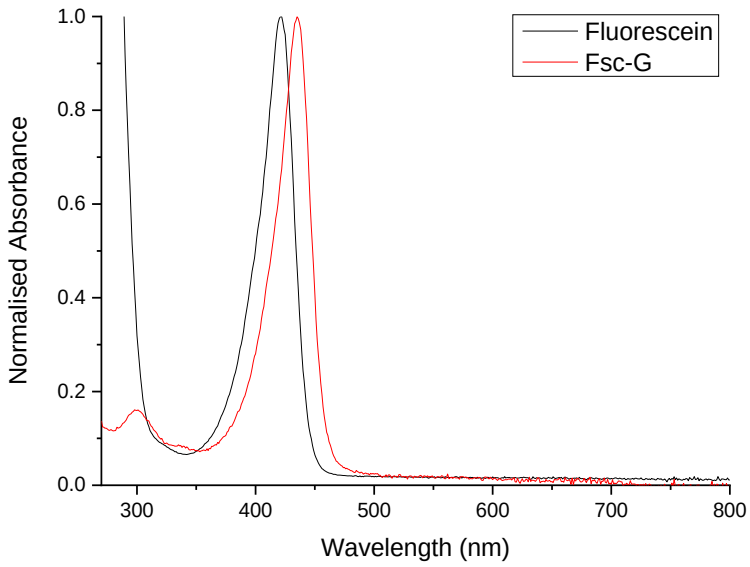

Figure 65: Normalised UV-vis spectrum of Fsc-G and its free dye fluorescein in acidic MeCN.

The UV-vis spectrum (Figure 65) of Fsc-G shows a strong visible peak at 435 nm, compared to 422 nm in fluorescein, giving a similar shift size to Pnz-G, but red shifted in this case. There is also the gain of a peak at 299 nm, similar to the 300 nm seen in non-visible absorbing hybrids, possibly linked to the attachment to the graphene by the aryl group within fluorescein, where attachment is expected.

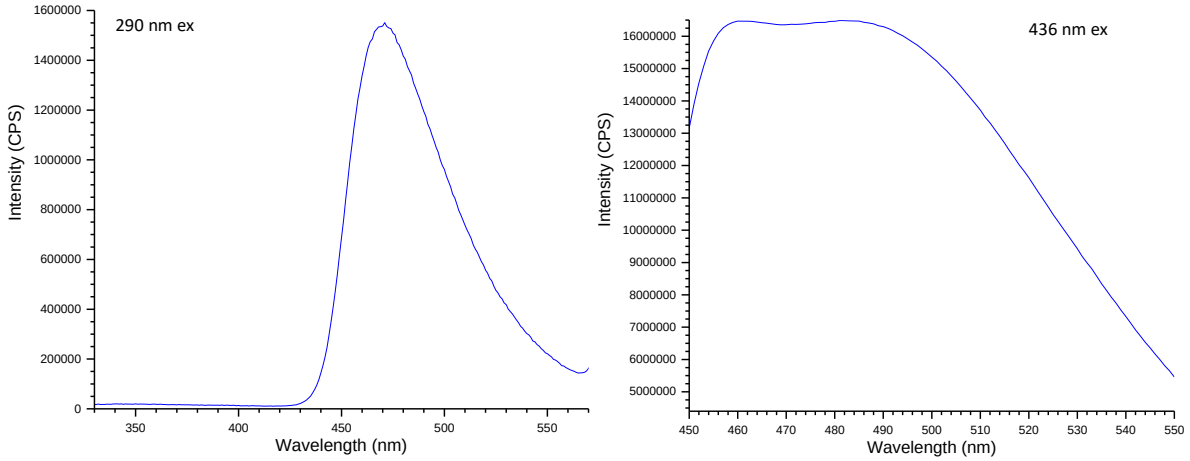

Figure 66: Fluorescence spectrum for Fsc-G in acidified MeCN with excitations stated on the spectra using 3 nm slit widths.

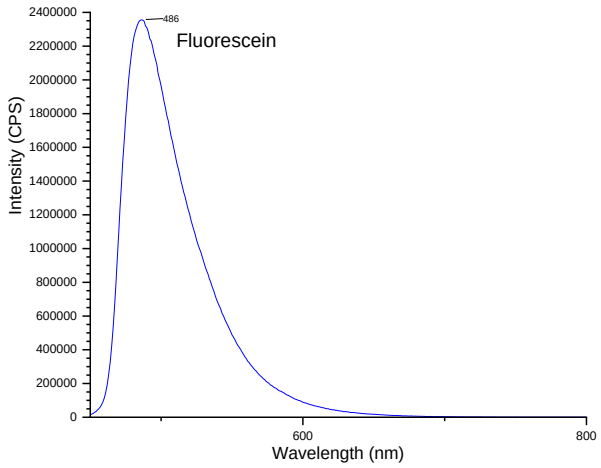

Figure 67: The fluorescence spectrum of fluorescein when excited at 436 nm. Maximum fluorescence peak is 486 nm and Slit widths 3 nm.

The emission spectra for Fsc-G were measured when the sample was excited with wavelength in the UV (290 nm) and the visible (436 nm) regions (Figure 66). The single emission band at 471 nm was recorded when the sample was excited with 290 nm, but a double peak structure at 461-483 nm was observed when the sample was excited with 436 nm. The second peak at 483 nm is likely due to a residual amount of fluorescein present as a side product, which can be formed during the reaction similar to the by-product observed for phenazine-graphene reaction. The spectrum of fluorescein on its own shows a typical emission peak at 480 nm (Figure 67). When excited with the wavelength of 436 nm, both fluorescein and Fsc-G absorb readily resulting in double peak structure observed in the emission spectrum of Fsc-G. In contrast, when excited with the wavelength of 290 nm, Fsc-G absorbs much more efficiently compared to fluorescein resulting in single band at 471 nm in the emission spectrum of Fsc-G. It could be assumed that any residue present is minute and within an acceptable

parameter for use in preliminary studies of photoactivity. The similarity in emission spectrum from both peaks is very promising that the fluorescein has attached to the graphene.

The powder pattern for Fsc-G is in some ways unique compared to other graphene hybrids studied in this project. This is due to the broadening of the peaks seen for graphene and the formation of sharp and resolved peaks at 17 ° and 29 °. This may coincide with the increased intensity ratio of the peaks at 20 ° and 21 °. Since each of the new peaks are much stronger when compared to the main graphene peak, it could be surmised that the modification has been more successful or had a greater effect on the crystal lattice than the previous dye-graphene hybrids. This could be due to the *in situ* nature of the reaction, which may be acting to prevent reductions or degradations of diazonium dye in solution.

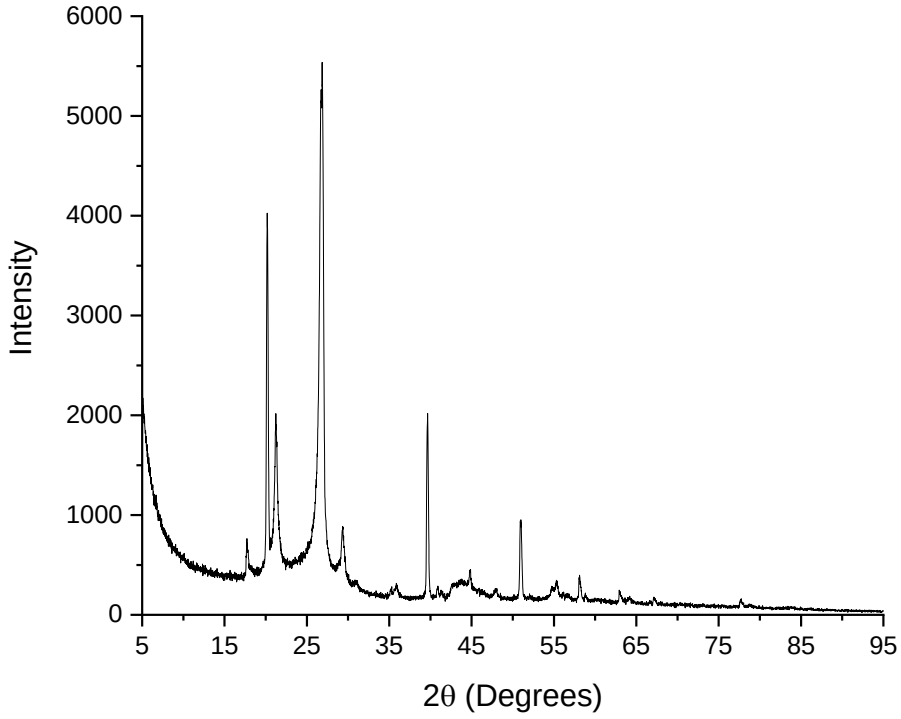

Figure 68: PXRD pattern for Fsc-G

Samples	2-theta	theta	2sin(theta)	d / Å
Fsc-G	26.85	13.42	0.46	3.32
Graphene	26.43	13.22	0.46	3.37

Table 12: Tabulated XRD main peak for Fsc-G and graphene.

PXRD for Fsc-G shown in Figure 68 gives a shifted graphitic peak of 2θ = 26.85 °, showing that the space between the layers is now smaller than seen in Pnz-G, alongside the peak being widened by approximately 35 % by FWHM method of peak width analysis. This shows a disruption to the order of the graphene and some loss of crystallinity,[(90)] likely caused by the breaking of the sp^2 system in graphene. However, the large quantity of new sharp and broad peaks could indicate contamination of

the crystal, potentially caused by the one-step process. However, despite a change in work up, some analyses were not able to be followed up due to the covid pandemic.

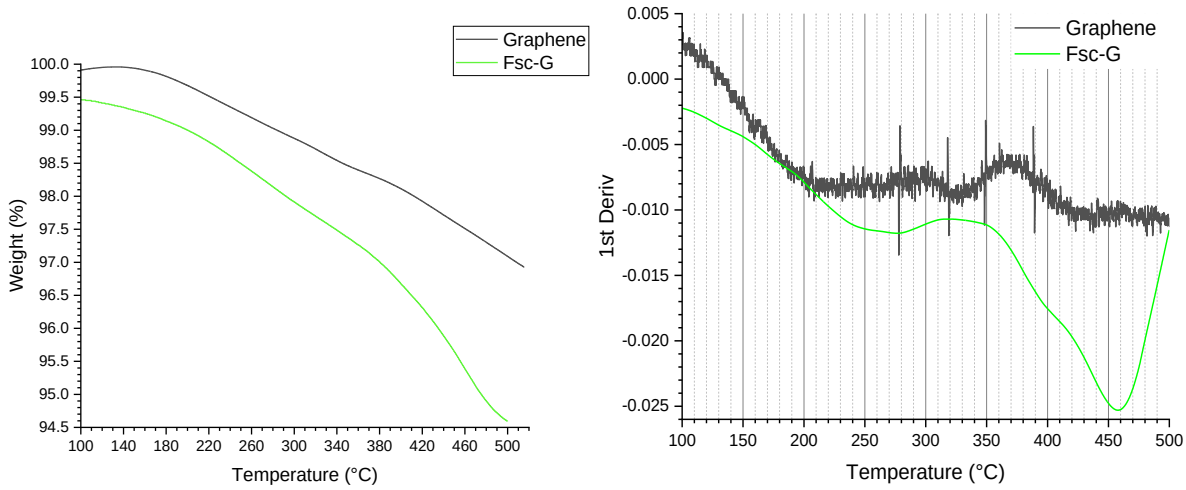

Figure 69: TGA and its first derivative (left and right respectively) for Fsc-G and graphene. Fsc-G first derivative plotted with a lowess smoothing.

The TGA for Fsc-G is shown in Figure 69. The first derivative has two distinct infection points at 275 °C and 460 °C. Neither are seen in pristine graphene and can be attributed to new physical properties in Fsc-G. It is reported that the degradation pattern for fluorescein within the temperature range would be [M-OH-CO_2H] according to literature TG-DTA-DTG studies.[185] Based on the total mass losses observed for Fsc-G (5.5 %) and unmodified graphene (3 %) at the final temperature, it can be concluded that the difference of 2.5 % is due to covalent modification. As [M-OH-CO_2H] corresponds to 18 % of fluorescein mass, it could be proposed that *ca*. 14 % of the surface was modified in the Fsc-G composite. However, this method of calculating the percentage surface modification assumes no other mass loss occurs and would require TGA of a fluorescein sample to be calculated with more certainty.

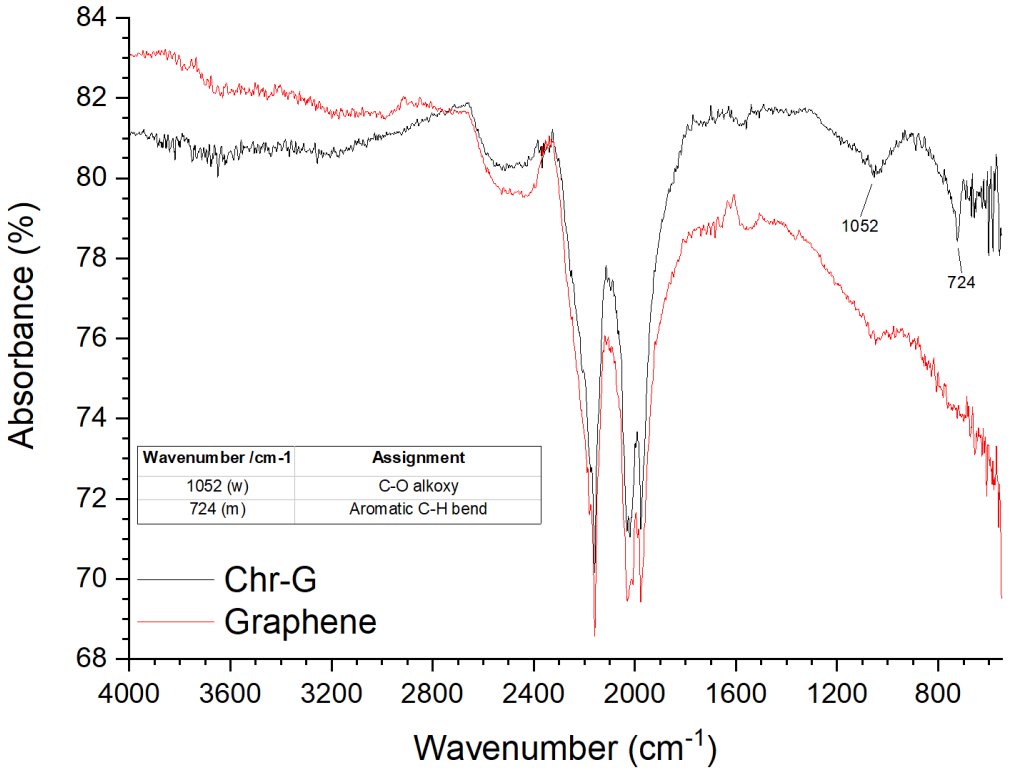

Figure 70: FTIR spectrum of Chr-G. Absorbance scale displays amount of light transmitted.

IR spectra of 2-methylchromone-Graphene (Chr-G), shown in Figure 70, was seen to be similar to both Fsc-G and Pnz-G, through changes in the FTIR bands from 1600 cm^{-1} which would be changes to aromatic structures as would be expected in an attachment at the basal plane. Strong bands for dyes are unexpected due to the modification percentage being a maximum of 20 % in small aryl molecules according to literature, though this is dependent on the analytical method used.[33]

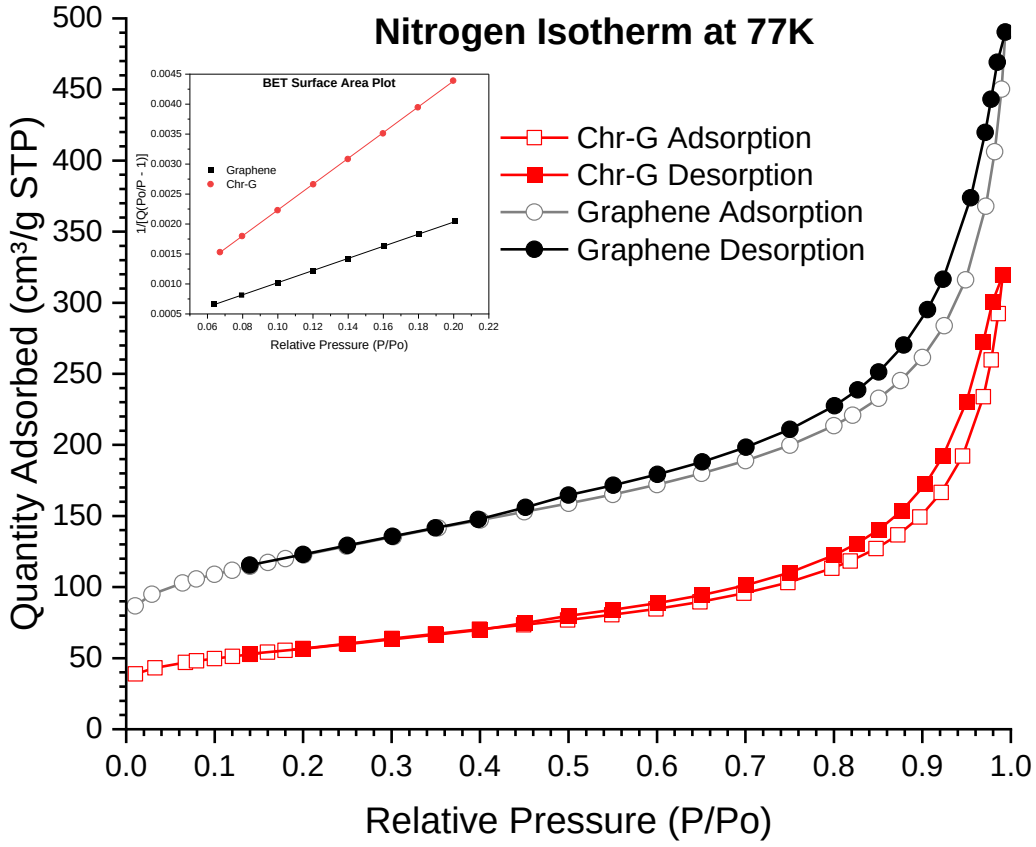

Figure 71: Nitrogen isotherm plot for Chr-G and graphene at 77K with inlaid BET surface area plot.

Sample	Single Point Surface Area (m^2/g)	BET Surface Area (m^2/g)	BET constant (C) value	Langmuir Surface Area (m^2/g)	t-Plot Micropore Area (m^2/g)	Average Pore Size (Å)
Graphene	426	430	888	586	126	53
Chr-G	198	201	264	276	41	72

Table 13: Tabulated surface area data for graphene nanoplatelets and Fsc-G.

BET analysis (Figure 71, Table 13) also gave an insight into the changes in the available surface of these hybrid materials, giving a surface area of 201.44 m^2/g, which is 47.2 % of the area the pristine graphene provides. The Langmuir area was 276.43 m^2/g, a fall to 41.4 % compared to pristine graphene. The pore size was also found to be 71.8 Å, an increase from 52.9 Å in graphene. This loss of available surface area is proposed to be due to the chemical attachment of chromone to graphene, likely creating similar effects seen with phenazine - where larger agglomerate stacks were formed.

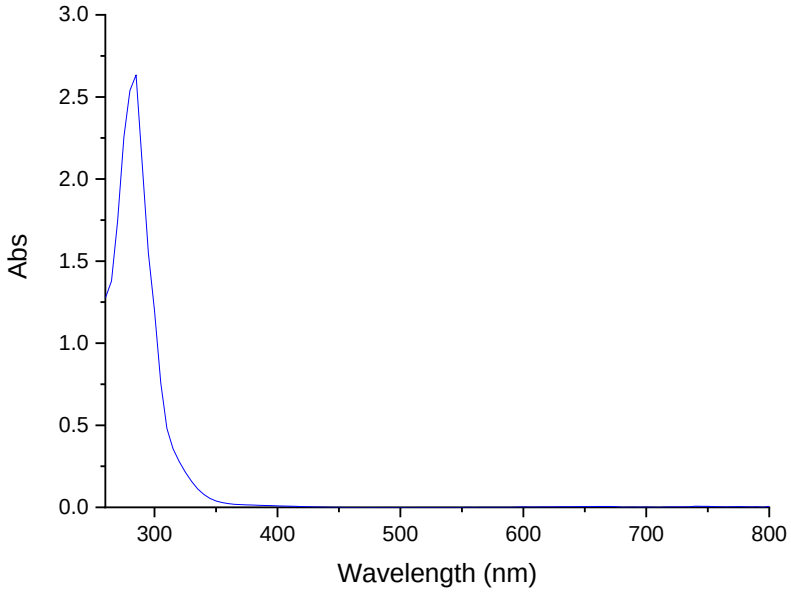

Figure 72: UV-vis spectrum of Chr-G in acidified MeCN.

The UV-vis spectrum of Chr-G was performed in acidified acetonitrile (Figure 72), once again due to the lack of precipitation in DMF. The spectrum shows that there is a UV peak at 285 nm, which is similar to that of the other UV absorbing material, Pur-G. Given that this is similar to a material seen previously, it has been postulated that attachment is the cause of the shift.

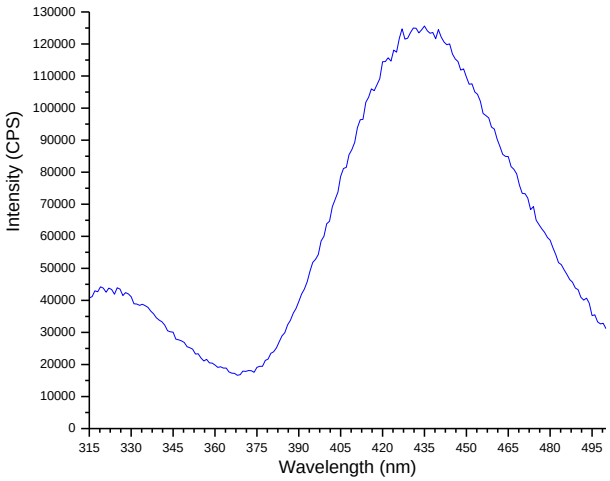

Figure 73: Fluorescence spectrum of Chr-G in acidified MeCN. Excitation at 290 nm and slit widths 3 nm.

The fluorescence spectrum for Chr-G was recorded and compared with one obtained for Pur-G since both contain similar UV-vis features, as shown in Figure 73. It was found that the fluorescence peaks are 322 nm and 432 nm, compared to Pur-G having peaks at 317 nm and 394 nm. In addition to the differences in peak positions, the peak ratios are also reversed, suggesting that they are different materials with different fluorescence signatures.

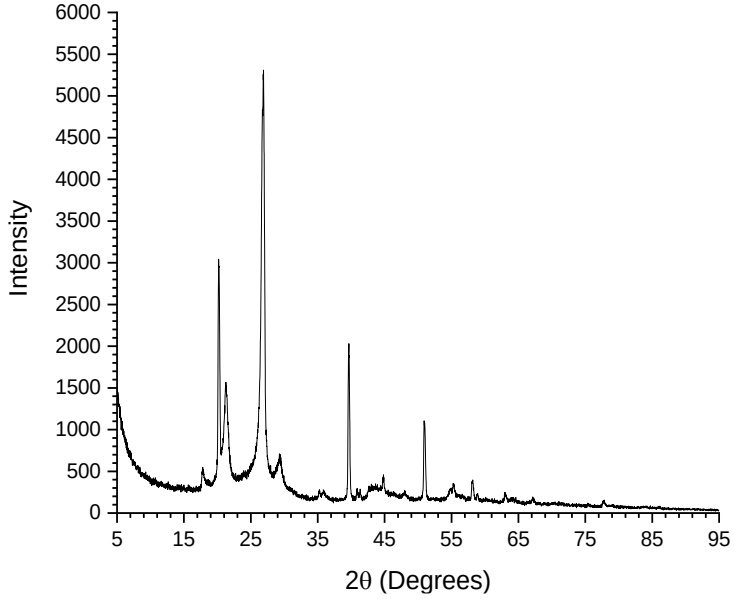

Figure 74: The powder x-ray diffraction pattern for Chr-G.

Sample	2-theta	theta	2sin(theta)	d / Å
Chr-G	26.89	13.44	0.46	3.31
Graphene	26.43	13.22	0.46	3.37

Table 14: Tabulated PXRD main peak for Chr-G and graphene.

The PXRD pattern for Chr-G (Figure 74, Table 14) is in some ways unique compared to the two step graphene hybrids studied in this project, but very similar to Fsc-G. This is due to the broadening of some peaks seen for graphene at higher diffraction angles but now also shows the broadening of the previously sharp and resolved peaks at 17 ° and 29 °. This may coincide with postulations made for Fsc-G, where the *in situ* methodology that has been utilised has improved stability and reactivity for the dyes with graphene. However, the broadening could indicate a reduced crystallinity and order to the structures[90] created by Chr-G, when compared to those of Fsc-G. As seen with Fsc-G, the large quantity of new sharp and broad peaks could indicate contamination of the crystal, potentially caused by the one-step process. However, despite a change in work up, some analyses were not able to be followed up due to the covid pandemic.

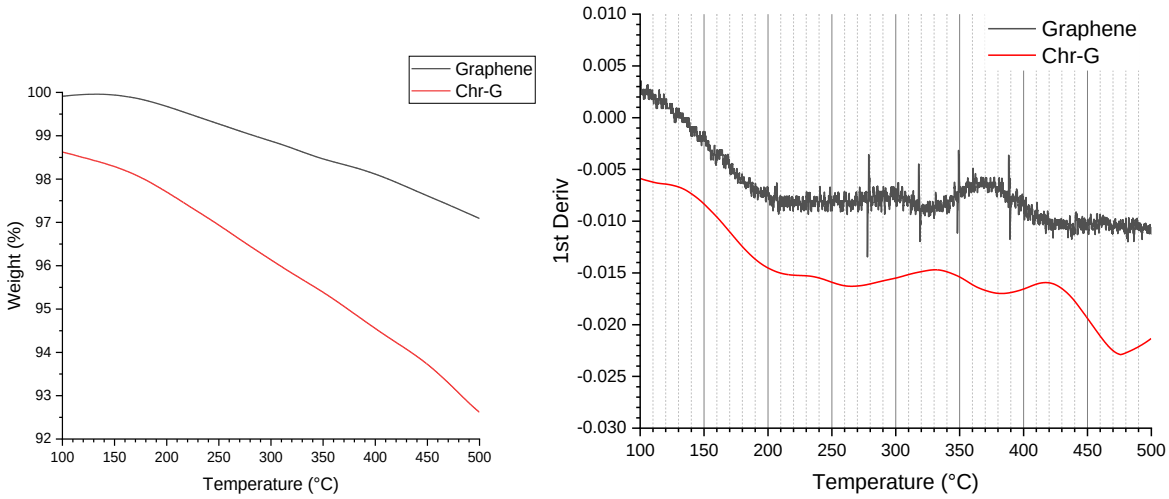

Figure 75: TGA and its first derivative (left and right respectively) of Chr-G and graphene. Chr-G first derivative plotted with lowess smoothing.

TGA of Chr-G is shown in Figure 75, and presents four inflection points to be assigned. These four points are at 215 °C, 265 °C, 382 °C and 475 °C. Unfortunately, it is difficult to assign these temperatures because we lack a suitable standard. Additionally, 2-methylchromone is reported (in Sigma Aldrich SDS documentation) to boil at 249.5 °C, which would make a standard unlikely to give useful data for this study. However, the final temperature of 475 °C is close to the temperatures previously observed in these hybrids for a degradation of the chemisorbed dye's aromatic system.[175]

3.3.7 Summary

To summarise, the hybrid materials show a shift in the graphitic peak to a higher 2θ value, which means that the spacing between the graphene sheets that is caused by π-π stacking is slightly decreasing. In addition, all the hybrids display a broadening of this peak, which suggests a decrease in the crystallinity of the material and would be expected if the surface of some sheets is being altered and modified in a way that breaks the sp^2 system. Since the modification is expected to be of a similar nature, the changes in the graphitic peak position should have a similar trend. Therefore, the width of the peak can reflect the quantity of modification taking place on the graphene surface through the effect of crystallinity defects and lattice strain on peak broadness.[186, 187] The width of the peak was found using a Voigtian fitting of the graphitic peak.[179] A Voigtian fitting is a more flexible plot than Gaussian or Lorentzian fitting and is a convolution of these two plots, avoiding the assumptions of both these plots which can result in systematic errors.[179] What is seen through this is that all hybrids show a 35-60 % broadening of the graphitic peak, suggesting greatly increased disorder within the crystal structure.[90] Chr-G and Fsc-G do not show an increase in broadening and suggests there is either less strain or no change in the crystallite size. [186, 187]

Sample	Graphitic Peak (2θ°)	Voigt FWMH (2θ°)
Graphene	26.4	0.20
Pnz-G	26.7	0.27
Pur-G	26.7	0.27
Thi-G	26.7	0.30
Fsc-G	26.8	0.19
Chr-G	26.9	0.20
Pnz-G.TFA	26.7	0.32
Pnz-G.HCl	26.7	0.29

Table 15: Changes seen in the graphitic peak of each material.

IR spectra generally show little change except within the fingerprint region. Due to the nature of the structures added, this is to be expected. However, the transmission baseline is unusually low and may be affecting the FTIR spectrum and the degree of the changes.

In TGA, there is a trend of the hybrids showing an increased mass loss rate compared to graphene, along with lacking an initial increase in mass. This suggests changes to the graphene that prevent the reaction that occurs. Additionally, they show some new mass loss spikes that do not match with graphene or the salts, which could be due to parts of the dyes now attached degrading but showing greater stability than when unattached suggesting a modification onto the graphene surface and in some cases could be compared to the known degradations of the dyes to give estimations of surface area coverage. However, more in-depth studies than what were undertaken would be necessary to give more accurate data on surface coverage, such as multiple TGA runs with altering concentrations of dye loading.

Fluorescence and UV-vis shows a similar pattern in those hybrids that could be compared to their free dyes, where the hybrid has a slightly shifted peak from the dye. However, where Pnz-G is blue shifted in UV-vis, Fsc-G is red shifted and this could be attributed to the site of binding for each. This is because Pnz-G binds between the chromophore and Graphene and Fsc-G binds through an aryl ring which is attached to the chromophore, increasing the distance between the chromophore and the graphene sheet.

3.4 Conclusions

To conclude, it has been shown, in this chapter, to be possible to expand upon the method first used in Chapter 2 [85] to fabricate two more graphene hybrids without alteration to the methodology. However, it has also been shown that not all dyes can be used to form stable diazonium salts. For this, a new one pot method was established and showed to be both effective and preferential due to the reduced use of solvents and other reagents to undertake the fabrication of dye-graphene composites.

IR spectra of these hybrids show similar pattern across the region, but Chr-G, Pur-G and Fsc-G show a particularly strong signals at 733 cm^{-1}, 1075 cm^{-1} and 726 cm^{-1}, respectively. This shows that the structures bound to the graphene can lead to changes deep in the fingerprint region within the bands for C-H and C-C bond vibrations and bends in aromatic systems.

Sample preparation methods for the UV-vis spectroscopy study of the new hybrids were altered to include a new solvent system. This also involved acidification of the solution being required and may be attributed to the surface potentials with these dyes. As would be expected, neither the purine nor the chromone hybrids had visible light absorption peaks, which may affect their visible light activity going forward. The fluorescein hybrid did show absorption in the visible region, which was shifted 13 nm compared to its free dye.

The PXRD pattern is unchanged in diffraction angles when compared to Pnz-G, but the intensity ratio of the pattern does change for some of the peaks that are determined as “new”. This indicates that the crystalline structure between hybrids is generally unchanged, but there is an increase in the graphene $2\theta = 26\ ^\circ$ peak position and width, which suggests more disorder and crystallinity loss in the samples, which would align with the concept of increased defects.[90]

TGA of the hybrids shows that there are some residues from their initial fabrication techniques, but that there are new inflection points seen in each sample that cannot be attributed to starting materials and tend to be closer to the decomposition onset of graphene in the literature for graphenes with defects in the lattice, which indicates some areas of the platelet powders have been modified and defects added to the sheets. One exception to the general trend of a 400+ °C inflection point is Thi-G, which could be a sign of there being little to no covalent bonding. Additionally, some TGA inflection points were able to be identified in Fsc-G from fluorescein to indicate possible dye loading of 7 %.

3.5 Experimental

3.5.1 Synthesis of 7H-purine-6-diazonium Tetrafluoroborate

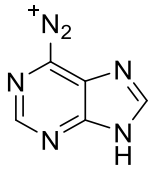

Scheme 29: The predicted structure of 7H-purine-6-diazonium tetrafluoroborate.

Adenine (0.68 g; 5.04 mmol) was dissolved in HBF_4 (7 mL, 50:50 in H_2O) and cold to 0-5 °C. Sodium nitrite (0.35 g; 5.04 mmol) was dissolved in H_2O (2 mL) and was added to the solution dropwise. The colour of the solution changed from colourless to pale yellow during the addition. Left stirring at 0-5 °C for 2 hours. Ethyl acetate used to precipitate the yellow solid in the freezer overnight. The yellow solid was isolated by filtration and dried on the filter.

Yield: 0.713 g; 3.05 mmol; 60.4 %

^{1}H NMR (500 MHz, d_6-DMSO) δ_H: 8.49 (1H, s, Ar-H), 8.45 (1H, s, Ar-H), 8.95 (1H, broad s, H-N pyridine); FTIR: 3567, 3391 cm^{-1} (N-H), 2193 cm^{-1} (diazonium $N^+{\equiv}N$), 1975-1000 cm^{-1} (aromatic system); UV-vis λ_{max} = 309 nm, λ = 437 nm, 588 nm; HRMS m/z (ESI+), expected 147.04 m/z, found 144.98 $[M+Na+H-N_2]^+$.

3.5.2 Synthesis of Fluorescein-4-diazonium Tetrafluoroborate

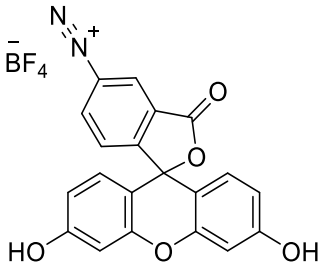

Scheme 30: The expected product for the diazonification of 4-aminofluorescein.

5-aminofluorescein (200 mg; 0.58 mmol) was dissolved in HBF_4 (2.5 mL, 50:50 in H_2O) and H_2O (100 mL) before cooling to 0-5 °C. $NaNO_2$ (40 mg; 0.58 mmol) was dissolved in H_2O (2 mL) and was added to the solution dropwise. The colour of the solution changed from colourless to pale yellow during the addition. Left stirring at 0-5 °C for 2 hours. Ethyl acetate used to precipitate the yellow solid in the freezer overnight. The yellow solid was isolated by filtration and dried on the filter. Deemed unsuccessful after analysis.*

Yield: 96 mg; 0.215 mmol.

IR: 2347 cm^{-1} (diazonium functional group); LCMS (ESI+) expected 446.0692, found 351.0863 ($M-N_2+H_2O$) and 348.0866 ($M-N_2+NH_2$).

*Reaction performed by Connor Sherwin under guidance of the author.

3.5.3 Synthesis of 2-Methylchromone Diazonium Tetrafluoroborate

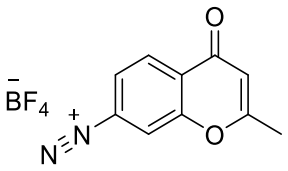

Scheme 31: The expected product for the diazonification of 7-amino-2-methylchromone.

4-amino-2-methylchromone (101 mg; 0.577 mmol) was dissolved in HBF_4 (2.5 mL, 50:50 in H_2O) and cold to 0-5 °C. $NaNO_2$ (40 mg; 0.58 mmol) was dissolved in H_2O (2 mL) and was added to the solution dropwise. The colour of the solution changed from colourless to pale yellow during the addition. Left stirring at 0-5 °C for 2 hours. Ethyl acetate used to precipitate the yellow solid in the freezer overnight. The yellow solid was isolated by filtration and dried on the filter. Deemed unsuccessful after analysis.* Yield: 200 mg; 0.73 mmol.

IR: 2349 cm^{-1} (diazonium functional group); ^1H NMR (400 MHz, CD_3OD) δ_H: 9.5 (1H, d, J = 4 Hz, Ar-H), 9.36 (1H, s, Ar-H), 9.28 (1H, d, J = 12 Hz, Ar-H), 9.15 (1H, d, J = 8 Hz, Ar-H), 8.51 (1H, s, Ar-H), 7.64 (1H, s, Ar-H), 7.52 (1H, s, Ar-H).

3.5.4 Synthesis of Thionine Diazonium Salt

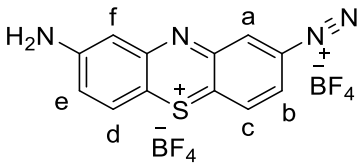

Scheme 32: The expected structure for the product of the diazonification of thionine acetate.

Thionine acetate (486 mg; 1.69 mmol) was dissolved into HBF_4 (5 mL, 50:50 in H_2O) and cooled to 0-5 °C using an ice bath. $NaNO_2$ (45 mg; 0.652 mmol) was dissolved in H_2O (2 mL) and added dropwise. The colour of the solution changed from blue to purple and was allowed to stir for 2 hours in the ice bath. Filtered the purple solid off in vacuo and washed with hexane before drying.

Yield: 491 mg; 1.27 mmol; 70.5 %

IR (cm^{-1}): 3544 (N-H stretch primary), 3322 (N-H stretch primary), 3101 (C-H alkene), 2245 (diazonium functional group), 1981 (C-H aromatic bending), 1599 – 1466 (C=C aromatic), 1015 (C-N stretch), 819 (C-H aromatic trisubstituted); LCMS (ESI+) expected 241.0542, found 259.9896 $(M+H_2O+H)^+$. ^1H NMR (500 MHz, CD_3OD) δ_H 8.21 (2H, dd, J = 9.0 and 2.3 Hz, Hb and He), 7.98 (2H d, J = 2.3 Hz, Ha and Hf), 6.96 (2H, d, J = 9.0 Hz, Hc and Hd). UV-vis (MeCN + H_2SO_4) λ_{max} = 274 nm, λ = 509 nm, 606 nm. Emission (excitation: 491 nm) = 643 nm.

*Reaction performed by Connor Sherwin under guidance of the author.

3.5.5 Synthesis of Purine-Graphene with Graphene Nano-platelets

7H-purine-6-diazonium tetrafluoroborate (100 mg; 0.425 mmol) was dissolved in EtOH (100 mL) and graphene was added (100 mg) and stirred under ambient conditions for 2 hours, before filtration *in vacuo*. Washed with acetone and dried in air for 30 minutes. Dry powder collected for analysis.

TEM = 0.285 nm, 0.423 nm, and 0.103 nm. UV-vis λ_{max} = 275 nm; emission = 317 nm and 400 nm, exc. 440 nm; BET = 237.49 m^2/g.

3.5.6 Synthesis of Thionine-Graphene

Thionine diazonium tetrafluoroborate (82 mg; 0.425 mmol) was dissolved in EtOH (100 mL) and graphene was added (100 mg) and stirred under ambient conditions for 2 hours, before filtration *in vacuo*. Washed with acetone and dried in air for 30 minutes. Dry powder collected for analysis.

UV-vis λ_{max} = 331 nm; emission = 413 nm, exc. 290 nm.

3.5.7 Synthesis of Fluorescein-Graphene with Graphene Nano-Platelets

4-aminofluorescein (92 mg; mmol) was dissolved in EtOH (100 mL) and HBF_4 (8 mL) was added to the mixture. Cooled to 0-5 °C and $NaNO_2$ (40 mg; mmol) was added dropwise. The reaction mixture was stirred for a further 2 hours while wrapped in foil. Upon completion, the mixture was divided into centrifuge tubes and centrifuged at 4500 rpm for 30 minutes, supernatant removed. Fresh solvent was added, and the procedure repeated until no yellow-green colour was visible and then one wash with water (15 mL) completed the washing process.

TEM = 0.331 nm and 0.356 nm. UV-vis λ_{max} = 435 nm, 299 nm; emission = 483 nm and 461 nm, exc. 436 nm; BET = 271.36 m^2/g.

3.5.8 Synthesis of Chromone-Graphene with Graphene Nano-Platelets

4-amino-2-methylchromone (82 mg; mmol) was dissolved in EtOH (100 mL) and HBF_4 (8 mL) was added to the mixture. Cooled to 0-5 °C and $NaNO_2$ (40 mg; mmol) was added dropwise. The reaction mixture was stirred for a further 2 hours while wrapped in foil. Upon completion, the mixture was divided into centrifuge tubes and centrifuged at 4500 rpm for 30 minutes, supernatant removed. Fresh solvent was added, and the procedure repeated until no yellow-green colour was visible and then one wash with water (15 mL) completed the washing process.

TEM = 0.397 nm and 0.429 nm. UV-vis λ_{max} = 285 nm; emission = 322 nm and 432 nm, exc. 290 nm; BET = 201.44 m^2/g.

Chapter 4: Study of Physisorption and Photocatalytic Activity

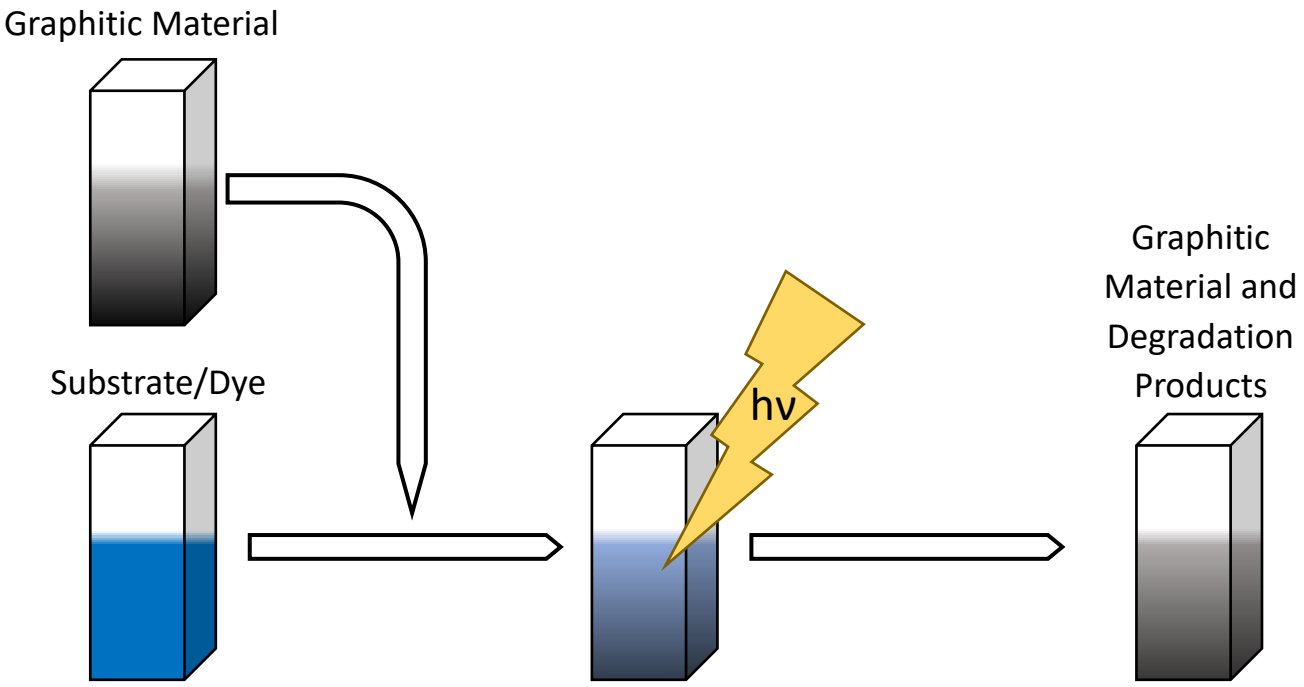

4.1 Abstract

In this chapter, the modified graphene materials were tested for photoactivity using two known wastewater dyes – MB and RhB. By using white light illumination during reactions, Pnz-G and Fsc-G were proven to be photoactive, while Pur-G showed some unexpected photoactivity. Chr-G was capable of dye removal, but the reactivity was not photo-enhanced during illuminated reactions.

During desorption studies and repeated experiments with the use of acidic, neutral, and alkaline conditions, it was proven that MB was irreversibly removed most efficiently by alkaline conditions. However, the removal degree of RhB varied between alkaline and neutral conditions, dependent upon the hybrid sample used.

4.2 Aims

The aim of this chapter was to test the photocatalytic degradation capacity for the hybrids using RhB and MB under several conditions, both with and without white light irradiation.

4.3 Results and discussion

4.3.1 Initial Catalytic Testing

In the initial phases of testing, it was necessary to first establish the correct concentrations of the composites and MB to be suitable for spectrophotometric analysis. The optimal concentration of MB (structure in Figure 76) was set at a 0.3 mg/mL stock concentration with 50 µL aliquots added to the 3 mL of water (1.6 µM), because the MB concentration was not so low that it was immediately consumed by the catalyst, hindering a true monitoring over a time period, and was not too high to obey Lambert-Beer law. To assess the stability of 1.6 µM of MB, the effect of different quantities of acid and alkali was studied upon the MB and MB with Pnz-G solutions.

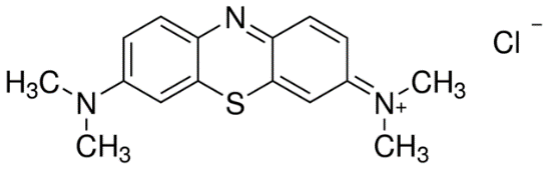

Figure 76: The structure of methylene blue, as described by Sigma Aldrich.

It was determined that 6 µL of 10 % trifluoroacetic acid (TFA) in 3 mL of water should be used for acidic conditions due to the low effect on MB alone and the large effect on Pnz-G with MB (Figure 77). This value was chosen to ensure that the presence of a catalyst is the factor affecting the change in the MB

UV-vis absorbance, while also matching the volume needed to shift the visible light absorption of the Pnz-G UV-vis spectrum. The same was determined for NaOH (1M) at 20 µL in 3 mL of water.

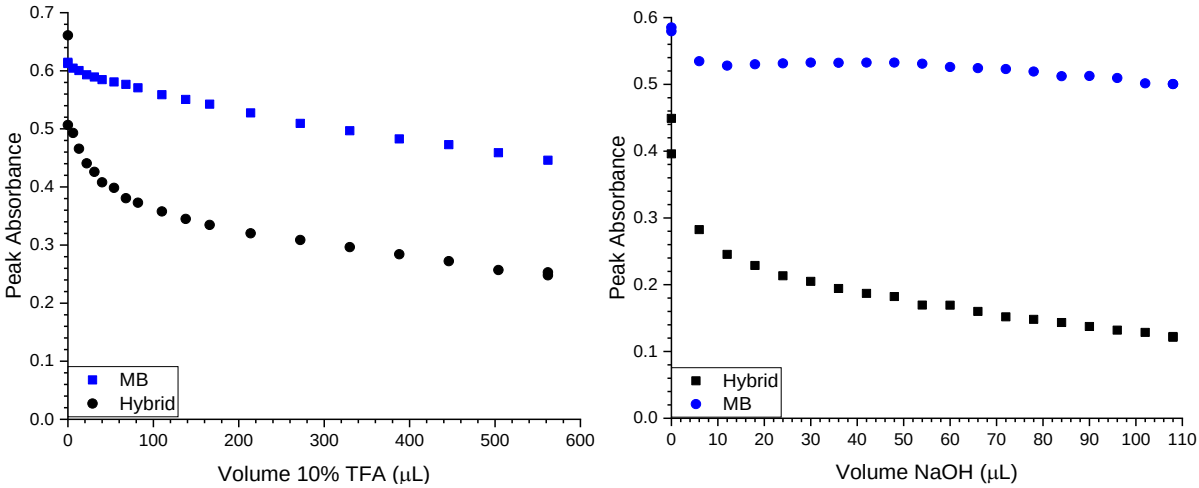

Figure 77: The titrations of 10 % aqueous TFA (left) and 1M NaOH (right) to solutions of MB with and without the presence of Pnz-G.

To understand the degradation behaviour of MB on its own, several tests have been carried out under various conditions such as pH and illumination (dark/light). In the 20-minute time period of the test of MB self-degradation in the different media (Figure 78), no difference between the tests carried out in acidic and neutral media under illuminated and non-illuminated conditions were observed. However, a significant increase in the degradation of MB (12 %) in alkaline medium under illumination was recorded. The low degradation in the dark matches with literature results,[188, 189] and the increased reactivity in alkaline solution has been observed in the literature for both MB and MB with catalysts, where it is believed that the sp^2 nitrogen is not attacked, but an amine substituent of MB is replaced in an oxygenation reaction.[190-192]

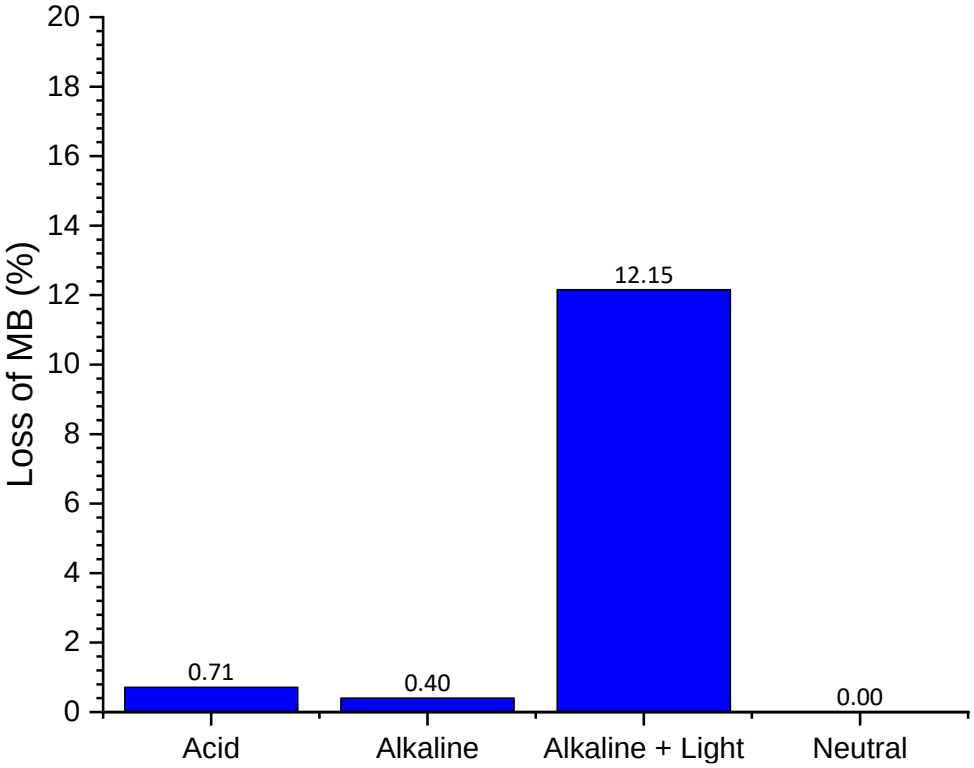

Figure 78: Degradation of MB without catalyst present. Light used was a white light LED station, as described in general methods, Chapter 2.

Next, the ability of non-modified graphene to remove MB was evaluated (Figure 79). The reactions were performed under light conditions at 100 µg quantities of graphene with the standard MB concentration previously described. The reaction was performed for 20 minutes; and no desorption treatment using EtOH after this time was carried out. A MB removal of 30 % and 32 % for neutral and alkaline conditions, respectively was observed. A limited removal of only 15 % was recorded under acidic conditions for MB. It is assumed that the reactivity of graphene is minimal, and the removal is due to adsorption, as shown by studies of MB adsorption to graphene and graphene oxide.[193, 194]

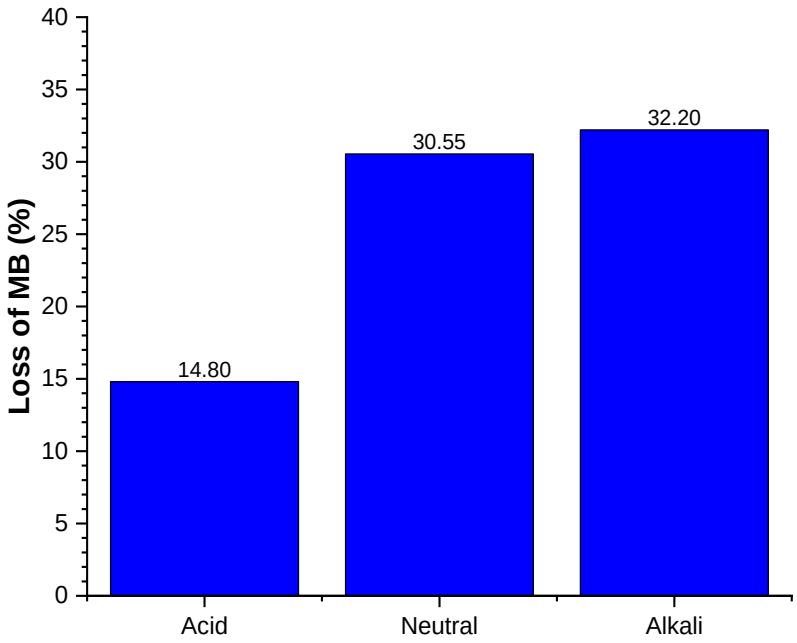

Figure 79: Removal of MB from solution by "pristine" graphene

4.3.2 Mass Loading Studies

In order to easily monitor the rate of any processes occurring, the dye removal test was run in a cuvette (3 mL). This initially created an issue for the method for weighing small quantities of the graphitic material, as quantities beyond a suitable level affected the transparency of the solution and made it difficult to accurately monitor the absorbance changes.

It was decided that the most effective method would be the ultra-sonication of the materials in water to create well dispersed stock solutions of a set 1 mg/mL concentration, allowing the use of volume for the mass of material added. This also required the solution to be sonicated to a fine suspension prior to each use to ensure any assumptions were valid.

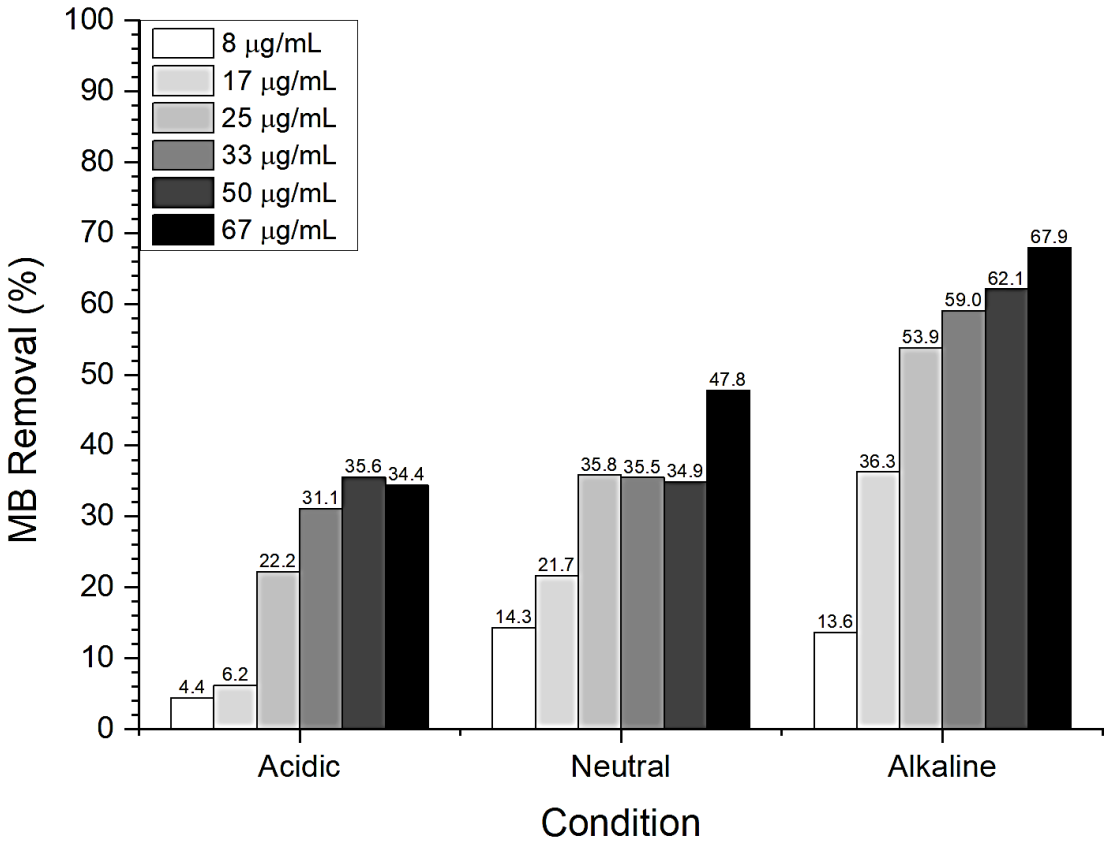

Figure 80: The mass loading studies of Pnz-G with 50 µL MB in solutions of 3 mL over a 20-minute period.

When testing Pnz-G it was found that, as expected, increasing the mass of Pnz-G generally increased the MB removal (Figure 80). The one deviation from the trend is the acidic conditions. Therefore, it was decided that the loading of Pnz-G catalyst would be 67 µg/mL for alkaline and neutral conditions, whilst 50 µL/mL would be used under the acidic conditions because the solution has low transmittance caused by higher aggregation of the graphitic platelets.

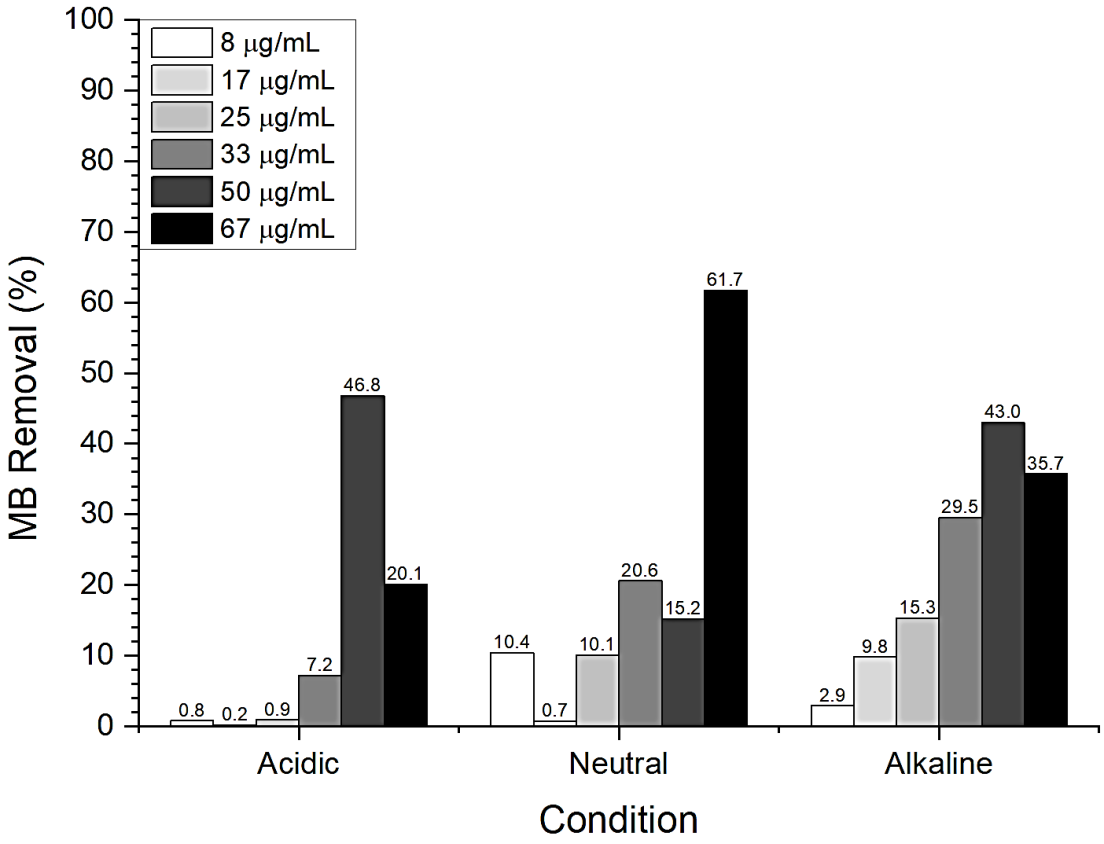

Figure 81: The mass loading studies of Fsc-G with 50 µL MB in solutions of 3 mL over a 20-minute period.

When testing Fsc-G it was found that, as expected, increasing the mass of Fsc-G generally increased the loss of MB, until it dropped after 50 µg/mL (Figure 81). There were slight exceptions again and were attributed to the same affects. The one deviation from the trend is the neutral conditions. Therefore, it was decided that the loading of Fsc-G catalyst would be 67 µg/mL for neutral conditions, whilst the acidic and alkaline conditions would utilise 50 µg/mL.

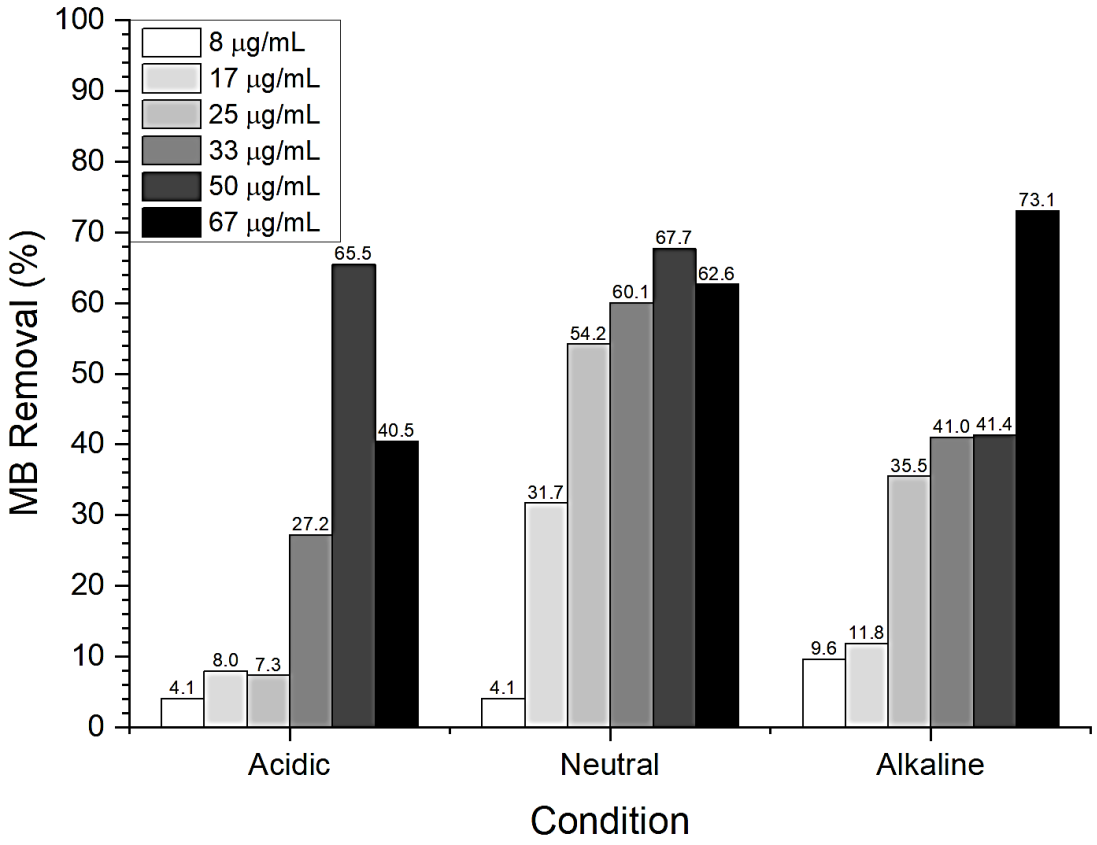

Figure 82: The mass loading studies of Pur-G with 50 µL MB in solutions of 3 mL over a 20-minute period.

When testing Pur-G it was found that it followed a similar trend except with the slightly lower mass of 50 µg/mL being optimal across two conditions (Figure 82). Here, the optimal concentration of Pur-G for acidic and neutral conditions was found to be 50 µg/mL, whilst alkaline conditions required 67 µg/mL concentration.

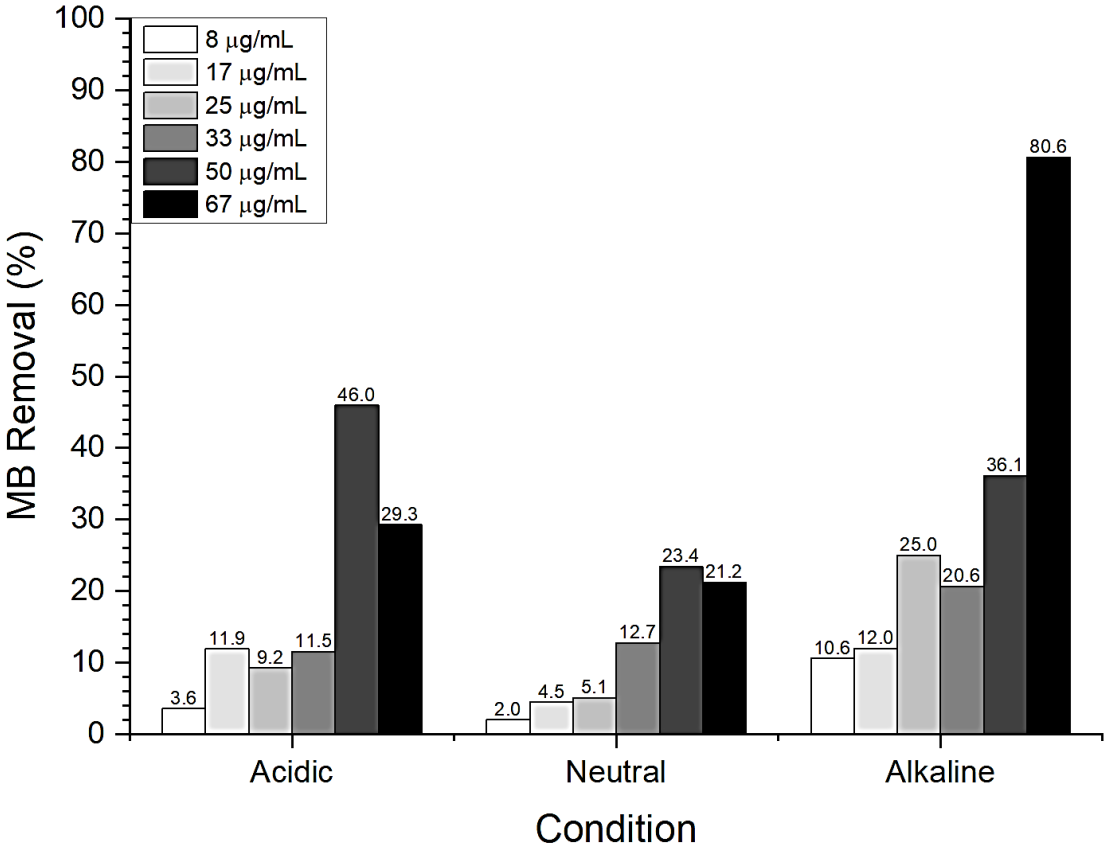

Figure 83: The mass loading studies of Chr-G with 50 µL MB in solutions of 3 mL over a 20-minute period.

When testing Chr-G it was found that it followed a similar trend to Pur-G (Figure 83). For Chr-G, both acidic and neutral conditions required 50 µg/mL, whilst alkaline conditions showed better activity with good transparency at 67 µg/mL.

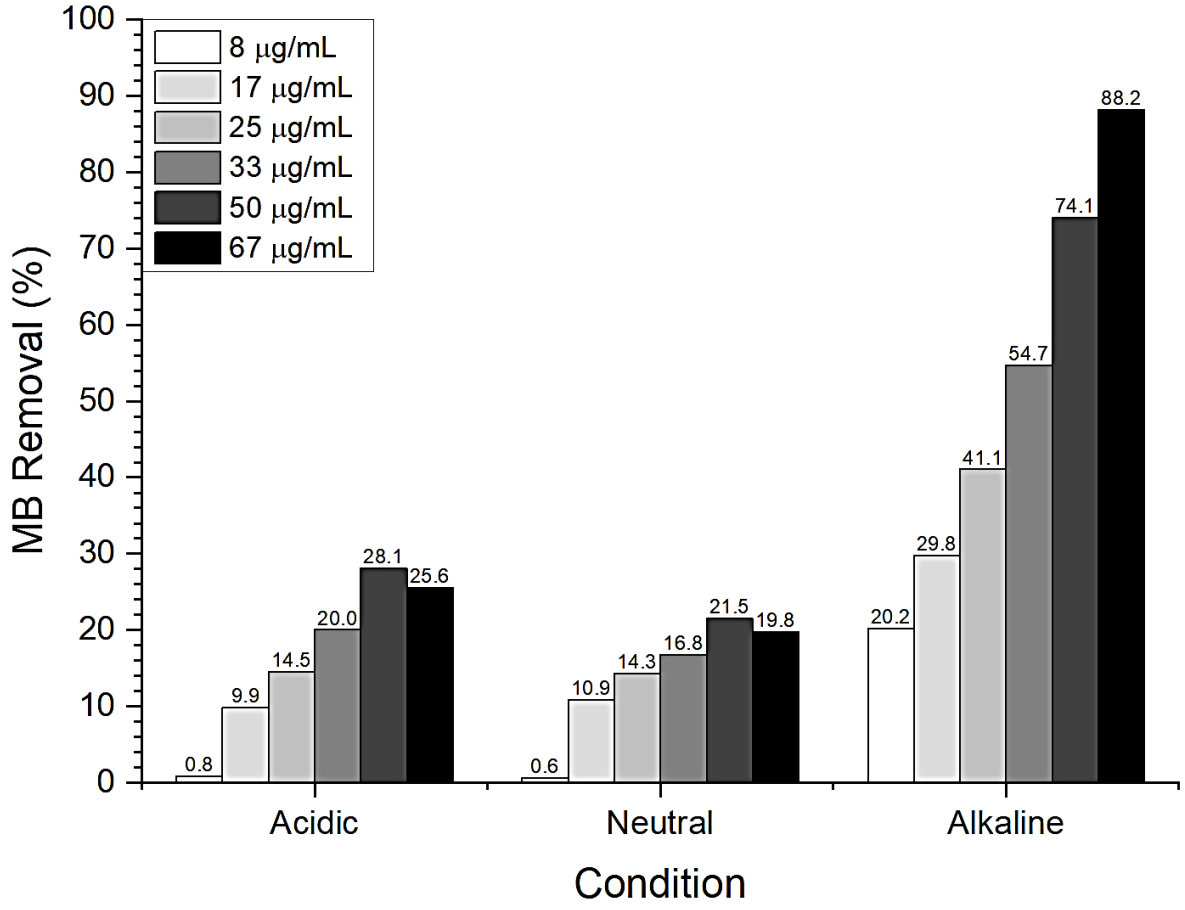

Figure 84: The mass loading studies of Thi-G with 50 µL MB in solutions of 3 mL over a 20-minute period.

For Thi-G, both acidic and neutral conditions preferred 50 µg/mL, with small increases up to 50 µg/mL and both conditions showing a similar removal level and trend (Figure 84). The alkaline conditions showed better activity with good transparency at 67 µg/mL, with a clear increasing trend of MB removal.

4.3.3 Catalysis vs Adsorption

Studies of MB Degradation Over 20 Minutes

Phenazine-Graphene

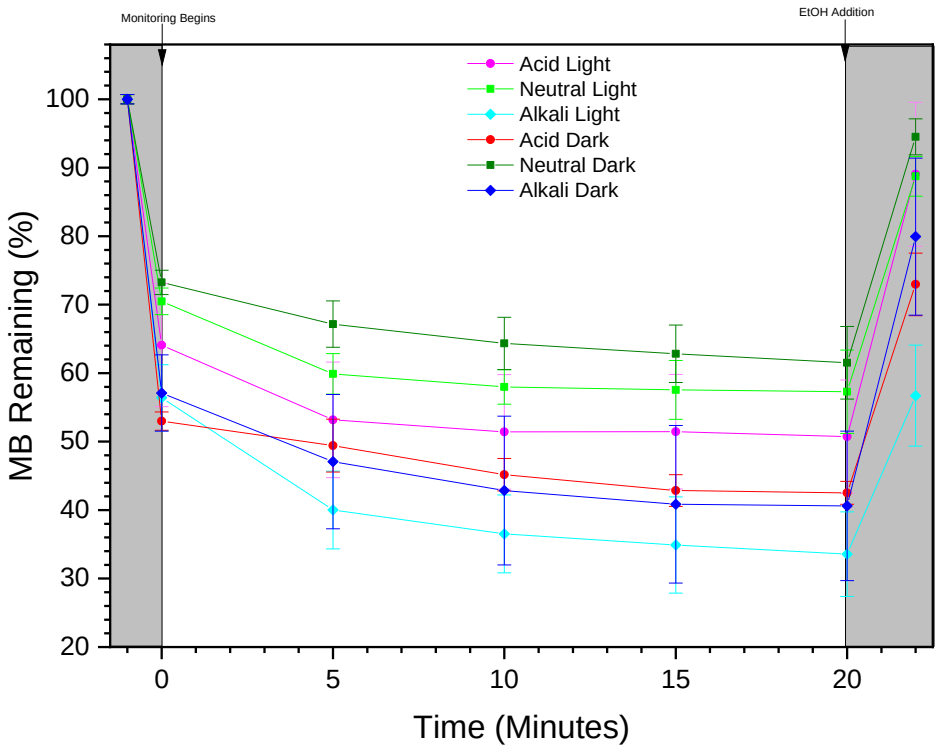

Figure 85: All conditions' kinetics data for the degradation of MB by Pnz-G. Catalyst loading = 67 µg/mL for alkaline and neutral conditions, 50 µg/mL for acidic conditions. MB concentration = 1.6 µM.

From Figure 85, both the light and dark processes for neutral conditions have low reactivity with MB, with a slight preference towards light induced conditions which could be expected with a light absorbing catalyst. The optical band gap of the catalyst could be a reasonable explanation for the acidic condition being the only pH condition that does not favour illumination by white light, as the presence of acid could be resulting in a change in the photoabsorbance properties of the catalyst and needs to be explored. This could also be understood through the generation of excited states of MB^{+}, formed when visible light is absorbed by MB, because it has weak oxidising capabilities which could be limiting the processes involved in this degradation.[69, 130]

The data for MB on its own (Figure 78) shows that the light-induced alkaline reaction is the most effective condition for MB degradation in aqueous solution. Figure 85 also shows that this condition is still the most effective when using Pnz-G as a catalyst. However, the processes slow down rapidly for Pnz-G, potentially due to the low quantity of catalyst and the pores/active sites becoming slowly blocked with reagents and/or products. This blockage can partly be explained by the quantity of MB desorbed from the surface upon the addition of ethanol, as quantities of MB are sticking to the surface during the process and suggests that adsorption is a more rapid process within the reaction being observed. This can be observed under all conditions undertaken in this part of the study.

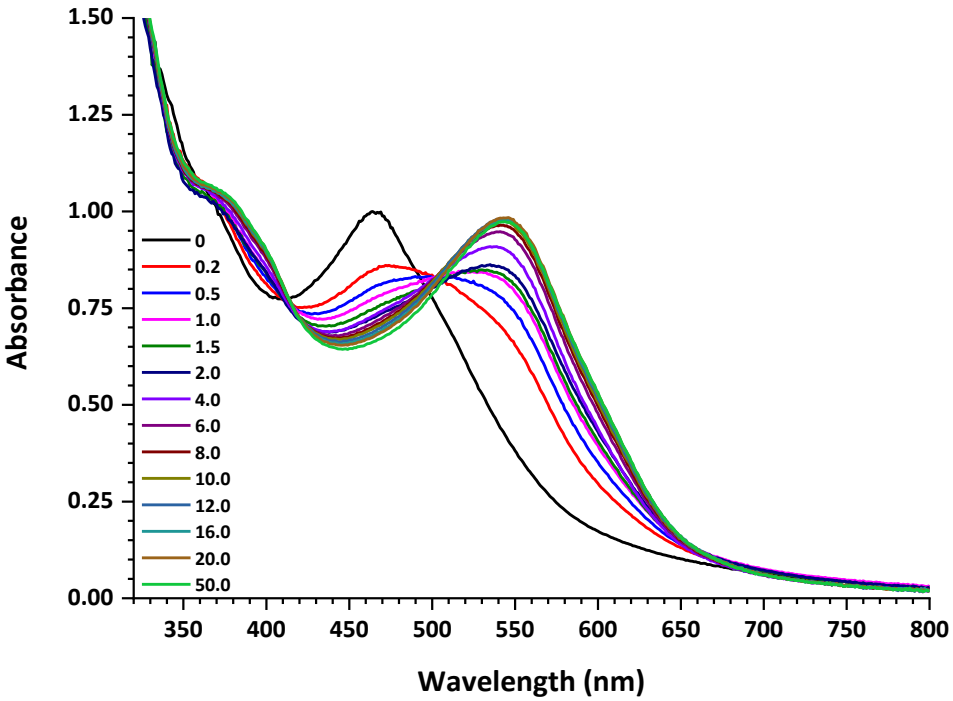

Figure 86: The shifting UV-vis spectrum of Pnz-G under acidic additions.

What is surprising is the negative effect of light on acidic conditions. However, when the acidic UV-vis spectrum was collected for Pnz-G (Figure 86) it showed a bathochromic shift. This would shift closer to the absorption of MB and may create an incompatibility in their energy levels for interaction, thereby hindering the reactivity of the catalyst with MB. Alternately, it may reduce how much light the catalyst is able to absorb for its photoactivated reactivity.

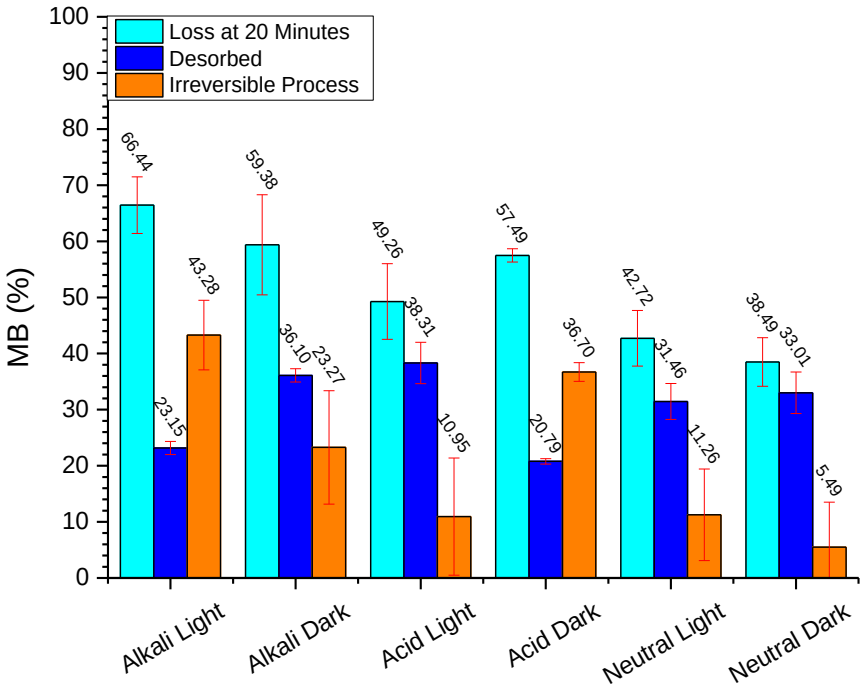

Figure 87: The testing of multiple conditions of MB reactivity with Pnz-G. Catalyst loading = 67 µg/mL for alkaline and neutral conditions, 50 µg/mL for acidic conditions. MB concentration = 1.6 µM.

Figure 87 shows how each condition removes MB from solution and what quantity is removed irreversibly, which is assumed to be caused by a degradation of MB. From the data collected in Figure 85 and Figure 87, alkaline conditions have the best total removal and irreversible removal within 20 minutes. This would be expected from Figure 78, since it is shown that MB has a higher degradation in alkaline solution. The best removal conditions in neutral and alkaline media are achieved under illumination with light. In contrast, the MB removal is more efficient in the dark when acidic conditions are used. From Figure 87, it can be concluded that alkali medium is most efficient, followed by acidic and neutral is least preferable.

One downside to the alkaline conditions for Pnz-G is the larger error within the dataset, which could suggest some catalyst instability under these conditions. However, despite these increased errors, alkaline conditions still prove to be the most effective.

When compared to TiO_2 in the literature, Pnz-G acts slightly less effectively for total removal from solution, but whilst using a significantly lower quantity of 67 µg/ml vs 0.5-2.5 mg/ml of TiO_2 in the literature.[116] This could show that Pnz-G is a better photocatalyst than TiO_2 for each of the conditions studied. However, using the same quantity was less feasible with the project's setup and limits the direct comparison with TiO_2.[116, 118] Pnz-G also reacts with MB at a much slower rate than a TiO_2 / graphene oxide composite that has been reported, according to neutral conditions reactions. So, although Pnz-G has seemingly made some improvements compared to TiO_2, it has not done so against some of the TiO_2 composites when under neutral conditions.[123]

Fluorescein-Graphene

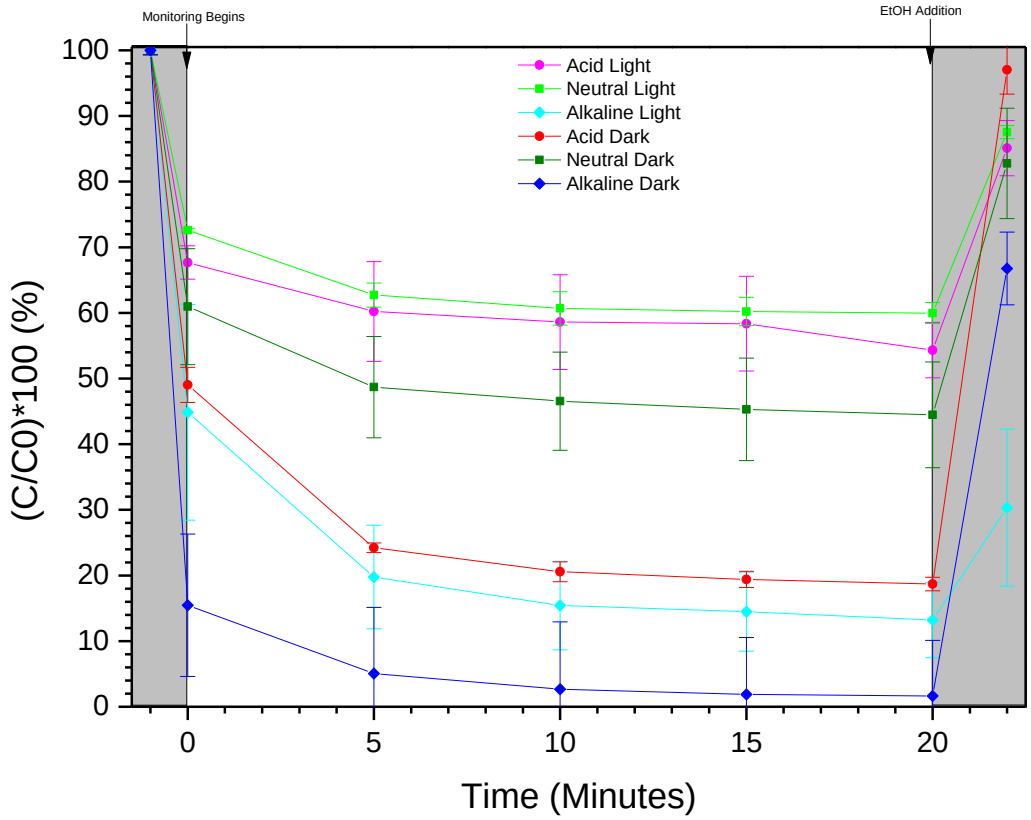

Figure 88: All conditions' kinetics data for the degradation of MB by Fsc-G. Catalyst loading = 67 µg/mL for neutral conditions, 50 µg/mL for alkaline and acidic conditions. MB concentration = 1.6 µM.

For Fsc-G kinetics (Figure 88), the adsorption rate for unilluminated alkaline conditions is very rapid, whilst the illuminated alkaline conditions have a slower adsorption rate, similar to that of the dark acidic conditions. It was also noted that the acidic and neutral conditions were the only ones to perform better in the dark, with a much lower adsorption and removal rate in the light. The reason for this could be the effects of illumination on both Fsc-G and MB resulting in an incompatibility for photocatalysis or for adsorption.

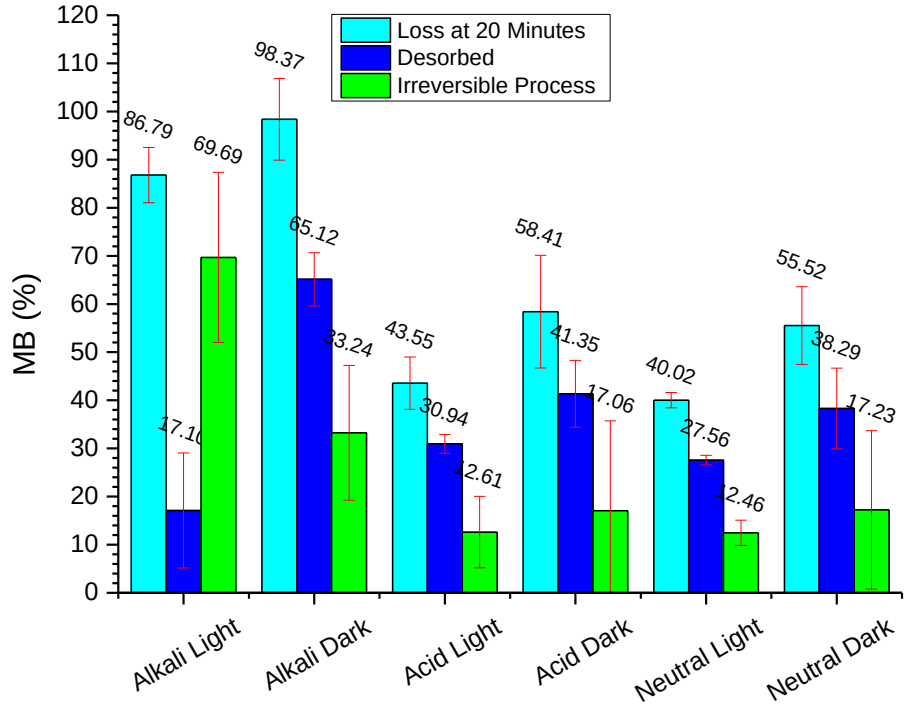

Figure 89: The testing of multiple conditions of MB reactivity with Fsc-G. Catalyst loading = 67 µg/mL for neutral conditions, 50 µg/mL for alkaline and acidic conditions. MB concentration = 1.6 µM.

The data in Figure 89 shows that Fsc-G displays an excellent ability to remove MB in the dark acidic conditions as well as in both alkaline conditions. Based on the results of the desorption tests carried out at the end of each experiment, the photocatalytic process is a key process in the degradation of MB under the white light illuminated alkaline conditions. Meanwhile the dark alkaline and dark acidic reactions both desorb a large proportion of the removed MB, suggesting little reactivity occurs under these conditions.

The data also suggests that the acidic and neutral conditions all have similar degradations, according to the data obtained during desorption tests. This could suggest that the effects of acidity seen in the case of Pnz-G have less effect on Fsc-G. This is most likely due to there being no change in the absorbance maximum for fluorescein dye between the cationic and neutral tautomers according to the literature.[195] Also a lack of light-initiated activity is observed in acidic and neutral conditions and can be explained by the fluorescein dye subunit. This is due to the increased light absorbance of fluorescein under basic conditions compared to neutral and milder acidic pH in aqueous media.[195, 196]

Compared to Pnz-G, Fsc-G shows much greater adsorption and degradation under the most optimal conditions. However, there is a larger error in the results for Fsc-G. These errors could be due to rapid processes being influenced increasingly by modification percentages, size of nanoplatelets and their stack numbers, resulting in multiple removal pathways of MB taking place in some kinetics plots.

When compared to the literature, the removal of MB shows a similar trend for the effect of pH as seen with TiO_2.[116] When considering the activity, the mass of catalyst used is much lower, and the MB concentration by a similar ratio. What can be seen is that the loss of MB shows a similar trend with rapid initial loss that plateaus near the end. In 20 minutes the rate is similar for the hybrid and TiO_2, but for neutral and acidic, the rate is reduced.[116] Compared to a TiO_2/GO nanocomposite, the removal of MB by Fsc-G is much slower in neutral conditions, while using similar concentrations of MB and a higher concentration of catalyst than used in our study.[123]

Purine-Graphene Kinetics

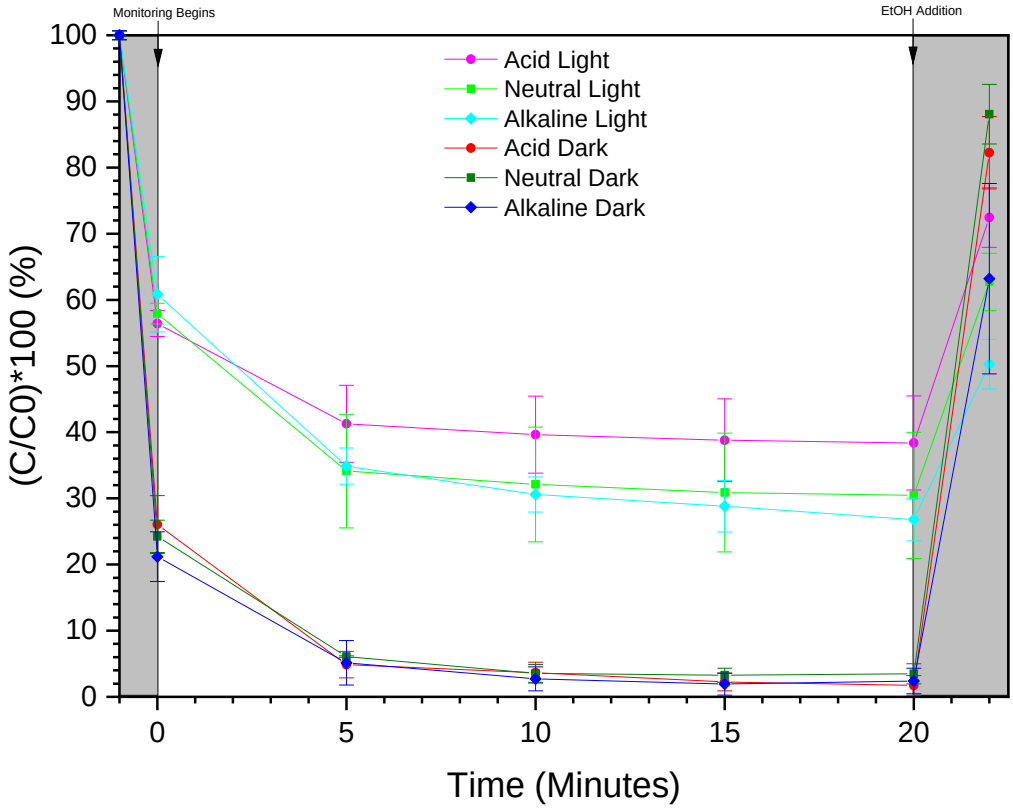

Figure 90: All conditions' kinetics data for the degradation of MB by Pur-G. Catalyst loading = 50 µg/mL for neutral and acidic conditions, 67 µg/mL for alkaline conditions. MB concentration = 1.6 µM.

The kinetics plot of Pur-G reacting with MB for 20 minutes (shown in Figure 90) suggests that the dark conditions are all excellent filters for MB. They each rapidly reach over 90 % removal of MB from solution; however, the desorption experiments show low reactivity for all but alkaline conditions. This is by no means a failure, as this process of dye removal can be used in filtration methods in wastewater treatment.

On the other hand, under the light conditions the hybrid material is a less effective adsorption filter, reaching only 60-75 % of MB removal. What they lack in adsorption, they make up for in catalytic

degradation, as each illuminated condition is an improved photocatalyst. This matches with the data seen for TiO_2 with MB and can shed some light on the mechanism of this reactivity.[116-118]

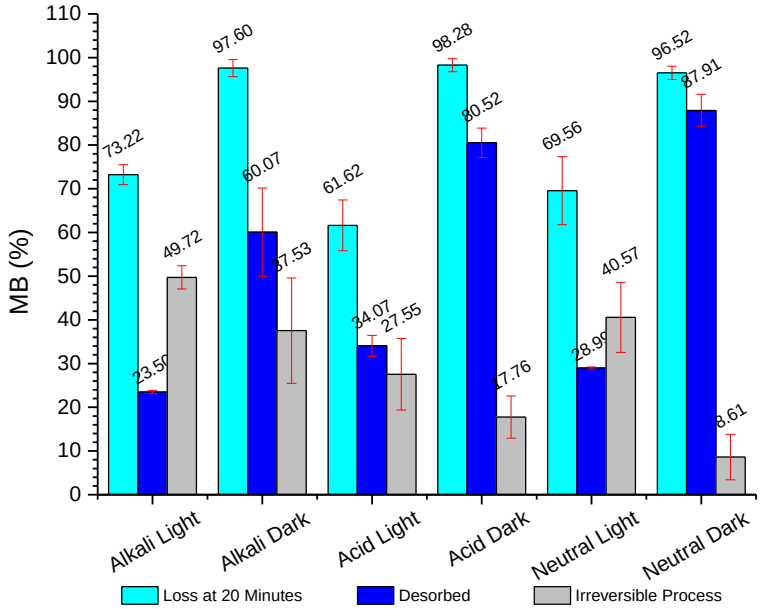

Figure 91: The testing of multiple conditions of MB reactivity with Pur-G. Catalyst loading = 50 µg/mL for neutral and acidic conditions, 67 µg/mL for alkaline conditions. MB concentration = 1.6 µM.

Pur-G gave surprising results, as it showed a generally improved reactivity under light illuminated conditions (seen in Figure 91). This increased irreversibility is more prevalent in neutral conditions and less so in acidic media. However, this should not be the case due to the lack of visible light absorbance in Pur-G, meaning that the only way light could be inducing an irreversible reaction is an effect from MB excitation.

Once again, alkaline media is the optimal conditions for the removal of MB with neutral being the second most optimal. One thing of interest to note, is that Pur-G becomes a very effective filter under all dark conditions, suggesting that a process occurring on the surface when illuminated is hindering the adsorption of MB or photoexcited MB. A positive note for Pur-G is the much smaller errors for the optimal system of illuminated alkaline conditions, though there is some overlap with the dark alkaline conditions for irreversible removal. Despite this, the illuminated sample appears to be better at MB degradation with greater reliability.

For total removal of MB under dark conditions, Pur-G is faster and more efficient than TiO_2, however the catalytic process is slower than TiO_2 under all conditions. Under illuminated conditions, the removal is improved under acidic conditions but is much less effective under neutral and alkaline conditions compared to TiO_2. The degradation percentage is much lower than that reported for TiO_2 under all conditions, whilst following a similar trend of increased degradation as pH increases.[116-118]

Compared to a TiO_2/GO nanocomposite, Pur-G removes MB from solution at an increased rate under dark conditions, but when illuminated the rate reduces to being close to that reported in the literature for TiO_2/GO.[123]

Chromone-Graphene Kinetics

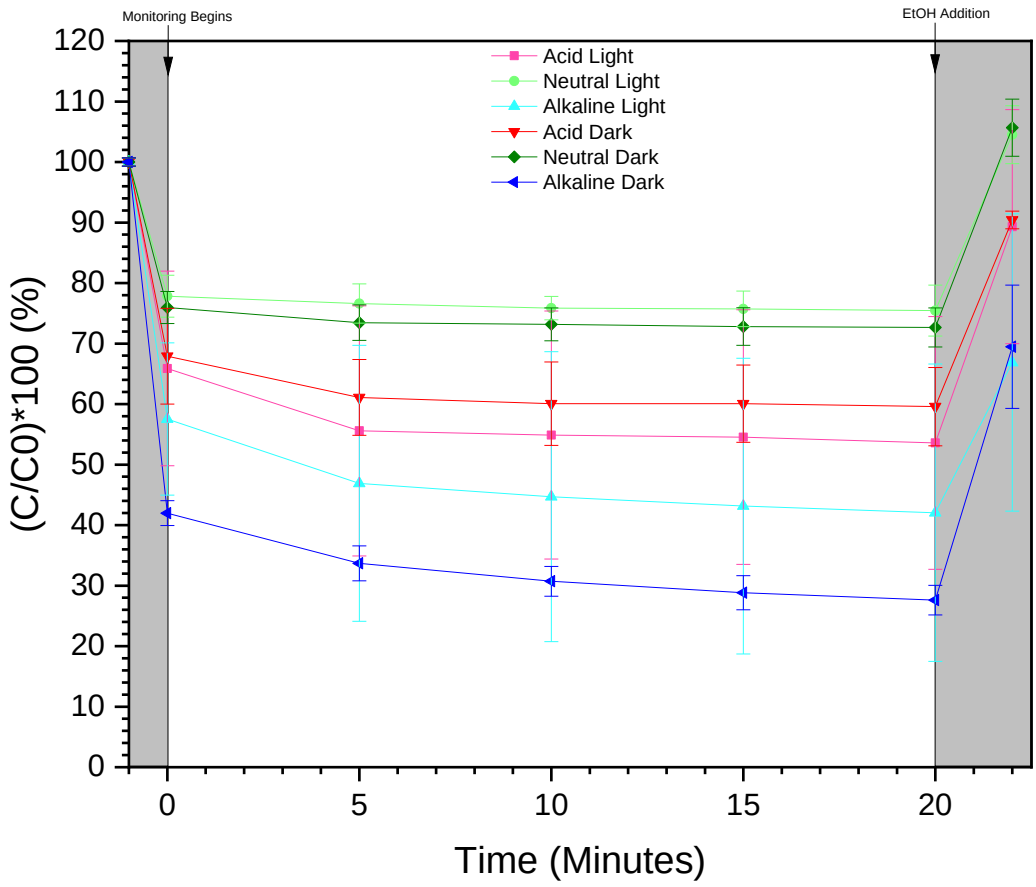

Figure 92: All conditions' kinetics data for the degradation of MB by Chr-G. Catalyst loading = 50 µg/mL for neutral and acidic conditions, 67 µg/mL for alkaline conditions. MB concentration = 1.6 µM.

Chr-G is seen to be among the least effective catalysts of those tested, as shown in Figure 92. The use of light illumination has no effect on degradation at any pH condition, so it cannot be deemed a photocatalyst. In acidic conditions, only 10 % of MB is degraded and 40 % of MB is removed from the solution. In neutral conditions, no catalytic degradation takes place and only 20 % of MB removal is detected. Alkaline conditions show 70 % of MB removal under no illumination, and 35 % degradation with or without illumination. This suggests chromone as a possible filtration material for wastewater mediation, but its catalytic activity is generally poor, compared to the other hybrids.

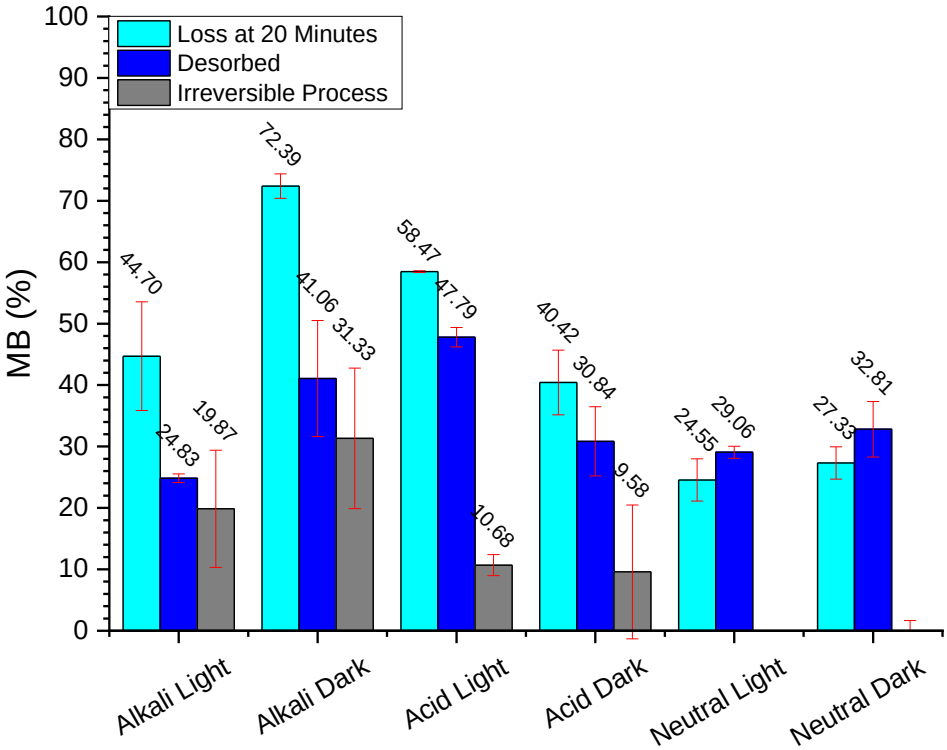

Figure 93: The testing of multiple conditions of MB reactivity with Chr-G. Catalyst loading = 50 µg/mL for neutral and acidic conditions, 67 µg/mL for alkaline conditions. MB concentration = 1.6 µM.

Chr-G showed a lack of activity in neutral conditions (Figure 93). A reason for this could be poor interactions between the chromone subunit and MB, resulting in a lack of irreversible chemical reactivity. Another reason could be that there is no light absorption to create an optical band gap with which to excite and undergo reactions to form any reactive species.[3, 7]

In acidic conditions the activity of the hybrid was low, but it was present with high variability in the dark. This could be due to light absorption by MB in illuminated conditions allowing more efficient MB removal through the degradation of the excited state, MB^+. In alkaline conditions, the reactivity was increased twofold to threefold from acidic conditions, with an increase in degradation from MB in solution without catalyst.

Chr-G has much lower rates than those reported for TiO_2 and TiO_2/GO nanocomposite and does not follow the usually reported trend of increased pH resulting in increased reactivity, due to neutral conditions showing no activity.[116-118]

Thionine-Graphene

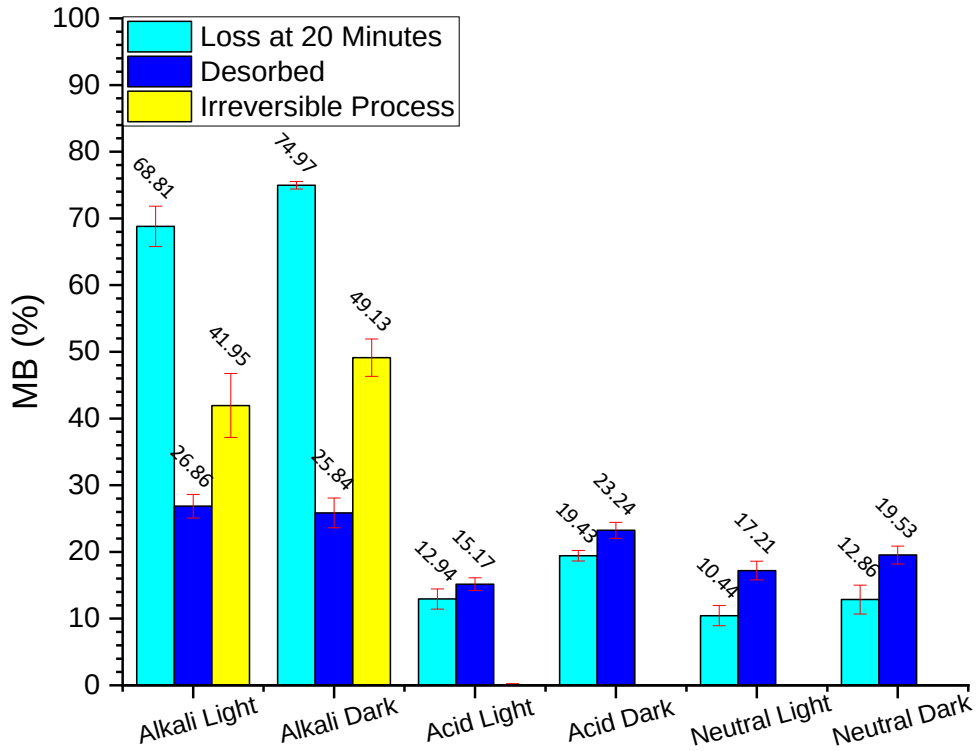

Figure 94: The testing of multiple conditions of MB reactivity with Thi-G. Catalyst loading = 50 µg/mL for neutral and acidic conditions, 67 µg/mL for alkaline conditions. MB concentration = 1.6 µM.

Unfortunately, it was found that Thi-G had no activity in neutral or acidic conditions (Figure 94), whilst having good activity in alkaline conditions. In the alkaline medium, it was found that the activity did not have a significant difference if light was used. This suggests that it is not a photocatalyst and may also suggest that it is only amplifying the activity of hydroxide degradation of MB via acting as a surface to bring the two reagents into close contact.

In some data sets, it seems that the desorbed levels of MB are higher than the adsorbed levels which are due to errors in the repeated experiments attributed to MB stock solutions or the differences in the catalyst that were used.

It can be postulated that the low visible light absorption of Thi-G could explain the lack of photoactivity and that it does not have suitable redox chemistry to act as a carbocatalyst to MB degradation outside of alkaline conditions.

No kinetics were recorded here due to a lack of reactivity and the alkaline conditions deemed to be mainly an effect of MB reacting with hydroxide on the heterogenous surface.

Thi-G is also much less effective than both TiO_2 and TiO_2 / GO by a large percentage, showing that it is in no way an improvement upon literature of TiO_2. It also shows an increased rate at higher pH as

seen in the literature though this could be due to MB's natural degradation in alkali being enhanced by the surface due to neutral and acidic being unreactive with similar absorbance.[116-118, 123]

Adsorption and Reuse Studies

Further studies were required to test the adsorption capacity and actual reactivity on the surface of the graphitic materials. Since the data for 2-hr kinetics shows a period in the first 20 minutes that involves adsorption as the main process for the MB removal (discussed later herein), it was decided to use this time period for desorption and adsorption kinetics study.

Adsorption Calibrations

With large surface area materials, a key factor is physisorption onto the surface. If this is not monitored, analysed, or accounted for, it cannot be made certain if catalysis or filtration is occurring. Such implications have been seen with GO mixed with MB, where the solid material became blue and left a colourless solution after adsorption, due to adsorption onto the surface via strong π-stacking interactions.[193, 197]

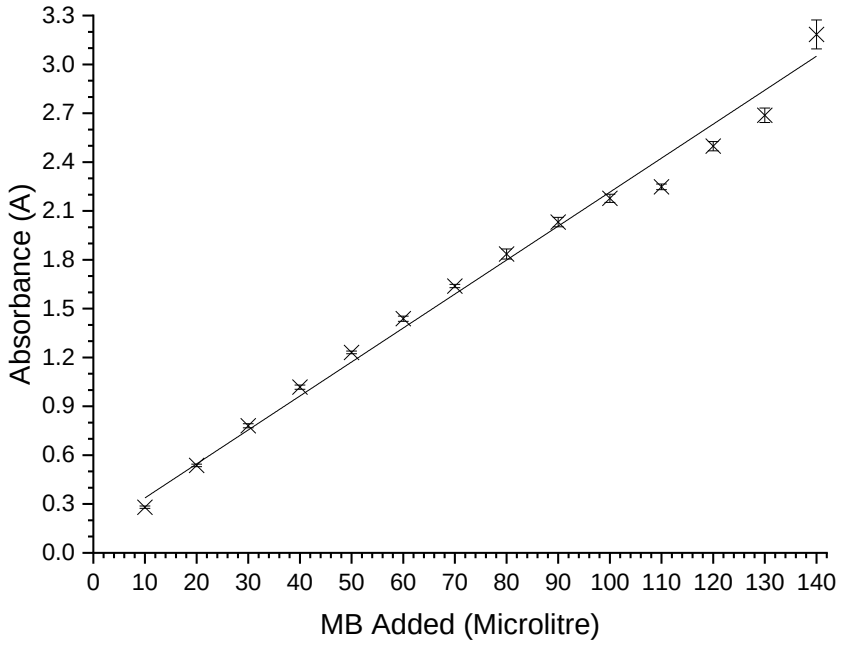

Figure 95: The calibration curve of MB from 10 µL to 140 µL addition.

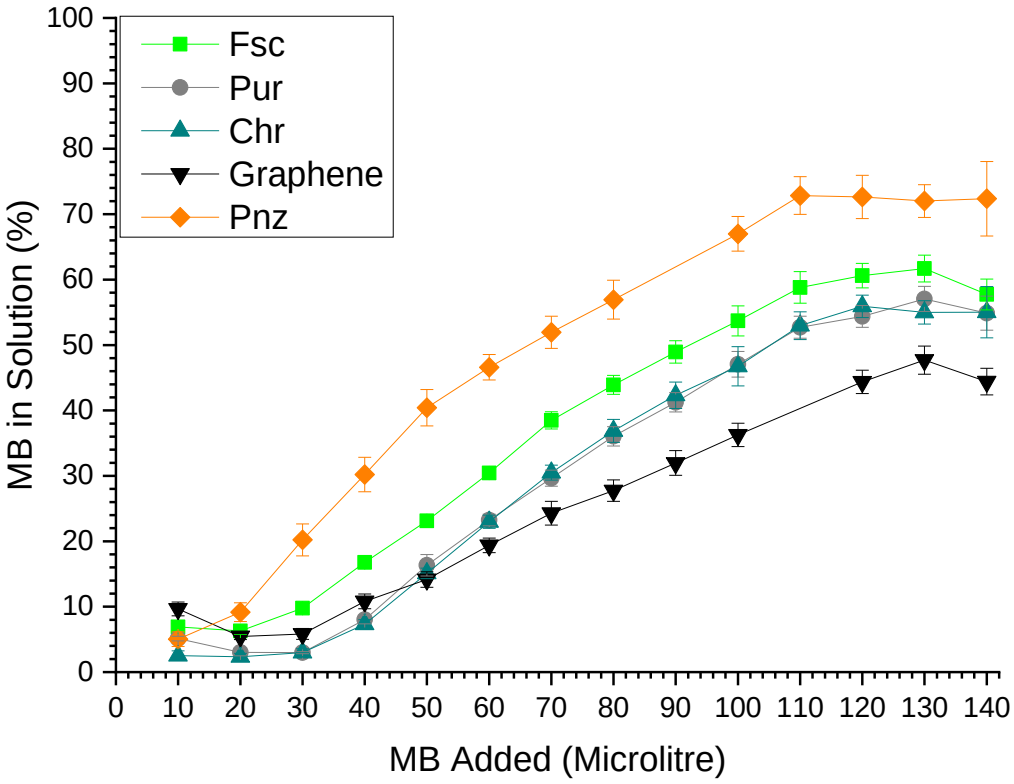

Figure 96: The percentage of MB in solution following portion additions to hybrids. Taken vs a calibration of identical additions. Catalyst loadings were as per previous neutral testing conditions.

As expected, graphene shows a very good adsorption of MB onto its surface, with a nearly linear fitting of the main dataset. It was found that graphene can adsorb MB to its surface up to the addition of 30 µL where the linear increase begins until 130 µL, where the final percentage point drops compared to the previous results. This could in fact be due to dimer formation in solution, which has been described in literature.[115] This is due to the concentration reaching 3.4×10^{-5} M, which according to the literature is in the range of 1×10^{-5} M and 1×10^{-4} M where dimer formation begins. This explains why the absorbance begins to plateau from here, as the peak monitored would remain the same and a second peak would begin to form at a higher wavelength.[115]

The hybrids show a similar trend to what has been seen in graphene. The trend also matches the trends seen in BET, as graphene has the largest surface area along with the most effective MB adsorption, Pnz-G has the lowest surface area and the worst adsorption for MB. Chr-G and Pur-G have similar surface areas where Pur-G has a slightly larger surface area and could be linked to the marginally lower MB concentration in solution at some data points. The break in the trend is Fsc-G, which has the largest surface area of the hybrids, but is the second worst adsorber of MB, which could suggest that the fluorescein moiety is blocking MB from adsorbing to the surface through its larger size compared to the other moieties studied.

Pnz-G shows the lowest absorbance of MB, with higher percentages of MB in solution than any other hybrid and reaching a maximum of 74 % at 110 µL. The data at 50 µL matches with previous 20 minutes dark alkaline kinetics data for the percentage of MB left in solution at the end of reaction. Additionally, as Pnz-G has the lowest BET and Langmuir surface area, this result would be expected as there is a smaller area to adsorb a of MB layer onto.

With Pnz-G, the capacity appears to only be 10 µL of MB before the blue colour gradually becomes more prominent and plateaus at 110 µL. The percentage of the added volume that is adsorbed then remains equivalent.

Fsc-G shows adsorption of 20 µL before reaching a peak of blue absorbance at 130 µL of MB added. The absorbance then decreases which could be due to a bilayer forming on the heterogeneous surface. In the case of Fsc-G hybrid, it shows a better adsorption capability of MB than Pnz-G but much worse than graphene, which is expected when compared the BET and Langmuir surface areas are compared in these materials.

Pur-G and Chr-G are the two examples of colourless UV absorbing dyes. Pur-G and Chr-G are both virtually identical in that they show very little of the blue colour until 30-40 µL of MB added and then the MB absorbance increases linearly until the dimer formation creates a plateau. This is likely an effect of the dye size attached to the graphene surface, given that the molecular coverage is expected to be below 20 % based on the literature and the dye size now has the greatest control over the availability of the graphene surface. Graphene with its much larger surface area has the greatest adsorption while Pnz-G with one of the larger dye molecules modified onto the surface (along with the lowest surface area measurements of the samples) has the lowest adsorption. It gives an insight of how the size and composition of the molecules can affect adsorption to the surface as well as providing some evidence that these materials are not the same as one another.

It also tells us that at the concentration of 50 µL added there should be detectible levels of MB in solution and no hybrid should show 100 % loss within a short duration, as seen in the kinetics plots.

2 hr Kinetics with Methylene Blue Solution

To gain a better understanding of the MB removal process, 2 hr tests have been carried out using a 1.6 µM solution of MB. For these tests, only the hybrids showing light activity and efficient dye removal were chosen. Pur-G was not studied here due to its unusual light activity which needed further understanding.

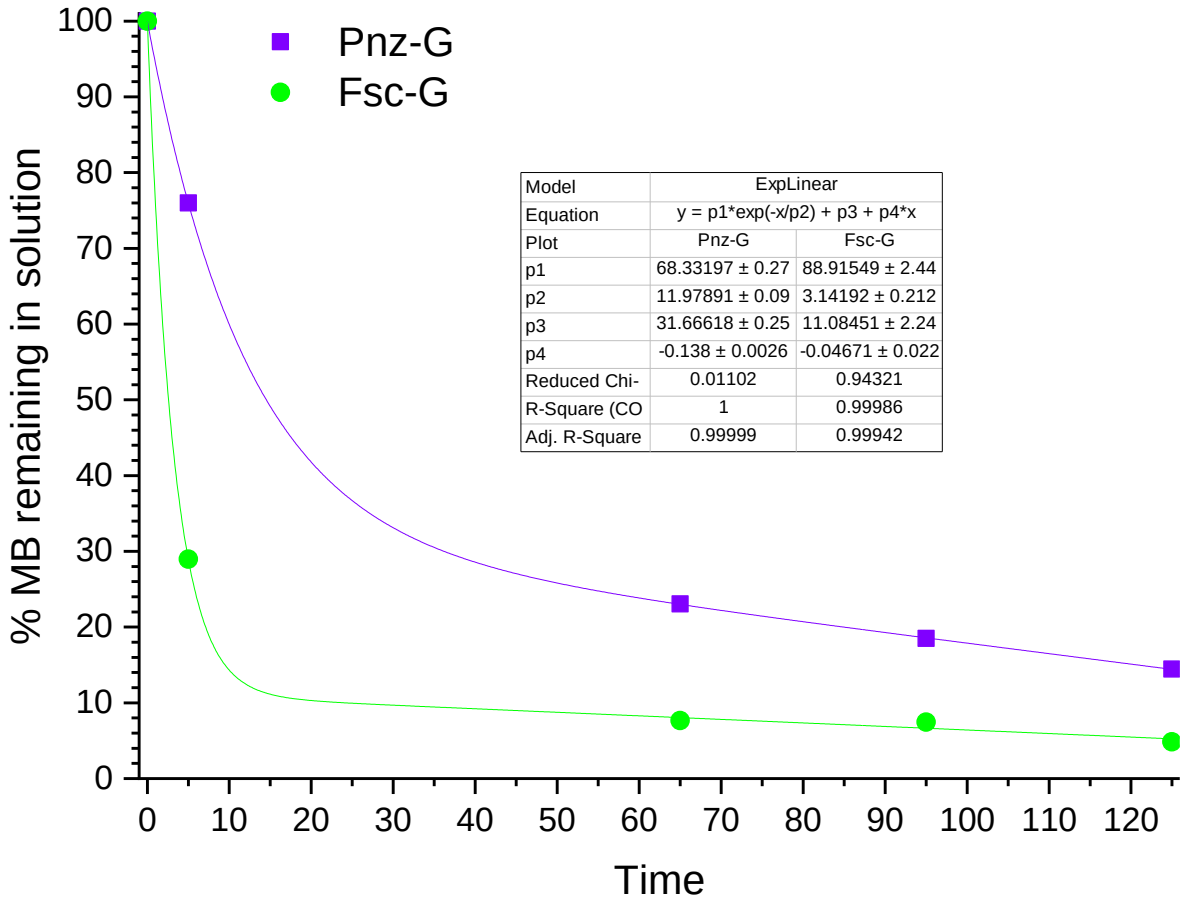

Model	ExpLinear	
Equation	y = p1*exp(-x/p2) + p3 + p4*x	
Plot	Pnz-G	Fsc-G
p1	68.33197 ± 0.27	88.91549 ± 2.44
p2	11.97891 ± 0.09	3.14192 ± 0.212
p3	31.66618 ± 0.25	11.08451 ± 2.24
p4	-0.138 ± 0.0026	-0.04671 ± 0.022
Reduced Chi-	0.01102	0.94321
R-Square (CO	1	0.99986
Adj. R-Square	0.99999	0.99942

Figure 97: The 2 hr kinetics for Fsc-G and Pur-G reactivity towards MB in alkaline media.

In the reaction studied over a two-hour period under illumination in alkaline media (Figure 97), Pnz-G showed a similar behaviour towards MB, moreover, Pnz-G is now able to reach 90 % dye removal in contrast to 66 % in the 20-minute test. It is also noticeable, that Fsc-G is a more optimal candidate for MB wastewater treatment due to a much faster and higher reactivity.

The plotted data can be fitted using exponential function, which appears to be due to a pseudo-second order nature of the degradation of MB by the hybrids.[198] In this plot, the adjusted R-square and R-square are close to 1 and tell us the fit is well matched, which is based upon the regression of the data. However, while Fsc-G has a very good chi-squared value, Pnz-G has a value far below 1, suggesting potential over-parametrisation of this fit, which is a slight contradiction of the prior statement. This may be part of the complexity and uncertainty of this reaction, as there is both a degradation reaction and adsorption taking place, creating a complex pseudo second order curve similar to those seen in literature of adsorption of various wastewater effluents, *e.g.* Congo red, RhB, fluoride, and Acid Blue, using a range of sorbents *e.g.* iron/chromium hydroxide, silica, fly ash, and chitin.[198, 199] This suggests a different contribution of each individual process, e.g. physisorption and catalytic degradation, on the overall MB removal when using these individual hybrids. An attempt

was made to use first order decay curves, however this showed an extreme under-parametrisation of Pnz-G and a minor under-parametrisation of Fsc-G.

From the plot (Figure 97), Fsc-G has such a rapid adsorption and subsequent processes in the first hour that there appears to be very little occurring within the linear portion (supported by the linear coefficient, P4, of only -0.047), with Pnz-G having a slower exponential process. Meanwhile, Pnz-G is still undergoing some processes after this fast, initial phase and it is a process slightly faster than that in Fsc-G, due to the P4 being -0.138.

P1 and P4 are the two being compared most due to P1 being the exponential coefficient and P4 being the linear coefficient, when referring to the equation shown by the table insert of Figure 97.

In both cases, the MB removal is completed after 65 min with a very little change observed at 120 min point. As the data fits well and the theory behind the plot type fits the proposed mechanism of reactivity, we can assume that the period of time is excessive. However, this does mean that when undertaking cycling reactions, this time period would be sufficient to degrade MB and have the catalyst prepared for a fresh addition of MB. However, it would be preferable to have data taken at times between 10 and 65 minutes if they were to be redone, alongside several repeats to ensure the data's reliability as this was mainly a preliminary study for reaction cycles.

Reaction Cycles using 0.8 µM Methylene Blue Solution

In this reaction, the concentration of MB in solution was monitored over time using UV-vis spectroscopy on a reactions performed in a cuvette. Both Pnz-G and Fsc-G were used in separate reactions and at the end of each 2 hour cycle, the initial concentration of MB was re-introduced. Using the data in the previous catalytic chapters and the data in Figure 96, an addition of 25 µL stock MB solution (0.8 µM in 3 mL cuvette) was determined as a suitable volume.

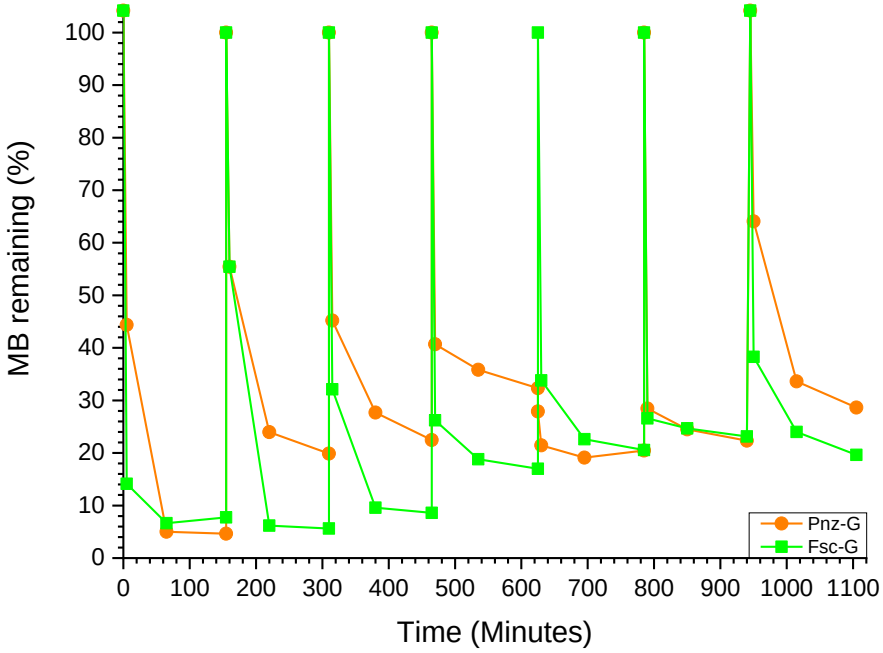

Figure 98: Reaction cycles for Pnz-G and Fsc-G when reacted with 25 µL of MB stock.

In Figure 98, Pnz-G shows 94-96 % removal of MB for only one cycle. It then maintains a similar removal for the following additions at ~80 % of MB. This shows that the graphitic material can be used repeatedly in light without breaking down over several uses. Additionally, this goes beyond the maximum MB adsorption in the adsorption study (Figure 96), suggesting that we have more than just a molecular sponge that can selectively adsorb MB. Values for remaining MB of over 100 % represent where the addition of fresh MB led to slightly increased MB concentration compared to the initial run.

The disadvantage of this experiment is that after a strong wash and extraction (post cycle 5 prior to cycle 6), Pnz-G loses some of the original degradation character and remains at approximately 70-75 % degradation of MB. This can be partly explained by the losses of the material during recollection (graphitic materials can easily adsorb to glass and plastic) as well as some possible irreversible damage to the dye attached to the surface or some irremovable side products acting as a catalytic poison.

Graphene-fluorescein however has three cycles of greater than 90 % degradation of the MB solution added. This shows a much stronger MB removal capability for Fsc-G. With the percentage removal of MB once again going beyond those shown for adsorption in Figure 96, it suggests the characteristics are more degradation based than adsorption. Also, the same disadvantage is found as in Pnz-G, however, the degradation after washing still maintains at ~80 %.

To show that the results of repeated cycles were not due to adsorbing MB as in Figure 96 on each cycle, washings were not performed until cycle 6.

4.3.4 Rhodamine B

The conditions used for the removal of RhB (Figure 99) were matched to those with MB, including the use of 50 µL of a 0.3 mg/mL (1.1 µM) stock of RhB in deionised water for the degradation kinetics. Acidic and alkaline solutions were set up in the ways described for MB and the quantity of catalyst used was taken from the optimal found in the MB degradation studies.

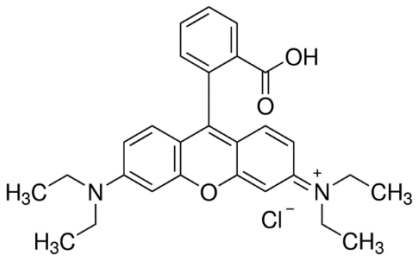

Figure 99: The structure of Rhodamine B, as described by Sigma Aldrich.

It was assumed that RhB would interact with graphene in the same way as MB, due to both being cationic dyes and graphene is an inert surface without modification or extreme conditions. In addition, literature shows the use of a Rhodamine dye with graphene as a photogate, also suggesting the lack of reactivity between this dye group and graphene.[25]

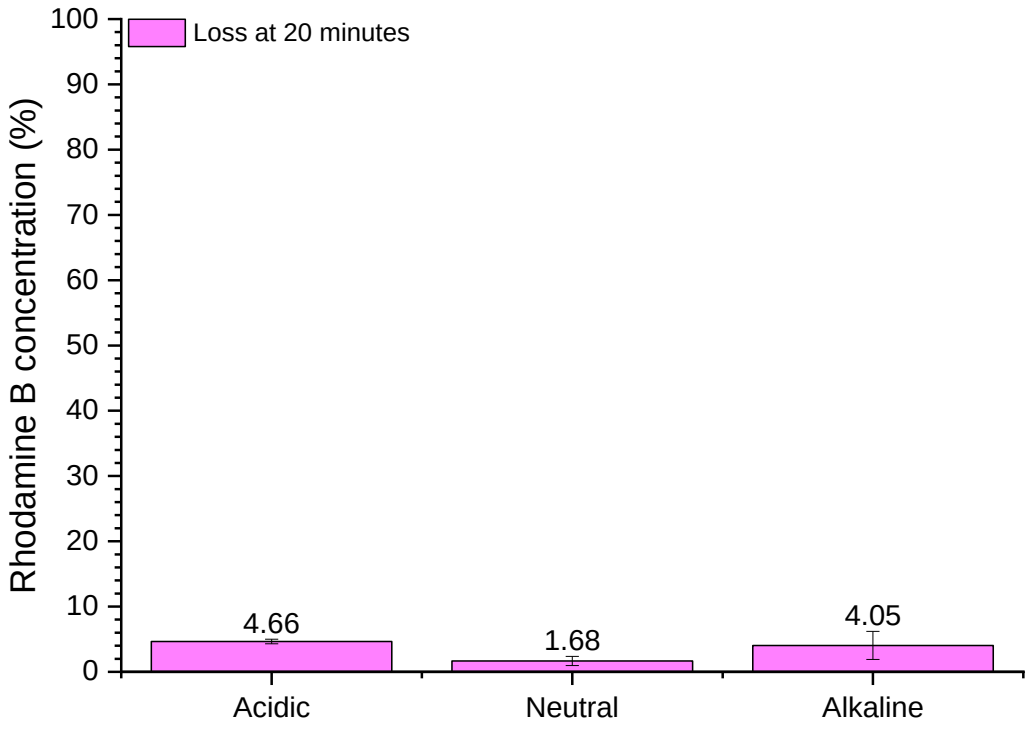

Figure 100: Degradation of RhB under different pH conditions under light illumination.

It was found that RhB has very low degradation under the different pH conditions under light illumination (Figure 100) when no other materials are present, though a preference for degradation is shown for both acidic and alkaline conditions.

Phenazine-Graphene

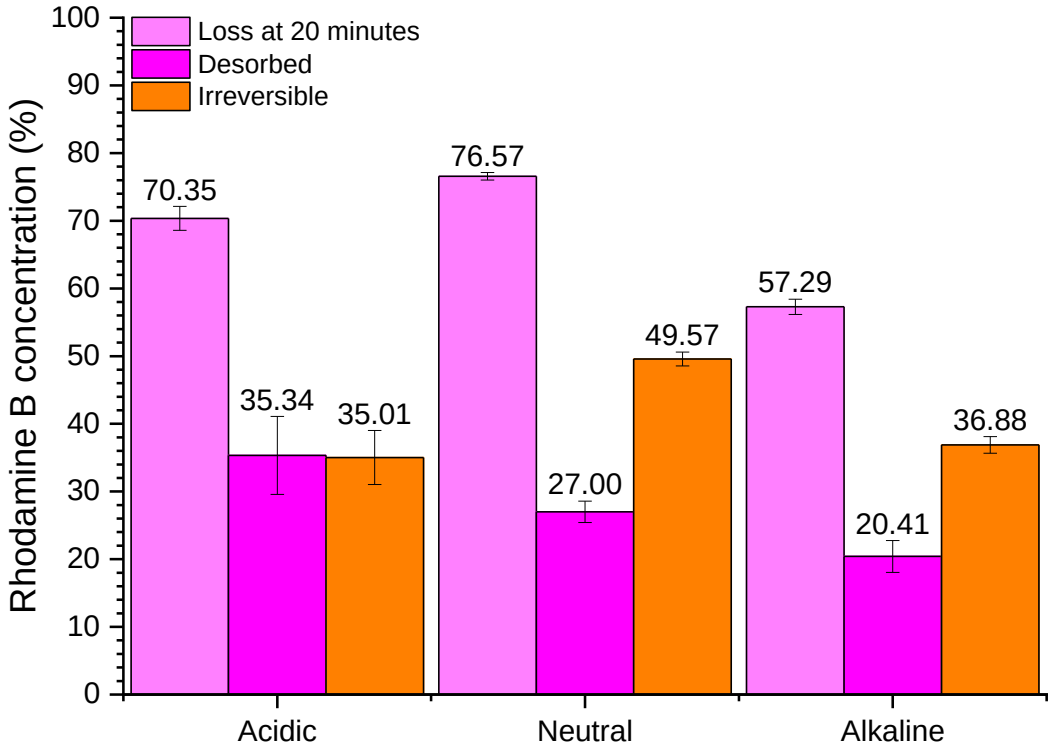

Figure 101: Light-illuminated degradation of RhB by Pnz-G in three different pH conditions. Catalyst loading = 67 µg/mL for alkaline and neutral conditions, 50 µg/mL for acidic conditions.

Condition	Degradation (% vs initial concentration)	Degradation (% vs lost concentration)
Acidic	35	50
Neutral	50	65
Alkaline	37	64

Table 16: The degradation percentages taken from comparison to initial and total removed RhB when reacted with Pnz-G in illuminated conditions.

It was found that the degradation of RhB was taking place across all pH conditions for Pnz-G. The alkaline conditions are the least effective for overall removal but show the greatest proportion of irreversible removal for the total RhB removed from solution. It was found that though 37 % of the RhB in the initial solution is degraded, 64 % of the RhB removed from the solution is degraded (see loss at 20 minutes in Figure 101). A similar quantity for the degradation in neutral conditions with 65 % of removed RhB is degraded, which could suggest alkaline conditions are not limited by the degradation process but by an adsorption process.

This suggests that the reaction mechanism at the surface may be similar for neutral and alkaline media but have limited adsorption onto the Pnz-G surface in the alkaline conditions, which may be controlled

by intermolecular forces that now prevent RhB molecules from achieving close proximity to the active sites on the surface.

The data also suggests that the interactions between dye and catalyst are an important factor as the neutral and alkali conditions lead to a similar outcome for Pnz-G, whilst the weaker acidic conditions do cause a shift in the absorption spectrum of the catalyst (Figure 86).

From the data, it can be said that Pnz-G works well under neutral conditions for the removal of RhB. It also shows that only pH conditions are selective between the degradation of MB and RhB when using Pnz-G.

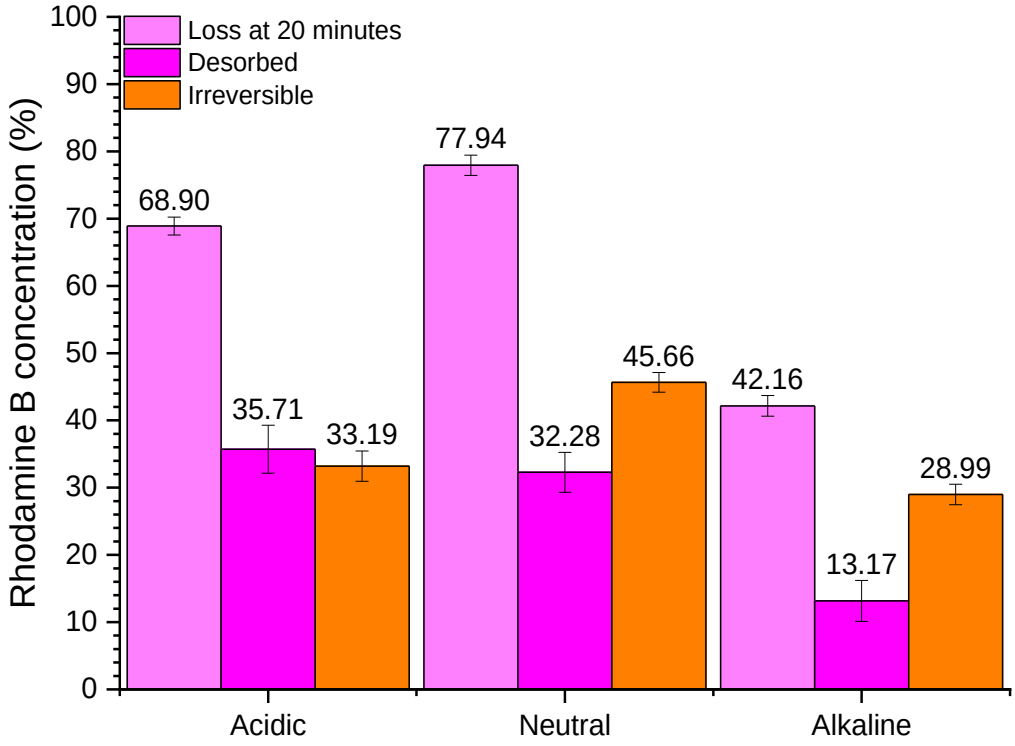

Figure 102: Dark degradation of RhB by Pnz-G in three different pH conditions. Catalyst loading = 67 µg/mL for alkaline and neutral conditions, 50 µg/mL for acidic conditions.

Condition	Degradation (% vs initial concentration)	Degradation (% vs lost concentration)
Acidic	33	48
Neutral	46	59
Alkaline	29	69

Table 17: The degradation percentages taken from comparison to initial and total removed RhB when reacted with Pnz-G.

Once again, all conditions show some efficiency in dark conditions (Figure 102), and alkaline conditions show a surprising minor increase compared to illuminated conditions. Acidic conditions show almost

no change in reactivity, while neutral conditions drop noticeably in degradation but not adsorption. This suggests that illumination has low importance for the acidic degradation of RhB with Pnz-G, which could be an indicator of irreversible adsorption. However, the alkaline and neutral conditions can be enhanced by white light, indicating a light-induced catalytic process.

What seems apparent for alkali medium is that the percentage removed from solution at 20 minutes has decreased along with the degradation. When looking at the percentage of removed substrate that is degraded, alkaline conditions maintain the same degradation and can suggest that a process linked to adsorption is limiting the activity of Pnz-G for RhB degradation.

Compared to P25 TiO_2, the degradation of RhB under visible light is much improved for both photocatalytic degradation and adsorption of RhB. [65] Compared to MCF-TiO_2 samples, Pnz-G also improved both the adsorption and visible light photocatalytic degradation of RhB, as the literature shows that none reach 30 % within the first hour using a 0.25 g/L catalyst concentration. [65] Compared to ZnS/graphene, the photocatalytic degradation is greatly improved due to there being very little degradation in ZnS/graphene compared to initial adsorption, and is also slightly improved against Bi_2S_3-ZnS/graphene nanocomposites.[125]

Fluorescein-Graphene

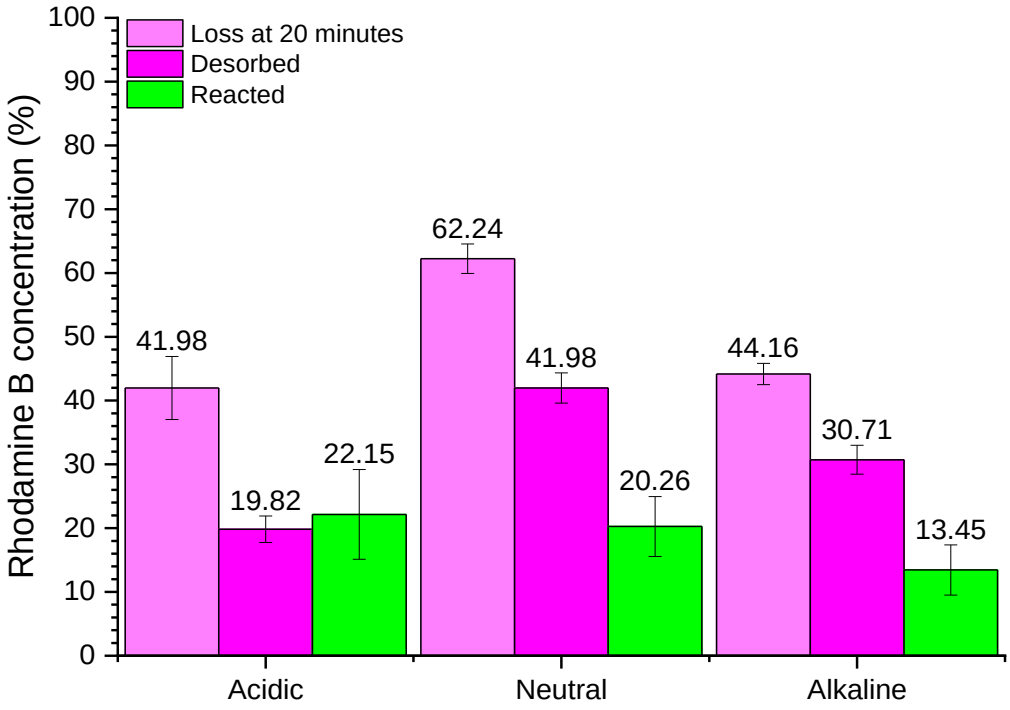

Figure 103: Light-illuminated degradation of RhB by Fsc-G in three different pH conditions. Catalyst loading = 67 µg/mL for neutral conditions, 50 µg/mL for alkaline and acidic conditions.

Condition	Degradation (% vs initial concentration)	Degradation (% vs lost concentration)
Acidic	22	47
Neutral	20	33
Alkaline	13	30

Table 18: The degradation percentages taken from comparison to initial and total removed RhB when reacted with Fsc-G in illuminated conditions.

RhB removal has been achieved in all pH conditions under illumination, as shown in Figure 103. However, it is much lower than that seen with MB. Notably, no condition exceeds 50 % degradation of either the RhB initially in solution or of what is adsorbed to the surface by 20 minutes.

It is possible that the close resemblance in structural features of RhB and fluorescein dye of Fsc-G are too similar for a favourable interaction between the catalysts and the substrate. This can include a competition between RhB and Fsc units on Fsc-G, when excited by light leading to a reduced redox activity. It provides a further suggestion to the concept of substrate-subunit interactions being highly important in the reaction mechanism.

Table 18 shows that the degradation on the surface is similar in alkaline and neutral conditions, as seen in the Pnz-G case. But here, the process is slower than under the acidic conditions. This could point to the alternative pathway through acidic conditions being less affected by the similarities in structure of the phenazine and the dye (RhB or MB).

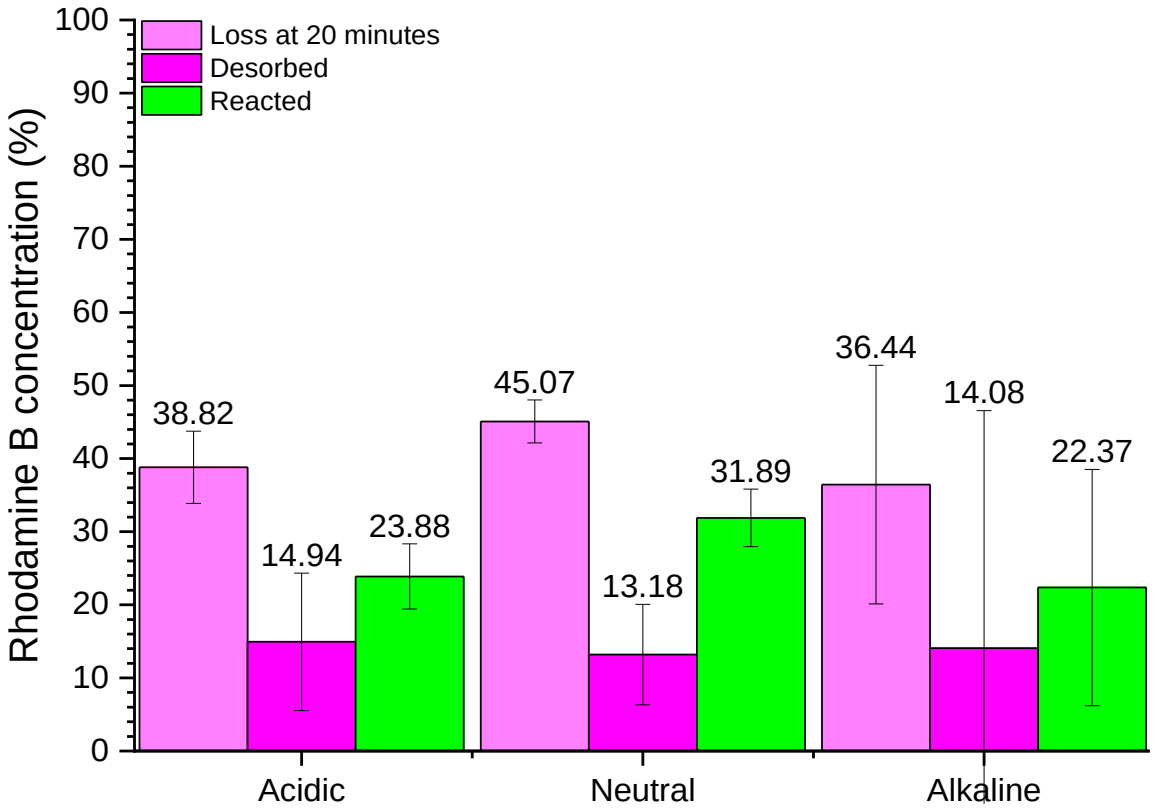

Figure 104: Dark degradation of RhB by Fsc-G in three different pH conditions. Catalyst loading = 67 µg/mL for neutral conditions, 50 µg/mL for alkaline and acidic conditions.

Condition	Degradation (% vs initial concentration)	Degradation (% vs lost concentration)
Acidic	24	62
Neutral	32	71
Alkaline	22	61

Table 19: The degradation percentages taken from comparison to initial and total removed RhB when reacted with Fsc-G.

When experiments are repeated in the dark (Figure 104), the acidic conditions have lower adsorption of RhB and an equal reacted percentage, suggesting that the surface reaction may have accelerated in the dark as the percentage of reacted versus the removed concentration is now 61.5 %. This is also the same in alkaline conditions, however the data is highly unreliable and prone to a wide variation. The reasons of such wide variation are uncertain, but a simple explanation could be the electrostatic repulsion between the similar structures of fluorescein and RhB, whose carboxylic acid functions would both be negatively charged. Also, if the reaction is proceeding by hydroxyl radicals, the fluorescein subunit may be as reactive as RhB towards them and hence cause a random attack on the surface and substrate, resulting in diminished reactivity in the high concentration of hydroxide anions.[164] However, there have been some unavoidable illumination occurring during scanning, which

could activate the catalyst and the already low reactivity could result in irreversible adsorption of the similar dye structures being seen as increased activity.

Neutral conditions show a greatly reduced adsorption of RhB from solution, but an increased reactivity. It also potentially suggests that the subunit and substrate are too similar for photocatalysis to occur effectively.

For the photoactivity of Fsc-G, the degradation of RhB is slightly improved against P25 and MCF/TiO_2 catalysts along with the adsorption. However, the dark activity is much more improved, though the data is much more variable and unreliable.[65] Compared to ZnS/graphene, the photocatalytic degradation is significantly improved in visible light, while the rate is not as high as that of Bi_3S_2-ZnS/graphene.[125]

Purine-Graphene

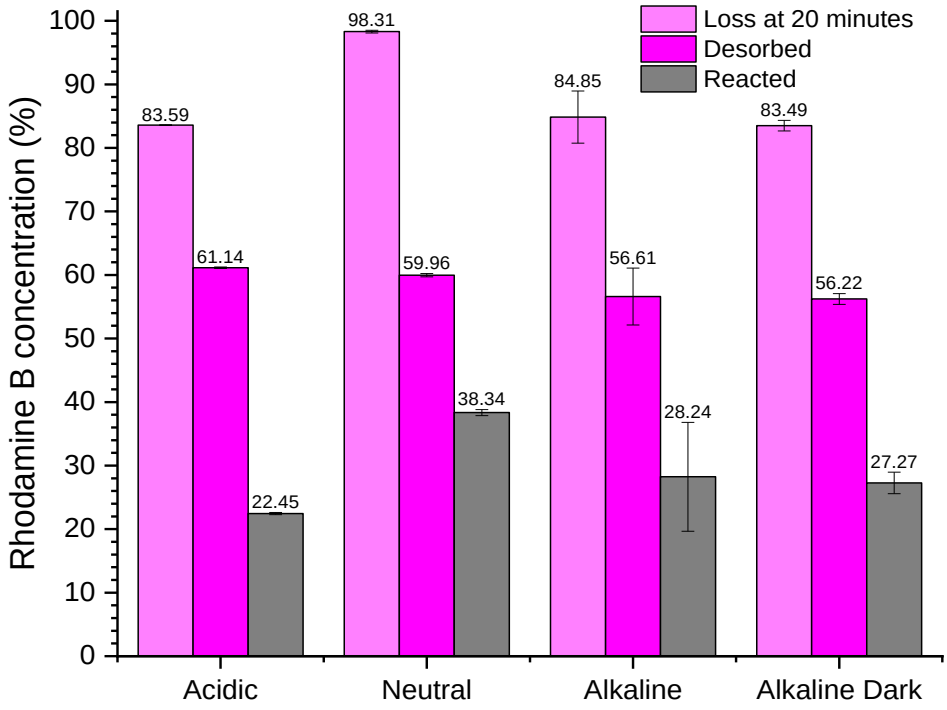

Figure 105: Degradation of RhB by Pur-G in three different pH conditions. Reactions performed in light unless otherwise stated in the conditions. Catalyst loading = 50 µg/mL for neutral and acidic conditions, 67 µg/mL for alkaline conditions.

The results of Pur-G with RhB (Figure 105) unfortunately lacked dark conditions for neutral and acidic media, which was not helped by events occurring around the time of final experiments. However, the data that was collected shows the reactivity with RhB is similar to that found for MB in acidic and neutral. However, the physisorption is increased in light conditions, which would suggest a lower reaction rate at the surface of Pur-G.

The reactivity and physisorption of Pur-G in the dark is almost identical to that of the light conditions, showing that as a catalyst, Pur-G is not light activated. Additionally, it helps to add to the concept that both the light absorption and interaction between substrate and dye subunit are a large part of the degradation of both RhB and MB.

The generally higher physisorption identified with RhB compared to MB suggests more preferential intermolecular interactions between Pur-G and dye, but also suggests that the surface degrades the dye at a slower rate, as the rates of adsorption and desorption from the surface of the catalyst appear to no longer be the limiting factor, potentially pointing to other processes such as fluorescence, now competing with the electron transfer processes.

Nonetheless, Pur-G has excellent filtration capabilities again for a dye material, whilst also having some mild catalytic capability (limited to less than 40 %) like the other hybrids studied.

Compared to the literature, the degradation is significantly faster than P25, ZnS-graphene, or MCF/TiO_2 composites as the literature shows they have little or no activity towards RhB. However, Bi_2S_3-ZnS/graphene is closer to the RhB removal activity of Pur-G when illuminated with visible light.[65, 125] This shows that though Pur-G does not effectively absorb light, its activity under illumination is very high compared to these literature examples.

Chromone-Graphene

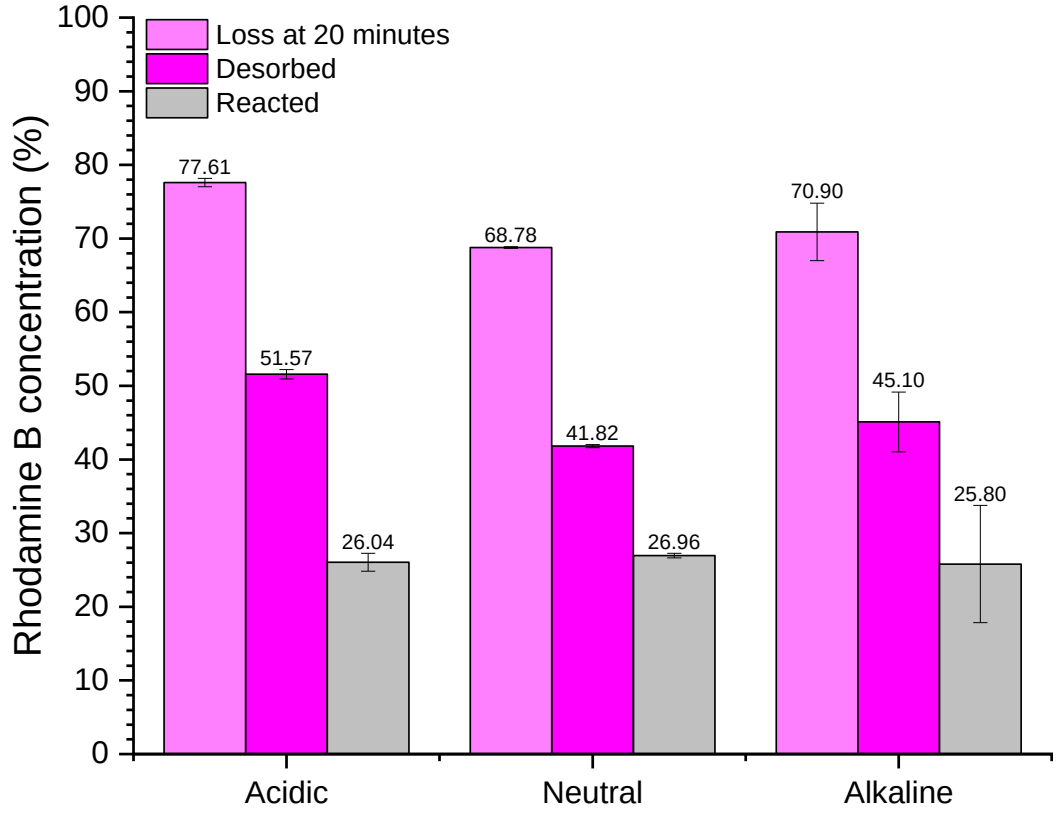

Figure 106: Light-illuminated degradation of RhB by Chr-G in three different pH conditions. Catalyst loading = 50 µg/mL for neutral and acidic conditions, 67 µg/mL for alkaline conditions.

Chr-G behaves almost identically in all conditions with RhB regarding percentage lost irreversibly, shown in Figure 106. The removal of RhB is slightly higher under acidic conditions leading to 78 % of the dye loss. The catalytic degradation of RhB against the overall amount removed from the solution is for acidic, neutral, and alkaline conditions are 33 %, 39 % and 36 %, respectively. The results are very similar showing no preference for pH change. A low catalytic reactivity can be attributed to Chr-G composite being visible light inactive, so any light induced activity is likely due to the activation of RhB.

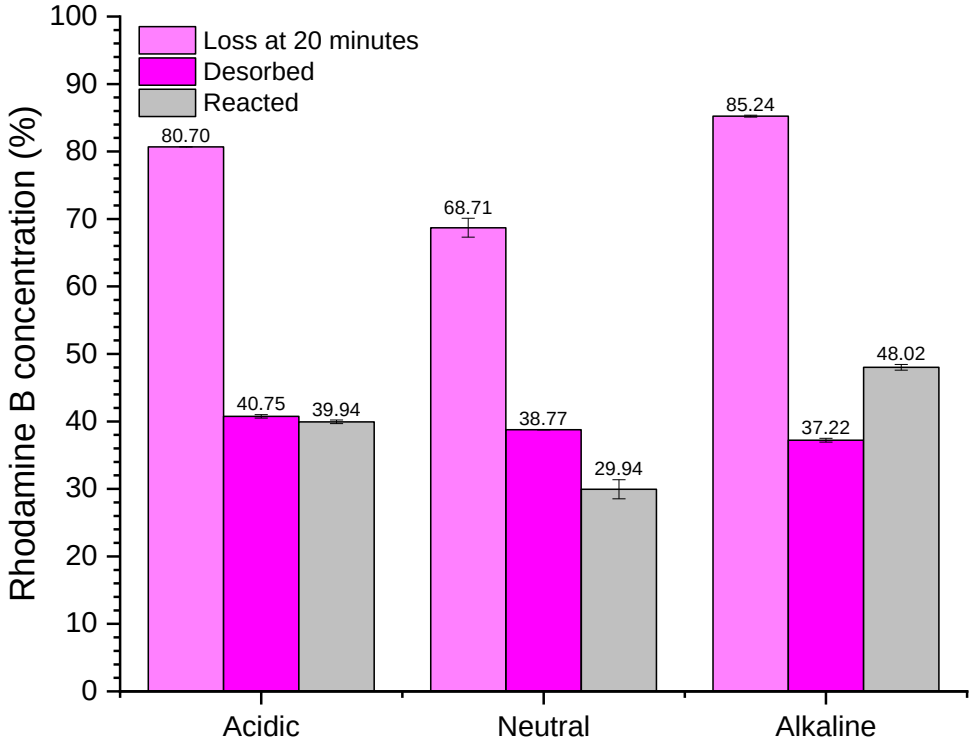

Figure 107: Dark degradation of RhB by Chr-G in three different pH conditions. Catalyst loading = 50 µg/mL for neutral and acidic conditions, 67 µg/mL for alkaline conditions.

When Chr-G was then exposed to RhB in the dark, it was found that alkaline conditions and acidic conditions are much more efficient. This helps to show that the hybrid is a catalyst as we are now increasing the percentage degradation to almost 50 %, without increasing the loss from solution by all processes (Figure 107). The mechanism could be suggested to be close to the surface of the catalyst and may be a reactive oxygen species attack of RhB, catalysed by Chr-G through either water splitting or oxygen reduction reactions to form the active species.[3, 7] In addition, the dark conditions may be preferable in both cases through the alignment of energy levels, if the substrate dye contributes to reactive oxygen species formation, as the excitation would cause higher levels to become occupied.

The dye removal results under neutral pH are virtually unchanged between dark and light conditions, as the adsorption is less than 1 % extra and degradation is increased by 3 %. This helps to confirm that this catalyst is not photo-activated, and that the dye's excitation has a limited effect at this pH. Since RhB does not alter its excitation when exposed to acid[195], it could be assumed RhB has little contribution to the catalytic process, in the case of Chr-G.

Also, it can be noted that the percentage of catalytic degradation compared to the total dye removed from the solution increases and equalises with the percentage of the dye adsorbed, indicating a potential for the catalytic process to take place.

Compared to the literature, the degradation is significantly faster than P25, ZnS-graphene, or MCF/TiO_2 composites as the literature shows they have little or no activity towards RhB. However, Bi_2S_3-ZnS/graphene is closer to the RhB removal activity of Chr-G when illuminated with visible light.[65, 125] However, since adsorption is high in all samples discussed, the activity may not be as seen by UV-vis data. This shows that though Chr-G does not effectively absorb light, its activity under illumination is very high compared to these literature examples.

Thionine-Graphene

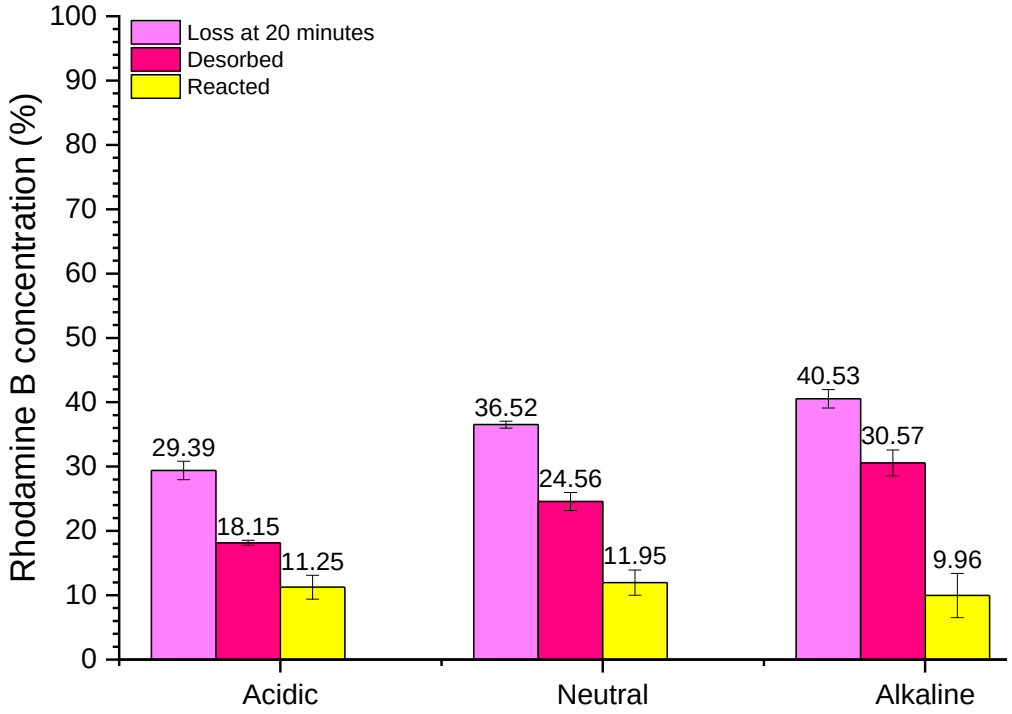

Figure 108: Light-illuminated degradation of RhB by Thi-G in three different pH conditions. Catalyst loading = 50 µg/mL for neutral and acidic conditions, 67 µg/mL for alkaline conditions.

For Thi-G it is seen that the pH conditions have no significant difference on degradation (Figure 108), displayed by the errors between the different experimental conditions overlapping significantly. The adsorption increases as pH increases, which can be explained by the acidic conditions making both the surface and substrate dye positively charged and creating electrostatic repulsion and reducing the adsorption of RhB to Thi-G. The degradation is also low under all conditions and shows Thi-G to be a poor photocatalyst.

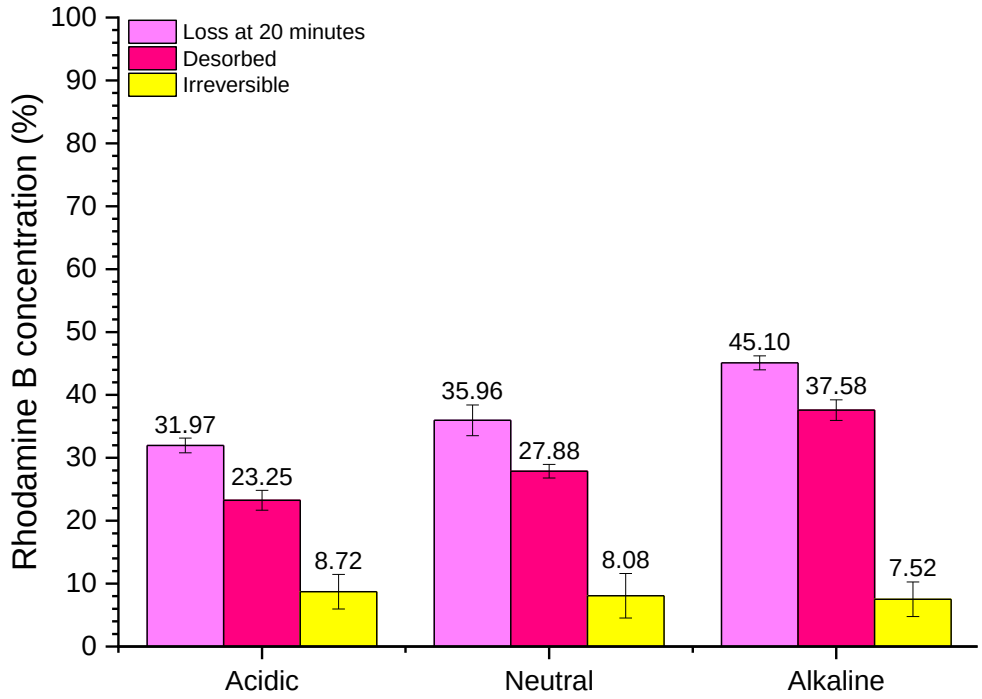

Figure 109: Dark degradation of RhB by Thi-G in three different pH conditions. Catalyst loading = 50 µg/mL for neutral and acidic conditions, 67 µg/mL for alkaline conditions.

The trend is the same in the dark (Figure 109), with a similar removal from solution at 20 minutes, but a slight reduction in the average amount degraded, which could be due to the lack of light illuminating the solution and exciting the dye or hybrid. Again, there is an overlap in errors, even with the light conditions which suggests little activity and little difference between all the conditions. The only significant difference is that there is an increase of adsorbed material in the dark alkaline conditions.

According to the literature, the activity of Thi-G is only improved when compared to ZnS/graphene and P25, neither of which are visible light absorbing. This shows the poor quality of this hybrid as a photocatalyst.[65, 125]

4.3.5 Reactivity Summary

The following tables summarise the data collected for the removal and degradation of MB and RhB by all catalysts under each condition studied.

	MB (total removal % / degraded %)					
	Light			Dark		
Catalyst	**Acid**	**Neutral**	**Alkali**	**Acid**	**Neutral**	**Alkali**
Pnz-G	49 / 11	43 / 11	66 / 43	57 / 37	38 / 5	59 / 23
Fsc-G	44 / 13	40 / 12	87 / 70	58 / 17	56 / 17	98 / 33
Pur-G	62 / 28	70 / 40	73 / 50	98 / 18	96 / 7	98 / 38
Chr-G	58 / 11	24 / 29	45 / 20	40 / 10	27 / 33	72 / 31
Thi-G	13 / 15	10 / 17	69 / 42	19 / 23	13 / 20	75 / 49

Table 20: The removal and degradation of MB under all conditions with each of the hybrid catalysts for 20 minutes.

The data in Table 20 shows that the best material for reversible removal is Pur-G under dark conditions. Meanwhile Fsc-G under alkaline conditions shows the best efficiency for MB irreversible removal. Generally, all hybrid materials under light conditions show improved irreversible and reversible MB removal in alkaline conditions, except for Chr-G where neutral conditions showed mildly improved irreversible removal and much reduced reversible removal. Fsc-G in dark alkaline conditions showed improved reversible but worse reversible removal, compared to illuminated alkaline conditions. The type of heteroatom within the moiety does not appear to be a strong factor for these hybrid materials.

	RhB (total removal % / degraded %)					
	Light			Dark		
Catalyst	**Acid**	**Neutral**	**Alkali**	**Acid**	**Neutral**	**Alkali**
Pnz-G	70 / 35	76 / 50	57 / 37	69 / 33	78 / 46	42 / 29
Fsc-G	42 / 22	62 / 20	44 / 13	39 / 24	45 / 32	36 / 22
Pur-G	84 / 22	98 / 38	85 / 28	N/A	N/A	83 / 27
Chr-G	77 / 26	69 / 27	71 / 26	81 / 40	69 / 30	85 / 48
Thi-G	29 / 11	36 / 12	40 / 10	32 / 9	36 / 8	45 / 8

Table 21: The removal and degradation of MB under all conditions with each of the hybrid catalysts for 20 minutes.

For RhB in Table 21, Pur-G shows to be the strongest irreversible remover of substrate but shows low irreversible removal. Most hybrids show similar or improved results compared to MB, with the exception of Fsc-G under alkaline conditions with light illumination and Thi-G irreversible removals in dark conditions. The most effective condition for RhB irreversible removal showed to be Pnz-G with light illumination under neutral conditions. However, Chr-G under dark alkaline conditions had a better irreversible removal with a close irreversible removal percentage.

From both sets of data, it can be determined that Thi-G is a generally very poor at the removal of RhB and MB, whilst Pur-G is a very good sponge-like material for dye removal. This result for Thi-G can be explained by a low surface coverage and covalent attachment of the dye to graphene which was suggested by TGA (Chapter 3).

4.4 Conclusion

In conclusion, the fabricated graphene materials, show a range of activity under various pH and illumination conditions. Illumination with light is beneficial to activate Pnz-G and Fsc-G and improves the hybrids reactivity towards MB and RhB. The Chr-G and Pur-G hybrids show more complex behaviour, and their activity can be attributed to a synergistic interaction between the hybrids and RhB or MB dyes. Here, visible light absorption by the dye substrates can result in their excitation and subsequently electron transfer processes increasing the overall dye removal. These materials show activity at a concentration range of 50-66.67 µg/mL, which is extremely low compared to the 0.2-2.5 mg/mL usually employed with catalysts such as TiO_2 as reported in the literature.[116-118]

Trends in reactivity show that MB has a slightly higher degradation with the catalysts than RhB, which means that RhB is more stable under the conditions of this study and is less easily degraded by the hybrids. Additionally, it was observed that light induction generally improves the degradation of MB with most of the hybrids, the notable exceptions to this being Thi-G and Chr-G. RhB degradation was much less affected by light and showed a trend of degrading or adsorbing similarly between conditions with or without white light illumination.

The hybrids' 20-minute activity shows a greatest degradation of MB of 70 % by Fsc-G and RhB degradation of 50 % for Pnz-G, each with light illumination, showing that these materials have photocatalytic properties. Meanwhile, those with lesser photocatalytic properties showed either mild catalytic properties or very good adsorbent properties.

In the reuse experiments with the photoactive hybrids a MB degradation of 80 % or greater can be achieved up to 5 repeated 2-hour cycles. Moreover, a decrease in the dye removal has been observed, when a washing process, which has the potential to remove small quantities of catalyst, was carried out.

4.5 Experimental

4.5.1 General Methods and Materials

A general method for the photocatalytic testing was to use a stock of MB is deionised water (50 µL; 0.3 mg/mL) in a plastic cuvette and made up to 3 mL with deionised water after catalyst addition (if applicable). This method was used unless otherwise stated in the appropriate experimental section.

UV-vis measurements for photocatalytic testing were performed in the range of 280 nm to 800 nm using a fast scan rate pre-set. Fluorescence measurements were taken using 3 nm slit widths on both slits, unless stated otherwise.

4.5.2 Initial Testing of Methylene Blue Stability

Dark Conditions: 50 µL of MB stock solution (0.3 mg/mL) was added to a quartz cuvette containing 3 mL of water. The resulted solution was scanned by UV-vis spectrophotometer. The MB solution was stirred in the dark for 20 minutes. After this, a UV-vis spectrum has been recorded. This procedure was applied to other dark conditions. For acidic conditions, TFA (6 µL; 10 % in water) was added prior the solution was left in the dark for 20 min. For basic conditions, NaOH (20 µL; 1 M; calculated pH = 10.8) was added prior the solution was left in the dark for 20 min.

Light Conditions: 50 µL of MB stock solution (0.3 mg/mL) was added to a quartz cuvette containing 3 mL of water. The resulted solution was scanned by UV-vis spectrophotometer. The MB solution was stirred under white light illumination (Lamp: nightsearcher workstar SMT LED Portable Rechargeable Floodlight (2200 Lumens per LED, 10 LED station)) for 20 minutes. After this, a UV-vis spectrum had been recorded. This procedure was applied to other light conditions. For acidic conditions, TFA (6 µL; 10 % in water) was added prior the solution was left in the dark for 20 min. For basic conditions, NaOH (20 µL; 1 M) was added prior the solution was left in the dark for 20 min.

Titrations

TFA: To a solution of 50 µL MB stock (0.3 mg/mL) in 3 mL of water, a solution of TFA (6 µL; 10 % in water) was added. The additions in microlitres then continued at steadily increasing volumes from 6 µL to 50 µL. The absorbance peak then began to plateau slowly and was stopped at 562 µL. This was then repeated with graphene and Pnz-G solutions (200 µL; 1 mg/mL) separately.

NaOH: To a solution of 50 µL MB stock (0.3 mg/mL) in H_2O (3 mL), a solution of NaOH (6 µL; 1 M) was added. The additions in microlitres (µL) then continued at 7, 9, 9, 9, 14, 14, 14, 24, 24, 24, 44, 44, 55.

This was where the absorbance had plateaued and a total of NaOH added had almost reached 600 µL. This was then repeated with graphene and Pnz-G solutions (200 µL; 1 mg/mL) separately.

4.5.3 Mass Loading Studies and Conditions Studies

All graphitic materials were treated in the same way.

Neutral: MB (50 µL; 0.3 mg/mL stock) was added to H_2O (3 mL) and was then scanned by UV-vis photospectroscopy. Graphitic hybrid solution (25 µL/ 50 µL/75 µL/ 100 µL/ 150 µL/ 200 µL; 1 mg/mL) was added to the solution and was stirred in the dark whilst held at 20 °C for 20 minutes. UV-vis was used to scan the reaction after this time and the data recorded.

Acidic: MB (50 µL; 0.3 mg/mL stock) was added to H_2O (3 mL) with TFA (6 µL; 10 % in water) and was then scanned by UV-vis photospectroscopy. Graphitic hybrid solution (25 µL/ 50 µL/75 µL/ 100 µL/ 150 µL/ 200 µL; 1 mg/mL) was added to the solution and was stirred in the dark whilst held at 20 °C for 20 minutes. UV-vis was used to scan the reaction after this time and the data recorded.

Alkaline: MB (50 µL; 0.3 mg/mL stock) was added to H_2O (3 mL) with NaOH (20 µL; 1 M) and was then scanned by UV-vis photospectroscopy. Graphitic hybrid solution (25 µL/ 50 µL/75 µL/ 100 µL/ 150 µL/ 200 µL; 1 mg/mL) was added to the solution and was stirred in the dark whilst held at 20 °C for 20 minutes. UV-vis was used to scan the reaction after this time and the data recorded.

They were also repeated several times with kinetics testing while using the optimal mass loading of each graphitic material as per the table below. Kinetics scans were taken in 5 minutely intervals.

Graphitic Material	Acidic Mass Load (µg)	Neutral Mass Load (µg)	Alkaline Mass Load (µg)
Pnz-G	150	200	200
Pur-G	150	150	200
Fsc-G	150	200	150
Chr-G	150	150	200
Thi-G	150	150	200

Table 22: The optimal mass loading of the graphitic hybrids.

4.5.4 2 Hours Kinetics

Pnz-G Alkaline: MB (50 µL; 0.3 mg/mL stock) was added to H_2O (3 mL) with NaOH (20 µL; 1 M) and was then scanned by UV-vis photospectroscopy. Pnz-G solution (200 µL; 1 mg/mL) was added to the solution and was stirred with light illumination whilst held at 20 °C for 2 hours. UV-vis was used to scan the reaction throughout the reaction and the data recorded.

Fsc-G Alkaline: MB (50 µL; 0.3 mg/mL stock) was added to H_2O (3 mL) with NaOH (20 µL; 1 M) and was then scanned by UV-vis photospectroscopy. Fsc-G solution (200 µL; 1 mg/mL) was added to the solution and was stirred with light illumination whilst held at 20 °C for 2 hours. UV-vis was used to scan the reaction throughout the reaction and the data recorded.

4.5.5 Adsorption and Reuse Studies

Neutral: MB (50 µL; 0.3 mg/mL stock) was added to H_2O (3 mL) and was then scanned by UV-vis photospectroscopy. Graphitic hybrid solution (optimal as per Table 22; 1 mg/mL) was added to the solution and was stirred in the dark for 20 minutes. UV-vis was used to scan the reaction after this time and the data recorded. Once the reaction was completed, ethanol (1 mL) was added to the solution and stirred gently before scanning the UV-vis again. This was then repeated with light illumination over the time period.

Acidic: MB (50 µL; 0.3 mg/mL stock) was added to H_2O (3 mL) with TFA (6 µL; 10 % in water) and was then scanned by UV-vis photospectroscopy. Graphitic hybrid solution (optimal as per Table 22; 1 mg/mL) was added to the solution and was stirred in the dark for 20 minutes. UV-vis was used to scan the reaction after this time and the data recorded. Once the reaction was completed, ethanol (1 mL) was added to the solution and stirred gently before scanning the UV-vis again. This was then repeated with light illumination over the time period.

Alkaline: MB (50 µL; 0.3 mg/mL stock) was added to H_2O (3 mL) with NaOH (20 µL; 1 M) and was then scanned by UV-vis photospectroscopy. Graphitic hybrid solution (optimal as per Table 22; 1 mg/mL) was added to the solution and was stirred in the dark for 20 minutes. UV-vis was used to scan the reaction after this time and the data recorded. Once the reaction was completed, ethanol (1 mL) was added to the solution and stirred gently before scanning the UV-vis again. This was then repeated with light illumination over the time period.

Adsorption: MB (0.3 mg/mL stock) was added in portions (10 µL) every 10 minutes to a solution of H_2O (3 mL) and NaOH (20 µL; 1 M) and was stirred throughout. Prior to each portion addition, the solution was scanned over the visible region by UV-vis photospectroscopy.

4.5.6 Reaction Cycles

Pnz-G Alkaline: MB (25 µL; 0.3 mg/mL stock) was added to H_2O (3 mL) with NaOH (20 µL; 1 M) and was then scanned by UV-vis photospectroscopy. Pnz-G solution (200 µL; 1 mg/mL) was added to the

solution and was stirred with white light illumination for 2 hours. This was continued with additions of MB (25 µL; 0.3 mg/mL stock) after each reaction and restarted. UV-vis was used to scan throughout the reaction and the data recorded.

Fsc-G Alkaline: MB (25 µL; 0.3 mg/mL stock) was added to H_2O (3 mL) with NaOH (20 µL; 1 M) and was then scanned by UV-vis photospectroscopy. Fsc-G solution (200 µL; 1 mg/mL) was added to the solution and was stirred with white light illumination for 2 hours. This was continued with additions of MB (25 µL; 0.3 mg/mL stock) after each reaction and restarted. UV-vis was used to scan throughout the reaction and the data recorded.

4.5.7 Rhodamine B

Neutral: RhB (50 µL; 0.3 mg/mL stock) was added to H_2O (3 mL) and was then scanned by UV-vis photospectroscopy. Graphitic hybrid solution (optimal as per Table 22; 1 mg/mL) was added to the solution and was stirred in the dark for 20 minutes. UV-vis was used to scan the reaction after this time and the data recorded. Once the reaction was completed, ethanol (1 mL) was added to the solution and stirred gently before scanning the UV-vis again. This was then repeated with light illumination over the time period.

Acidic: RhB (50 µL; 0.3 mg/mL stock) was added to H_2O (3 mL) with TFA (6 µL; 10 % in water) and was then scanned by UV-vis photospectroscopy. Graphitic hybrid solution (optimal as per Table 22; 1 mg/mL) was added to the solution and was stirred in the dark for 20 minutes. UV-vis was used to scan the reaction after this time and the data recorded. Once the reaction was completed, ethanol (1 mL) was added to the solution and stirred gently before scanning the UV-vis again. This was then repeated with light illumination over the time period.

Alkaline: RhB (50 µL; 0.3 mg/mL stock) was added to H_2O (3 mL) with NaOH (20 µL; 1 M) and was then scanned by UV-vis photospectroscopy. Graphitic hybrid solution (optimal as per Table 22; 1 mg/mL) was added to the solution and was stirred in the dark for 20 minutes. UV-vis was used to scan the reaction after this time and the data recorded. Once the reaction was completed, ethanol (1 mL) was added to the solution and stirred gently before scanning the UV-vis again. This was then repeated with light illumination over the time period.

Chapter 5: Mechanistic Study into Catalytic Activity

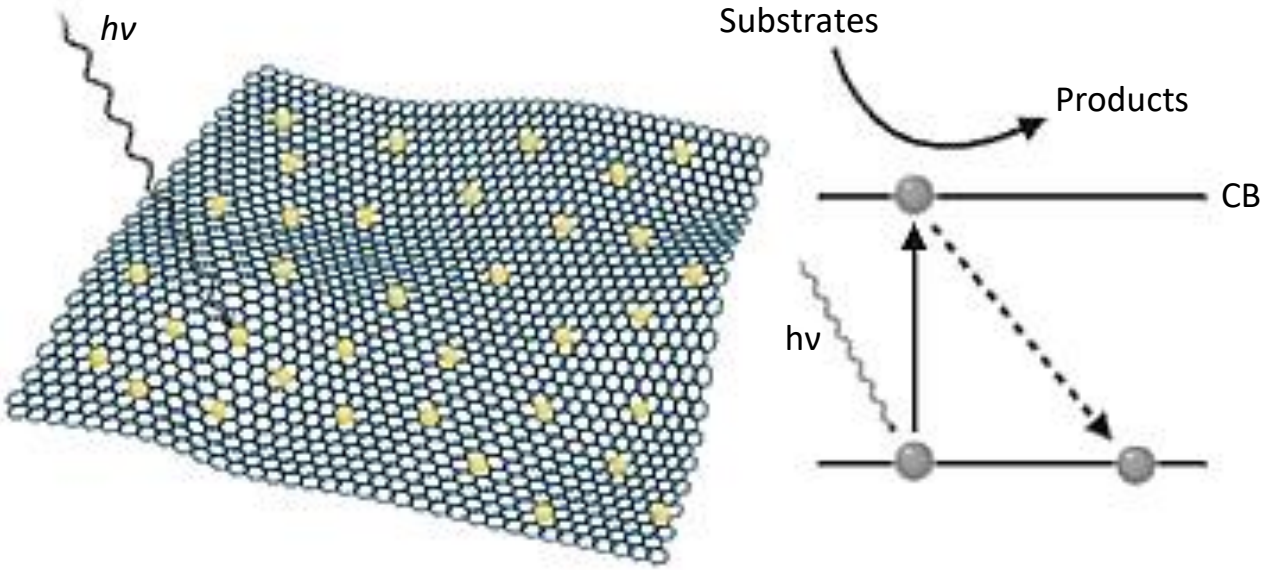

Created using BioRender.com

5.1 Abstract

In this chapter, the mechanisms behind the (photo)catalytic activity of the graphitic hybrids are discussed. In this study we have observed a tendency towards the production of hydroxy radicals, likely through a redox process of the hybrid materials with either water or oxygen in aqueous media. We can also report a lack of reductive processes occurring from the tests and that oxidation is the most common process seen. We report that through tests with organic probes, we were able to detect that these radicals were forming in solution. Furthermore, we report some low levels of activity of the graphitic hybrids with benzyl alcohol.

5.2 Aims

The aim of this chapter was to test the hybrids in a way to determine their mechanism of reactivity, through the use of redox reactions and probes for the detection of reactive species being formed.

5.3 Results and Discussion

5.3.1 Initial Redox Testing

To begin the study of the mechanisms through which these graphitic hybrids function, it was necessary to investigate whether organic redox reactions can be promoted by them. Since MB was degraded by the hybrids, there is a good possibility that oxidation is a dominating process, so it was the first avenue of exploration in these tests. Also, due to the results seen with RhB, it was decided that neutral conditions would be used first, because the result with MB could have been influenced by its innate reactivity with hydroxide anions.

The first four compounds (nitrobenzene, benzyl alcohol, 3-amino-benzyl alcohol and 4-methoxy benzyl alcohol) were chosen for the test based on a literature study,[129] which demonstrated a quick screening method to test the redox capability of a catalyst. The oxidation reaction involves the conversion of a benzyl alcohol into its corresponding aldehyde or carboxylic acid. The test compounds have been chosen to accommodate a range of known oxidation potentials (E_{ox}): E_{ox} (Benzyl alcohol) = *ca*. +1.5 V (vs standard calomel electrode; SCE),[200] E_{ox} (amino-benzyl alcohol) = +0.62 V (vs silver-silver chloride electrode; SSE),[201] E_{ox} (4-methoxybenzyl alcohol) = +1.5 V (vs SCE).[200] The starch-iodide paper has been used as the method to detect the oxidative process (by detection of H_2O_2 or $O_2^{\cdot-}$ formation). Nitrobenzene has been chosen as a negative control as it is generally used to test reduction process. [129]

The controls showed no response, apart from benzyl alcohol, which can react with water without a catalyst. The tests in the presence of Pnz-G all showed a positive result, which should not have been the case for nitrobenzene since nitrobenzene should undergo reductive reactions. This led to an uncertainty in the other positive results that can be seen in Table 23.

Conditions	**Benzyl Alcohol**	**3-Amino-Benzyl Alcohol**	**4-Methoxy Benzyl Alcohol**	**Nitrobenzene**
Pnz-G	Purple result on starch-iodide	Purple result on Starch-Iodide	Purple result on Starch-Iodide	Purple result on Starch-Iodide
Solvent	Delayed, light purple response	No response	No response	No response
MDAP	No response	No response	No response	No response
MDAP & Solvent	No response	No response	No response	No response
Graphene	No response	No response	No response	No response
Graphene & Solvent	No response	No response	No response	No response

Table 23: The set of initial reactions to test the oxidation reaction of Pnz-G as a model.

A test of Pnz-G in water without any other compounds present also gave a positive result. The pH of the solution has been tested showing to be neutral.

Additionally, graphene and MDAP individually have shown no activity which supports findings from the reactivity studies with MB and RhB dyes described in Chapter 4.

5.3.2 Benzyl Alcohol Redox Reaction to Test Hydroxy Radical Mechanism vs Oxidation Mechanism

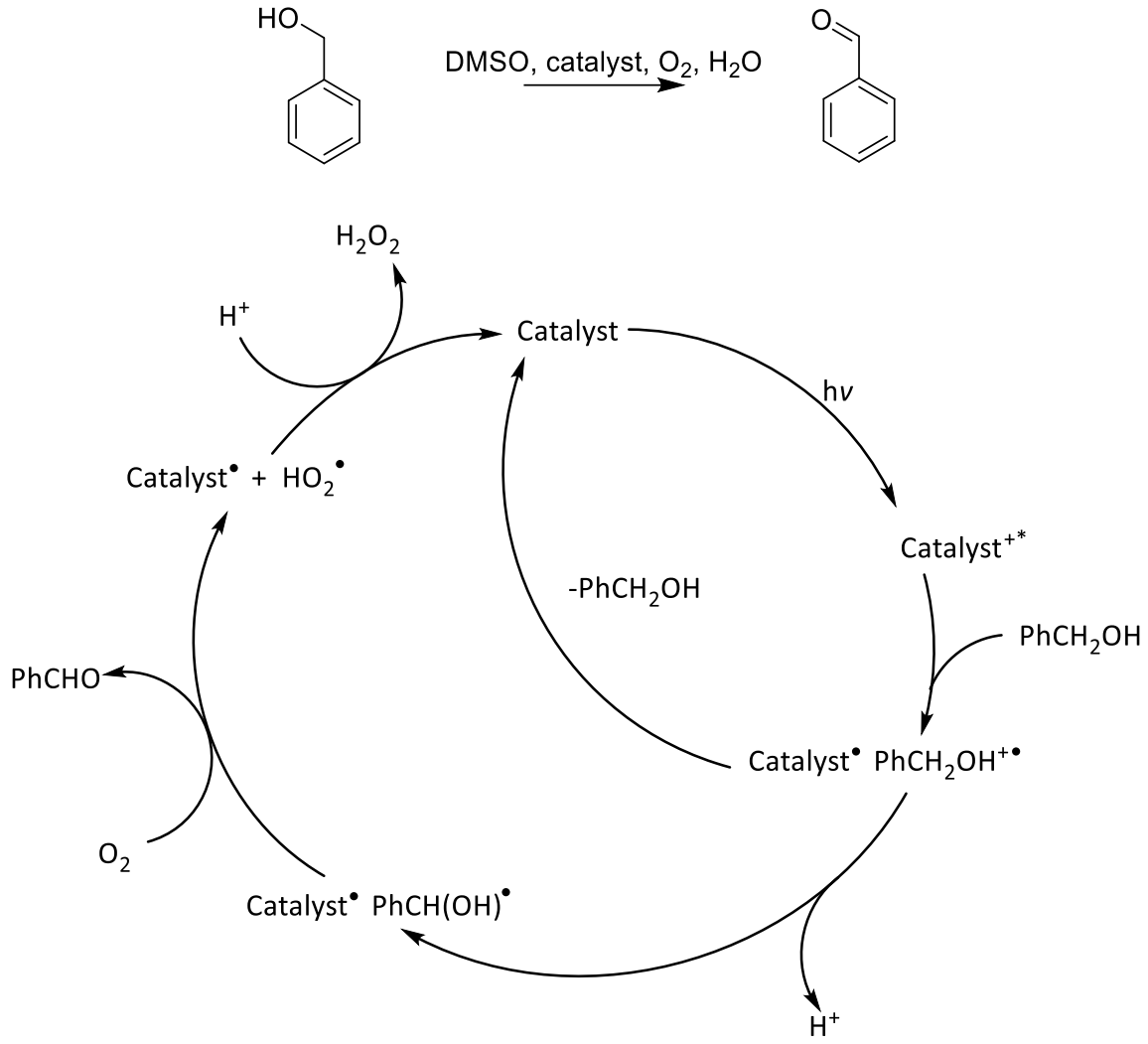

Scheme 33: The scheme and a postulated mechanism[70] for the conversion of benzyl alcohol to benzaldehyde in water with oxygen bubbled into solution. Catalyst = Pnz-G, Fsc-G, Pur-G or Chr-G.

Benzyl alcohol was once again used in an alternative method. For this set of reactions, it was decided that the influence of oxygen, water and hydroxide would be compared prior to the testing of all hybrids.

Initially the test was undertaken in 10 mL benzyl alcohol with 0.3 mL of DMSO added to the solution in the presence of a catalytic quantity of Pnz-G. Then oxygen was bubbled into the solution for 15 minutes before sealing and allowing the mixture to stir for 6 hrs with light illumination. The reaction was monitored every hour via TLC analysis (1:1 hexane/EtOAc initially, then 3:1 hexane/EtOAc after first point). This mixture was analysed by MS and later NMR (Figure 110). Here, most of the material was still benzyl alcohol, but a small aldehyde peak was also present, showing a very low reactivity under these conditions.

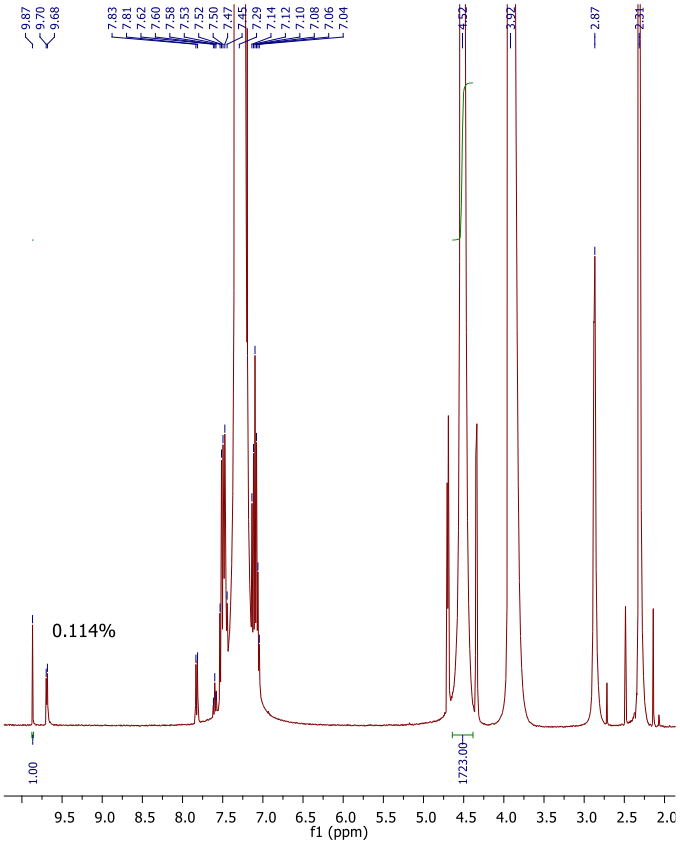

Figure 110: ^{1}H NMR of the reaction mix of benzyl alcohol and benzaldehyde in oxygenated non-aqueous conditions with Pnz-G. Taken in $CDCl_3$.

Following this result, water may be an integral part of the reaction process. Therefore, it was decided to add 2.8 mL (1 equivalent) of water to benzyl alcohol and DMSO, in the presence of the hybrid, followed by the same oxygenation process under illumination with white light for 6 hours. The mixture was analysed by ^{1}H NMR. By analysing the ratio between the aldehyde proton signal (9.87 ppm) from newly formed benzaldehyde and the signal of CH_2 group of benzyl alcohol (4.52 ppm) it was possible to get an approximate percentage of conversion of benzyl alcohol to benzaldehyde (0.158 %), which suggested a mild improvement when using water in the solution. This is in agreement with the postulation of a water-based catalysis, where water is needed for the formation of the reactive species the data could point to a mechanism involving the oxygen reduction reaction producing strong oxidising agents such as peroxide in a two-electron transfer step.[10, 202]

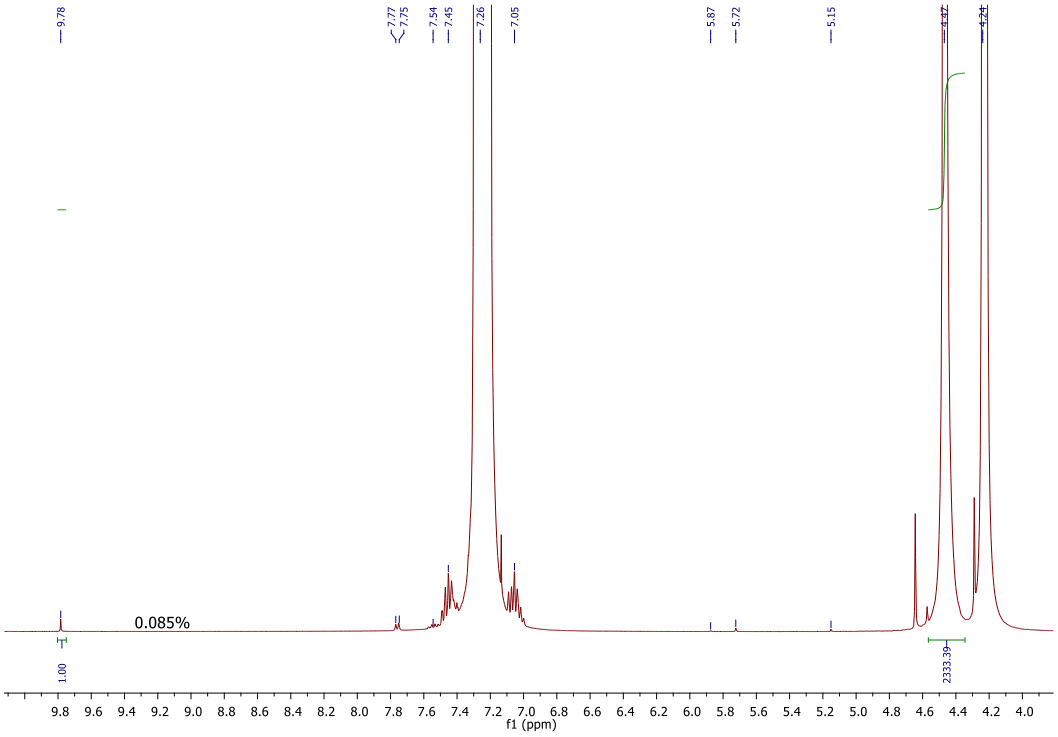

Figure 111: ^{1}H NMR of the reaction mix of benzyl alcohol and benzaldehyde with Pnz-G. Taken in $CDCl_3$.

The reaction was also repeated without water or oxygen saturation, but this showed very low activity (Figure 111). Next, the same reaction was tested without oxygen but with water and it was found that the conversion percentage dropped only slightly in comparison to water and oxygen containing conditions. This poses the idea that both oxygen level and water are needed for the reaction but with water having a much more dominant effect. From these findings it was concluded that water and oxygen are required for the catalysis of this type of reaction.

Due to the high activity of Pnz-G for dye removal in alkaline media, it was decided to investigate the reactivity of the catalyst with benzyl alcohol carried out in alkaline conditions with oxygen bubbled and water present. Using the conditions established for MB and RhB, 0.06 mL of NaOH (1 M) was added to the solution keeping the water content unchanged. The results showed a slight decrease in the conversion compared to either Pnz-G with oxygen bubbled in water or just water experiments, showing that NaOH has no positive effect on the oxidation of benzyl alcohol.

Using the optimal conditions for Pnz-G and the optimal mass loading for each individual catalyst, the reaction was undertaken with Pur-G, Fsc-G and Chr-G. The difference between these experiments is that Chr-G and Pur-G were run in the dark. The NMR data of these reactions (Table 24) showed that Fsc-G had an almost identical conversion percentage as Pnz-G, which would suggest a very similar mechanism of reactivity. Meanwhile, the conversion percentage for Chr-G is decreased to a similar value seen in Pnz-G under alkaline conditions.

Entry	Hybrid	Oxygen	Water	Conversion (%)
1	X	√	√	0.017
2	Pnz-G	√	x	0.114
3	Pnz-G	√	√	0.158
4	Pnz-G	x	√	0.146
5	Pnz-G	x	x	0.085
6	Pnz-G	√	√ - alkaline	0.133
7	Fsc-G	√	√	0.154
8	Chr-G	√	√	0.136
9	Pur-G	√	√	0.163
Literature	TiO_2	√	x	0.2

Table 24: The conversion conditions and percentages for benzyl alcohol, as calculated through NMR spectroscopy. One literature source is added for comparison.[131, 203]

Compared to the literature, the dye-graphene hybrids are slightly less effective than TiO_2 for benzyl alcohol conversion, however it can be noted that this reaction was performed for 5 hours and using a white light source, compared to 6 hours and UV light in the literature.[97, 131, 203] As seen with other comparisons, the quantity of catalyst used is also much smaller than the literature's 0.1-0.3 g.[131, 203] It can also be noted that the same conversion by Pd/TiO_2 yields 2.7 % benzaldehyde and was increased to 81.9 % by increasing the temperature to 90 °C, which could be used to modify the conditions used in future.[203] These conditions were not used in this instance as the reactions were used to understand the results observed in Chapter 4 and therefore were kept as close as possible to the conditions in Chapter 4.

5.3.3 Hydroxy Radical Testing

The initial tests with benzyl alcohols indicated a potential mechanism involving hydroxy radicals. To prove this hypothesis, it was determined that the use of probes specific for hydroxy radical detection was necessary. Thus, terephthalic acid (TA) and naphthalene boronic acid have been chosen as the model compounds.

Terephthalic Acid

The first fluorescent probe used for the detection of hydroxy radicals was TA, which is a positive probe that gains a fluorescent signature around 425 nm when hydroxy radicals are present, in the literature.[204]

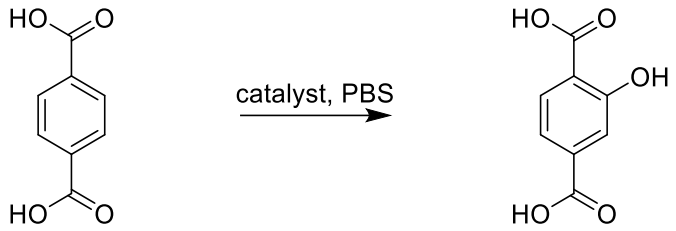

Scheme 34: The conversion of terephthalic acid to hydroxy-terephthalic acid in PBS buffered water. Catalyst = Pnz-G, Fsc-G, Pur-G or Chr-G.

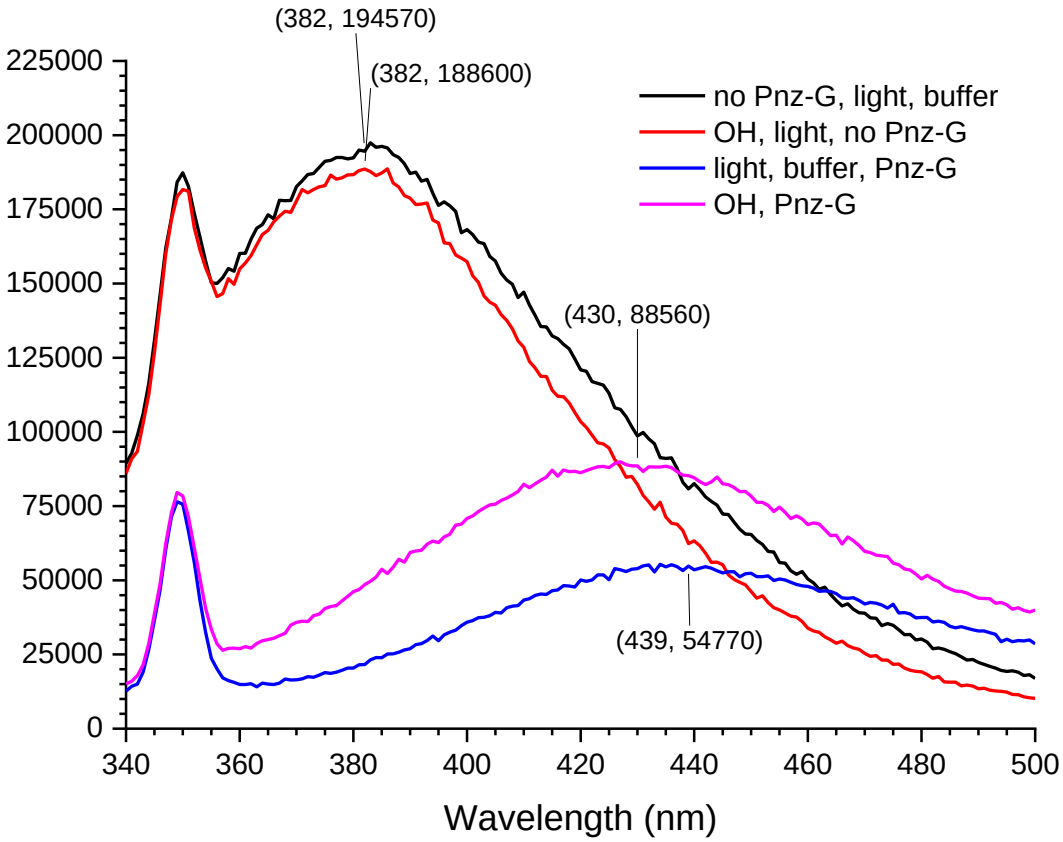

Figure 112: The emission spectra of the reaction mixtures of TA and Pnz-G. Ex 325 nm, Em 431 and 440 nm. 3 nm slit widths. Concentration of TA = 9 µM.

The neutral and basic conditions were both tested for Pnz-G, Pur-G, Fsc-G, Chr-G (Figure 112). Acidic conditions were untested due to the insolubility of TA.

For the experiments carried out in neutral conditions, an aqueous phosphate buffered saline (PBS; at pH 7) were used in order to solubilise TA in water. The reaction solution was made up to saturation, which was a concentration of 9 µM of TA. During the experiment, a control was set up to monitor any changes in TA fluorescence caused by a potential precipitation of TA. However, no changes have been detected.

The reaction of TA in the presence of Pnz-G showed a new peak at 439 nm, which can be attributed to the formation of hydroxy-terephthalic acid from TA. A total conversion within the 1-hour time period was achieved, when 9 µM of TA and 2 mg of Pnz-G in 3 mL of PBS were used. The catalyst was also filtered off using 0.22-micron pore size syringe filters prior to fluorescence measurements to ensure it would not interfere with the signals.

However, it was decided that the loading of catalyst was likely excessive for the quantity of TA in solution, so the alteration was made to match the loading of Pnz-G to those used in the tests with MB. The results obtained were similar, with only the 439 nm peak remaining after 1 hour of illumination with Pnz-G. This result strengthens the postulation that hydroxy radicals are being formed in solution and are responsible for the reactivity seen with Pnz-G.

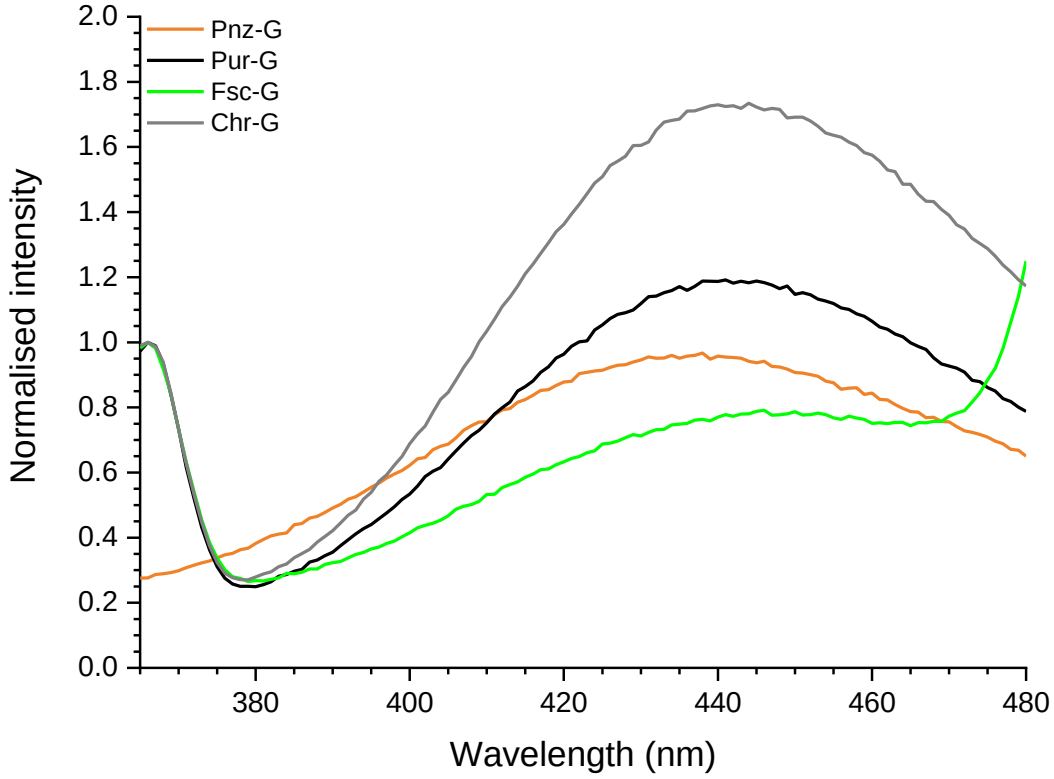

Figure 113: The emission spectrum for all hybrids when reacted with TA in phosphate buffered water. Ex 325 nm, Em approx. 440 nm, 3 nm slit widths. TA concentration was 9 µM.

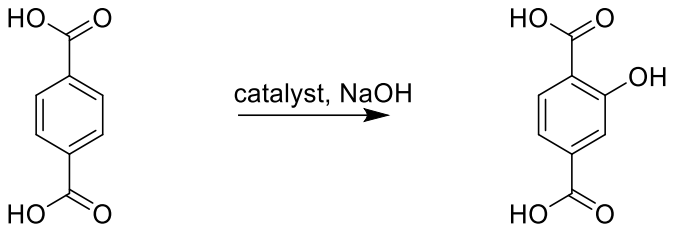

Scheme 35: The conversion of terephthalic acid to hydroxy-terephthalic acid in sodium hydroxide solution. Catalyst = Pnz-G, Fsc-G, Pur-G or Chr-G.

When this test was repeated with Pur-G, Fsc-G and Chr-G, the results showed a change in the exact peak position, 442 nm, 446 nm and 442 nm for Pur-G, Fsc-G and Chr-G, respectively (Figure 113). This observation supports the idea that the active hybrids promote the formation of hydroxy radicals in this reaction and this process occurs in the dark for Pur-G and Chr-G, whilst it was light induced for Fsc-G and Pur-G. This suggests a capability to form ROS forming materials through the simple modification of graphene layers without the intricacies of single layer modification.

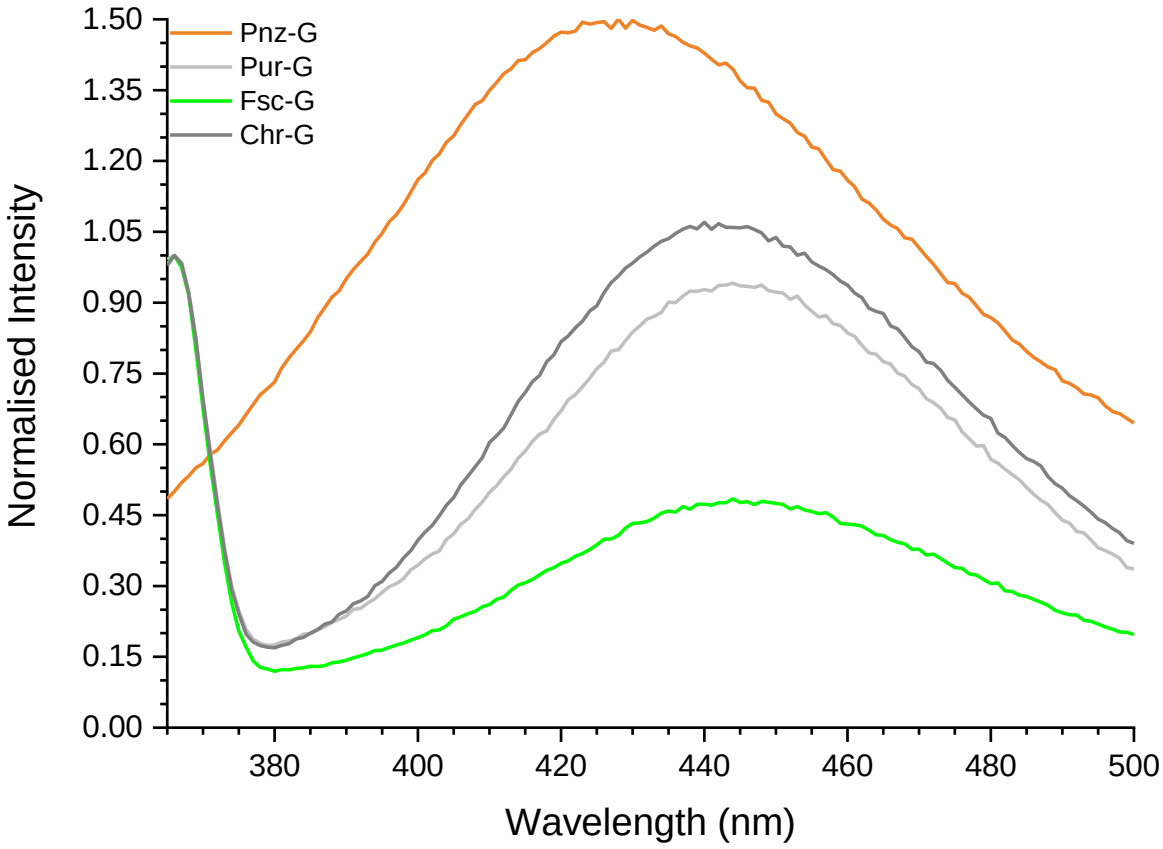

Figure 114: The emission spectrum for all hybrids when reacted with TA in water and sodium hydroxide. Ex 325 nm, Em approx. 440 nm (Pur-G, Fsc-G, Chr-G), 430 nm (Pnz-G), 3 nm slit widths. TA concentration was 9 µM.

Under the alkaline conditions, there is a small change in the position of the emission band to that observed in the neutral conditions (Figure 114). The reason for this is unclear as the entire spectrum has a blue shift. However, an effect due to errors in the excitation wavelength can be excluded as this experiment was repeated several times.

The formation of similar fluorescence maxima suggests that the same reaction occurs, which is the hydroxylation of TA by hydroxy radicals, as postulated for neutral conditions. This is also supported by the fact that hybrids have fluorescent signatures outside of this region, as described in Chapters 2 and 3. However, the counts are much lower in alkali conditions for Chr-G and Pur-G, which suggests a lower radical formation activity in alkaline conditions. This explains the reduced reactivity of hybrids towards RhB in alkaline conditions, whilst allowing the high reactivity towards MB to be accounted by MB degradation in alkaline media.

Meanwhile Pnz-G, which maintained fair reactivity in alkaline media, has a much greater count than in neutral conditions. This suggests that the hybrid has a greater photoactivity when exposed to alkaline conditions.

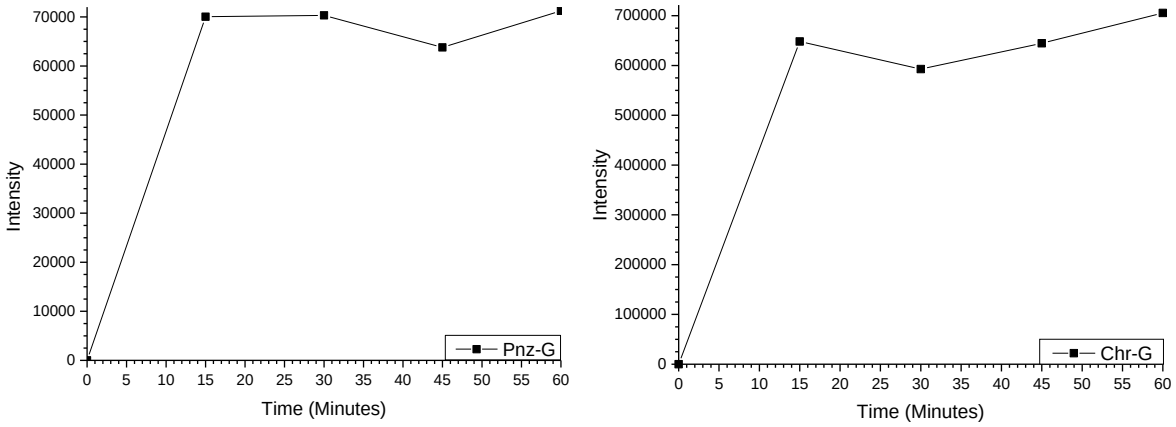

Figure 115: The kinetics plot for Pnz-G (left) and Chr-G (right) hydroxylation of TA in PBS solution at pH 7.

To understand the kinetics of the process, the hydroxylation of TA with a lower loading of catalyst was attempted. An aliquot from the solution was taken, filtered and scanned every 15 minutes during illumination (Figure 115). It was found that at 15 minutes the reaction was almost complete, and the fluorescence plateaued within the next 15 minutes. This indicates that the reaction is rapid and that it would be difficult to monitor kinetics unless a way could be found to get a higher concentration of TA in the solution without increasing the volume.

The reaction was analysed by HRMS to identify potential products formed in the reaction. The reaction does convert terephthalic acid leading to either a mono-hydroxylated or a multi-hydroxylated product. This shows that this reaction can continue to go rapidly and helps to explain a shift observed in Pnz-G's

products. It also shows that there is insufficient TA in solution for this reaction to be kinetically studied under these conditions, as the fluorescence peak for TA is lost within 15 minutes and the new peak is unchanged from 15 minutes.

These results strongly suggest hydroxy radical formation being the cause of reactivity in these materials. However, this analysis is limited by the substrate concentration and requires alternative tests. Also, it requires testing of the acidic conditions to narrow down the mechanistic reasons for the reactivity observed for these hybrids.

2-Naphthylboronic Acid Study

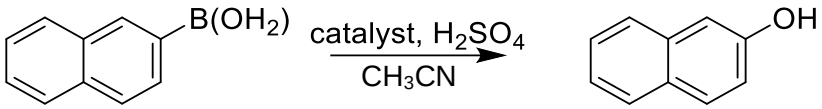

Scheme 36: The expected conversion of naphthalene-2-boronic acid to 2-naphthol in acetonitrile and sulphuric acid.

For a second test, it was decided that naphthalene-2-boronic acid would be useful as a probe for acidic conditions, which were previously untested. The probe is used to detect hydroxyl radicals through a conversion to naphthol, as described in scheme 36.

The reaction with naphthalene-2-boronic acid was carried out in acetonitrile, due to its low solubility in water, with a small volume of concentrated sulphuric acid (98 %). A low reactivity was observed, and it was postulated that the low water content, in comparison to the TA reactions, could be a contributing factor in this.

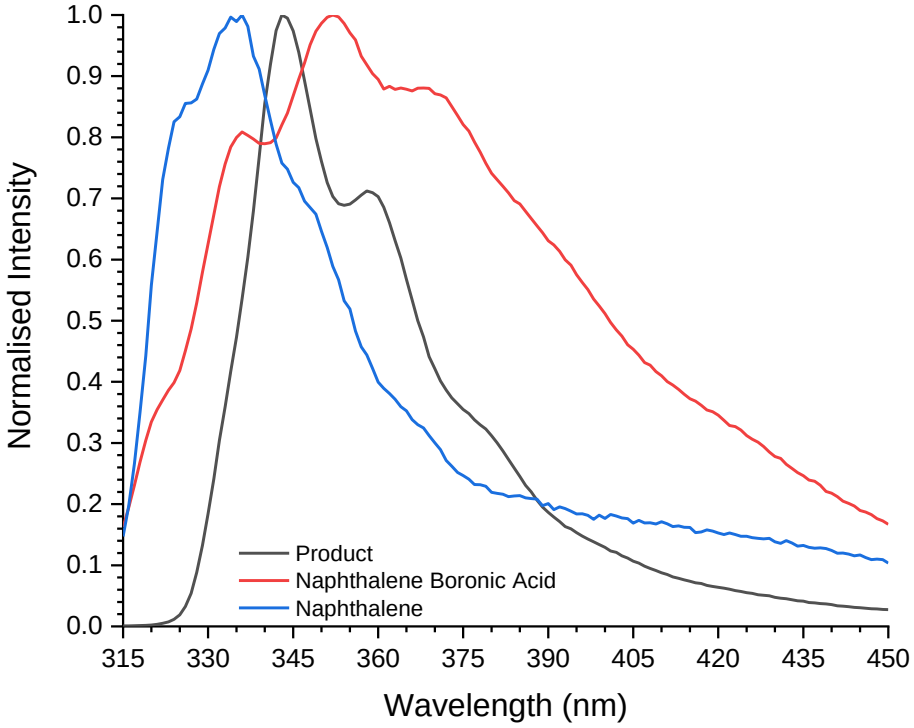

Figure 116: The normalised emission spectra of i) the products formed by mixing Pnz-G and 2-naphthylboronic acid, ii) naphthalene and iii) naphthalene boronic acid in acetonitrile and sulphuric acid. Excitation wavelength = 290 nm, 3 nm slit widths.

However, it also became apparent that the reaction pathway under these conditions with Pnz-G were not as simple as with TA. This was due to the shifting/formation of two additional peaks (Figure 116). Also, these peaks do not match the fluorescence peak of 2-naphthol reported in the literature where naphthalene boronic acid was a probe[172] and were assumed to be due to a dissociation type reaction forming naphthol and naphthalene. Therefore, it was necessary to analyse the fluorescence of the starting material and products individually, in order to understand the mechanism and reactivity for this probe. The naphthalene 2-boronic acid showed a main peak with two shoulders (Figure 116, red), which were assumed to be due to small quantities of naphthalene and 2-naphthol, either as impurities of manufacture or slow dissociation reactions with water. Naphthalene showed an emission peak at approximately 334 nm, which matches one of the shoulders in the naphthalene 2-boronic acid and is missing from the reaction product. This could explain previous lack of reactivity in acidic media, as the data shows that there is not a single reaction involving hydroxyl occurring, as seen in neutral and alkaline media with terephthalic acid. However, the actual pathway involved is uncertain.

The reaction products were analysed by HRMS (Figure 117). Boronic acid was still present in the mixture at 254.0991 m/z, while 2-naphthol was detectable at 167.0258 m/z and 202.0067 m/z when paired with sodium and potassium ions, respectively. The interesting peak was a 282.2686 m/z, which

would match with di-2-naphthylborinic acid, which could be an alternate product of the reaction. NMR data also suggests that di-2-naphthylborinic acid may be present in the crude product.

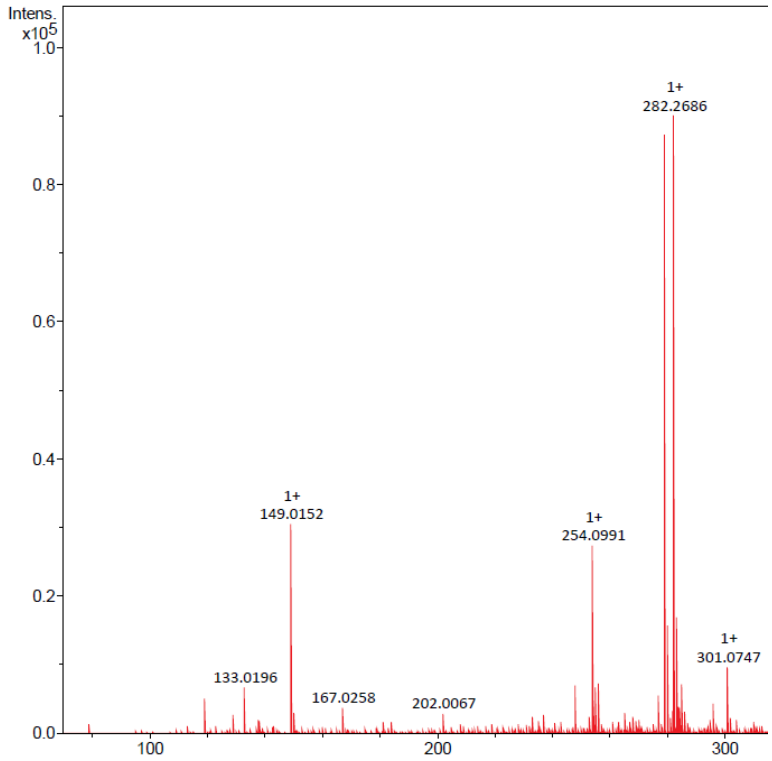

Figure 117: HRMS of the photochemical conversion of naphthalene 2-boronic acid by Pnz-G.

5.4 Conclusion

From the data collected in this chapter and previous chapters, the most likely mechanism for the active hybrids is the formation of reactive oxygen species for the degradation of the pollutants. Given some of the reactions reduced reactivity when there were low water or alkaline levels could suggest a mechanism involving the formation of hydroxy radicals from water or hydroxide, whilst the marginal increase in activity when bubbling O_2 into benzyl alcohol could suggest an oxygen based pathway.[124] Using STS data, it can be seen that the electronic band gap of Pnz-G is from -0.45 eV to 0.65 eV, while the optical band gap is approximately 1.95 eV. As the Pnz-unit is responsible for the light absorption, the photoactivity can be defined by HOMO-LUMO values of the dye. It can be estimated from STS data and optical band gap that the energy of HOMO is -1.3 eV and LUMO is +0.65 eV. Given this, the most likely processes in the dark reactions are oxygen-based radical species formation, such as O_2/H_2O_2 and $O_2/O_2^{-\cdot}$ which could each lead to the formation of hydroxyl radicals.[70, 97, 124] With illumination, the potential would be much more negative than the oxygen and water redox reactions would require, suggesting that there could be an electron transfer to the substrate dye or the graphene surface under light excitation.[124] For the other dyes, it could be suggested that illumination for Fsc-G was similar to

with Pnz-G, whilst Chr-G and Pur-G may only use the O_2/H_2O_2 mechanism with reduced effectivity due to different HOMO-LUMO to Pnz-G due to the different attached molecules and their different, but unanalysed band gaps. This also explains the low reactivity in acidic conditions as $2H^+$ converts two dioxygen radicals to H_2O_2 and O_2, reducing the active species in solution.[205]

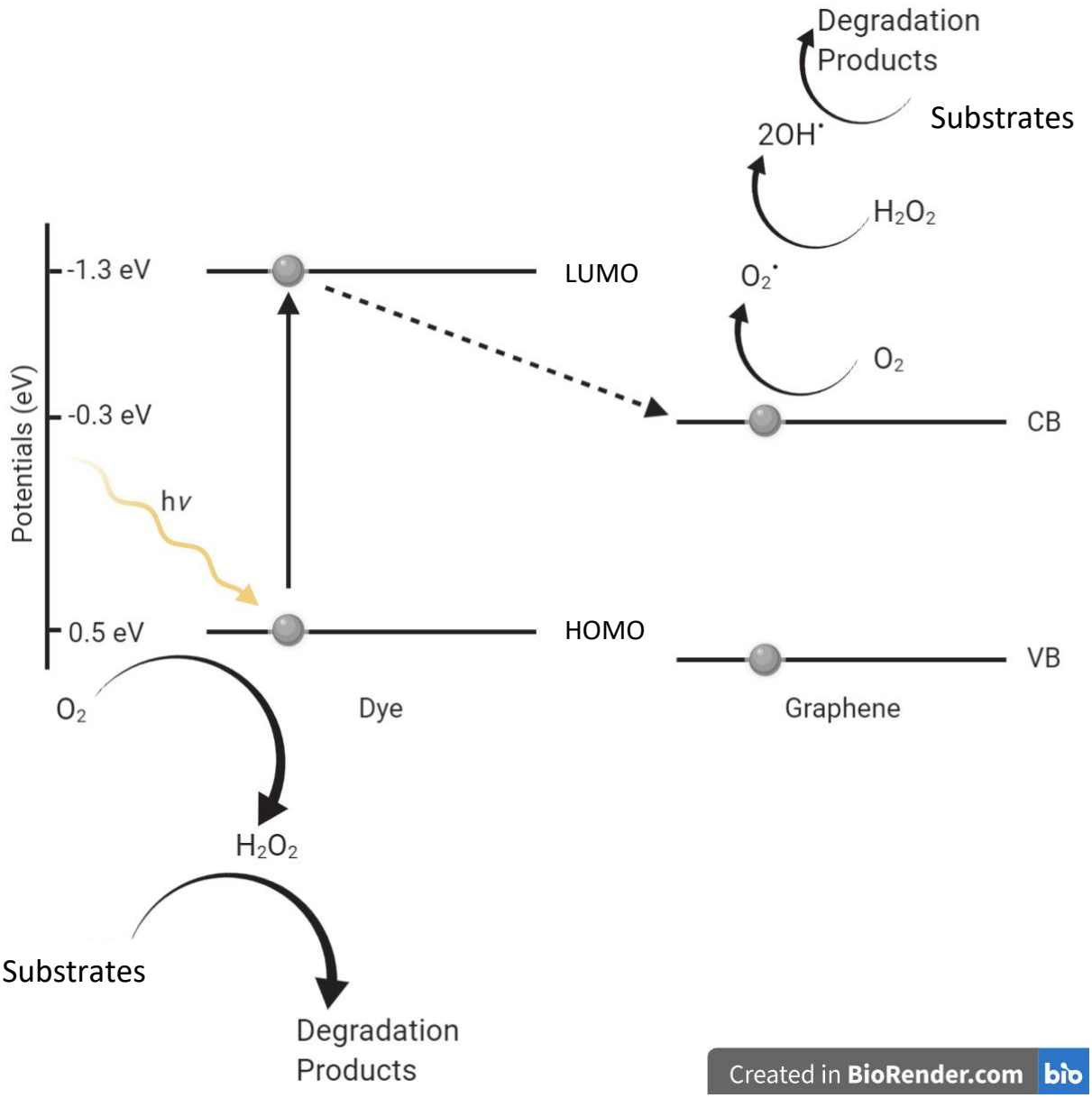

Figure 118: The postulated mechanism of Pnz-G using STS data, reaction mechanisms and information from literature sources (124, 205). Not to scale. Created with BioRender.com.

The mechanistic studies of the hybrid materials suggest a pathway involving the hydroxy radical formation as part of their catalytic activity. The positive results involving terephthalic acid as a fluorescence probe for the hydroxy radical detection show the formation of hydroxylated TA product, with no remaining signal from the starting material. Additionally, this reaction is rapid enough that the

original terephthalic acid fluorescence peak is no longer visible after 15 minutes. However, the kinetics of the process is difficult to monitor due to a low solubility of TA in water.

In addition, naphthyl 2-boronic acid shows a possible dissociative reaction, whereby both naphthalene and 2-naphthol are formed at slower rates, giving some unusual and difficult to explain data. The main fluorescence peak does appear to be naphthalene, making the reactivity in acidic medium more complex.

It has also been shown that this process is much slower when the conditions are altered to benzyl alcohol being the substrate and solvent. With small quantities of water present the catalytic process's activity increases, suggesting that these graphitic (photo)catalysts catalyse through an oxygen reduction process.

In order to fully understand this, it may be necessary to expand the range of organic molecules tested for activity to other probes, especially for the acidic conditions which were not fully explained in this work.

5.5 Experimental

5.5.1 Initial Redox Testing

A solution of a substrate in H_2O (100 µL; 4.1 mM) was added into each well of a 24-well plate, as shown in Figure 119, followed by the addition of the catalyst suspension (Pnz-G (1 mg), MDAP (1 mg) or graphene (1 mg) in 1 mL) as described. The reaction was run for 2 hours and followed by starch iodide test and pH test.

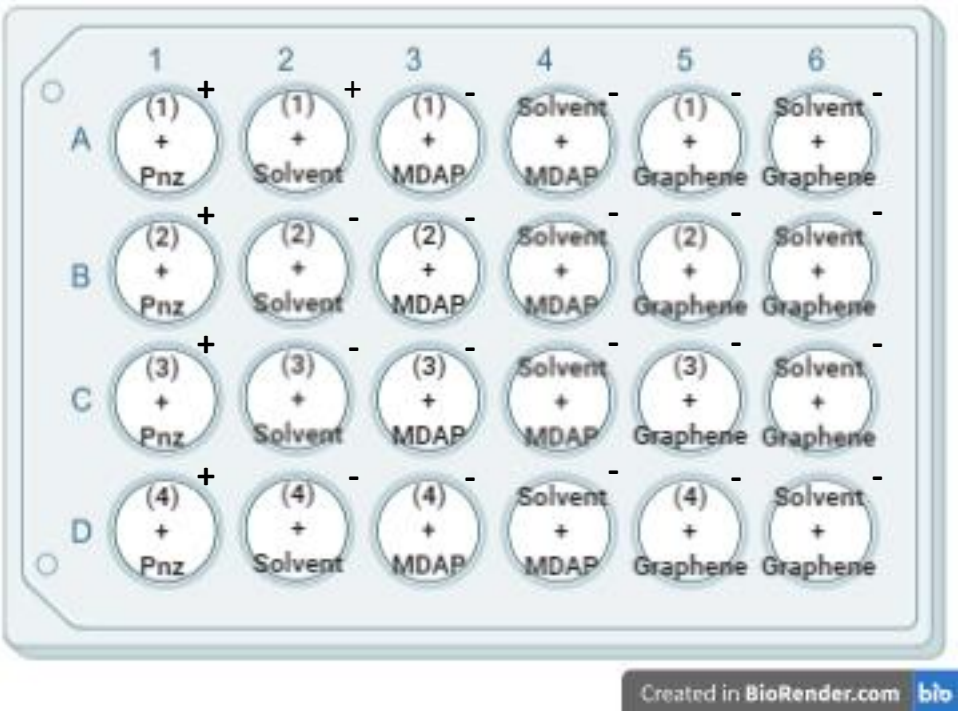

Figure 119: The well plate setup used for the reaction with the reagents listed in each well. (1) = benzyl alcohol; (2) = aminobenzyl alcohol; (3) = 4-methoxybenzyl alcohol; (4) = nitrobenzene. + = positive test, - = negative test. Created using BioRender.com.

The control of Pnz-G with water was run separately at the same scale and repeated due to the positive starch iodide test.

5.5.2 Benzyl Alcohol Study

Ambient: Pnz-G (1.5 mg) was added to a solution of benzyl alcohol (5 mL) and DMSO (0.15 mL). The solution was stirred and illuminated with white light. At 5 hours the reaction was analysed by NMR spectroscopy. Conversion = 0.085 %.

Ambient with water: Pnz-G (1.5 mg) was added to a solution of benzyl alcohol (5 mL), H_2O (1.8 mL) and DMSO (0.15 mL). The solution was stirred and illuminated with white light. At 5 hours the reaction was analysed by NMR spectroscopy. Conversion = 0.146 %

Oxygen bubbled: Pnz-G (3 mg) was added to a solution of benzyl alcohol (10 mL) and DMSO (0.3 mL). The solution was bubbled with oxygen gently for 15 minutes before sealing and illuminating with white light. The reaction was monitored hourly by TLC. The first mixture attempted was 1:1 EtOAc/hexane with an aliquot of starting material which was not suitable. This was then changed to 3:1 hexane/EtOAc, which provided suitable Rf. At 5 hours the new band had no longer changed in size, so the reaction was analysed. GCMS showed very small amounts of aldehyde, LCMS was inconclusive, whilst NMR gave an aldehyde peak with the ability to get a percentage conversion. Conversion = 0.114 %.

Oxygen bubbled with water: Pnz-G (1.5 mg) was added to a solution of benzyl alcohol (5 mL), H_2O (1.8 mL) and DMSO (0.15 mL). The solution was stirred and illuminated with white light. At 5 hours the reaction was analysed by NMR spectroscopy. Conversion = 0.158 %.

This was repeated with the other active catalysts (1.5 mg). The conversions were as follows:
Pur-G = 0.163 %; Fsc-G = 0.154 %; Chr-G = 0.136 %.

Oxygen bubbled with alkaline water: Pnz-G (1.5 mg) was added to a solution of benzyl alcohol (5 mL), H_2O (1.6 mL), NaOH solution (0.2 mL; 1 M) and DMSO (0.15 mL). The solution was stirred and illuminated with white light. At 5 hours the reaction was analysed by NMR spectroscopy. Conversion = 0.133 %.

5.5.3 Terephthalic Acid

Neutral: A stock of TA (15 mg) was made up in PBS (100 mL). The stock (3 mL) was added to a cuvette with Pnz-G (150 µg). The reaction was run for 1 hr with light illumination and analysed by fluorescence spectroscopy. This was then repeated with the other active hybrids using the same mass loading.

Alkaline: A stock of TA (15 mg) was made up in water (100mL) with NaOH solution (6.6 mL; 1 M). The stock (3 mL) was added to a cuvette with Pnz-G (150 µg). The reaction was run for 1 hr with light illumination and analysed by emission spectroscopy with excitation at 312 nm and emission at 432 nm. This was then repeated with the other active hybrids using the same mass loading.

Both procedures were repeated with Fsc-G, Pur-G and Chr-G using optimised masses from Chapter 4.

5.5.4 Naphthalene 2-Boronic Acid Study

H_2O (0.75 mL) and H_2SO_4 (98 %; 0.75 mL) were added to acetonitrile (15 mL) and naphthalene 2-boronic acid (25 mg) was dissolved into the solution. This was divided into five portions, with one standard and the others had catalyst added. The additions were Pnz-G (1.1 mg) or Pur-G (0.8 mg) or Fsc-G (1.2 mg) or Chr-G (1.2 mg). The reaction was run for 1 hour 20 minutes then it was filtered and analysed by fluorescence spectroscopy. For Pnz-G and Fsc-G the reaction was done under light illumination.

6. Thesis Conclusion and Future Work

From the work carried out in this project, it can be concluded that five hybrids had been formed from the reaction of graphene with organic diazonium salts. Previous literature has shown that diazonium salts are one of many ways to modify the graphene sheet and have an approximate 20 % coverage maximum, though these hybrids are approximated as having a maximum of 14 % coverage by TGA analysis. [32, 33] It has also been shown in the literature that modification of surfaces can increase the activity of the surface through the addition of active molecules or clusters such as dyes or TiO_2. [102, 106, 110]

The methodology used was split into two groups: (i) a two-step diazonification reaction using tetrafluoroboric acid to form and isolate a stable diazonium, followed by mixing the diazonium with graphene in ethanol and white light illumination to chemically graft the dye to the graphene surface; and (ii) a one-pot method which combines the two steps into one reactive mixture allowing for the use of less thermally stable diazonium salts in hybrid fabrication. This synthesis is the first example of a dye directly attached to graphene without the use of linkers or bridges.

The hybrids were characterised using various analytical techniques. PXRD analysis showed a slight shift in the PXRD peak of 2θ = 0.3-0.5 ° for the graphitic region along with an increase in the width of this peak by between 35-60 % for most hybrids, whilst Fsc-G and Chr-G showed 0 and 5 % decrease in width respectively. This suggested a loss of crystallinity and increase of disorder in most cases, which is also confirmed by Raman spectra where intensity of the D-band of the spectrum increases in respect to the G-band for Pnz-G. UV-vis and fluorescence analysis also showed changes from the free dyes to the hybrid materials, further suggesting modification due to changes to the chromophore. For Fsc-G the UV-vis was red shifted to 435 nm from 422 nm, whilst other hybrids were blue shifted such as Pnz-G with a shift from 480 nm to 465 nm. Fluorescence showed a 30 nm red shift for Pnz-G and a 10 nm blue shift for Fsc-G.

During the photoactivity tests, these hybrids were shown to have effect on the degradation of MB and RhB, both with and without light. It was noted that there was a trend for an increased reactivity with increased pH for the degradation MB. Pnz-G and Fsc-G both showed very good photoinduced activities with 44 % and 70 % irreversible removal, respectively, over a 20-minute period and using a concentration range of 50-67 µg/mL. It was shown that Fsc-G and Pnz-G can perform repeatable full degradation over several 2-hour cycles. Their activity can be regenerated by washing the samples when the degradation rate or total begins to reduce. Generally, the hybrids showed to be more effective when the solution was illuminated with white light than when it was not irradiated. In some conditions, they can also compete with TiO_2 as a catalyst for these reactions.[114, 117]

RhB showed less promising reactivities and had little effect when irradiated with white light compared to the data obtained in the dark. This could be due to the RhB excitation not creating the instability that MB excitation does, or it could be an ineffectiveness of the hybrids (or the hybrids activity pathway) at degrading RhB. The best examples were shown to be Pnz-G in neutral conditions and illuminated with white light for 76 % removal and 50 % degradation, an improvement over its activity with MB. The best reversible removal of RhB was observed with neutral conditions Pur-G while illuminated with white light. Compared to other literature photocatalysts tested on RhB, the more active hybrids were able to perform similarly or better, which is a promising start for these hybrids. [65, 124]

When studying the mechanism, it was shown that benzyl alcohol could be converted to benzaldehyde by all the hybrids in their most optimal conditions. However, this reaction could only show up to 0.16 % conversion and requires further study to find optimal conditions for such reactions if they were to be an application for these materials. Additionally, it was found that both water and oxygen had an importance within this reaction. This linked to a low reactivity with naphalene-2-boronic acid, which lead to the formation of multiple products in acidic media and suggested that the reduced water content of the reaction could hinder the hybrids' reactivity. Then, fluorescence monitoring of terephthalic acid in alkali and neutral conditions showed a rapid and complete conversion to hydroxy-terephthalic acid, which showed that the mechanism involves the reactive hydroxyl radical.

Using STS data for Pnz-G and the reactions above, it was suggested that the reactivity was likely due to a redox pathway involving oxygen and the formation of either peroxide (which could break down to hydroxyl radicals) or the formation of superoxide radical (which could interact with water to form hydroxyl radicals and other reactive oxygen species).[124] This was due to the low reactivity without the addition of water to the reaction mixture and the optimum condition requiring oxygen bubbling into the solution. STS gave approximation for the energy levels of Pnz-G which give an idea of how well the hybrid can interact with oxygen and water, which is proposed as being preferable with H_2O_2 or $O_2^{\cdot}$ formation.

This work still leaves some questions open, as the reactivity with benzyl alcohol is much reduced compared to MB, and there is question as to whether the introduction of a third part of the system, such as TiO_2, could aid the catalytic performance of these hybrids as seen with TiO_2 and graphene oxide.[123] There are also further tests of activity with a scaled up quantity of catalyst and substrate, in order to move closer towards real word application. Alternatively, more organic dyes could be investigated in graphene modification to catalyse the degradation of wastewater dyes and oxidation

reactions. The scale of testing for the hybrid materials could also be expanded from those seen to a greater number shown within the literature for both organic molecules and inorganic materials.[70, 129]

Additionally, some analyses were unable to be completed, especially for Thi-G and would be good to be completed in future works in this area. Each hybrid could undergo solid state NMR analysis to better understand the structure and zeta-potential could be used to see the stability of the dispersed graphitic platelets in solution. There is also the possibility to use gradually increasing concentrations of the dyes and TGA or UV-vis analysis to gain a clearer insight into the percentage of the surface that has been modified by the dyes used.

The methodology for the fabrication of the hybrids could also be scaled up to make a larger quantity, which could then be used for application testing. The methodology could be expanded to other materials that can interact with diazonium functional groups, similarly to graphene, to allow modification of their surfaces. Applications could be in catalysis of organic reactions similar to those tested herein, the treatment of dyehouse wastewater, or test the capability to function within a solar cell.

The methodology could also be altered and used to form hydro- and aerogels from such materials and create a three-dimensional catalytic material. This would result in a greater ease in the application, isolation, and reuse of the materials, as some experiments showed gradual loss of material during cleaning cycles. This would also include the development of methods to attempt gelation of the materials made in this thesis and ensure they are still catalytically active.

An investigation into the electrochemical properties, through methods such as cyclic voltammetry in organic solvents, could be used to further study the hybrids described in the thesis. This could be attempted under both illuminated, dark and ambient conditions to see the difference made by the light illumination. Additionally, this could be performed to test for any oxygen-based reaction if oxygen is permitted into the system, rather than degassing the oxygen out.

7. References

1. Novoselov, K.S., Geim, A.K., Morozov, S.V., Jiang, D., Zhang, Y., Dubonos, S.V., Grigorieva, I.V. and Firsov, A.A. Electric Field Effect in Atomically Thin Carbon Films. *Science.* 2004, **306**(5696), p.666.
2. Sergeeva, N.N., Chaika, A.N., Walls, B., Murphy, B.E., Walshe, K., Martin, D.P., Richards, B.D.O., Jose, G., Fleischer, K., Aristov, V., Molodtsova, O.V., Shvets, I.V. and Krasnikov, S.A. A photochemical approach for a fast and self-limited covalent modification of surface supported graphene with photoactive dyes. *Nanotechnology.* 2018, **29**(27), p.275705.
3. Hu, M., Yao, Z. and Wang, X. Graphene-Based Nanomaterials for Catalysis. *Industrial and Engineering Chemistry Research.* 2017, **56**, pp.3477 - 3502.
4. Torres, T. Graphene chemistry. *Chemical Society Reviews.* 2017, **46**(15), pp.4385-4386.
5. Singh, V., Joung, D., Zhai, L., Das, S., Khondaker, S.I. and Seal, S. Graphene based materials: Past, present and future. *Progress in Materials Science.* 2011, **56**(8), pp.1178-1271.
6. Krishnan, A., Dujardin, E., Treacy, M.M.J., Hugdahl, J., Lynum, S. and Ebbesen, T.W. Graphitic cones and the nucleation of curved carbon surfaces. *Nature.* 1997, **388**(6641), pp.451-454.
7. Li, X., Yu, J., Wageh, S., Al-Ghamdi, A.A. and Xie, J. Graphene in Photocatalysis: A Review. *Small.* 2016, **48**, pp.6640-6696.
8. Faraldos, M. and Bahamonde, A. Environmental applications of titania-graphene photocatalysts. *Catalysis Today.* 2017, **285**, pp.13-28.
9. Spettel, K.E. and Damrauer, N.H. Exploiting Conformational Dynamics of Structurally Tuned Aryl-Substituted Terpyridyl Ruthenium(II) Complexes to inhibit Charge Recombination in Dye-Sensitized Solar Cells. *Journal of Physical Chemistry.* 2016, **120**, pp.10815-10829.
10. Navalon, S., Dhakshinamoorthy, A., Alvaro, M., Antonietti, M. and Garcia, H. Active sites on graphene-based materials as metal-free catalysts. *Chemical Society Reviews.* 2017, **46**(15), pp.4501-4529.
11. Wang, H.-X., Wang, Q., Zhou, K.-G. and Zhang, H.-L. Graphene in Light: Design, Synthesis and Applications of Photo-active Graphene and Graphene-Like Materials. *Small.* 2013, **9**(8), pp.1266-1283.
12. Wang, Q.H., Jin, Z., Kim, K.K., Hilmer, A.J., Paulus, G.L.C., Shih, C.-J., Ham, M.-H., Sanchez-Yamagishi, J.D., Watanabe, K., Taniguchi, T., Kong, J., Jarillo-Herrero, P. and Strano, M.S. Understanding and controlling the substrate effect on graphene electron-transfer chemistry via reactivity imprint lithography. *Nature Chemistry.* 2012, **4**, pp.724-732.
13. Navalón, S., Herance, J.R., Álvaro, M. and García, H. Covalently Modified Graphenes in Catalysis, Electrocatalysis and Photoresponsive Materials. 2017, **23**(61), pp.15244-15275.
14. Eigler, S., Hu, Y., Ishii, Y. and Hirsch, A. Controlled functionalization of graphene oxide with sodium azide. *Nanoscale.* 2013, **5**, pp.12136-12139.
15. Li, J., Li, M., Zhou, L.-L., Lang, S.-Y., Lu, H.-Y., Wang, D., Chen, C.-F. and Wan, L.-J. Click and Patterned Functionalization of Graphene by Diels−Alder Reaction. *Journal of the American Chemical Society.* 2016, **138**, pp.7448-7451.
16. Frank, B., Blume, R., Rinaldi, A., Trunschke, A. and Schlögl, R. Oxygen Insertion Catalysis by sp^2 Carbon. 2011, **50**(43), pp.10226-10230.
17. Hirsch, A., Englert, J.M. and Hauke, F. Wet Chemical Functionalization of Graphene. *Accounts of Chemical Research.* 2013, **46**(1), pp.87-96.
18. Gupta, V.K., Yola, M.L., Atard, N., Ustundag˘, Z. and Solak, A.O. A novel sensitive Cu(II) and Cd(II) nanosensor platform: Grapheneoxide terminated p-aminophenyl modified glassy carbon surface. *Electrochimica Acta.* 2013, **112**, pp.541-548.
19. Ambrosi, A., Chua, C.K., Bonanni, A. and Martin, P.M. Electrochemistry of Graphene and Related Materials. *Chemical Reviews.* 2014, **114**, pp.7150-7188.
20. Wang, S., Cui, Z. and Cao, M. A reactive-template strategy for high yeild synthesis of N-doped graphene and its modification by introduction of cobalt species for significantly enhanced oxygen reduction reaction. *Electrochimica Acta.* 2016, **210**, pp.328-336.

21. Wang, X., Wang, J., Wang, D., Dou, S., Ma, Z., Wu, J., Tao, L., Shen, A., Ouyang, C., Liu, Q. and Wang, S. One-pot synthesis of nitrogen and sulfur co-doped graphene as efficient metal-free electrocatalysts for the oxygen reduction reaction. *Chemical Communications.* 2014, **50**(37), pp.4839-4842.
22. Zhang, S., Li, J., Wang, X., Huang, Y., Zeng, M. and Xu, J. In Situ Ion Exchange Synthesis of Strongly Coupled Ag@AgCl/g-C_3N_4 Porous Nanosheets as Plasmonic Photocatalyst for Highly Efficient Visible-Light Photocatalysis. *Applied Materials and Interfaces.* 2014, **6**, pp.22116-22125.
23. Jackson, M.N., Oh, S., Kaminsky, C.J., Chu, S.B., Zhang, G., Miller, J.T. and Surendranath, Y. Strong Electronic Coupling of Molecular Sites to Graphitic Electrodes via Pyrazine Conjugation. *Journal of the American Chemical Society.* 2018, **140**(3), pp.1004-1010.
24. Nikhil, Pandey, R.K., Sahu, P.K., Singh, M.K. and Prakash, R. Fast grown self-assembled polythiophene/graphene oxide nanocomposite thin films at air–liquid interface with high mobility used in polymer thin film transistors. *Journal of Materials Chemistry C.* 2018, **6**(37), pp.9981-9989.
25. Lee, Y., Kim, H., Kim, S., Whang, D. and Cho, J.H. Photogating in the Graphene–Dye–Graphene Sandwich Heterostructure. *ACS Applied Materials & Interfaces.* 2019, **11**(26), pp.23474-23481.
26. Solis-Frenandez, P., Bissett, M. and Ago, H. Synthesis, structure and applications of graphene-based 2D heterostructures. *Chemical Society Reviews.* 2017, **46**(15), pp.4572-4613.
27. Romanova, I.P., Musina, E.I., Nafikova, A.A., Zverev, V.V., Yakhvarov, D.G. and Sinyashin, O.G. Modification of fullerene C_{60} by phosphorylated diazo compounds. *Russian Chemical Bulletin, International Edition.* 2003, **52**(8), pp.1750-1757.
28. Benazzi, E., Summers, G.H., Black, F.A., Sazanovich, I.V., Clark, I.P. and Gibson, E.A. Assembly, charge-transfer and solar cell performance with porphyrin-C_{60} on NiO for p-type dye-sensitized solar cells. 2019, **377**(2152), p.20180338.
29. Criado, A., Melchionna, M., Marchesan, S. and Prato, M. The Covalent Functionalization of Graphene on Substrates. *Angewandte Chemie International Edition.* 2015, **54**, pp.10734-10750.
30. Hopkinson, M.N., Tlahuext-Aca, A. and Glorius, F. Merging Visible Light Photoredox and Gold Catalysis. *Accounts of Chemical Research.* 2016, **49**, pp.2261-2272.
31. Schroll, P., Hari, D.P. and König, B. Photocatalytic Arylation of Alkenes, Alkynes and Enones with Diazonium Salts. *Chemistry Open.* 2012, **1**(3), pp.130-133.
32. Hari, D.P. and König, B. The Photocatalyzed Meerwein Arylation: Classic Reaction of Aryl Diazonium Salts in a New Light. *Angewandte Chemie International Edition.* 2013, **52**, pp.4734-4743.
33. Paulus, G.L.C., Wang, Q.H. and Strano, M.S. Covalent Electron Transfer Chemistry of Graphene with Diazonium Salts. *Accounts of Chemical Research.* 2013, **46**(1), pp.160-170.
34. Salmi, Z., Benmehdi, H., Lamouri, A., Decorse, P., Jouini, M., Yagci, Y. and Chehimi, M.M. Preparation of MIP grafts for quercetin by tandem aryl diazonium surface chemistry and photopolymerization. *Microchimica Acta.* 2013, **180**, pp.1411-1419.
35. Tanaka, M., Sawaguchi, T., Sato, Y., Yoshioka, K. and Niwa, O. Surface Modification of GC and HOPG with Diazonium, Amine, Azide, and Olefin Derivatives. *Langmuir.* 2011, **27**(1), pp.170-178.
36. Bakas, I., Salmi, Z., Gam-Derouich, S., Jouini, M., Lépinay, S., Carbonnier, B., Akila Khlifi, R.K., Geneste, F., Yagcie, Y. and Chehimia, M.M. Molecularly imprinted polymeric sensings layers grafted from aryl diazonium-modified surfaces for electroanalytical applications. A mini review. *Surface Interface Analysis.* 2014, **46**, pp.1014-1020.

37. Cougnon, C., Gohier, F., Belanger, D. and Mauzeroll, J. In Situ Formation of Diazonium Salts from Nitro Precursors for Scanning Electrochemical Microscopy Patterning of Surfaces. *Angewandte Chemie International Edition.* 2009, **48**, pp.4006-4008.
38. Bouriga, M., Chehimi, M.M., Combellas, C., Decorse, P., Kanoufi, F.d.r., Deronzier, A. and Pinson, J. Sensitized Photografting of Diazonium Salts by Visible Light. *Chemistry of Materials.* 2013, **25**, pp.90-97.
39. Liming, Z., Lin, Z., Mingmei, Y., Zhirong, L., Qin, X., Hailin, P. and Zhongfan, L. Photo-induced Free Radical Modification of Graphene. *Small.* 2013, **9**(8), pp.1134-1143.
40. Christie, R. *Colour Chemistry.* Royal Society of Chemistry, 2001.
41. Hari, D.P., Schroll, P. and König, B. Metal-Free, Visible-Light-Mediated Direct C−H Arylation of Heteroarenes with Aryl Diazonium Salts. *Journal of the American Chemical Society.* 2012, **134**, pp.2958-2961.
42. Wang, H., Zhanga, J., Wua, Y., Huanga, H., Lia, G., Zhanga, X. and Wang, Z. Surface modified MXene Ti_3C_2 multilayers by aryl diazonium salts leading to large-scale delamination. *Applied Surface Science.* 2016, **384**, pp.287-293.
43. Kaplan, A., Yuan, Z., Benck, J.D., Govind Rajan, A., Chu, X.S., Wang, Q.H. and Strano, M.S. Current and future directions in electron transfer chemistry of graphene. *Chemical Society Reviews.* 2017, **46**(15), pp.4530-4571.
44. Park, J. and Yan, M. Covalent Functionalization of Graphene with Reactive Intermediates. *Accounts of Chemical Research.* 2012, **46**(1), pp.181-189.
45. Shul, G., Ruiz, C.A.C., Rochefort, D., Brooksby, P.A. and Bélanger, D. Electrochemical functionalization of glassy carbon electrode by reduction of diazonium cations in protic ionic liquid. *Electrochimica Acta.* 2013, **106**, pp.378-385.
46. Bousa, D., Jankovsky, O., Sedmidubsky, D., Luxa, J., Sturala, J., Pumera, M. and Sofer, Z. Mesomeric Effects of Graphene Modified with Diazonium Salts: Substituent Type and Position Influence its Properties. *Chemistry a European Journal.* 2015, **21**, pp.17728 - 17738.
47. Liu, H., Chen, S., Steigerwald, M.L., Nuckolls, C. and Brus, L.E. Photochemical Reactivity of Graphene. *Journal of the American Chemical Society.* 2009, **131**, pp.17099-17101.
48. *H55827 4-Methoxybenzenediazonium tetrafluoroborate, 98%* [Online]. 2019. [Accessed 30.07]. Available from: https://www.alfa.com/en/catalog/H55827/
49. Yang, T., Zhang, W., Liu, R., Cui, J. and Deng, C. Preparation and photocatalytic properties of visible light driven Ag-AgBr-RGO composite. *Separation and Purification Technology.* 2018, **190**, pp.278-287.
50. Song, S., Menga, A., Jiang, S., Cheng, B. and Jiang, C. Construction of Z-scheme Ag_2CO_3/N-doped graphene photocatalysts with enhanced visible-light photocatalytic activity by tuning the nitrogen species. *Applied Surface Science.* 2017, **396**, pp.1368-1374.
51. Putri, L.K., Ong, W.-J., Chang, W.S. and Chai, S.-P. Heteroatom doped graphene in photocatalysis: A review. *Applied Surface Science.* 2015, **358**, pp.2-14.
52. Low, J., Yu, J., Li, Q. and Cheng, B. Enhanced visible-light photocatalytic activity of plasmonic Ag and graphene co-modified Bi_2WO_6 nanosheets. *Physical Chemistry Chemical Physics.* 2014, **16**, p.1111.
53. Liu, S., Liu, C., Wang, W., Cheng, B. and Yu, J. Unique photocatalytic oxidation reactivity and selectivity of TiO_2–graphene nanocomposites. *Nanoscale.* 2012, **4**(10), pp.3193-3200.
54. Lian, Y., Zhu, W., Yao, W., Yi, H., Hu, Z., Duan, T., Cheng, W., Wei, X. and Hu, G. A biomass carbon mass coated with modified TiO_2 nanotube/graphene for photocatalysis. *New Journal of Chemistry* 2017, **41**, p.4212.
55. Al-Marri, A.H., Khan, M., Khan, M., Adil, S.F., Al-Warthan, A., Alkhathlan, H.Z., Tremel, W., Labis, J.P., Siddiqui, M.R.H. and Tahir, M.N. Pulicaria glutinosa Extract: A Toolbox to Synthesize Highly Reduced Graphene Oxide-Silver Nanocomposites. *International Journal of Molecular Sciences.* 2015, **16**, pp.1131-1142.

56. Li, X., Huang, X., Xi, S., Miao, S., Ding, J., Cai, W., Liu, S., Yang, X., Yang, H., Gao, J., Wang, J., Huang, Y., Zhang, T. and Liu, B. Single Cobalt Atoms Anchored on Porous N-Doped Graphene with Dual Reaction Sites for Efficient Fenton-like Catalysis. *Journal of the American Chemical Society.* 2018, **140**(39), pp.12469-12475.
57. Ranjan, P., Tiwary, P., Chakraborty, A.K., Mahapatra, R. and Thakur, A.D. Graphene oxide based free-standing films for humidity and hydrogen peroxide sensing. *Journal of Materials Science: Materials in Electronics.* 2018, **29**(18), pp.15946-15956.
58. Guo, S., Liu, N., Ding, W., Pang, X., Ding, Z. and Chen, Y. Graphene oxide modified waterborne polyurethane-based dye with high color-fastness performance. *Journal of Applied Polymer Science.* 2021, **138**(19), p.50390.
59. Gust, D., Moore, T.A. and Moore, A.L. Realizing artificial photosynthesis. *Faraday Discussions.* 2012, **155**, pp.9-26.
60. Gust, D., Moore, T.A. and Moore, A.L. Solar Fuels via Artificial Photosynthesis. *Accounts of Chemical Research.* 2009, **42**(12), pp.1890-1898.
61. Meyer, T.J. Chemical Approaches to Artificial Photosynthesis. *Accounts of Chemical Research.* 1989, **22**(5), pp.163-170.
62. Willkomm, J., Orchard, K.L., Reynal, A., Pastor, E., Durrant, J.R. and Reisner, E. Dye-sensitised semiconductors modified with molecular catalysts for light-driven H_2 production. *Chemical Society Reviews.* 2016, **45**, pp.9-23.
63. Marchelek, M., Grabowska, E., Klimczuk, T., Lisowski, W. and Zaleska-Medynska, A. Various types of semiconductor photocatalysts modified by CdTe QDs and Pt NPs for toluene photooxidation in the gas phase under visible light. *Applied Surface Science.* 2016, **393**, pp.262-275.
64. Bai, Y., Mora-Sero, I., Angelis, F.D., Bisquert, J. and Wang, P. Titanium Dioxide Nanomaterials for Photovoltaic Applications. *Chemical Reviews.* 2014, **144**, pp.10095-10130.
65. Schneider, J., Matsuoka, M., Takeuchi, M., Zhang, J., Horiuchi, Y., Anpo, M. and Bahnmann, D.W. Understanding TiO_2 Photocatalysis: Mechanisms and Materials. *Chemical Reviews.* 2014, **114**, pp.9919-9986.
66. Kapilashrami, M., Zhang, Y., Liu, Y.-S., Hagfeldt, A. and Guo, J. Probing the Optical Property and Electronic Structure of TiO_2 Nanomaterials for Renewable Energy Applications. *Chemical Reviews.* 2014, **114**, pp.9662-9707.
67. Grätzel, M. Dye-sensitized solar cells. *Journal of Photochemistry and Photobiology C: Photochemistry Reviews.* 2003, **4**, pp.145-153.
68. Bamfield, P. *Chromic Phenomena: Technological Applications of Colour Chemistry.* 2 ed. Royal Society of Chemistry, 2010.
69. Marin, M.L., Santos-Juanes, L., Arques, A., Amat, A.M. and Miranda, M.A. Organic Photocatalysts for the Oxidation of Pollutants and Model Compounds. *Chemical Reviews.* 2012, **112**(3), pp.1710-1750.
70. Fukuzumi, S. and Ohkubo, K. Selective photocatalytic reactions with organic photocatalysts. *Chemical Science.* 2013, **4**(2), pp.561-574.
71. Ohkubo, K., Suga, K. and Fukuzumi, S. Solvent-free selective photocatalytic oxidation of benzyl alcohol to benzaldehyde by molecular oxygen using 9-phenyl-10-methylacridinium. *Chemical Communications.* 2006, (19), pp.2018-2020.
72. O'Regan, B. and Grätzel, M. A low-cost, high-efficiency solar cell based on dye-sensitized colloidal TiO2 films. *Nature.* 1991, **353**(6346), pp.737-740.
73. Buitrago, E., Novello, A.M. and Meyer, T. Third-Generation Solar Cells: Toxicity and Risk of Exposure. 2020, **103**(9), p.e2000074.
74. Marri, A.R., Black, F.A., Mallows, J., Gibson, E.A. and Fielden, J. Pyridinium p-DSSC dyes: An old acceptor learns new tricks. *Dyes and Pigments.* 2019, **165**, pp.508-517.

75. Chew, S., Wang, P., Wong, O., Hong, Z., He, M., Zhang, R., Kwong, H., Tang, J., Sun, S., Lee, C.S. and Lee, S.-T. Photoluminescence and electroluminescence of 3-methyl-8-dimethylaminophenazine. *Synthetic Metals.* 2006, **156**, pp.185-189.
76. Podemska, K., Podsiadly, R., Orzel, A. and Sokolowska, J. The photochemical behavior of benzo[a]pyrido[20,10:2,3]imidazo [4,5-c]phenazine dyes. *Dyes and Pigments.* 2013, **99**(3), pp.666-672.
77. Wang, W., Preville, P., Morin, N., Mounir, S., Cai, W. and Siddiqui, M.A. Hepatitis C Viral IRES Inhibition by Phenazine and Phenazine-Like Molecules. *Bioorganic & Medicinal Chemistry Letters.* 2000, **10**, pp.1151-1154.
78. Bisschop, A., Bergsma, J. and Konings, W.N. Site of Interaction between Phenazine Methosulphate and the Respiratory Chain of Bacillus subtilis. *European Journals of Biochemistry.* 1979, **93**, pp.396-374.
79. Wu, S.-W., Huang, H.Y., Guo, Y.C. and Wang, C.M. ALO-Patternable Artificial Flavin: Phenazine, Phenothiazine, and Phenoxazine. *Journal of Physical Chemistry C.* 2008, **112**, pp.9370-9376.
80. Villa, K., Manzanares Palenzuela, C.L., Sofer, Z., Matějková, S. and Pumera, M. Metal-Free Visible-Light Photoactivated C_3N_4 Bubble-Propelled Tubular Micromotors with Inherent Fluorescence and On/Off Capabilities. *ACS Nano.* 2018, **12**(12), pp.12482-12491.
81. Choi, W.S., Choi, I.S., Lee, J.K. and Yoon, K.R. Preparation of fluorescein-functionalized electrospun fibers coated with TiO_2 and gold nanoparticles for visible-light-induced photocatalysis. *Materials Chemistry and Physics.* 2015, **163**, pp.213-218.
82. Sjöback, R., Nygren, J. and Kubista, M. Absorption and fluorescence properties of fluorescein. *Spectrochimica Acta Part A: Molecular and Biomolecular Spectroscopy.* 1995, **51**(6), pp.L7-L21.
83. Mallard, L.M., Pimenta, M.A., Dresselhaus, G. and Dresselhaus, M.S. Raman Spectroscopy in Graphene. *Physics Reports.* 2009, **473**(5), pp.51-87.
84. Ferrari, A.C. Raman spectroscopy of graphene and graphite: Disorder, electron–phonon coupling, doping and nonadiabatic effects. *Solid State Communications.* 2007, **143**, pp.47-67.
85. Martin, D.P., Tariq, A., Richards, B.D.O., Jose, G., Krasnikov, S.A., Kulak, A. and Sergeeva, N.N. White light induced covalent modification of graphene using a phenazine dye. *Chem Commun.* 2017, **53**(77), pp.10715-10718.
86. Bottari, G., Herranz, M.A., Wibmer, L., Volland, M., Guldi, L.R.-P.D.M., Hirsch, A., Martin, N., D'Souza, F. and Torres, T. Chemical functionalization and characterization of graphene-based materials. *Chemical Society Reviews.* 2017, **46**(15), pp.4464-4500.
87. Guan, Y., Cao, W., Guan, H., Lei, X., Wang, X., Tu, Y., Marchetti, A. and Kong, X. A novel polyalcohol-coated hydroxyapatite for the fast adsorption of organic dyes. *Colloids and Surfaces A: Physicochemical and Engineering Aspects.* 2018, **548**, pp.85-91.
88. Ungar, T. Microstructural parameters from X-ray diffraction peak broadening. *Scripta Materialia.* 2004, **51**(8), pp.777-781.
89. Law, D. and Zhou, D. Chapter 3 - Solid-State Characterization and Techniques. In: Qiu, Y. et al. eds. *Developing Solid Oral Dosage Forms (Second Edition)*. Boston: Academic Press, 2017, pp.59-84.
90. Scrivens, G., Ticehurst, M. and Swanson, J.T. Chapter 7 - Strategies for Improving the Reliability of Accelerated Predictive Stability (APS) Studies. In: Qiu, F. and Scrivens, G. eds. *Accelerated Predictive Stability*. Boston: Academic Press, 2018, pp.175-206.
91. Jendrzejewska, I., Zajdel, P., Pietrasik, E., Barsova, Z. and Goryczka, T. Application of X-ray powder diffraction and differential scanning calorimetry for identification of counterfeit drugs. *Monatshefte für Chemie - Chemical Monthly.* 2018, **149**(5), pp.977-985.
92. Kozma, K., Surta, T.W., Molina, P.I., Lyubinetsky, I., Stoxen, W., Byrne, N.M., Dolgos, M. and Nyman, M. Probing the local structure of crystalline $NaBiO_3{\cdot}XH_2O$ and its acidified derivatives. *Journal of Solid State Chemistry.* 2018, **263**, pp.216-223.

93. Munir, K.S., Qian, M., Li, Y., Oldfield, D.T., Kingshott, P., Zhu, D.M. and Wen, C. Quantitative Analyses of MWCNT-Ti Powder Mixtures using Raman Spectroscopy: The Influence of Milling Parameters on Nanostructural Evolution. *Advanced Engineering Materials.* 2015, **17**(11), pp.1660-1669.
94. Aghjeh, M.R., Kazerouni, Y., Otadi, M., Khonakdar, H.A., Jafari, S.H., Ebadi-Dehaghani, H. and Mousavi, S.H. A combined experimental and theoretical approach to quantitative assessment of microstructure in PLA/PP/Organo-Clay nanocomposites; wide-angle X-ray scattering and rheological analysis. *Composites Part B: Engineering.* 2018, **137**, pp.235-246.
95. Düring, J., Alex, W., Zika, A., Branscheid, R., Spiecker, E. and Gröhn, F. Dendrimer–Dye Assemblies as Templates for the Formation of Gold Nanostructures. *Macromolecules.* 2017, **50**(18), pp.6998-7009.
96. Willkomm, J., Muresan, N.M. and Reisner, E. Enhancing H_2 evolution performance of an immobilised cobalt catalyst by rational ligand design. *Chemical Science.* 2015, **6**, pp.2727-2736.
97. Kou, J., Lu, C., Wang, J., Chen, Y., Xu, Z. and Varma, R.S. Selectivity Enhancement in Heterogeneous Photocatalytic Transformations. *Chemical Reviews.* 2017, **117**, pp.1445-1514.
98. Tai, S.-H. and Chang, B.K. Effect of nitrogen-doping configuration in graphene on the oxygen reduction reaction. *RSC Advances.* 2019, **9**(11), pp.6035-6041.
99. Favereau, L., Makhal, A., Pellegrin, Y., Blart, E., Petersson, J., Göransson, E., Hammarström, L. and Odobel, F. A Molecular Tetrad That Generates a High-Energy Charge-Separated State by Mimicking the Photosynthetic Z-Scheme. *Journal of the American Chemical Society.* 2016, **138**, pp.3752-3760.
100. Asahi, R., Morikawa, T., Irie, H. and Ohkawa, T. Nitrogen-Doped Titanium Dioxide as Visible-Light-Sensitive Photocatalyst: Designs, Developments, and Prospects. *Chemical Reviews.* 2014, **114**, pp.9824-9852.
101. Granone, L.I., Sieland, F., Zheng, N., Dillert, R. and Bahnemann, D.W. *Photocatalytic conversion of biomass into valuable products: a meaningful approach?* [Critical Review]. 2018. At: Royal Society of Chemistry: Royal Society of Chemistry.
102. Ma, Y., Wang, X., Jia, Y., Chen, X., Han, H. and Li, C. Titanium Dioxide-Based Nanomaterials for Photocatalytic Fuel Generations. *Chemical Reviews.* 2014, **114**, pp.9987-10043.
103. Augugliaro, V., Camera-Roda, G., Loddo, V., Palmisano, G., Palmisano, L., Parrino, F. and Puma, M.A. Synthesis of vanillin in water by TiO_2 photocatalysis. *Applied Catalysis B: Environmental.* 2012, **111-112**, pp.555-561.
104. Ksibi, M., Amor, S.B., Cherif, S., Elaloui, E., Houas, A. and Elaloui, M. Photodegradation of lignin from black liquor using a UV/TiO2 system. *Journal of Photochemistry and Photobiology A: Chemistry.* 2003, **154**, pp.211-218.
105. Chong, R., Li, J., Ma, Y., Zhang, B., Han, H. and Li, C. Selective conversion of aqueous glucose to value-added sugar aldose on TiO_2-based photocatalysts. *Journal of Catalysis.* 2014, **314**, pp.101-108.
106. Youngblood, W.J., Lee, S.-H.A., Kobayashi, Y., Hernandez-Pagan, E.A., Hoertz, P.G., Moore, T.A., Moore, A.L., Gust, D. and Mallouk, T.E. Photoassisted Overall Water Splitting in a Visible Light-Absorbing Dye-Sensitized Photoelectrochemical Cell. *Journal of the American Chemical Society.* 2009, **131**, pp.926-927.
107. Diak, M., Klein, M., Klimczuk, T., Lisowski, W., Remita, H., Zaleska-Medynska, A. and Grabowska, E. Photoactivity of decahedral TiO_2 loaded with bimetallic nanoparticles: Degradation pathway of phenol-1- ^{13}C and hydroxyl radical formation. *Applied Catalysis B: Environmental.* 2017, **200**, pp.56-71.
108. Zhang, J., Xia, Z. and Dai, L. Carbon-based electrocatalysts for advanced energy conversion and storage. *Science Advances.* 2015, **1**(7), p.e1500564.

109. Xiong, Z., Zhang, L.L., Ma, J. and Zhao, X.S. Photocatalytic degradation of dyes over graphene-gold nanocomposite under visible light irradiation. *Chem. Commun.* 2010, **46**(33), pp.6099-6101.
110. Appavu, B. and Thiripuranthagan, S. Visible active N, S co-doped TiO_2/graphene photocatalysts for the degradation of hazardous dyes. *Journal of Photochemistry and Photobiology A: Chemistry.* 2017, **340**, pp.146-156.
111. Mou, Z., Dong, Y., Li, S., Du, Y., Wang, X., Yang, P. and Wang, S. Eosin Y functionalized graphene for photocatalytic hydrogen production from water. *International Journal of Hydrogen Energy.* 2011, **36**(15), pp.8885-8893.
112. Cotto-Maldonado, M.d.C., Duconge, J., Morant, C. and Márquez, F. Fenton Process for the Degradation of Methylene Blue using Different Nanostructured Catalysts. *American Journal of Engineering and Applied Sciences.* 2017, **10**(2), pp.373-381.
113. Yang, G., Lin, Q., Hu, X., Wu, Y. and Zhang, Z. Improvement the Activity and Selectivity of Fenton System in the Oxidation of Alcohols. *Journal of Catalysts.* 2014, **2014**, p.6.
114. Kuo, W.S. and Ho, P.H. Solar Photocatalytic decolorization of methylene blue in water. *Chemosphere.* 2001, **45**, pp.77-83.
115. Heger, D., Jirkovsky, J. and Klan, P. Aggregation of Methylene Blue in Frozen Aqueous Solutions Studied by Absorption Spectroscopy. *Journal of Physical Chemistry A.* 2005, **109**, pp.6702-6709.
116. Houas, A., Lachheb, H., Ksibi, M., Elaloui, E., Guillard, C. and Herrmann, J.-M. Photocatalytic degradation pathway of methylene blue in water. *Applied Catalysis B: Environmental.* 2001, **31**, pp.145-157.
117. Lachheb, H., Puzenat, E., Houas, A., Ksibi, M., Elaloui, E., Guillard, C. and Herrmann, J.-M. Photocatalytic degradation of various types of dyes (Alizarin S, Crocein Orange G, Methyl Red, Congo Red, Methylene Blue) in water by UV-irradiated titania. *Applied Catalysis B: Environmental.* 2002, **39**, pp.75-90.
118. Lakshmi, S., Renganathan, R. and Fujita, S. Study on TiO_2 mediated photocatalytic degradation of methylene blue. *Journal of Photochemistry and Photobiology A: Chemistry.* 1995, **88**, pp.163-167.
119. Liu, S., Yu, J. and Jaroniec, M. Tunable Photocatalytic Selectivity of Hollow TiO_2 Microspheres Composed of Anatase Polyhedra with Exposed {001} Facets. *Journal of the American Chemical Society.* 2010, **132**, pp.11914-11916.
120. Xue, B. and Zou, Y. Uniform distribution of ZnO nanoparticles on the surface of graphene and its enhanced photocatalytic performance. *Applied Surface Science.* 2018, **440**, pp.1123-1129.
121. Ruan, C., Zhang, L., Qin, Y., Xu, C., Zhang, X., Wan, J., Peng, Z., Shi, J., Li, X. and Wang, L. Synthesis of porphyrin sensitized TiO2/graphene and its photocatalytic property under visible light. *Materials Letters.* 2015, **141**, pp.362-365.
122. Xu, T., Zhang, L., Cheng, H. and Zhu, Y. Significantly enhanced photocatalytic performance of ZnO via graphene hybridization and the mechanism study. *Applied Catalysis B: Environmental.* 2011, **101**, pp.382-387.
123. Khan, S.A., Arshad, Z., Shahid, S., Arshad, I., Rizwan, K., Sher, M. and Fatima, U. Synthesis of TiO_2/Graphene oxide nanocomposites for their enhanced photocatalytic activity against methylene blue dye and ciprofloxacin. *Composites Part B: Engineering.* 2019, **175**, p.107120.
124. Yang, H., Wang, P., Wang, D., Zhu, Y., Xie, K., Zhao, X., Yang, J. and Wang, X. New Understanding on Photocatalytic Mechanism of Nitrogen-Doped Graphene Quantum Dots-Decorated BiVO4 Nanojunction Photocatalysts. *ACS Omega.* 2017, **2**(7), p.3766 − 3773.
125. Liu, F., Shao, X. and Yang, S. Bi_2S_3–ZnS/graphene complexes: Synthesis, characterization, and photoactivity for the decolorization of dyes under visible light. *Materials Science in Semiconductor Processing.* 2015, **34**, pp.104-108.

126. Hsieh, S.H., Chen, W.J. and Yeh, T.H. Degradation of methylene blue using ZnSe–graphene nanocomposites under visible-light irradiation. *Ceramics International.* 2015, **41**(10, Part A), pp.13759-13766.
127. Goettmann, F., Fischer, A., Antonietti, M. and Thomas, A. Chemical Synthesis of Mesoporous Carbon Nitrides Using Hard Templates and Their Use as a Metal-Free Catalyst for Friedel–Crafts Reaction of Benzene. 2006, **45**(27), pp.4467-4471.
128. Long, J., Xie, X., Xu, J., Gu, Q., Chen, L. and Wang, X. Nitrogen-Doped Graphene Nanosheets as Metal-Free Catalysts for Aerobic Selective Oxidation of Benzylic Alcohols. *ACS Catalysis.* 2012, **2**(4), pp.622-631.
129. Poznik, M. and Konig, B. Fast colorimetric screening for visible light photocatalytic oxidation and reduction reactions. *Reaction Chemistry & Engineering.* 2016, **1**(5), pp.494-500.
130. Zhang, X., Rakesh, K.P., Ravindar, L. and Qin, H.-L. Visible-light initiated aerobic oxidations: a critical review. *Green Chemistry.* 2018, **20**(21), pp.4790-4833.
131. Feng, W., Wu, G., Li, L. and Guan, N. Solvent-free selective photocatalytic oxidation of benzyl alcohol over modified TiO_2. *Green Chemistry.* 2011, **13**(11), pp.3265-3272.
132. Schilling, W., Riemer, D., Zhang, Y., Hatami, N. and Das, S. Metal-Free Catalyst for Visible-Light-Induced Oxidation of Unactivated Alcohols Using Air/Oxygen as an Oxidant. *ACS Catalysis.* 2018, **8**(6), pp.5425-5430.
133. Gazi, S. and Ananthakrishnan, R. Bromodimethylsulfonium bromide as a potential candidate for photocatalytic selective oxidation of benzylic alcohols using oxygen and visible light. *RSC Advances.* 2012, **2**(20), pp.7781-7787.
134. Roy, S., Saswati, Lima, S., Dhaka, S., Maurya, M.R., Acharyya, R., Eagle, C. and Dinda, R. Synthesis, structural studies and catalytic activity of a series of dioxidomolybdenum(VI)-thiosemicarbazone complexes. *Inorganica Chimica Acta.* 2018, **474**, pp.134-143.
135. Keshipour, S. and Khezerloo, M. Gold nanoparticles supported on cellulose aerogel as a new efficient catalyst for epoxidation of styrene. *Journal of the Iranian Chemical Society.* 2017, **14**(5), pp.1107-1112.
136. Primo, A., Neatu, F., Florea, M., Parvulescu, V. and Garcia, H. Graphenes in the absence of metals as carbocatalysts for selective acetylene hydrogenation and alkene hydrogenation. *Nature Communications.* 2014, **5**(1), p.5291.
137. Hu, H.W., Xin, J.H., Hu, H. and Wang, X.W. Structural and mechanistic understanding of an active and durable graphene carbocatalyst for reduction of 4-nitrophenol at room temperature. *Nano Research.* 2015, **8**(12), pp.3992-4006.
138. Hu, H., Wang, X., Miao, D., Wang, Y., Lai, C., Guo, Y., Wang, W., Xin, J.H. and Hu, H. A pH-mediated enhancement of the graphene carbocatalyst activity for the reduction of 4-nitrophenol. *Chemical Communications.* 2015, **51**(93), pp.16699-16702.
139. Bauer, H., Thum, K., Alonso, M., Fischer, C. and Harder, S. Alkene Transfer Hydrogenation with Alkaline-Earth Metal Catalysts. *Angewandte Chemie International Edition.* 2019, **58**(13), pp.4248-4253.
140. Tike, M.A. and Mahajani, V.V. Studies in catalytic transfer hydrogenation of soybean oil using ammonium formate as donor over 5% Pd/C catalyst. *Chemical Engineering Journal.* 2006, **123**(1), pp.31-41.
141. Adu-Mensah, D., Mei, D., Zuo, L., Zhang, Q. and Wang, J. A review on partial hydrogenation of biodiesel and its influence on fuel properties. *Fuel.* 2019, **251**, pp.660-668.
142. Lawal, A.M., Hart, A., Daly, H., Hardacre, C. and Wood, J. Catalytic Hydrogenation of Short Chain Carboxylic Acids Typical of Model Compound Found in Bio-Oils. *Industrial & Engineering Chemistry Research.* 2019.
143. Chen, B., Dingerdissen, U., Krauter, J.G.E., Lansink Rotgerink, H.G.J., Möbus, K., Ostgard, D.J., Panster, P., Riermeier, T.H., Seebald, S., Tacke, T. and Trauthwein, H. New developments in hydrogenation catalysis particularly in synthesis of fine and intermediate chemicals. *Applied Catalysis A: General.* 2005, **280**(1), pp.17-46.

144. Navlani-García, M., Mori, K., Salinas-Torres, D., Kuwahara, Y. and Yamashita, H. New Approaches Toward the Hydrogen Production From Formic Acid Dehydrogenation Over Pd-Based Heterogeneous Catalysts. 2019, **6**(44).
145. Jiao, F., Guo, H., Zhao, L., Liu, J., Chai, Y., Mintova, S. and Liu, C. Selective hydrogenation of alkenes using ZIF-67 shell membrane deposited on platinum/alumina core catalyst. *Microporous and Mesoporous Materials.* 2019, **276**, pp.98-106.
146. Fan, X., Yao, Y., Xu, Y., Yu, L. and Qiu, C. Visible-Light-Driven Photocatalytic Hydrogenation of Olefins Using Water as the H Source. *ChemCatChem.* 2019, **11**(11), pp.2596-2599.
147. Meriç, N., Arslan, N., Kayan, C., Rafikova, K., Zazybin, A., Kerimkulova, A. and Aydemir, M. Catalysts for the asymmetric transfer hydrogenation of various ketones from [3-[(2S)-2-[(diphenylphosphanyl)oxy]-3-phenoxypropyl]-1-methyl-1H-imidazol-3-ium chloride] and $[Ru(\eta6\text{-arene})(\mu\text{-Cl})Cl]_2$, $Ir(\eta5\text{-}C_5Me_5)(\mu\text{-Cl})Cl]_2$ or $[Rh(\mu\text{-Cl})(cod)]_2$. *Inorganica Chimica Acta.* 2019, **492**, pp.108-118.
148. Wang, Y., Huang, Z., Leng, X., Zhu, H., Liu, G. and Huang, Z. Transfer Hydrogenation of Alkenes Using Ethanol Catalyzed by a NCP Pincer Iridium Complex: Scope and Mechanism. *Journal of the American Chemical Society.* 2018, **140**(12), pp.4417-4429.
149. Vásquez, P.B., Tabanelli, T., Monti, E., Albonetti, S., Bonincontro, D., Dimitratos, N. and Cavani, F. Gas-Phase Catalytic Transfer Hydrogenation of Methyl Levulinate with Ethanol over ZrO_2. *ACS Sustainable Chemistry & Engineering.* 2019, **7**(9), pp.8317-8330.
150. Tabanelli, T., Paone, E., Blair Vasquez, P., Pietropaolo, R., Cavani, F. and Mauriello, F. Transfer hydrogenation of methyl and ethyl levulinate promoted by a ZrO2 catalyst: a comparison of batch vs continuous gas-flow conditions. *ACS Sustainable Chemistry & Engineering.* 2019.
151. Padmanaban, S., Gunasekar, G.H., Lee, M. and Yoon, S. Recyclable Covalent Triazine Framework-based Ru Catalyst for Transfer Hydrogenation of Carbonyl Compounds in Water. *ACS Sustainable Chemistry & Engineering.* 2019, **7**(9), pp.8893-8899.
152. Limvorapitux, R., Chou, L.-Y., Young, A.P., Tsung, C.-K. and Nguyen, S.T. Coupling Molecular and Nanoparticle Catalysts on Single Metal–Organic Framework Microcrystals for the Tandem Reaction of H_2O_2 Generation and Selective Alkene Oxidation. *ACS Catalysis.* 2017, **7**(10), pp.6691-6698.
153. O. V. Arapova, O. G. Ellert, R. S. Borisov, A. V. Chistyakov, A. Yu. Vasil'kov, M. V. Tsodikov and Gekhman, A.E. Effect of the Method of Synthesizing a Nickel-Containing Catalyst on Lignin Conversion in Liquid-Phase Hydrodepolymerization. *Petroleum Chemistry.* 2019, **59**(1), pp.111-119.
154. Wang, Y., Wang, D., Li, X., Li, G., Wang, Z., Li, M. and Li, X. Investigation on the Catalytic Hydrogenolysis of Lignin over NbOx–Ni/ZnO–Al_2O_3. *Industrial & Engineering Chemistry Research.* 2019.
155. Yan, J.-M., Li, S.-J., Yi, S.-S., Wulan, B.-R., Zheng, W.-T. and Jiang, Q. Anchoring and Upgrading Ultrafine NiPd on Room-Temperature-Synthesized Bifunctional NH_2-N-rGO toward Low-Cost and Highly Efficient Catalysts for Selective Formic Acid Dehydrogenation. 2018, **30**(12), p.1703038.
156. Grad, O., Mihet, M., Dan, M., Blanita, G., Radu, T., Berghian-Grosan, C. and Lazar, M.D.J.J.o.M.S. Au/reduced graphene oxide composites: eco-friendly preparation method and catalytic applications for formic acid dehydrogenation. 2019, **54**(9), pp.6991-7004.
157. Navlani-García, M., Mori, K., Kuwahara, Y. and Yamashita, H. Recent strategies targeting efficient hydrogen production from chemical hydrogen storage materials over carbon-supported catalysts. *NPG Asia Materials.* 2018, **10**(4), pp.277-292.
158. Ding, Y., Zheng, H., Cheng, J., Xu, H., Sun, M. and Yan, G. Platinum supported on reduced graphene oxide as a catalyst for the electrochemical hydrogenation of soybean oils. *Solid State Sciences.* 2019, **92**, pp.46-52.

159. Zhang, X., Qu, N., Fan, Q., Yang, H. and Liu, A. Palladium nanoparticles hosted in graphene-based 2-dimension polyelectrolyte brushes for enhanced hydrogenation selectivity of o-chloronitrobenzene. *Applied Surface Science.* 2019, **485**, pp.230-237.
160. Han, C., Meng, P., Waclawik, E.R., Zhang, C., Li, X.-H., Yang, H., Antonietti, M. and Xu, J. Palladium/Graphitic Carbon Nitride (g-C_3N_4) Stabilized Emulsion Microreactor as a Store for Hydrogen from Ammonia Borane for Use in Alkene Hydrogenation. *Angewandte Chemie International Edition.* 2018, **57**(45), pp.14857-14861.
161. Fukui, M., Omori, Y., Kitagawa, S.-y., Tanaka, A., Hashimoto, K. and Kominami, H. Visible light-induced diastereoselective semihydrogenation of alkynes to cis-alkenes over an organically modified titanium(IV) oxide photocatalyst having a metal co-catalyst. *Journal of Catalysis.* 2019, **374**, pp.36-42.
162. Li, W., Cui, X., Junge, K., Surkus, A.-E., Kreyenschulte, C., Bartling, S. and Beller, M. General and Chemoselective Copper Oxide Catalysts for Hydrogenation Reactions. *ACS Catalysis.* 2019, **9**(5), pp.4302-4307.
163. Li, B. and Xu, Z. A Nonmetal Catalyst for Molecular Hydrogen Activation with Comparable Catalytic Hydrogenation Capability to Noble Metal Catalyst. *Journal of the American Chemical Society.* 2009, **131**(45), pp.16380-16382.
164. Gligorovski, S., Strekowski, R., Barbati, S. and Vione, D. Environmental Implications of Hydroxyl Radicals (•OH). *Chemical Reviews.* 2015, **115**(24), pp.13051-13092.
165. Mazzone, G., Galano, A., Alvarez-Idaboy, J.R. and Russo, N. Coumarin–Chalcone Hybrids as Peroxyl Radical Scavengers: Kinetics and Mechanisms. *Journal of Chemical Information and Modeling.* 2016, **56**(4), pp.662-670.
166. Marino, T., Russo, N. and Galano, A. A deeper insight on the radical scavenger activity of two simple coumarins toward OOH radical. *Computational and Theoretical Chemistry.* 2016, **1077**, pp.133-138.
167. Soh, N., Makihara, K., Ariyoshi, T., Seto, D., Maki, T., Nakajima, H., Nakano, K. and Imato, T. Phospholipid-linked Coumarin: A Fluorescent Probe for Sensing Hydroxyl Radicals in Lipid Membranes. *Analytical Sciences.* 2008, **24**(2), pp.293-296.
168. Jayaram, D.T., Runa, S., Kemp, M.L. and Payne, C.K. Nanoparticle-induced oxidation of corona proteins initiates an oxidative stress response in cells. *Nanoscale.* 2017, **9**(22), pp.7595-7601.
169. Liu, C., Li, X., Wu, Y. and Qiu, J. Copper-catalyzed protodeboronation of arylboronic acids in aqueous media. *RSC Advances.* 2014, **4**(97), pp.54307-54311.
170. Wang, X., Zhang, L., Lin, H., Nong, Q., Wu, Y., Wu, T. and He, Y. Synthesis and characterization of a ZrO_2/g-C_3N_4 composite with enhanced visible-light photoactivity for rhodamine degradation. *RSC Advances.* 2014, **4**(75), pp.40029-40035.
171. Sun, Y., Wang, W., Zhang, L. and Sun, S. The photocatalysis of Bi_2MoO_6 under the irradiation of blue LED. *Materials Research Bulletin.* 2013, **48**(10), pp.4357-4361.
172. Sun, X., Xu, S.-Y., Flower, S.E., Fossey, J.S., Qian, X. and James, T.D. “Integrated” and “insulated” boronate-based fluorescent probes for the detection of hydrogen peroxide. *Chemical Communications.* 2013, **49**(75), pp.8311-8313.
173. Solntsev, K.M., Huppert, D. and Agmon, N. Solvatochromism of β-Naphthol. *The Journal of Physical Chemistry A.* 1998, **102**(47), pp.9599-9606.
174. Suppan, P. The Chemistry of Excited Molecules. In: *Chemistry and Light*. Thomas Graham House, The Science Park, Cambridge: The Royal Society of Chemistry, 1994, pp.87-162.
175. Farivar, F., Yap, P.L., Hassan, K., Tung, T.T., Tran, D.N.H., Pollard, A.J. and Losic, D. Unlocking thermogravimetric analysis (TGA) in the fight against “Fake graphene” materials. *Carbon.* 2021, **179**, pp.505-513.
176. PerkinElmer. *Thermogravimetric Analysis (TGA): A Beginner's Guide.* [Leaflet]. PerkinElmer, Inc: PerkinElmer, Inc, 2010.

177. Mamane, V., Mercier, G., Abdul Shukor, J., Gleize, J., Azizan, A., Fort, Y. and Vigolo, B. Chemi- vs physisorption in the radical functionalization of single-walled carbon nanotubes under microwaves. *Beilstein journal of nanotechnology.* 2014, **5**, pp.537-545.
178. Chouhan, A., Mungse, H.P. and Khatri, O.P. Surface chemistry of graphene and graphene oxide: A versatile route for their dispersion and tribological applications. *Advances in Colloid and Interface Science.* 2020, p.102215.
179. Langford, J.I. and Louër, D. Powder diffraction. *Reports on Progress in Physics.* 1996, **59**(2), pp.131-234.
180. Clayden, J., Greeves, N. and Warren, S. *Organic Chemistry.* 2nd ed. New York, United States: Oxford University Press Inc., 2012.
181. Chai, M., Holley, A.K. and Kruskamp, M. Encapsulating fluorescein using adipic acid self-assembly on the surface of PPI-3 dendrimer. *Chemical Communications.* 2007, (2), pp.168-170.
182. Crespo-Hernández, C.E., Martínez-Fernández, L., Rauer, C., Reichardt, C., Mai, S., Pollum, M., Marquetand, P., González, L. and Corral, I. Electronic and Structural Elements That Regulate the Excited-State Dynamics in Purine Nucleobase Derivatives. *Journal of the American Chemical Society.* 2015, **137**(13), pp.4368-4381.
183. Alzate-Carvajal, N., Acevedo-Guzmán, D.A., Meza-Laguna, V., Farías, M.H., Pérez-Rey, L.A., Abarca-Morales, E., García-Ramírez, V.A., Basiuk, V.A. and Basiuk, E.V. One-step nondestructive functionalization of graphene oxide paper with amines. *RSC Advances.* 2018, **8**(28), pp.15253-15265.
184. Song, Y., Gao, Y., Rong, H., Wen, H., Sha, Y., Zhang, H., Liu, H.-J. and Liu, Q. Functionalization of graphene oxide with naphthalenediimide diamine for high-performance cathode materials of lithium-ion batteries. *Sustainable Energy & Fuels.* 2018, **2**(4), pp.803-810.
185. Arshad, M., Masud, K., Saeed, A., Qureshi, A.H. and Shabir, G. Thermogravimetric and differential thermal analyses of fluorescein dye in inert and static air atmosphere. *Journal of Thermal Analysis and Calorimetry.* 2018, **131**(2), pp.1385-1390.
186. Yogamalar, R., Srinivasan, R., Vinu, A., Ariga, K. and Bose, A.C. X-ray peak broadening analysis in ZnO nanoparticles. *Solid State Communications.* 2009, **149**(43), pp.1919-1923.
187. Balzar, D. X-Ray Diffraction Line Broadening: Modeling and Applications to High-Tc Superconductors. *J Res Natl Inst Stand Technol.* 1993, **98**(3), pp.321-353.
188. Kaya-Özkiper, K., Uzun, A. and Soyer-Uzun, S. Red mud- and metakaolin-based geopolymers for adsorption and photocatalytic degradation of methylene blue: Towards self-cleaning construction materials. *Journal of Cleaner Production.* 2020, p.125120.
189. Minamoto, C., Fujiwara, N., Shigekawa, Y., Tada, K., Yano, J., Yokoyama, T., Minamoto, Y. and Nakayama, S. Effect of acidic conditions on decomposition of methylene blue in aqueous solution by air microbubbles. *Chemosphere.* 2021, **263**, p.128141.
190. LI, C., LU, P., SHI, R., WENHAOWANG, GE, X. and LI, Y. *Method for degrading methylene blue in alkaline solution under sunlight*. 2017.
191. Namal, O.O. and Kalipci, E. Adsorption kinetics of methylene blue using alkali and microwave-modified apricot stones. *Separation Science and Technology.* 2019, **54**(11), pp.1722-1738.
192. Mills, A., Hazafy, D., Parkinson, J., Tuttle, T. and Hutchings, M.G. Effect of alkali on methylene blue (C.I. Basic Blue 9) and other thiazine dyes. *Dyes and Pigments.* 2011, **88**(2), pp.149-155.
193. Montes-Navajas, P., Asenjo, N.G., Santamaría, R., Menéndez, R., Corma, A. and García, H. Surface Area Measurement of Graphene Oxide in Aqueous Solutions. *Langmuir.* 2013, **29**(44), pp.13443-13448.
194. Liu, T., Li, Y., Du, Q., Sun, J., Jiao, Y., Yang, G., Wang, Z., Xia, Y., Zhang, W., Wang, K., Zhu, H. and Wu, D. Adsorption of methylene blue from aqueous solution by graphene. *Colloids and Surfaces B: Biointerfaces.* 2012, **90**, pp.197-203.

195. McHedlov-Petrossyan, N.O., Kukhtik, V.I. and Alekseeva, V.I. Ionization and Tautomerism of Fluorescein, Rhodamine B, N,N-Diethylrhodol and Related Dyes in Mixed and Nonaqueous Solvents. *Dyes and Pigments.* 1994, **24**(1), pp.11-35.
196. Martin, M.M. and Lindqvist, L. The pH dependence of fluorescein fluorescence. *Journal of Luminescence.* 1975, **10**(6), pp.381-390.
197. Zhang, F., Li, Y.-H., Li, J.-Y., Tang, Z.-R. and Xu, Y.-J. 3D graphene-based gel photocatalysts for environmental pollutants degradation. *Environmental Pollution.* 2019, **253**, pp.365-376.
198. Simonin, J.-P. On the comparison of pseudo-first order and pseudo-second order rate laws in the modeling of adsorption kinetics. *Chemical Engineering Journal.* 2016, **300**, pp.254-263.
199. Ho, Y.S. and McKay, G. Pseudo-second order model for sorption processes. *Process Biochemistry.* 1999, **34**(5), pp.451-465.
200. Zhang, W., Carpenter, K.L. and Lin, S. Electrochemistry Broadens the Scope of Flavin Photocatalysis: Photoelectrocatalytic Oxidation of Unactivated Alcohols. *Angewandte Chemie International Edition.* 2020, **59**(1), pp.409-417.
201. Barham, A.S. Electrochemical studies of 3-aminophenol and 3-aminobenzyl Alcohol in Aqueous Solutions at Different pH Values. *International Journal of Electrochemical Science.* 2015, **10**(6), pp.4742-4751.
202. Zheng, C., He, G., Xiao, X., Lu, M., Zhong, H., Zuo, X. and Nan, J. Selective photocatalytic oxidation of benzyl alcohol into benzaldehyde with high selectivity and conversion ratio over $Bi_4O_5Br_2$ nanoflakes under blue LED irradiation. *Applied Catalysis B: Environmental.* 2017, **205**, pp.201-210.
203. Du, M., Zeng, G., Ye, C., Jin, H., Huang, J., Sun, D., Li, Q., Chen, B. and Li, X. Solvent-free photo-thermocatalytic oxidation of benzyl alcohol on Pd/TiO2 (B) nanowires. *Molecular Catalysis.* 2020, **483**, p.110771.
204. Ahmed, A.Y., Kandiel, T.A., Oekermann, T. and Bahnemann, D. Photocatalytic Activities of Different Well-defined Single Crystal TiO_2 Surfaces: Anatase versus Rutile. *The Journal of Physical Chemistry Letters.* 2011, **2**(19), pp.2461-2465.
205. Moniz-Barreto, J.P. and Fell, D.A. Simulation of free radical reactions: a multi-compartment Monte Carlo approach. *Biochemical Society Transactions.* 1995, **23**(2), pp.298S-298S.

8. Appendix

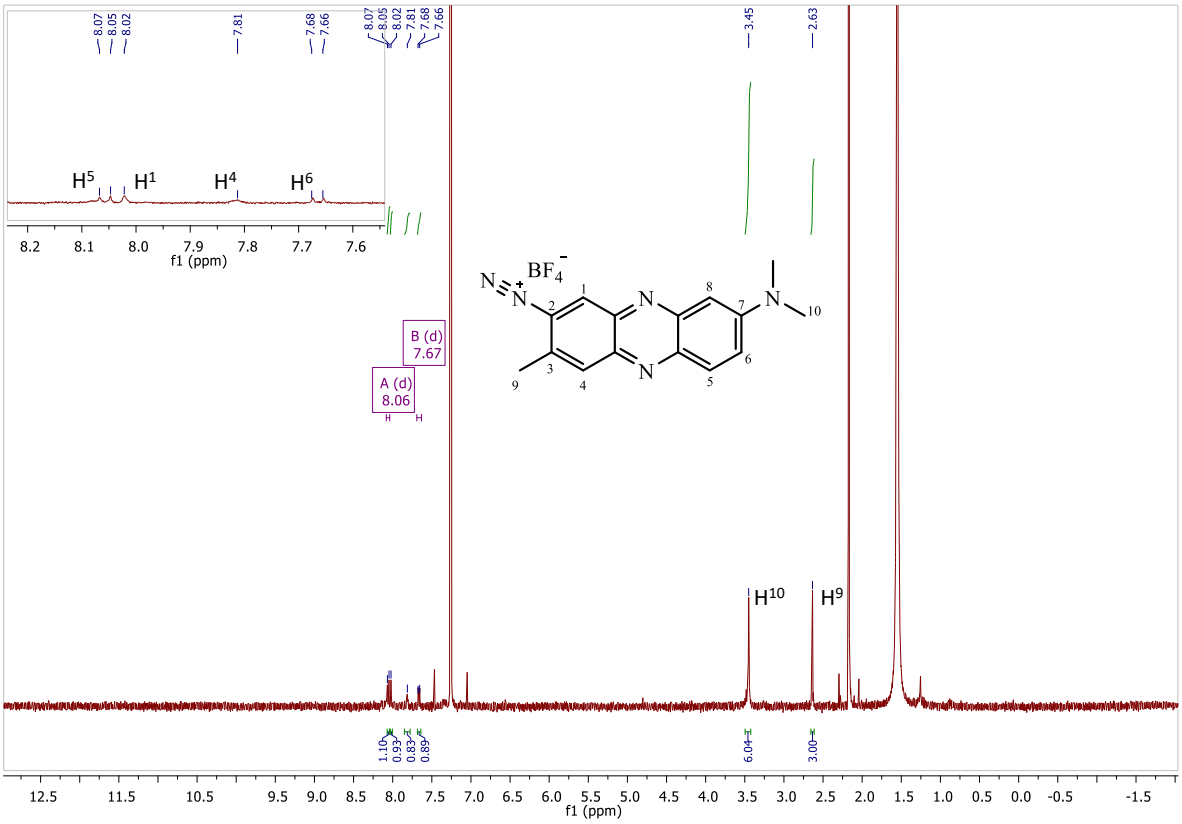

*Figure 120: ^{1}H NMR of diazonium **1** in $CDCl_3$ at 500 MHz.*

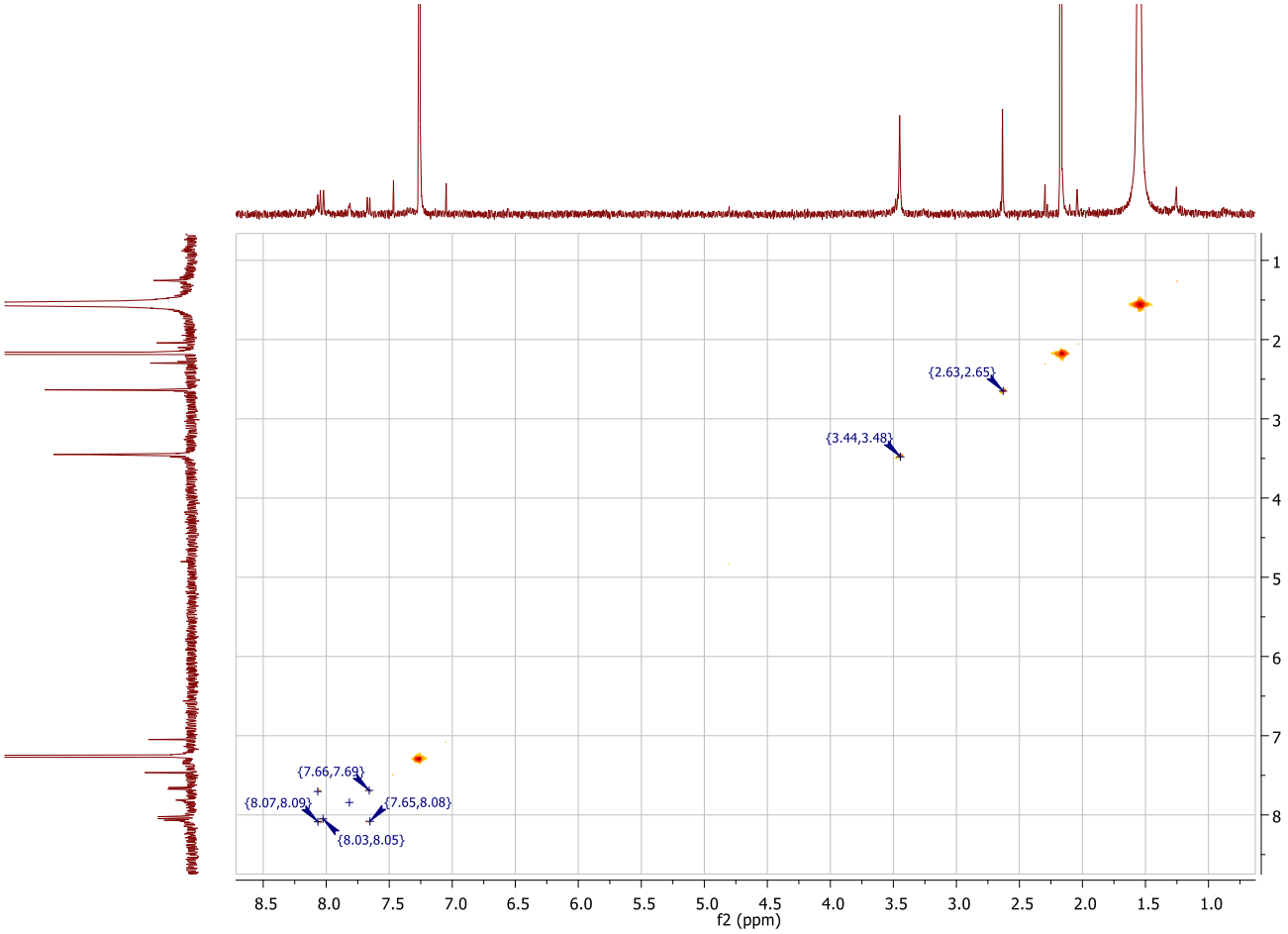

*Figure 121: The Correlated Spectroscopy (COSY) of diazonium **1** in $CDCl_3$ at 500 MHz.*

Chemical Shift δ	Number of Hydrogens	Multiplicity	Coupling constant J	Assignment
8.06	1	d	10.2	H^5
8.02	1	s	-	H^1
7.81	1	s	-	H^4
7.67	1	d	10.3	H^6
3.45	6	s	-	H^{10}
2.63	3	s	-	H^9

*Table 25: The tabulated ^1H NMR data for diazonium **1**.*

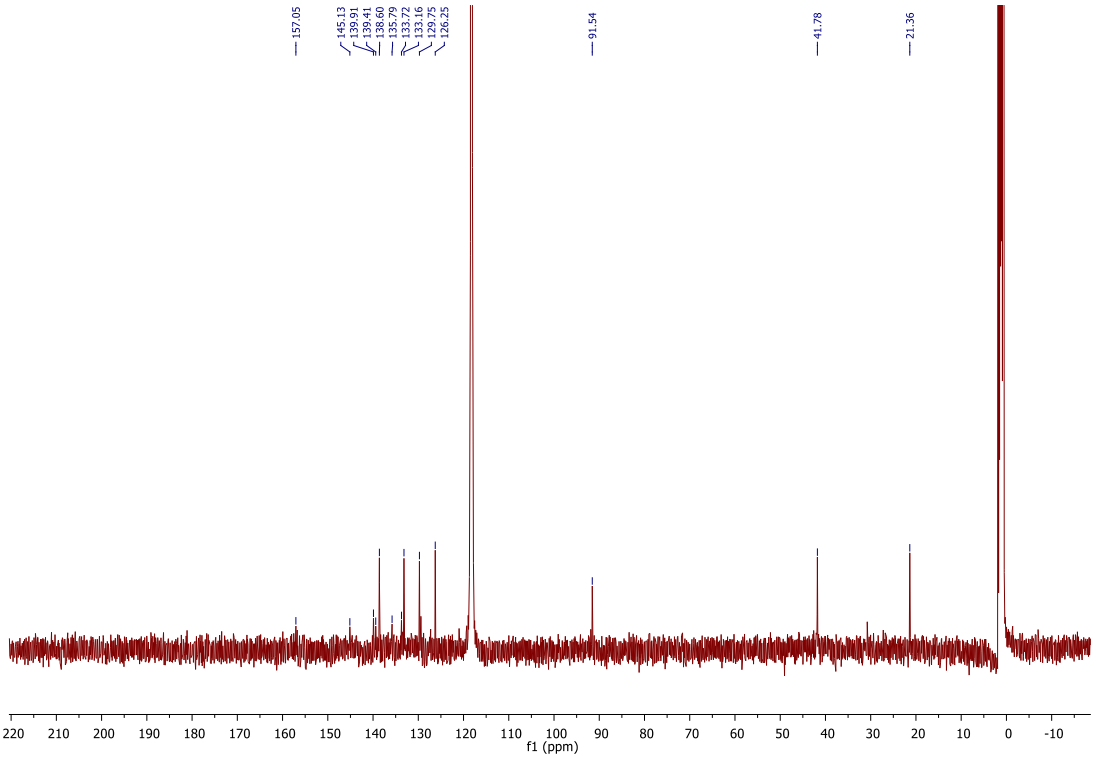

*Figure 122: ^{13}C NMR of diazonium **1** in d_3-MeCN at 400 MHz.*

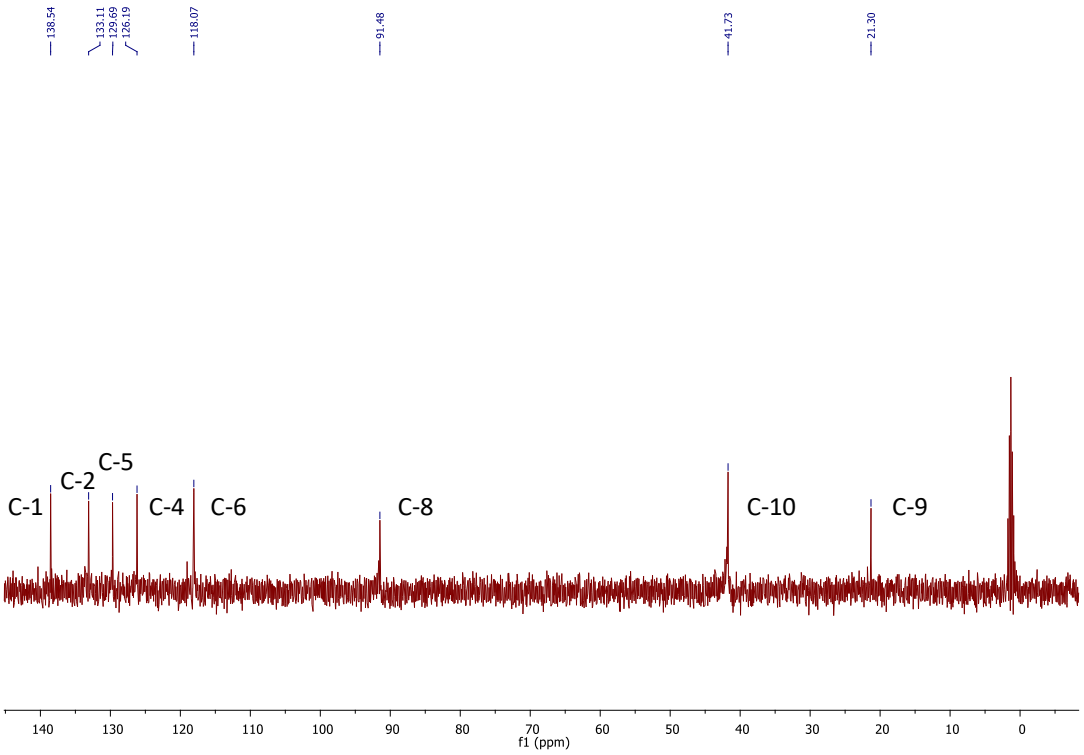

*Figure 123: Dept 135 of diazonium **1** in d_3-MeCN at 400 MHz.*

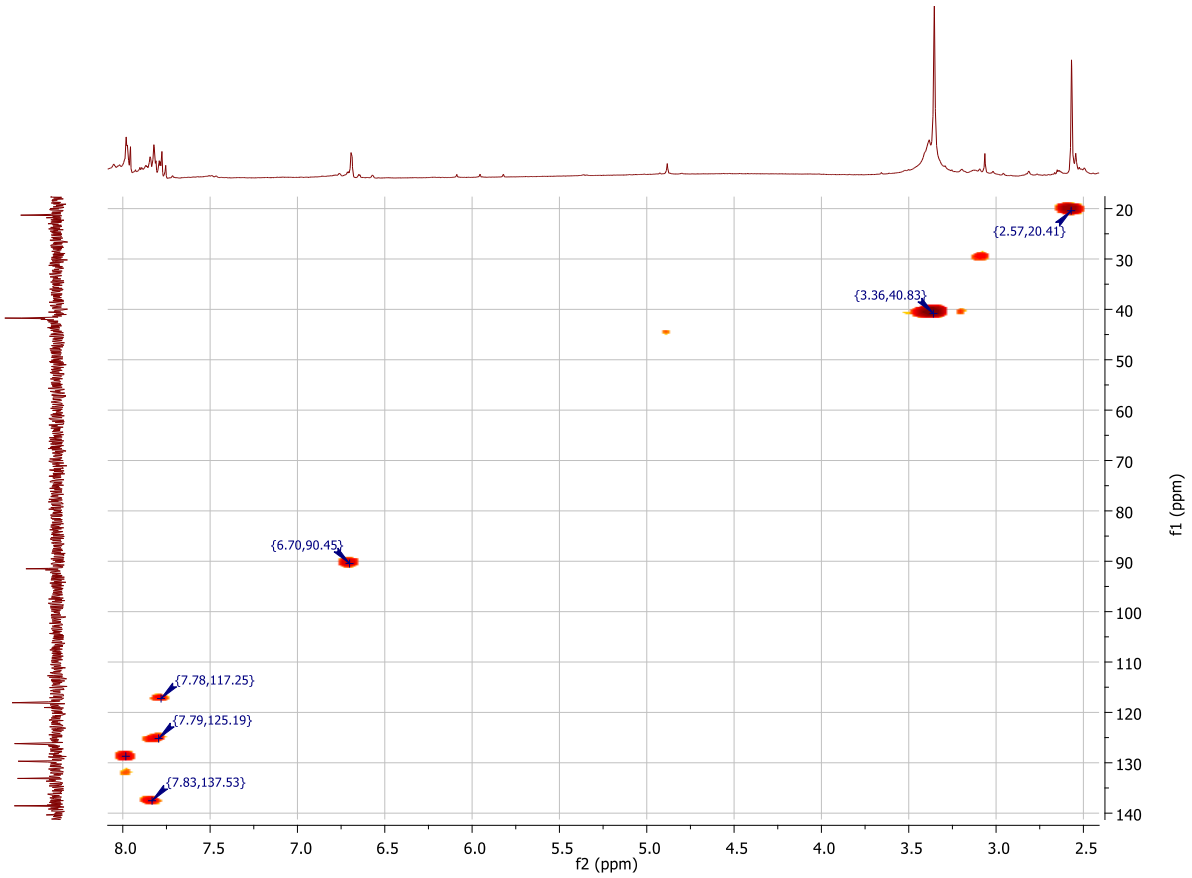

*Figure 124: The HMQC of diazonium **1** in d_3-MeCN at 400 MHz.*

Chemical Shift δ	Assignment
21.4	C-9
41.8	C-10
91.5	C-8
118.07	C-6
126.3	C-4
129.7	C-5
133.7	C-2
135.8	C-8a
138.6	C-1
139.4	C-5a
139.9	C-3
145.1	C-7
157.1	C-4a

*Table 26: Tabulated ^{13}C data for diazonium **1**.*

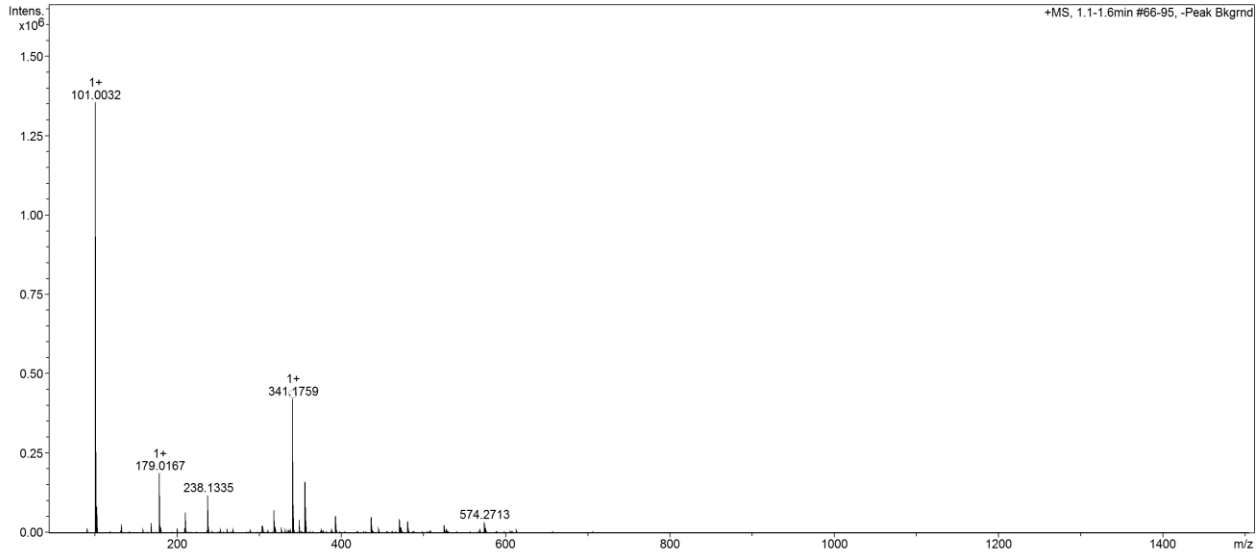

*Figure 125: The mass spectrum for diazonium **1** in d_6-DMSO.*

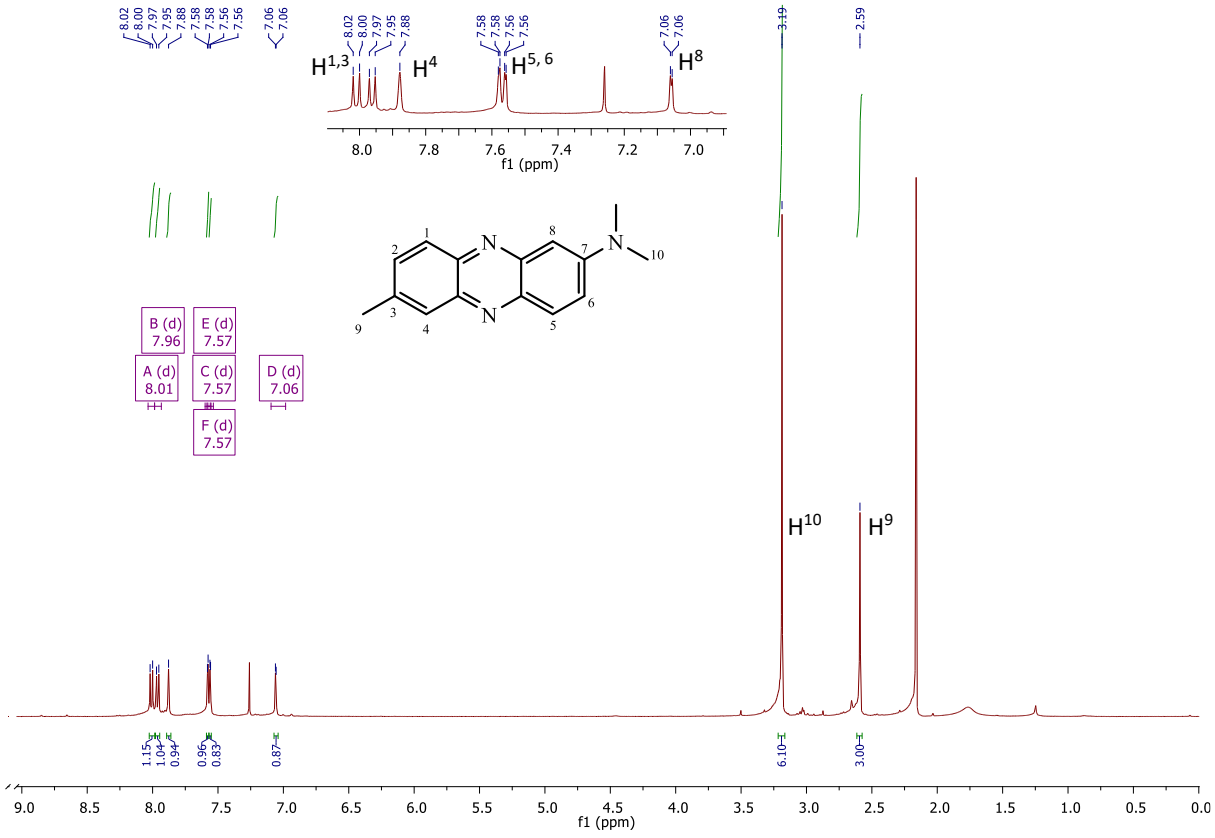

Figure 126: The ^{1}H NMR of MDAP in $CDCl_3$ at 500 MHz.

Chemical Shift δ	Number of Hydrogens	Multiplicity	Coupling constant J	Assignment
8.01	1	d	9.6	H^1
7.96	1	d	8.8	H^3
7.88	1	s	-	H^4
7.57	2	dd	9.5, 2.3	H^6 and H^5
7.06	1	d	2.6	H^8
3.19	6	s	-	H^{10}
2.59	3	s	-	H^9

Table 27: Tabulated ^1H NMR of MDAP in $CDCl_3$ at 500 MHz

Chemical Shift δ	Assignment
21.9	C-9
40.5	C-10
103.0	C-8
122.6	C-6
127.8	C-4
128.0	C-1
130.0	C-2
133.0	C-5
137.4	C-5a
137.9	C-1a
139.4	C-4a
145.1	C-3
150.8	C-7

Table 28: The ^{13}C NMR data for MDAP

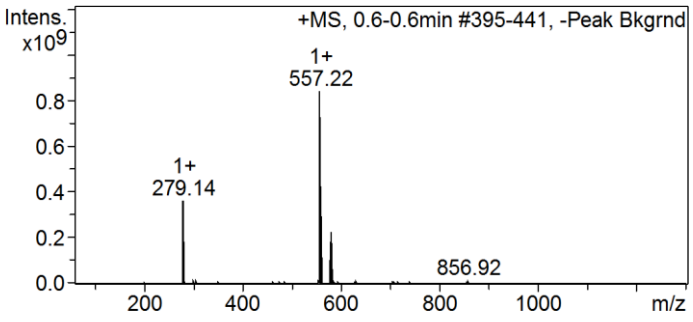

Figure 127: Failed reaction of fullerene and phenazine diazonium.

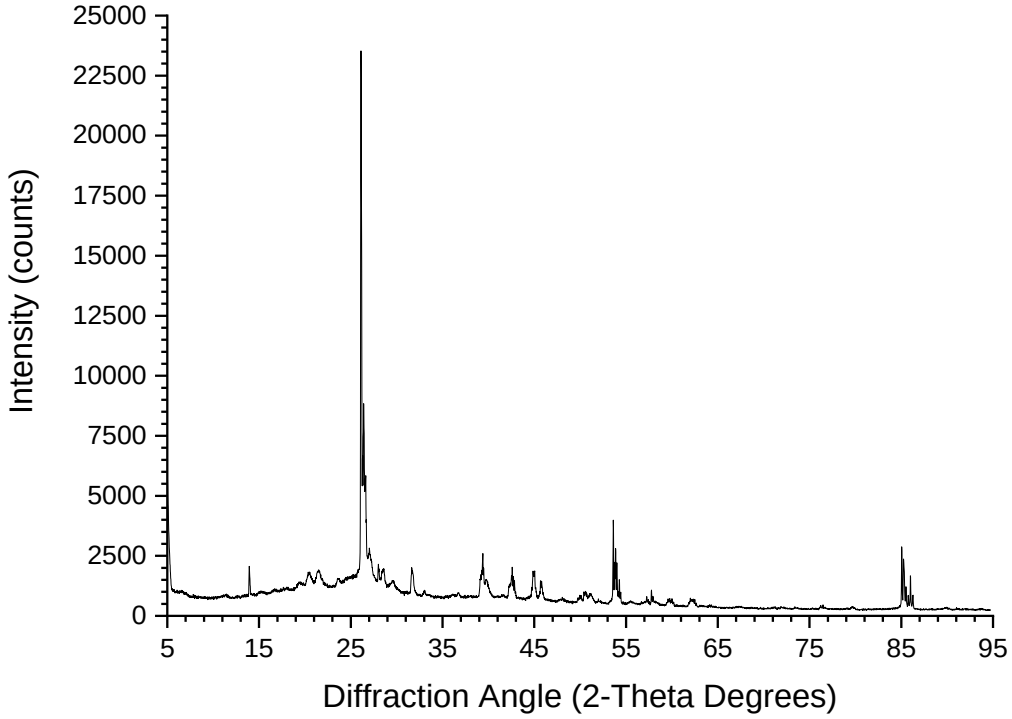

Figure 128: PXRD of phenazine diazonium salt from 2ϑ = 5 to 95 °.

2θ	θ	2sin(θ)	d / Å
13.92	6.96	0.24	6.35
20.37	10.18	0.35	4.36
21.50	10.75	0.37	4.13
26.10	13.05	0.45	3.41
26.40	13.20	0.46	3.37
26.61	13.30	0.46	3.35
27.03	13.52	0.47	3.30
28.00	14.00	0.48	3.18
28.62	14.31	0.49	3.12
29.70	14.85	0.51	3.01
31.67	15.84	0.54	2.82
33.09	16.54	0.57	2.70
39.79	19.90	0.68	2.26
42.60	21.30	0.73	2.12
44.86	22.43	0.76	2.02
45.81	22.90	0.78	1.98

Table 29: The data collected from the PXRD in Figure 128.

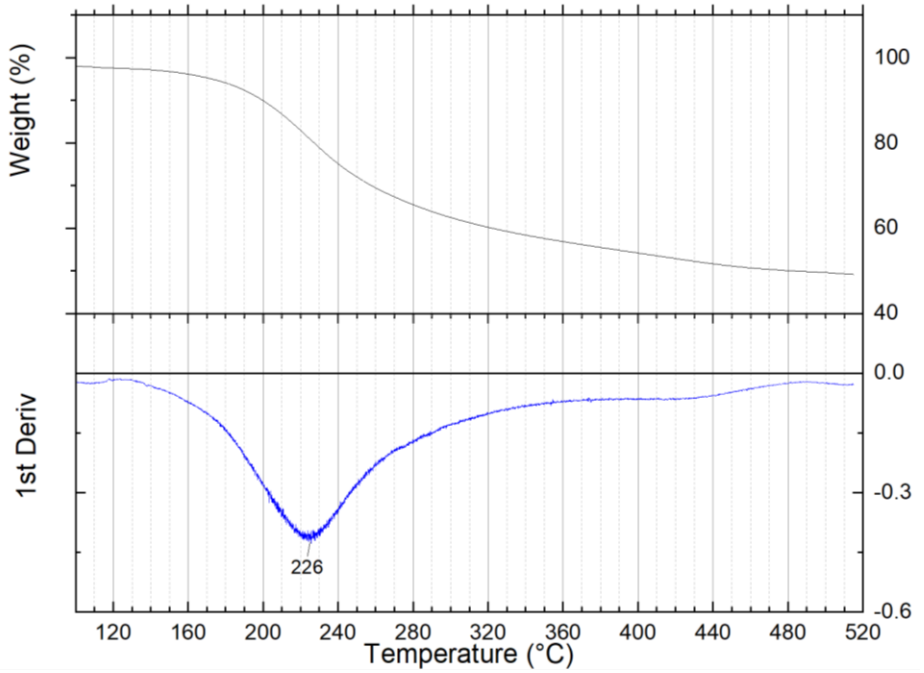

*Figure 129: TGA and first derivative of Diazonium **1**, showing an inflection point at 226 °C.*

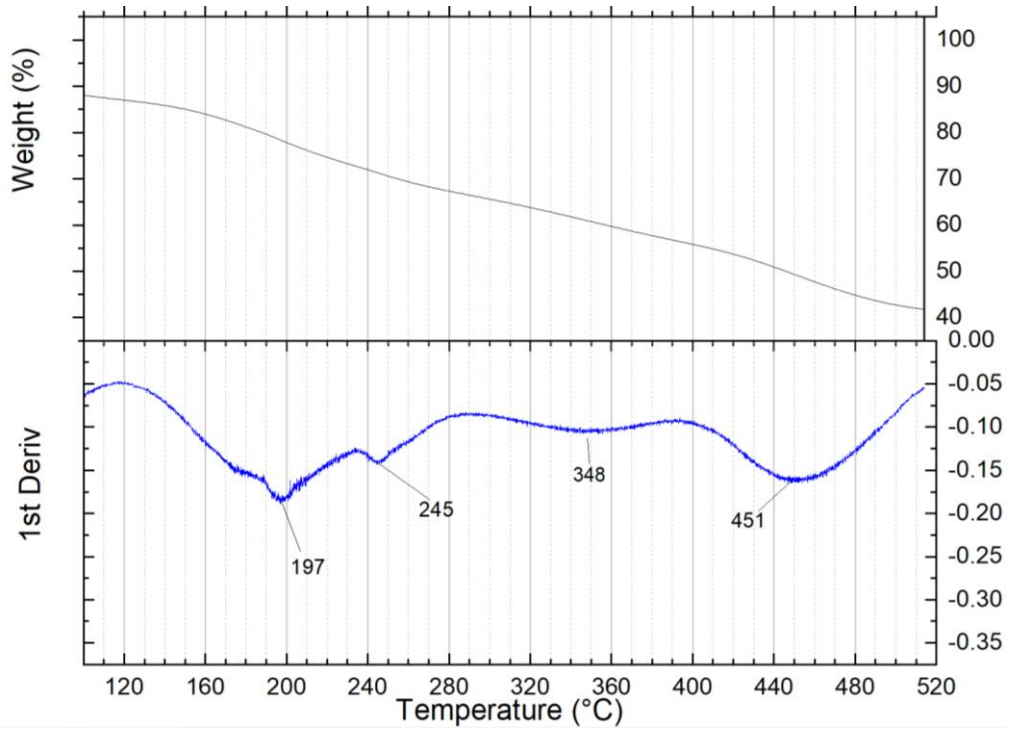

Figure 130: TGA of MDAP and first derivative, showing inflection points at 197 ,245, 348 and 451 °C .

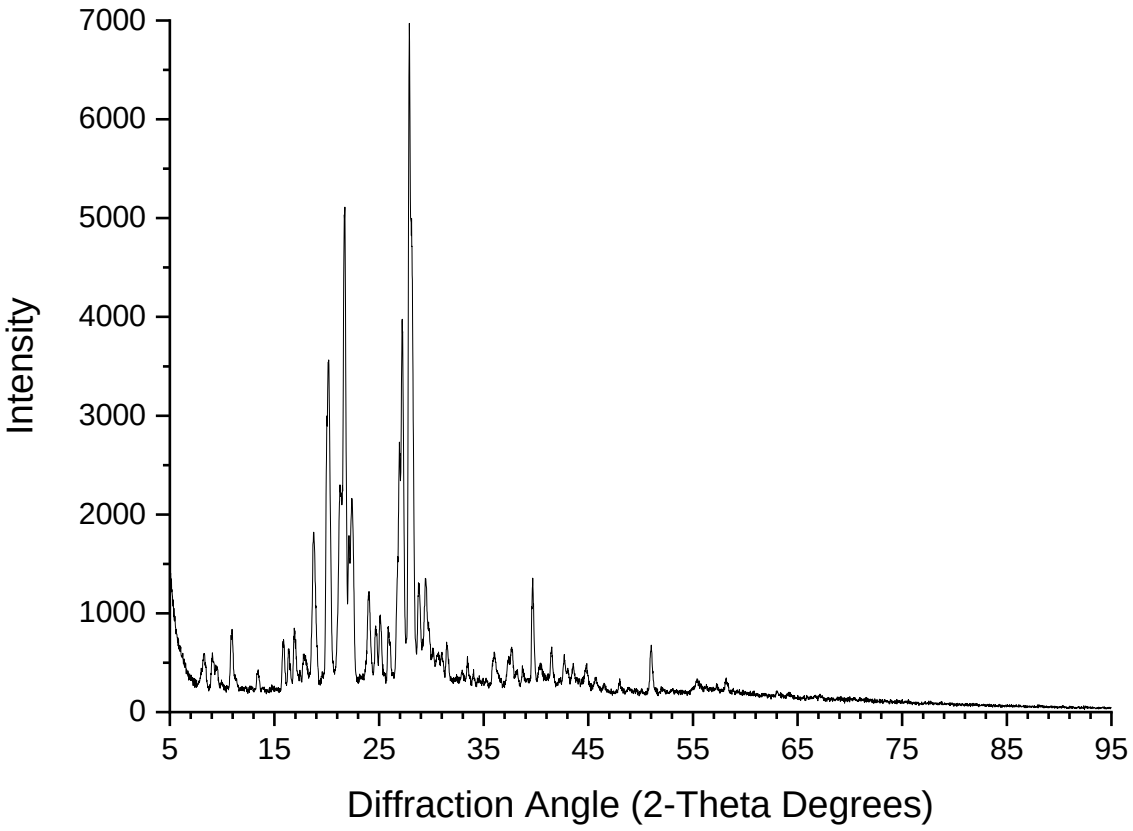

Figure 131: PXRD of MDAP from 2ϑ = 5 to 95 °.

2θ	θ	2sin(θ)	d / Å
10.94	5.47	0.19	8.08
16.89	8.44676	0.29	5.24
18.74	9.37	0.32	4.73
20.18	10.09	0.35	4.40
21.66	10.83	0.38	4.10
22.44	11.22	0.39	3.96
27.19	13.59	0.47	3.28
27.90	13.95	0.48	3.20
28.85	14.42	0.50	3.09
29.44	14.72	0.51	3.03
39.69	19.84	0.68	2.27
51.01	25.51	0.86	1.79

Table 30: The data taken from the PXRD in Figure 131.

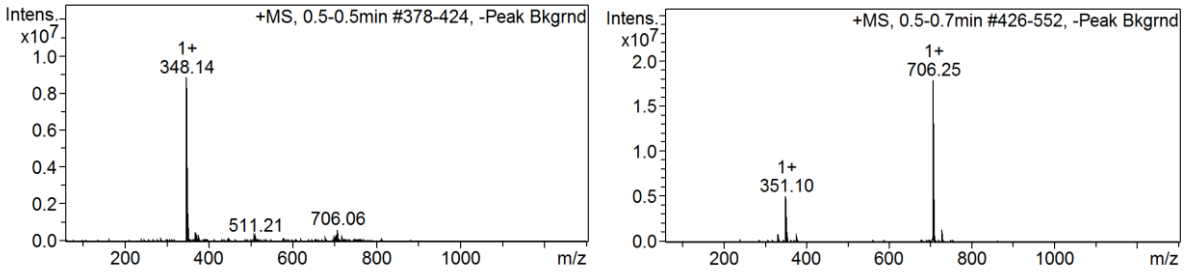

Figure 132: The mass spec data for fluorescein diazonium salt showing 5-aminofluorescein starting material (left) and reaction product (right).

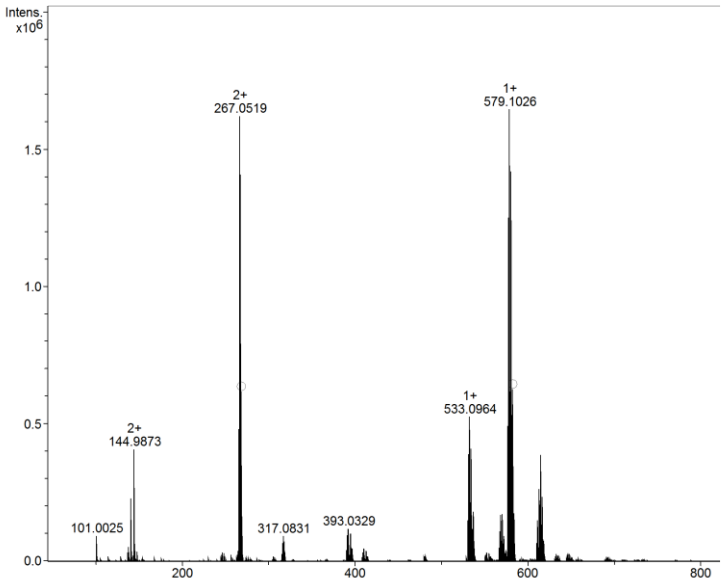

Figure 133: HRMS of 7H-purine-6-diazonium tetrafluoroborate.

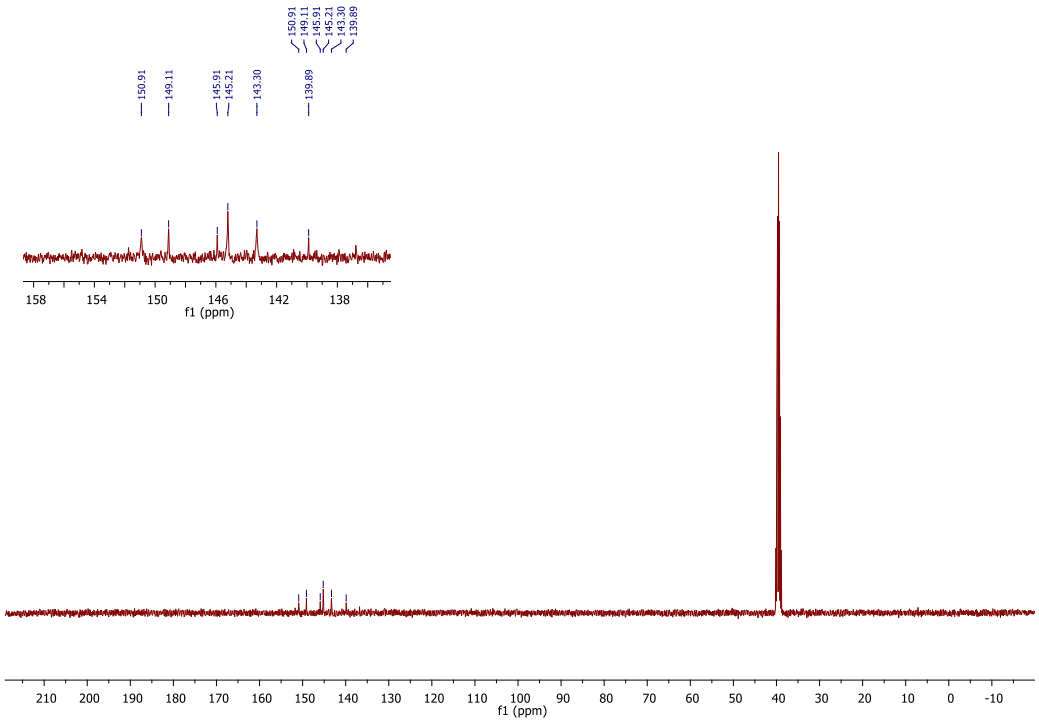

Figure 134: ^{13}C NMR of purine diazonium salt in d_6-DMSO.

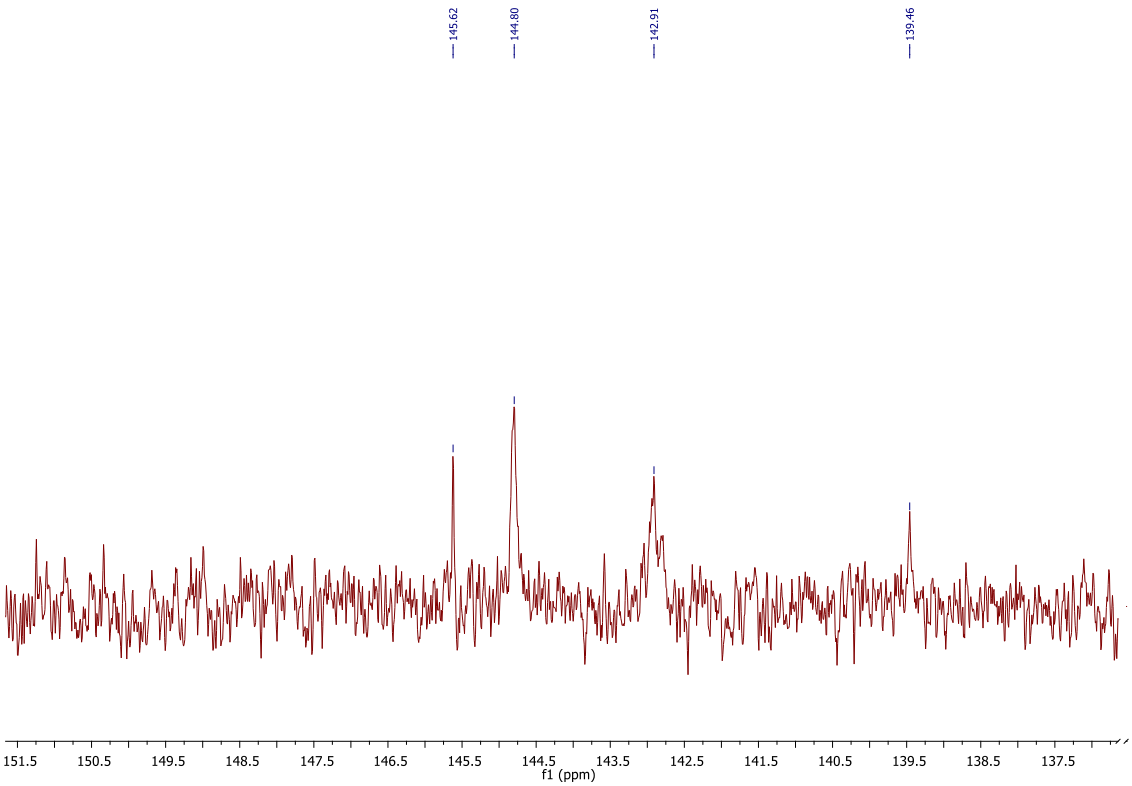

Figure 135: Dept 135 ^{13}C NMR of purine diazonium salt

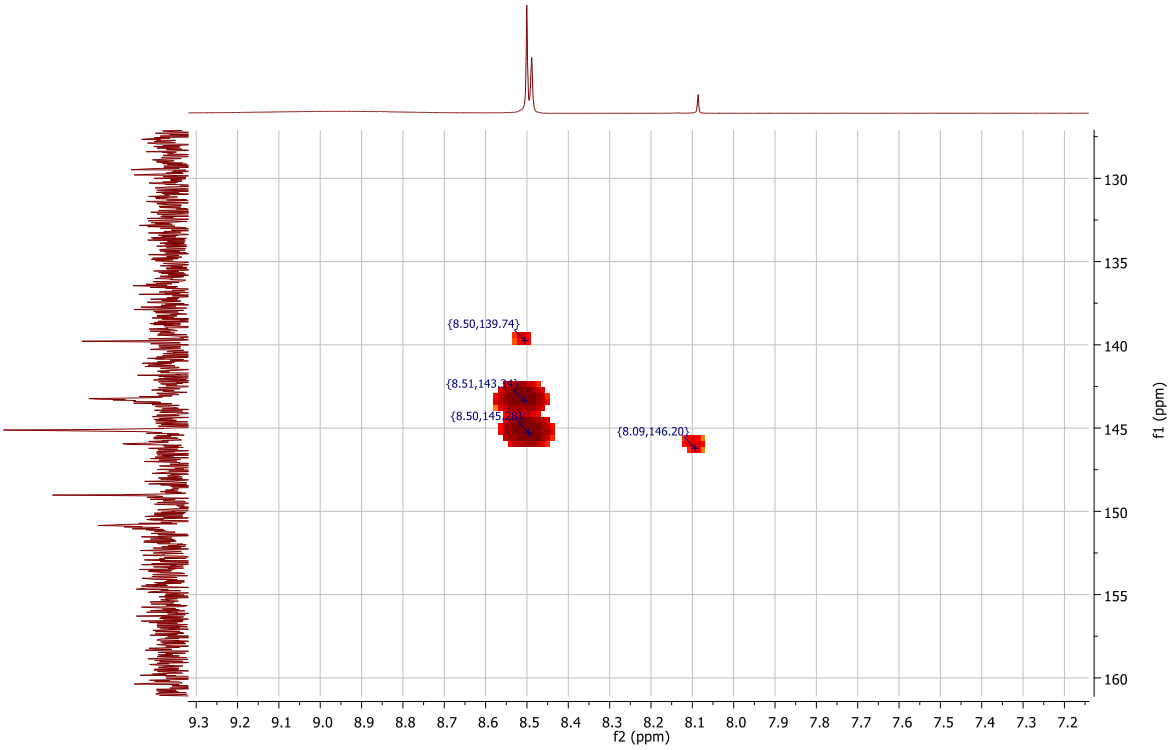

Figure 136: HMQC of purine diazonium salt in d_6-DMSO.

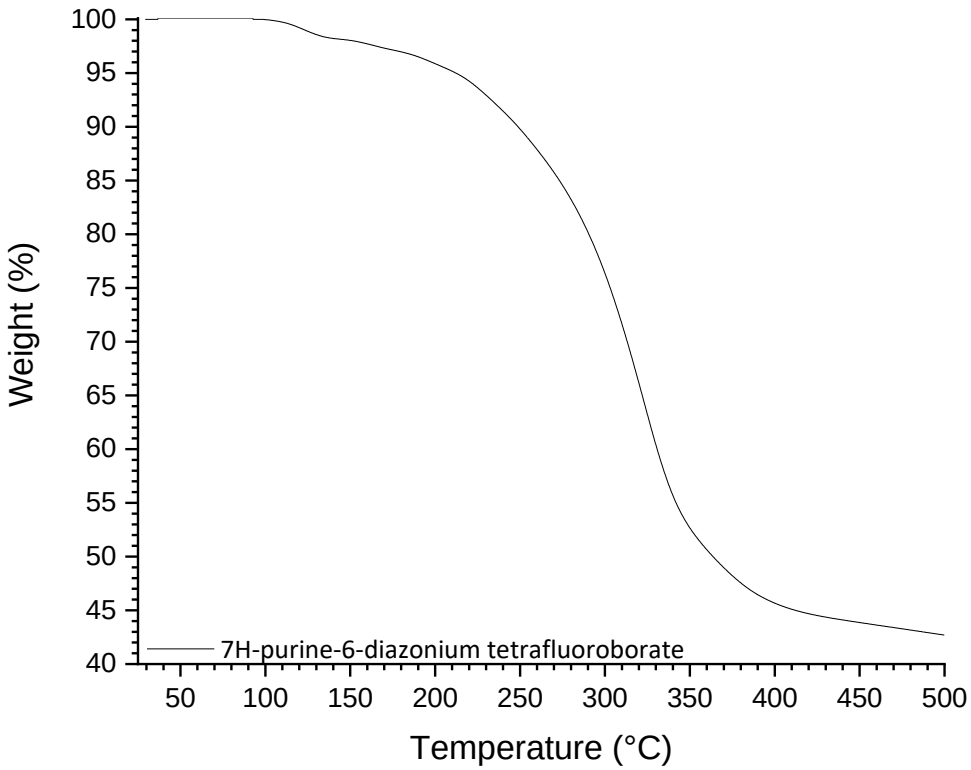

Figure 137: TGA of purine diazonium salt

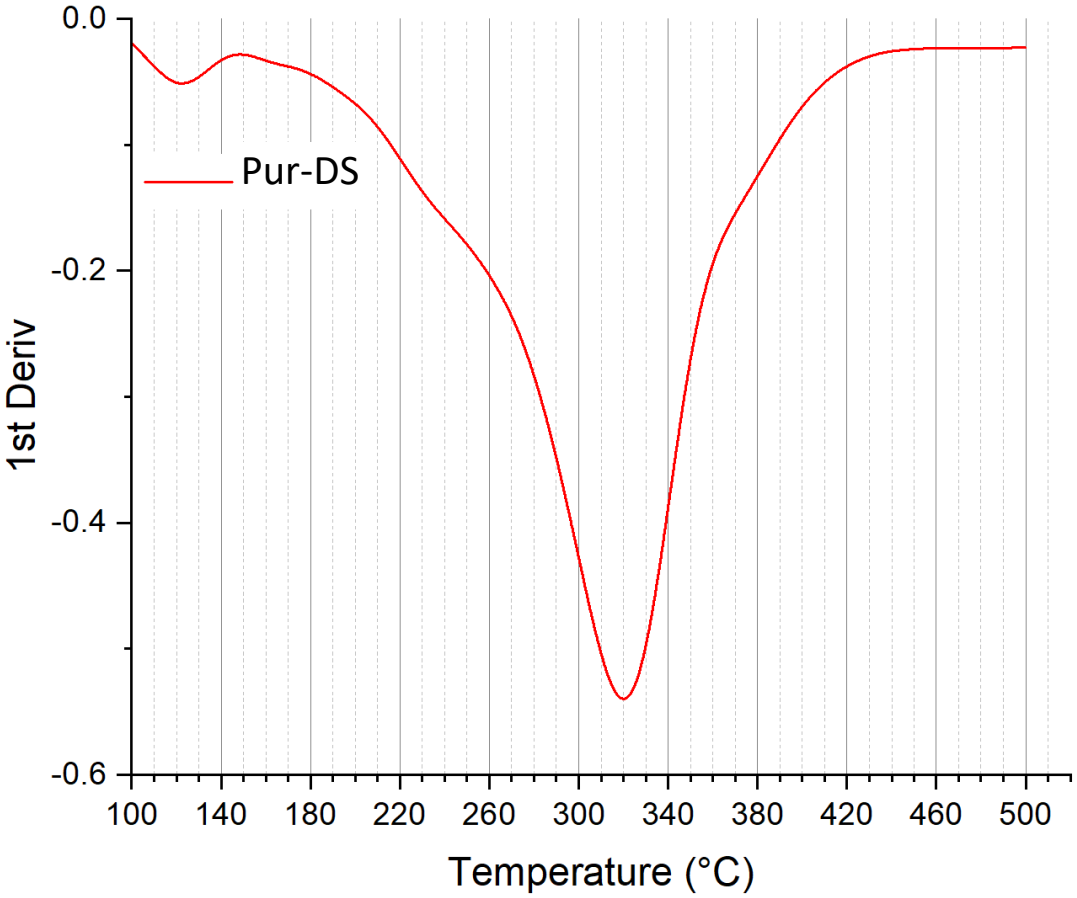

Figure 138: TGA first derivative of purine diazonium salt (Pur-DS)

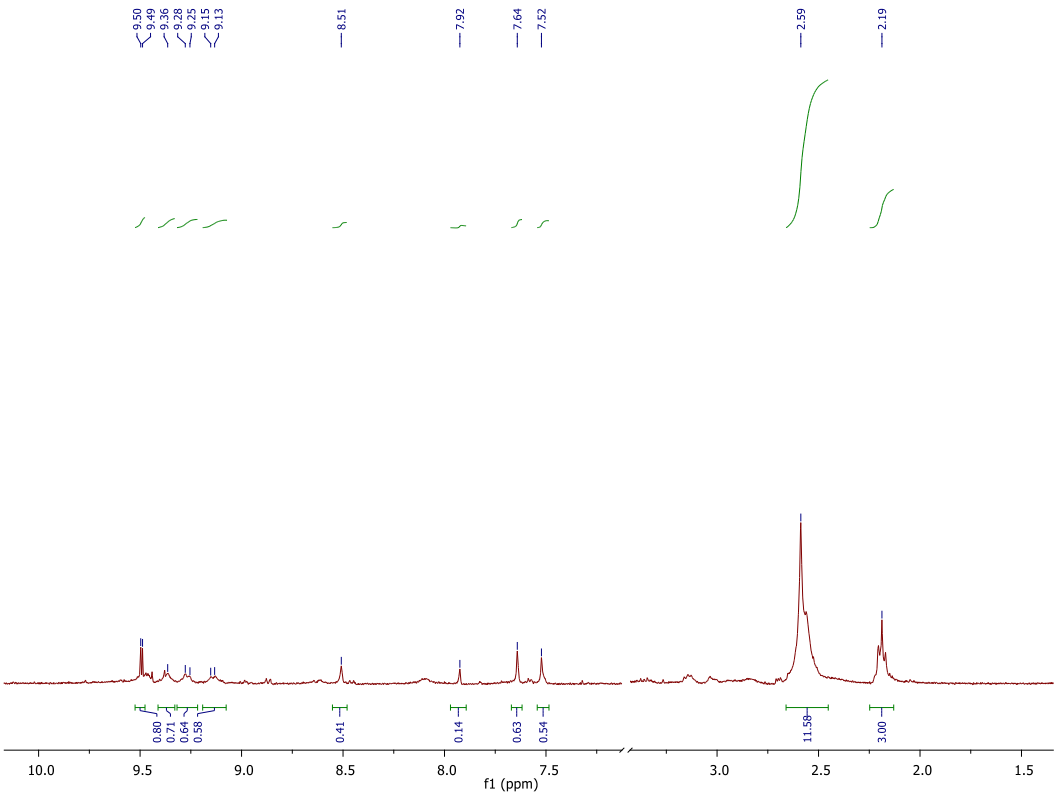

Figure 139: The ^{1}H NMR spectrum of the reaction to form chromone diazonium salt in d_4-methanol.

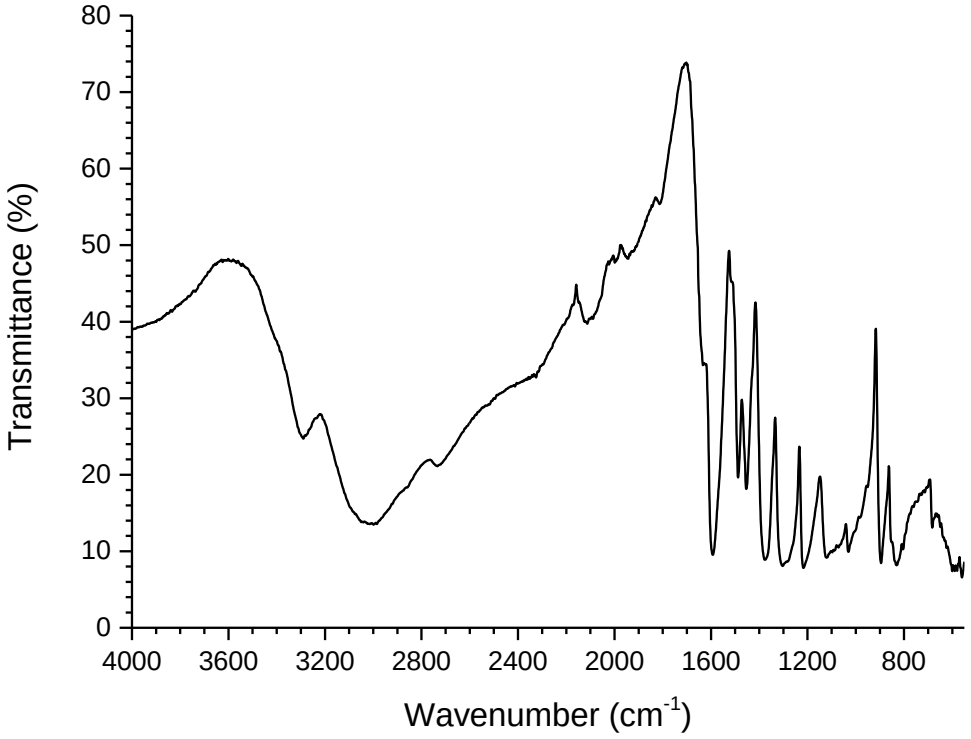

Figure 140: FTIR spectrum of thionine for comparison purposes.

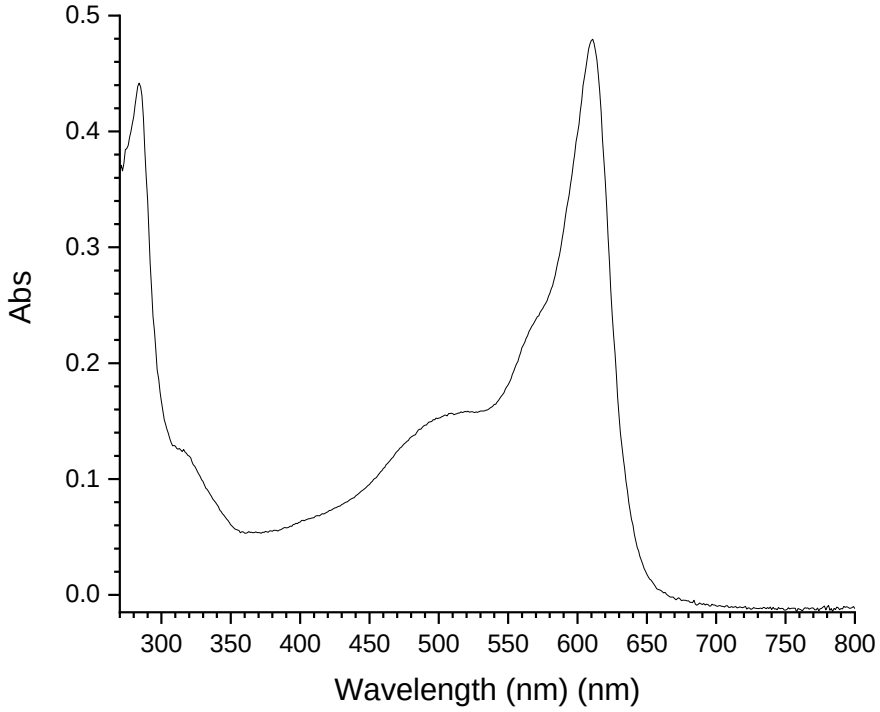

Figure 141: Thionine UV-vis for reference in MeCN with H_2SO_4.

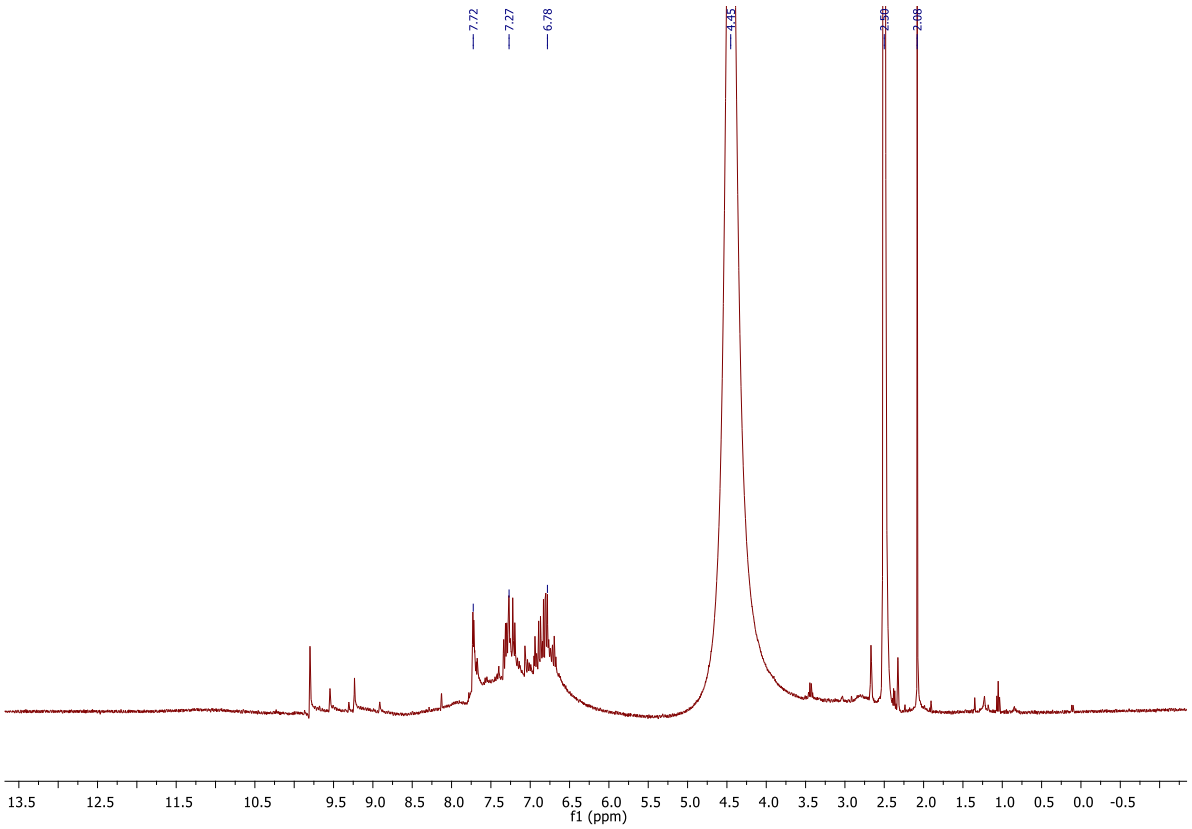

Figure 142: The ^{1}H NMR of thionine diazonium salt in d_6-DMSO, showing a degradation of the product.

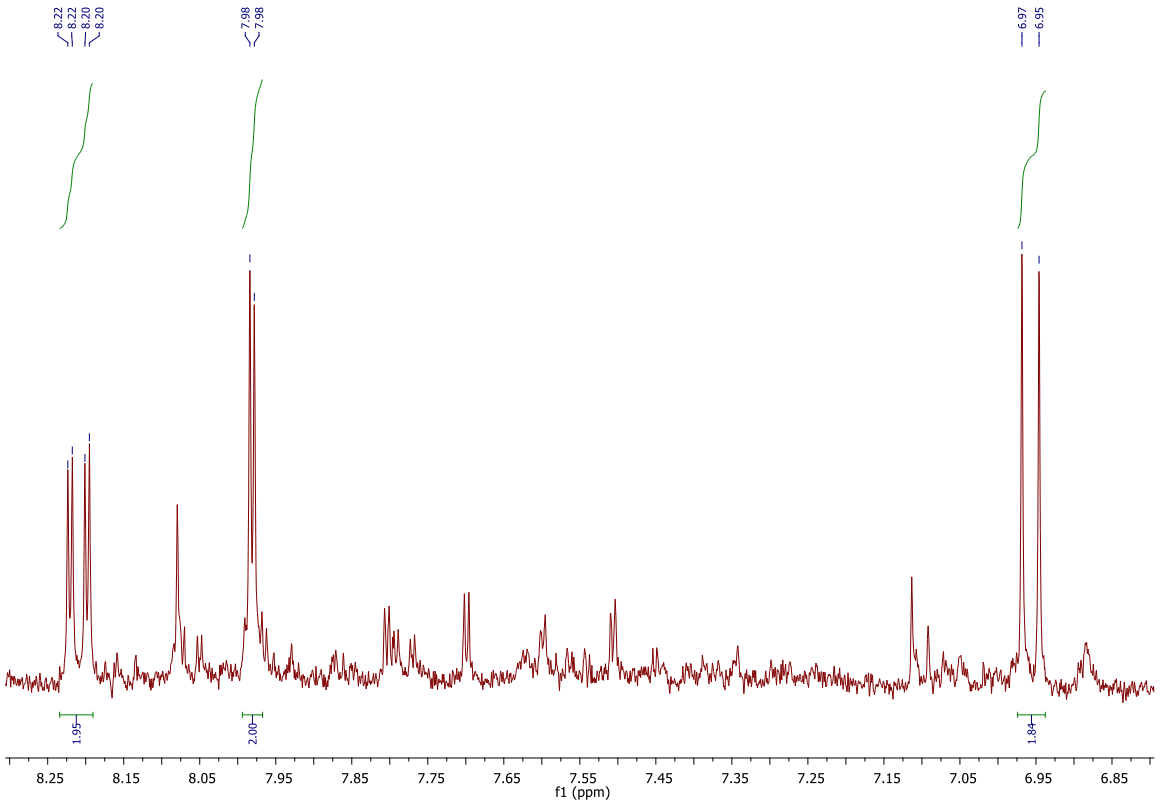

Figure 143: ^{1}H NMR spectrum of thionine diazonium salt, showing degradation in the solvent used. Taken in CD_3OD.

Chemical Shift δ	No. of Hydrogens	Multiplicity	J/ Hz	Assignment
6.96	2	d	9.0	Ha and Hf
7.98	2	d	2.3	Hc and Hd
8.21	2	dd	9.0, 2.3	Hb and He

Table 31: The NMR data for thionine diazonium salt in tabulated form. CD_3OD solvent.

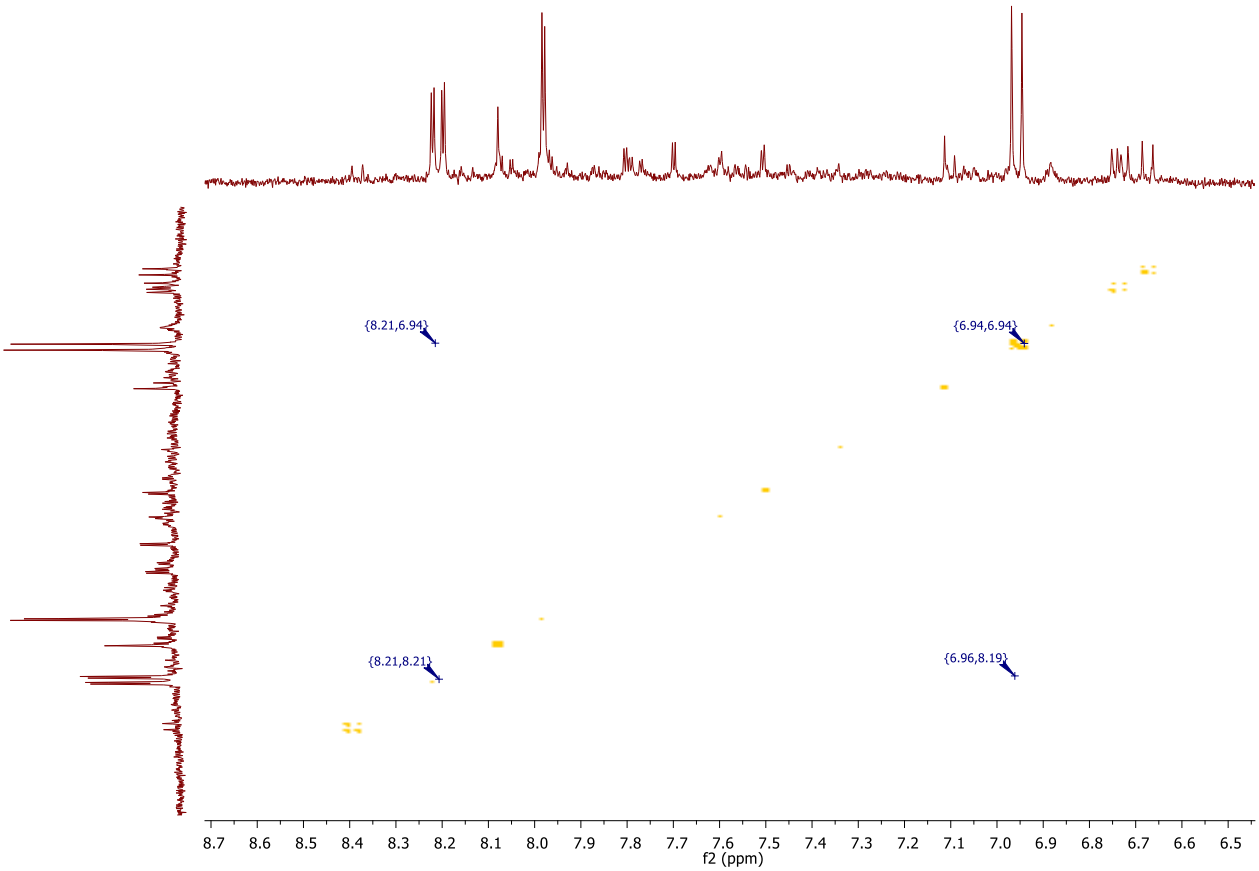

Figure 144: The 2D COSY of thionine diazonium salt in d_4-methanol

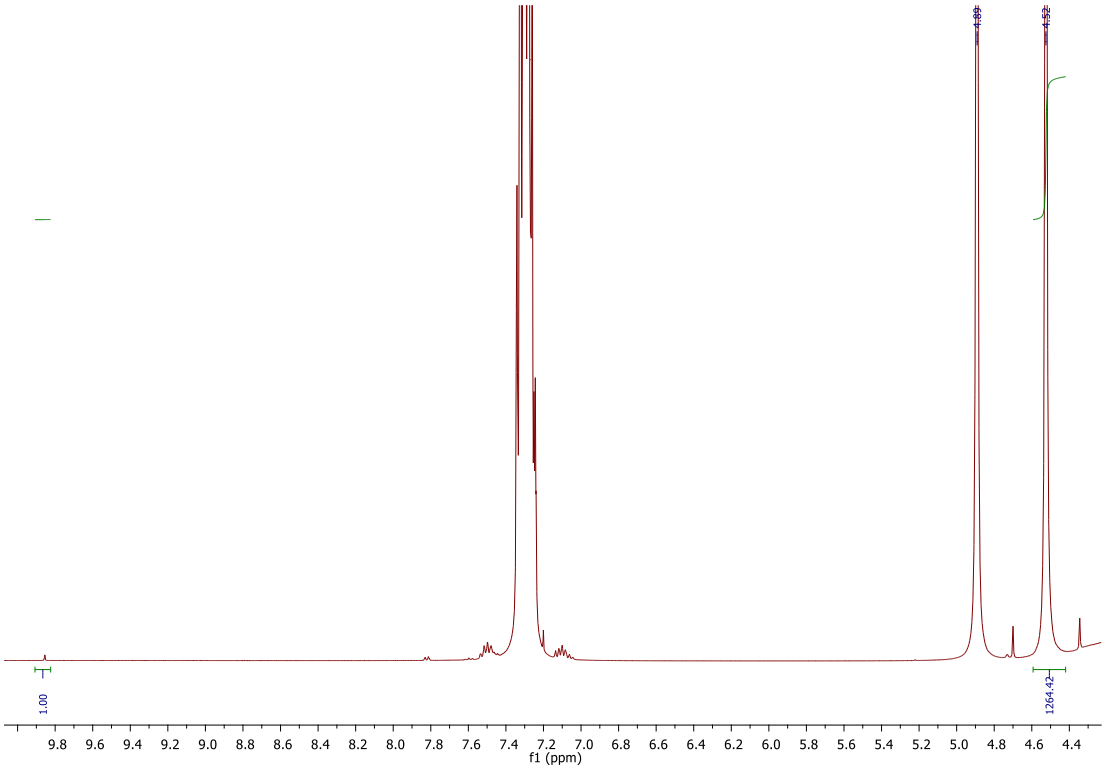

Figure 145: ^{1}H NMR of the reaction mix of benzyl alcohol and benzaldehyde in aqueous conditions with Pnz-G. Taken in $CDCl_3$.

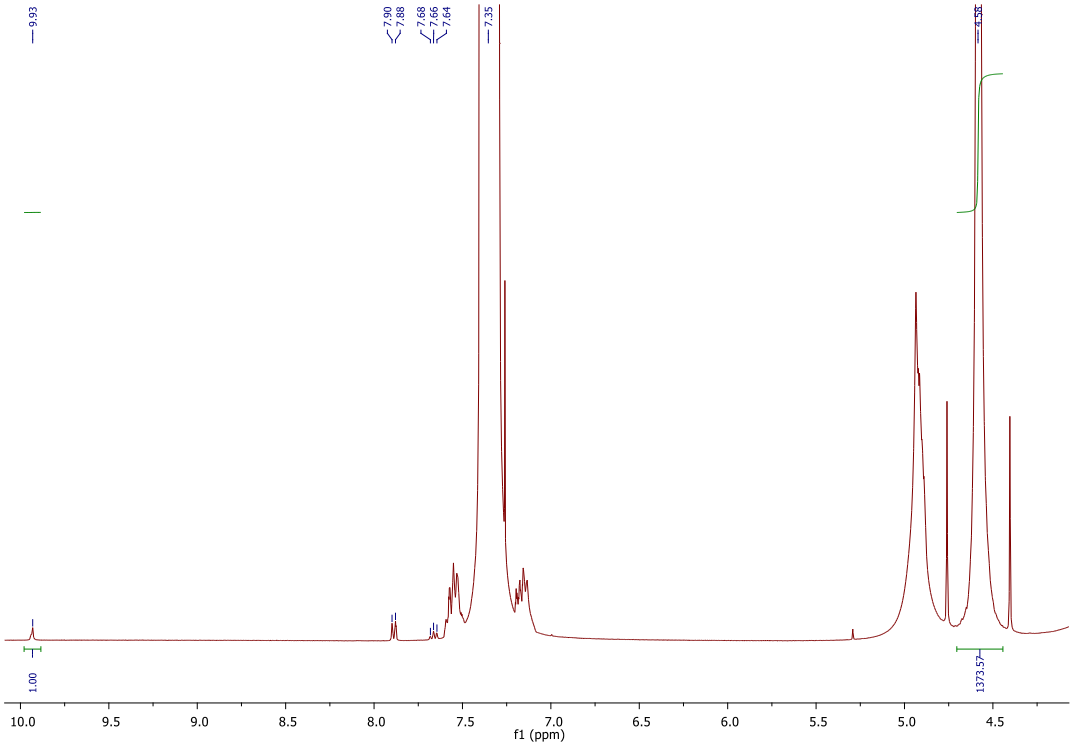

Figure 146: ^{1}H NMR of the reaction mix of benzyl alcohol and benzaldehyde in aqueous conditions with Pnz-G. Taken in $CDCl_3$.

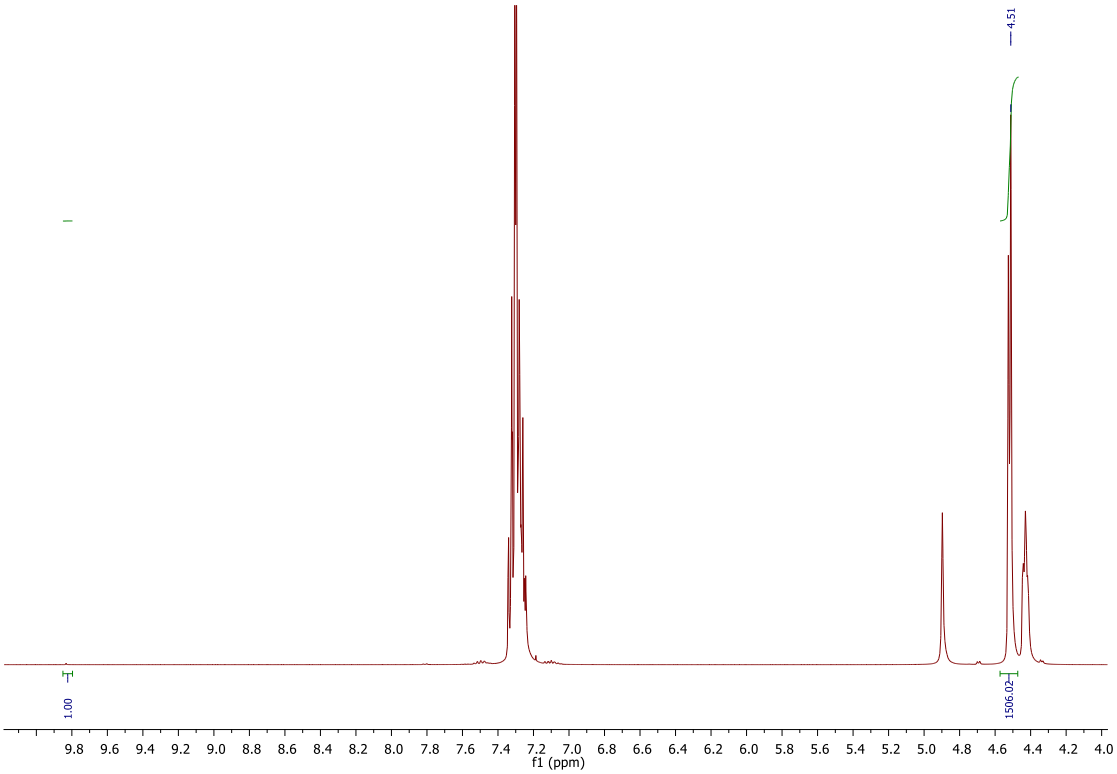

Figure 147: ^{1}H NMR of the reaction mix of benzyl alcohol and benzaldehyde in alkaline conditions with Pnz-G. Taken in $CDCl_3$.

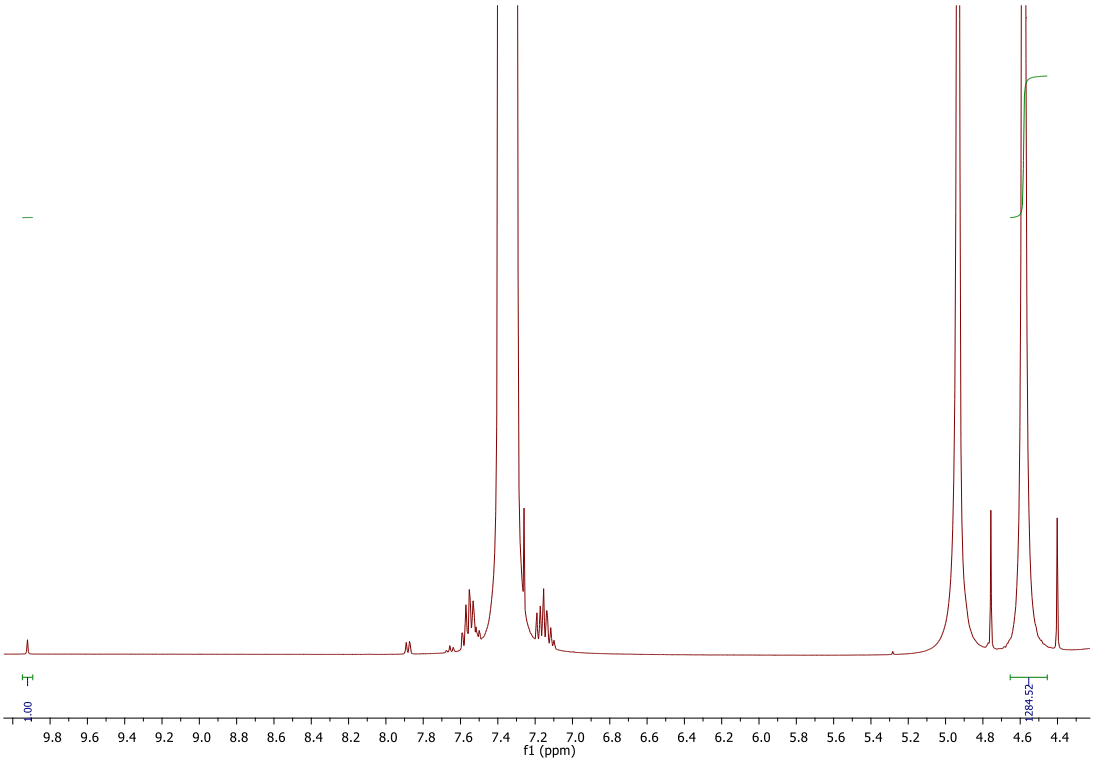

Figure 148: ^{1}H NMR for Benzyl alcohol oxidation with Pur-G. NMR taken in $CDCl_3$.

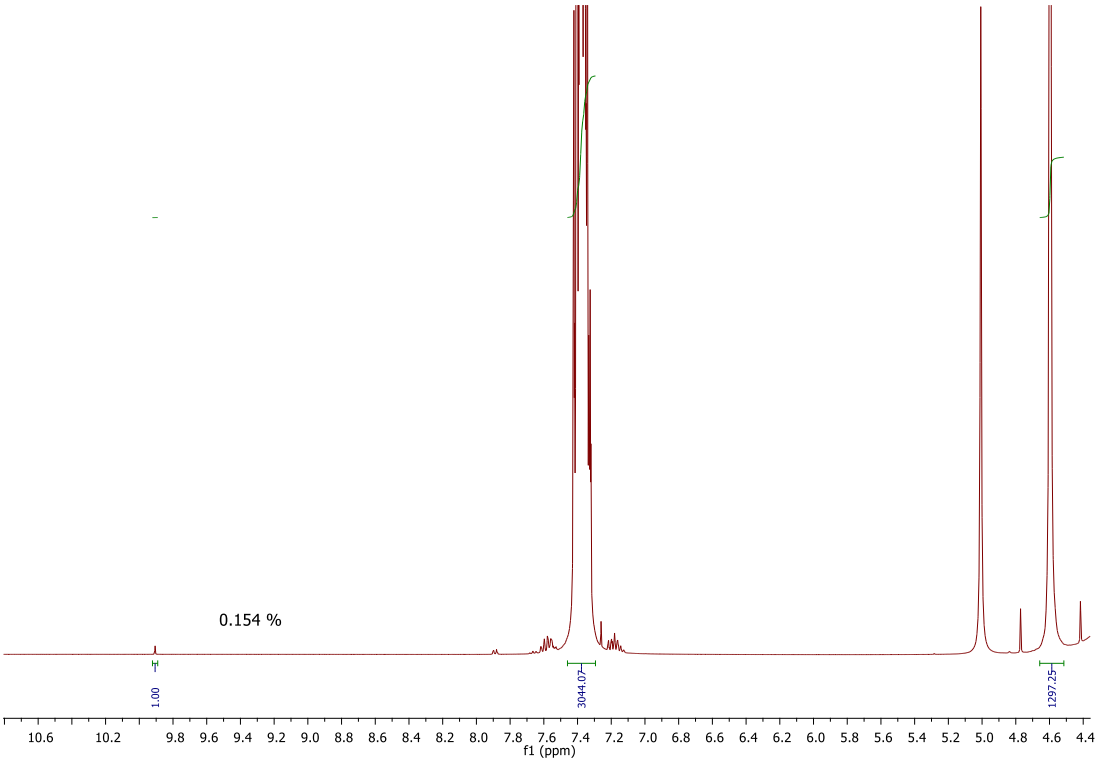

Figure 149: ^{1}H NMR for Benzyl alcohol oxidation with Fsc-G. NMR taken in $CDCl_3$.

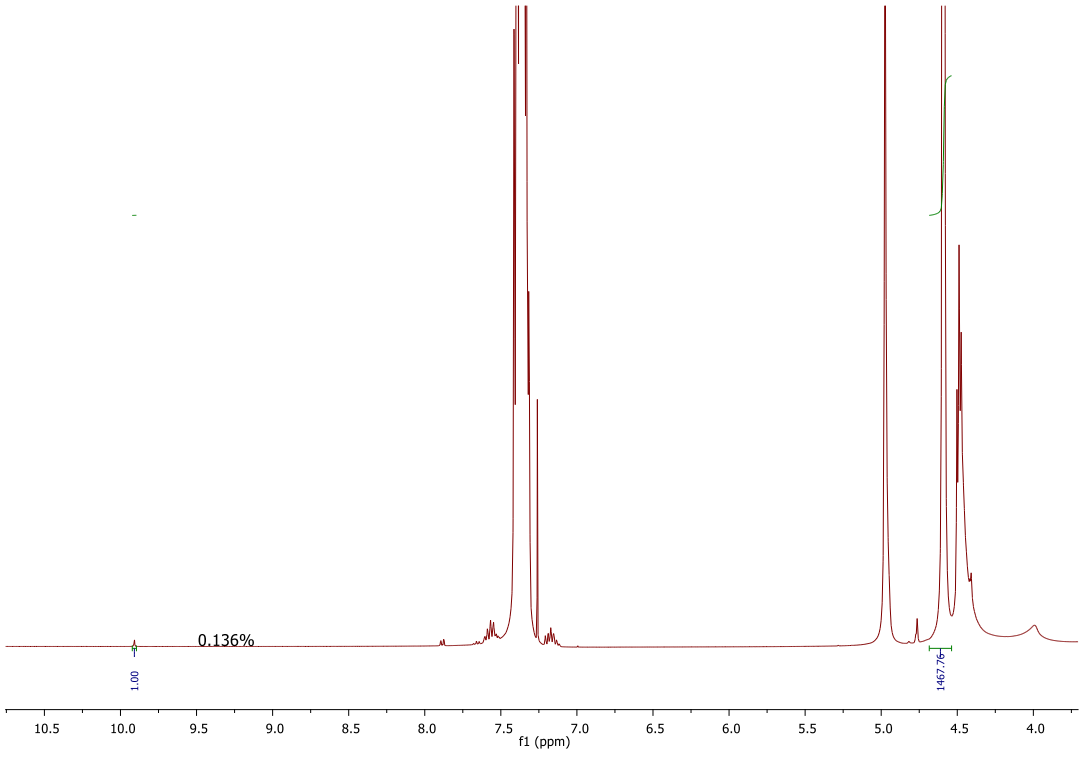

Figure 150: ^{1}H NMR for Benzyl alcohol oxidation with Chr-G. NMR taken in $CDCl_3$.

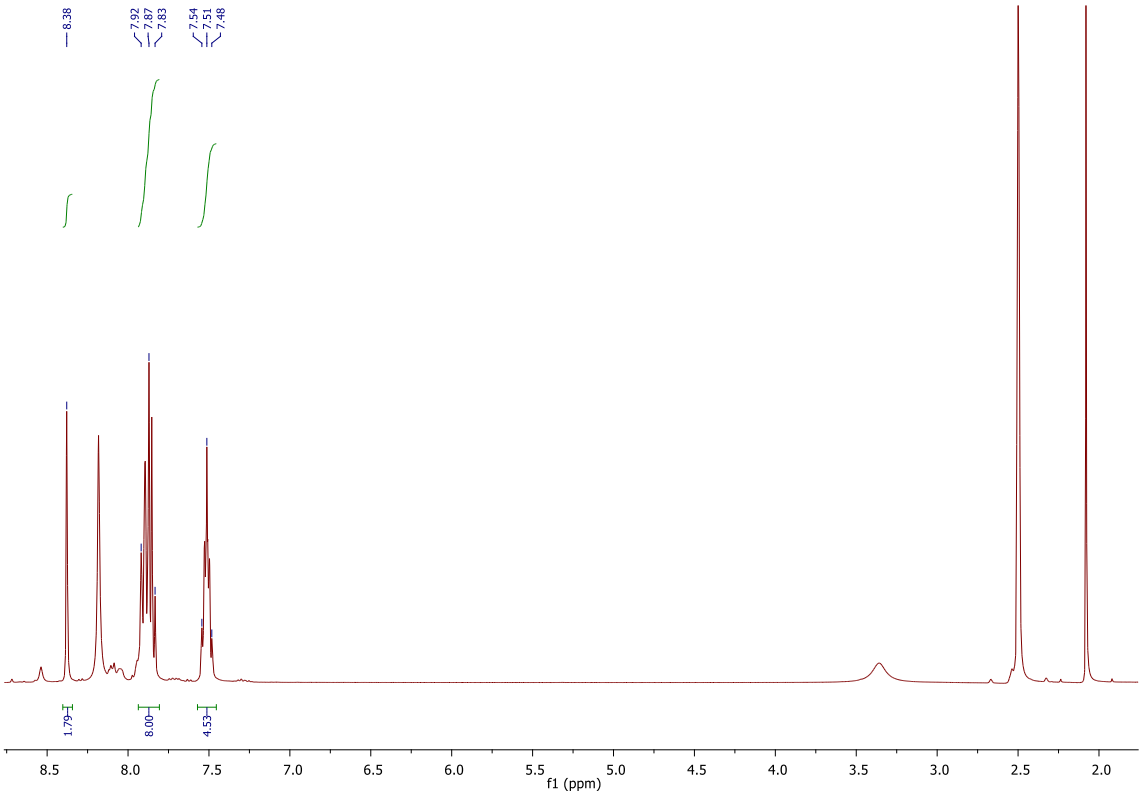

Figure 151: ^{1}H NMR spectrum of 2-naphylboronic acid reaction, suggesting the presence of di-2-naphthylborinic acid, taken in d_6-DMSO.

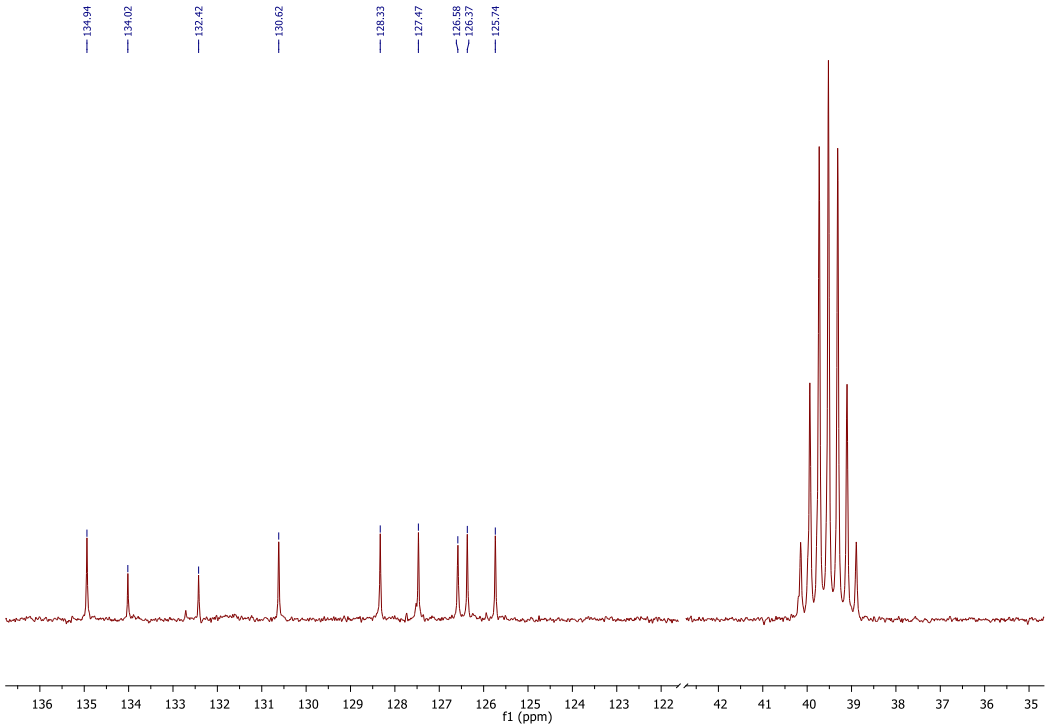

Figure 152: ^{13}C NMR spectrum of 2-naphylboronic acid reaction, suggesting the presence of di-2-naphthylborinic acid, taken in d_6-DMSO.